

1. REPORT NUMBER CA12-2149	2. GOVERNMENT ASSOCIATION NUMBER	3. RECIPIENT'S CATALOG NUMBER
4. TITLE AND SUBTITLE The Feasibility of Using Buckling-Restrained Braces for Long-Span Bridges A Case Study		5. REPORT DATE September 2011
7. AUTHOR Joel Lanning, Gianmario Benzoni, Chia-Ming Uang		6. PERFORMING ORGANIZATION CODE
9. PERFORMING ORGANIZATION NAME AND ADDRESS Department of Structural Engineering Jacobs School of Engineering University of California, San Diego La Jolla, California 92093-008		8. PERFORMING ORGANIZATION REPORT NO.
12. SPONSORING AGENCY AND ADDRESS California Department of Transportation Division of Engineering Services 1801 30th Street., MS #9-2/5I Sacramento, California 95816		10. WORK UNIT NUMBER
15. SUPPLEMENTARY NOTES		11. CONTRACT OR GRANT NUMBER 65A0358
		13. TYPE OF REPORT AND PERIOD COVERED Final Report
		14. SPONSORING AGENCY CODE

Prepared in cooperation with the State of California Department of Transportation.

16. ABSTRACT

This report summarizes a case study investigating the feasibility of using buckling-restrained braces for use on long-span bridges. In particular, the case study presented considers the feasibility of using buckling-restrained braces in a seismic retrofit for the Vincent Thomas Bridge which is located near the Palos-Verde Fault in Long Beach, California. The existing seismic response mitigation system includes viscous fluid dampers that incur damage, characterized by loss of the viscous fluid, as a result of ambient bridge motion. In an effort to provide a maintenance-free system for the bridge, this research focuses on simulated structural response of the bridge outfitted with buckling-restrained braces to ascertain both their seismic and serviceability performance requirements. This report does not address the many design-oriented issues involved with actual implementation of such a retrofit scheme, which would require a detailed evaluation of the bridge structure and further consideration of the likely forces imparted upon the bridge by the buckling-restrained braces. Utilization of buckling-restrained braces is currently uncommon on U.S. bridge structures, and therefore the study reveals some unique testing opportunities. Performing such testing would confirm the ability of buckling-restrained braces to sustain the required simulated near-fault seismic deformational demands, and would expand upon the available test data for buckling-restrained braces for bridge applications in the US.

17. KEY WORDS Buckling-Restrained Brace, BRB, Long-Span Bridges, Vincent Thomas Bridge, Near-Fault, Near-Field	18. DISTRIBUTION STATEMENT No restrictions. This document is available to the public through the National Technical Information Service, Springfield, Virginia 22161
19. SECURITY CLASSIFICATION (of this report) Unclassified	20. NUMBER OF PAGES 160
	21. COST OF REPORT CHARGED

DISCLAIMER STATEMENT

This document is disseminated in the interest of information exchange. The contents of this report reflect the views of the authors who are responsible for the facts and accuracy of the data presented herein. The contents do not necessarily reflect the official views or policies of the State of California or the Federal Highway Administration. This publication does not constitute a standard, specification or regulation. This report does not constitute an endorsement by the Department of any product described herein.

For individuals with sensory disabilities, this document is available in alternate formats. For information, call (916) 654-8899, TTY 711, or write to California Department of Transportation, Division of Research, Innovation and System Information, MS-83, P.O. Box 942873, Sacramento, CA 94273-0001.



**STRUCTURAL SYSTEMS
RESEARCH PROJECT**

Report No.
SSRP-11/09

**THE FEASIBILITY OF USING BUCKLING-
RESTRAINED BRACES FOR LONG-SPAN
BRIDGES: A CASE STUDY**

by

**JOEL LANNING
GIANMARIO BENZONI
CHIA-MING UANG**

Final Report Submitted to the California Department of
Transportation under Contract No. 65A0358

September 2011

Department of Structural Engineering
University of California, San Diego
La Jolla, California 92093-0085

University of California, San Diego
Department of Structural Engineering
Structural Systems Research Project

Report No. SSRP-11/09

**The Feasibility of Using Buckling-Restrained Braces for
Long-Span Bridges: A Case Study**

by

Joel Lanning

Graduate Student Researcher

Gianmario Benzoni

Research Scientist of Structural Engineering

Chia-Ming Uang

Professor of Structural Engineering

Final Report to Submitted to the California Department of Transportation
under Contract No. 65A0358

Department of Structural Engineering
University of California, San Diego
La Jolla, California 92093-0085

September 2011

ABSTRACT

This report summarizes a case study investigating the feasibility of using buckling-restrained braces for use on long-span bridges. In particular, the case study presented considers the feasibility of using buckling-restrained braces in a seismic retrofit for the Vincent Thomas Bridge which is located near the Palos-Verde Fault in Long Beach, California. The existing seismic response mitigation system includes viscous fluid dampers that incur damage, characterized by loss of the viscous fluid, as a result of ambient bridge motion. In an effort to provide a maintenance-free system for the bridge, this research focuses on simulated structural response of the bridge outfitted with buckling-restrained braces to ascertain both their seismic and serviceability performance requirements. This report does not address the many design-oriented issues involved with actual implementation of such a retrofit scheme, which would require a detailed evaluation of the bridge structure and further consideration of the likely forces imparted upon the bridge by the buckling-restrained braces. Utilization of buckling-restrained braces is currently uncommon on U.S. bridge structures, and therefore the study reveals some unique testing opportunities. Performing such testing would confirm the ability of buckling-restrained braces to sustain the required simulated near-fault seismic deformational demands, and would expand upon the available test data for buckling-restrained braces for bridge applications in the US.

ACKNOWLEDGEMENTS

Funding for this research was provided by the California Department of Transportation under Contract No. 65A0358 with Dr. Charly Sikorsky as the project manager. The authors also would like to acknowledge Lian Duan, Richard Heninger, Don Lee, and Li-Hong Sheng for providing advice to this project.

TABLE OF CONTENTS

ABSTRACT	i
ACKNOWLEDGEMENTS	ii
TABLE OF CONTENTS	iii
LIST OF FIGURES	v
LIST OF TABLES	vii
1. INTRODUCTION	1
1.1 Problem Statement	1
1.2 Research Objective and Scope	3
2. BUCKLING-RESTRAINED BRACES	12
2.1 Device Description.....	12
2.2 Structural Performance and Testing of Proprietary Devices	13
2.3 Finite Element Modeling	15
3. MODELING OF THE VINCENT THOMASE BRIDGE	24
3.1 Structural Analysis Software	24
3.1.1 ADINA Model.....	24
3.1.2 Perform-3D Model	25
3.1.3 Correlation	26
3.2 Seismic Input Motions	26
3.2.1 Site Specific Design-Level Earthquake	26
3.2.2 Site Recorded Earthquakes	30
3.2.3 Ambient Bridge Motion.....	31
3.3 Existing Bridge Model Design-Level Response	31
4. SEISMIC RESPONSE EVALUATION OF BRB-RETROFIT OF VTB: A PARAMETRIC STUDY	47
4.1 Introduction.....	47
4.2 BRB Design Parameters.....	48
4.3 Global Parametric Study	50
4.3.1 Effect of BRB Post-Yield Stiffness	50
4.3.2 Effect of BRB Yield Strength.....	51
4.3.3 Perform-3D and ADINA Global Response Comparison	52
4.3.4 Concluding Remarks	53
4.4 Parametric Study with Local Adjustment of BRB Parameters	53

4.4.1 Effect of γ_{S-C} on Bridge Response	54
4.4.2 Effect of γ_{S-T} on Bridge Response	55
4.4.3 Effect of γ_{M-T} on Bridge Response	56
4.4.4 Effect of L_{S-C} on Bridge Response.....	57
4.4.5 Effect of L_{S-T} on Bridge Response.....	57
4.4.6 Effect of L_{M-T} on Bridge Response.....	58
4.4.7 Insensitivity of Length Variation on Adjacent BRBs.....	58
4.5 Final Parametric Refinement and Concluding Remarks.....	58
4.6 Bridge Superstructure Demands and Capacities	60
4.6.1 Tower.....	60
4.6.2 Cable Bent	62
4.6.3 Span Trusses	62
4.7 BRB Demands and Capacities	62
4.8 Feasibility and Required Data.....	64
5. SERVICEABILITY EVALUATION	100
5.1 Introduction.....	100
5.2 Method Used to Obtain BRB Serviceability Demand	100
5.2.1 Demands and Performance.....	101
6. SUMMARY, CONCLUSIONS, AND RECOMMENDATIONS.....	105
6.1 Summary	105
6.2 Conclusions.....	105
6.3 Recommendations.....	106
REFERENCES.....	109
Appendix A – ADINA/Perform-3D Model Correlation Study	112
Appendix B – Seismic Ground Motion Recorded at VTB Site.....	125
Appendix C – Additional Serviceability Considerations.....	133

LIST OF FIGURES

Figure 1.1 Vincent Thomas Bridge.....	6
Figure 1.2 Schematic of Existing Structural Configuration.....	7
Figure 1.3 Photos of Viscous Dampers.....	8
Figure 1.4 VTB Instrumentation Layout and Recorded Event Timeline.....	9
Figure 1.5 Photos of VTB Damper Disassembly and Internal Damage.....	10
Figure 1.6 Damaged Viscous Damper Hysteretic Behavior.....	11
Figure 2.1 Examples of Typical Buckling-Restrained Brace Anatomy.....	19
Figure 2.2 Examples of All-Steel Buckling-Restrained Braces.....	19
Figure 2.3 AISC Standard Loading Protocol for Buckling-Restrained Braces.....	20
Figure 2.4 Example of Resilient BRB Performance.....	20
Figure 2.5 BRB Bilinear Model and Justification.....	21
Figure 2.6 Additional Bilinear BRB Model Justification.....	22
Figure 2.7 Examples of Tested BRB Cumulative Ductility and Maximum Strain.....	23
Figure 3.1 Seismic Site Overview of VTB.....	34
Figure 3.2 Bent 10 Longitudinal Ground Motion (Moffatt and Nichol 1996).....	35
Figure 3.3 East Tower Transverse Ground Motion (Moffatt and Nichol 1996).....	36
Figure 3.4 Bent 10 Longitudinal Ground Motion (Earth Mechanics 2011).....	37
Figure 3.5 East Tower Transverse Ground Motion (Earth Mechanics 2011).....	38
Figure 3.6 Design-Level Earthquake Pseudo-Acceleration Response Spectra ($\zeta=5\%$)....	39
Figure 3.7 Design-Level Earthquake, West Side Longitudinal.....	40
Figure 3.8 Design-Level Earthquake, East Side Longitudinal.....	41
Figure 3.9 Design-Level Earthquake, West Side Transverse.....	42
Figure 3.10 Design-Level Earthquake, East Side Transverse.....	43
Figure 3.11 Design-Level Earthquake, West Side Vertical.....	44
Figure 3.12 Design-Level Earthquake, East Side Vertical.....	45
Figure 3.13 Original* and Modified Longitudinal West Side Ground Displacements....	46
Figure 4.1 Depiction of BRB Stiffness and Strength Space.....	73
Figure 4.2 BRB Schemes and Length Variation.....	74
Figure 4.3 Effect of BRB Post-Yield Stiffness, α , on VTB Response: Main/Tower.....	75
Figure 4.4 Effect of BRB Yield Strength, γ , on VTB Response: Side/Cable Bent.....	76
Figure 4.5 Effect of BRB Yield Strength, γ , on VTB Response: Side/Tower.....	77
Figure 4.6 Effect of BRB Yield Strength, γ , on VTB Response: Main/Tower.....	78
Figure 4.7 Comparison of Perform-3D and ADINA Responses: Side/Cable Bent.....	79
Figure 4.8 Comparison of Perform-3D and ADINA Responses: Side/Tower.....	80
Figure 4.9 Comparison of Perform-3D and ADINA Responses: Main/Tower.....	81
Figure 4.10 Effect of Local BRB Yield Strength, γ , on VTB Response: Side/Cable Bent.....	82
Figure 4.11 Effect of Local BRB Yield Strength, γ , on VTB Response: Side/Tower.....	83
Figure 4.12 Example of Main Span BRB East and West Out of Phase.....	84
Figure 4.13 Effect of Local BRB Yield Strength, γ , on VTB Response: Main/Tower....	85
Figure 4.14 Local Parameter Refinement: Side/Cable Bent.....	86
Figure 4.15 Localized Parameter Refinement: Side/Tower.....	87
Figure 4.16 Localized Parameter Refinement: Main/Tower.....	88
Figure 4.17 Local Parameter Refinement: Adjacent Location Insensitivities.....	89

Figure 4.18 Final Feasible BRB Solutions	90
Figure 4.19 Design-Level Earthquake Main Span Acceleration Response	91
Figure 4.20 Example Cumulative Energy Dissipation Time Histories.....	92
Figure 4.21 BRB and Damper Energy Dissipation Comparison by Location.....	93
Figure 4.22 Tower Seismic Force Demand Envelopes: Design-Level Earthquake.....	94
Figure 4.23 Design-Level Earthquake BRB and Damper Axial Force Phase Relation....	95
Figure 4.24 1994 Northridge Earthquake BRB Axial Force Phase Relation	96
Figure 4.25 Cable Bent Seismic Force Demand Envelopes: Design-Level Earthquake ..	96
Figure 4.26 Example BRB Results As Reported by Takeuchi et al. (2008).....	97
Figure 4.27 BRB Retrofit Design-Level Earthquake Axial Strain Time Histories	98
Figure 4.28 Design-Level Earthquake BRB and Damper Hysteretic Behavior	99
Figure 5.1 Recorded and Interpolated Ambient Motion of VTB Southeast Tower.....	103
Figure 5.2 Deck-to-Tower Relative Displacement due to Ambient Vibration.....	104
Figure A.1 ADINA Locked versus Unlocked Foundation Model Responses	119
Figure A.2 Modification Required for Eigenvalue Analysis Comparison	120
Figure A.3 Modified Model Span Mode Shapes	120
Figure A.4 Fourier Analysis of Ambient Deck Response	121
Figure A.5 Fourier Analysis of Tower Longitudinal Ambient Response.....	122
Figure A.6 Fourier Analysis of Tower Transverse Ambient Response.....	122
Figure A.7 Tower Mode Shapes	123
Figure A.8 ADINA versus Perform-3D Dynamic Time History Response Comparison	124
Figure B.1 Moderate-level Site Recorded Earthquakes, West Longitudinal.....	125
Figure B.2 Moderate-level Site Recorded Earthquakes, East Longitudinal	126
Figure B.3 Moderate-level Site Recorded Earthquakes, West Transverse	127
Figure B.4 Moderate-level Site Recorded Earthquakes, East Transverse	128
Figure B.5 Low-Level Site Recorded Earthquakes, West Longitudinal	129
Figure B.6 Low-Level Site Recorded Earthquakes, East Longitudinal.....	130
Figure B.7 Low-Level Site Recorded Earthquakes, West Transverse.....	131
Figure B.8 Low-Level Site Recorded Earthquakes, East Transverse	132
Figure C.1 VTB Influence Line Loading.....	141
Figure C.2 West Side BRB Axial Stress Influence Lines, 1 kip Line Load.....	142
Figure C.3 East Side BRB Axial Stress Influence Lines, 1 kip Line Load	143
Figure C.4 Live Load Maximum Force Effect Patterns	144
Figure C.5 Live Load Maximum Force Effect Continuous Lane Patterns	145
Figure C.6 BRB Stress with Live Load Scale Factor, Service II Load Pattern 2	146
Figure C.7 BRB Stress with Live Load Scale Factor, Service II Load Pattern 3	146
Figure C.8 BRB Stress with Live Load Scale Factor, Live Load Deflection Pattern 2..	147
Figure C.9 BRB Stress with Live Load Scale Factor, Live Load Deflection Pattern 3..	147
Figure C.10 Main and Side Span End Hinges	148
Figure C.11 Illustration of Truss Rotation to BRB Axial Deformation	148
Figure C.12 Schematic Representation of Inclined BRB Orientation	149
Figure C.13 Effect of BRB Inclination	149

LIST OF TABLES

Table 1.1 Existing Viscous Damper Properties	5
Table 2.1 Examples of Tested Proprietary BRB Properties and Performance	17
Table 2.2 Examples Post-yield Stiffnesses	18
Table 3.1 Input Ground Motion Information	32
Table 3.2 Modified Earth Mechanics Records Used as Design-Level Input Motion	32
Table 3.3 Response of Existing Bridge Model with Fully Effective and Ineffective Viscous Dampers	33
Table 4.1 Parametric Matrices for Global Adjustment of BRB Mechanical Properties...	65
Table 4.2 Parametric Matrices for Local Adjustment of BRB Mechanical Properties	66
Table 4.3 Examples of Varied Characteristic Values	67
Table 4.4 BRB Retrofit and Damper Model Design-Level Earthquake	68
Table 4.5 BRB Retrofit and Damper Model 1994 Northridge Responses	69
Table 4.6 BRB Retrofit and Damper Model 1987 Whittier Responses.....	69
Table 4.7 BRB Retrofit and Damper Model 2008 Inglewood Responses	70
Table 4.8 BRB Retrofit and Damper Model 2009 Chino Hills Responses	70
Table 4.9 Damper Model Natural Periods and Modal Effective Mass Fractions.....	71
Table 4.10 BRB Retrofit Model Natural Periods and Modal Effective Mass Fractions ..	71
Table 4.11 Comparison of BRB Axial Force Demands	72
Table 4.12 Damper to Tower Connection Capacities and Demands	72
Table A.1 Summary of Modified Model Span Modes	117
Table A.2 Summary of Span Modes Obtained from Fourier Analysis.....	117
Table A.3 Summary of Tower Modal Analysis.....	118
Table C.1 Fatigue Stress Demands Due to AASHTO Fatigue Truck.....	140
Table C.2 Vehicular Live Load BRB Maximum Stress and Ductility Demands	140

1. INTRODUCTION

1.1 Problem Statement

The Vincent Thomas Bridge (VTB) is one of several major bridges in California which are managed by Caltrans. The span serves as the connection between San Pedro and Terminal Island near Long Beach, California on Route 47. Caltrans designed the bridge in 1960 and construction was completed in 1964. It has also undergone two major seismic retrofits, one in 1980 and the other in 1996.

The superstructure consists of a main span of 1500 feet and two side spans of 506 feet which are suspended from two steel towers. Leading to the suspended spans are additional twenty approach spans, ten on either side of the bridge, which are supported by reinforced concrete bents. The roadway is approximately 52 feet wide, which provides 4 lanes of traffic. A clear navigation height of 185 feet is provided by the suspended main span (Moffatt and Nichol 1996).

The suspended spans, which are most important for the current study, are built on two steel stiffening trusses tied together by transverse steel trusses. Spanning the transverse trusses are steel W-section stringers, upon which the concrete roadway rests. Suspender ropes support the spans from two anchored suspension cables that bear on cable saddles atop the steel towers and cable bents. Figure 1.1(a) contains a photograph of the considered portion of the bridge structure, and Figure 1.1(b) provides a labeled elevation view of the structure. Schematic representations, Figure 1.2, shows the general configuration as well as some important aspects of the bridge structure including the deck lateral restraints and span support conditions.

The Vincent Thomas Bridge was first retrofitted for seismic performance and instrumented with seismic sensors in 1980. This retrofit included cable restrainers, abutment seat shear key extensions, and girder lateral supports. These structural changes are of less significance to the current research than the more recent retrofit, as they do not concern the suspended spans. The seismic sensors were installed at 26 locations throughout the structure (Moffatt and Nichol 1996). These sensors record acceleration at various points throughout the structure. The sensor locations are displayed in Figure 1.4.

The second retrofit, which is currently in place on the existing structure, consists of various types of strengthening of approach footings, columns, bent caps, and end diaphragms. Additionally, the retrofit included tower reinforcement and modifications to bearings, trusses, deck, cable saddles, deck shear connectors, and suspender ropes. Most pertinent to the current study are viscous dampers which were installed between the cable bents and side spans, as well as between the tower and both side and main spans. The viscous damper locations are schematically depicted in Figure 1.2, and the devices are visible in satellite photographs shown in Figure 1.3 for further reference. The installation of the dampers was intended to limit the displacement across the span to tower expansion joints and mitigate impact of the bridge deck to the cellular steel towers due to earthquake excitation (Moffatt and Nichol 1996). The behavior of the viscous dampers is governed by the equation:

$$P_{damper} = Cv^n \quad (1.1)$$

where C = viscous damping constant,

v = relative velocity of the member ends, and

n = viscous damping force velocity exponent (= 1.0),

Physical characteristics of these dampers together with the design axial capacity, $P_{n,damper}$, are listed in Table 1.1.

$$P_{n,damper} = Cv_{max} \quad (1.2)$$

where v_{max} = damper maximum design velocity

Given that 50 years of service have already been provided by the VTB, it has undergone a number of seismic events. Since the installation of the sensor array in 1980, several events have been recorded. This is valuable information for model validation and comparison. However it is important to distinguish the proper structural configuration that was present during which event. Therefore, a timeline is provided in Figure 1.4(b) showing which configuration applies to which recorded event. The records used from these events are further discussed in Section 3.2.2.

In recent years Caltrans has reported concerns about increased movement of the VTB during ambient conditions characterized by wind and traffic loading. Maintenance and

inspection has revealed leakage of the viscous fluid from the dampers currently in-place. Evidence of this is provided in the observed damage to the dampers in the form of internal wearing marks that lead to the leakage. Photos from a disassembled device are provided in Figure 1.5, and show an example of the internal damage. A few studies have been conducted to investigate the effect of the damaged dampers (Benzoni et al. 2008; Graziotti 2010). Increased bridge seismic response and impact-like damper force time history responses are observed when simulations account for damaged damper conditions (Figure 1.6). This led to concerns over the viability of the current seismic response mitigation configuration, due to the amount of maintenance required to keep the dampers 100% full and effective. When damper conditions are taken to 0% effective, the bridge response due to the design-level earthquake is very poor and impact is likely to occur. This analysis has been independently performed and is presented and discussed in Section 3.3.

Regardless of the seismic concerns, the ambient motion is reportedly excessive, causing increased wear and tear on structural components such as bolts and connections. Therefore, any proposed seismic mitigation retrofit should aim to also mitigate ambient motion of the bridge.

1.2 Research Objective and Scope

The problems with the viscous dampers on the VTB have motivated the search for a replacement device or retrofit scheme. Out of this situation arose the opportunity to conduct research exploring the feasibility of using buckling-restrained braces (BRBs) on long-span bridges. In particular, this research considers BRBs as a replacement for the existing viscous dampers and aims to determine whether the seismic response of the VTB can feasibly be mitigated by commercially available BRBs.

An actual retrofit of the bridge itself is not proposed, but rather a parametric study is performed to determine a feasible set of BRB parameters, that define the primary characteristics of the braces, which result in sufficiently mitigated VTB seismic response. The practicality of these parameters, with respect to commercially available BRBs, will determine the feasibility of their use on the VTB, and long-span bridges in general. A detailed design-oriented review of the existing bridge structure would be required for actual BRB implementation on the VTB, and is beyond the scope of this report.

These braces, BRBs, are a relatively new structural member which can serve either primarily as a structural fuse or an energy dissipation device. Originally developed for buildings, they are slowly beginning to be implemented in bridges (Carden et al. 2004; Usami et al. 2005; Kanaji et al. 2008). These research projects and implementation plans utilize BRBs as structural fuses, which are intended to protect the remaining structure from seismic damage.

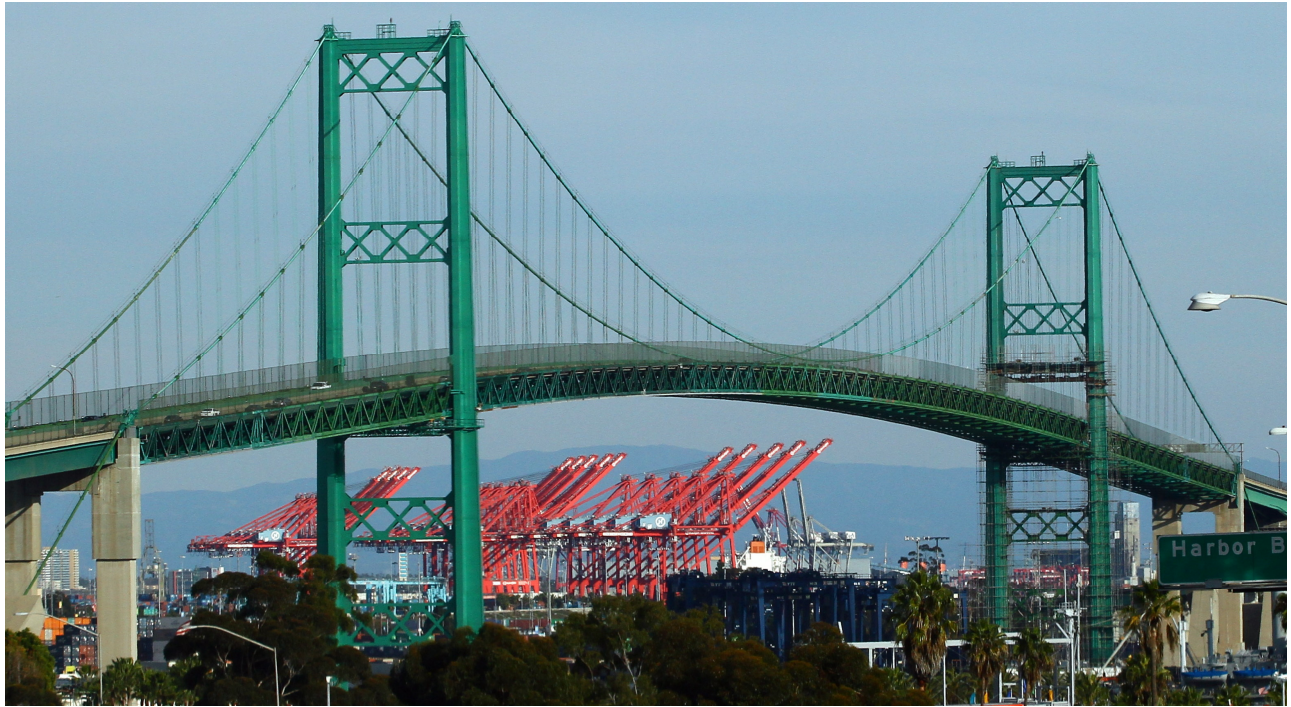
However, for this project the braces would ideally replace the existing viscous dampers and function primarily as energy dissipation devices, and provide equal or better overall bridge response. The dampers were primarily intended to limit the relative displacement between the towers and the suspended spans, thereby mitigating the ability of the spans to impact the cellular steel towers, The braces would also serve to increase the bridge stiffness, which would aid in mitigating motion under service conditions. Furthermore, among several attractive features of BRBs is the fact that they are relatively maintenance free due to their simple construction.

This report summarizes the work accomplished in the feasibility phase of the project. Parametric studies have been carried out to identify the properties required for a feasible BRB retrofit solution. The following sections will provide additional information about BRBs, the models used to predict the member demands, a description of feasible solutions, and a discussion of a proposed test program that would be required for actual implementation of BRB into the VTB structure.

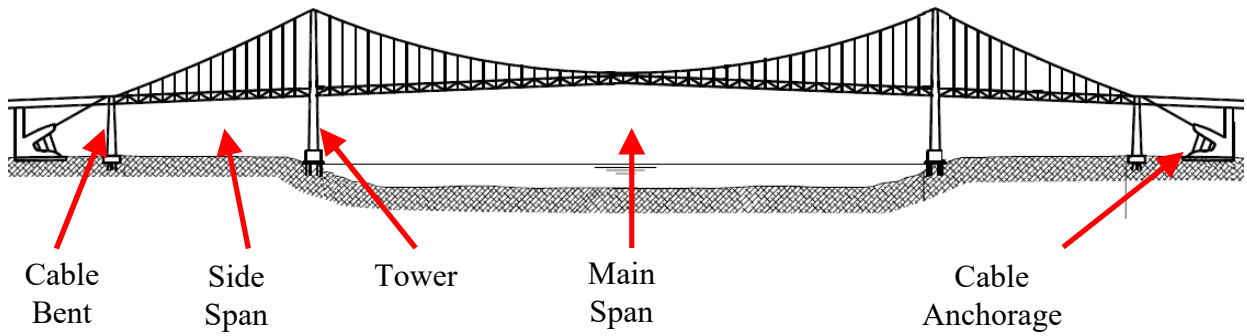
Table 1.1 Existing Viscous Damper Properties

Location	Mid-Stroke Length	Design Axial Capacity, $P_{n,damper}^*$ (kips)	Total Number of Units	Velocity Exponent, n ($P_{damper} = Cv^n$)
Cable Bent to Side	14'-2"	265	16	1.0
Tower to Side	12'-10"	75	16	1.0
Tower to Main	15'-1"	200	8	1.0

*See Eq. 1.2

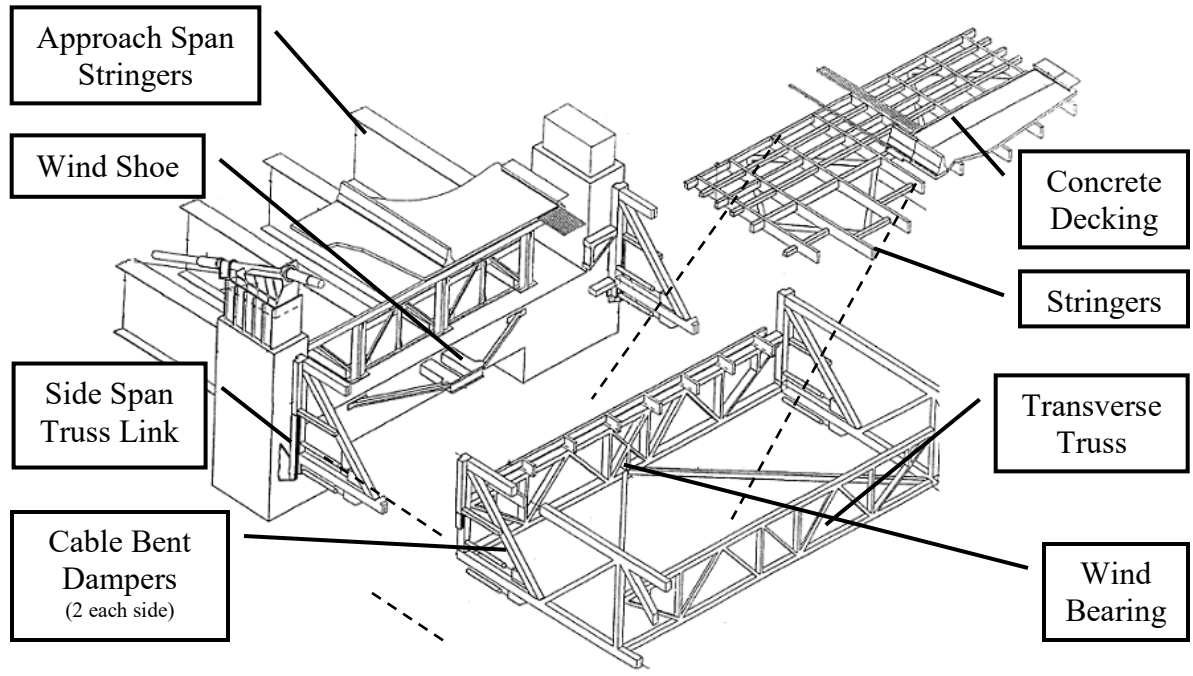


(a) Photo

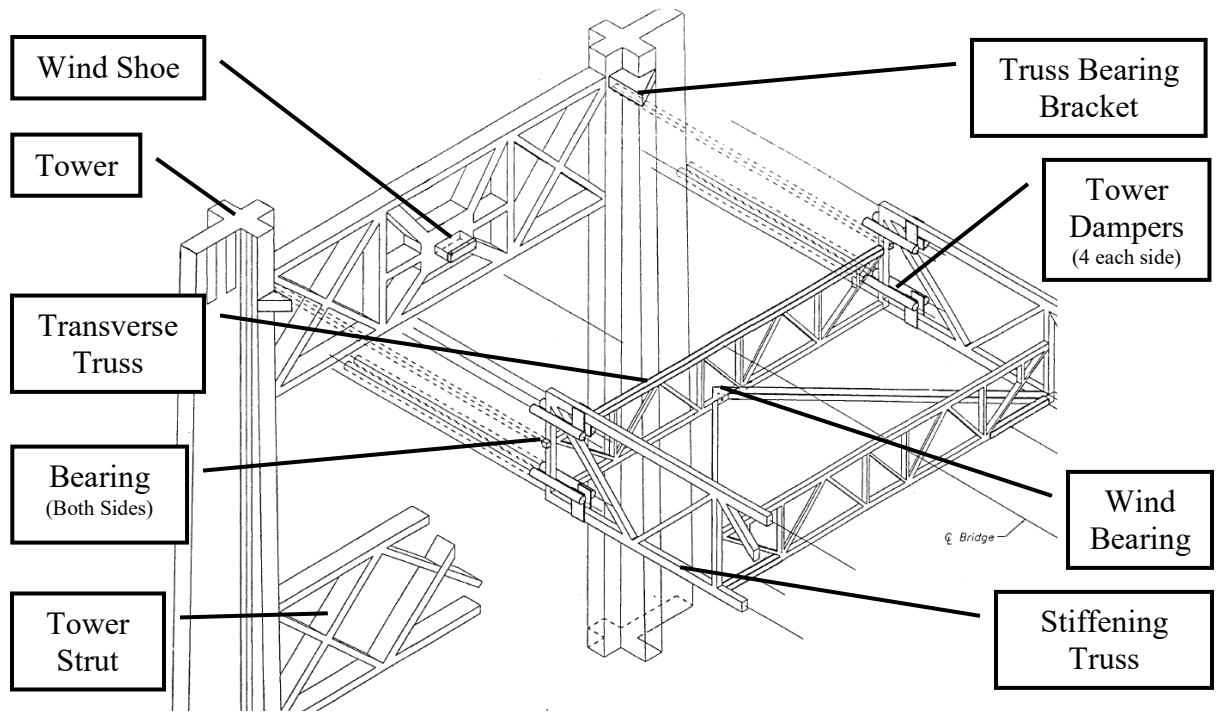


(b) Elevation View

Figure 1.1 Vincent Thomas Bridge

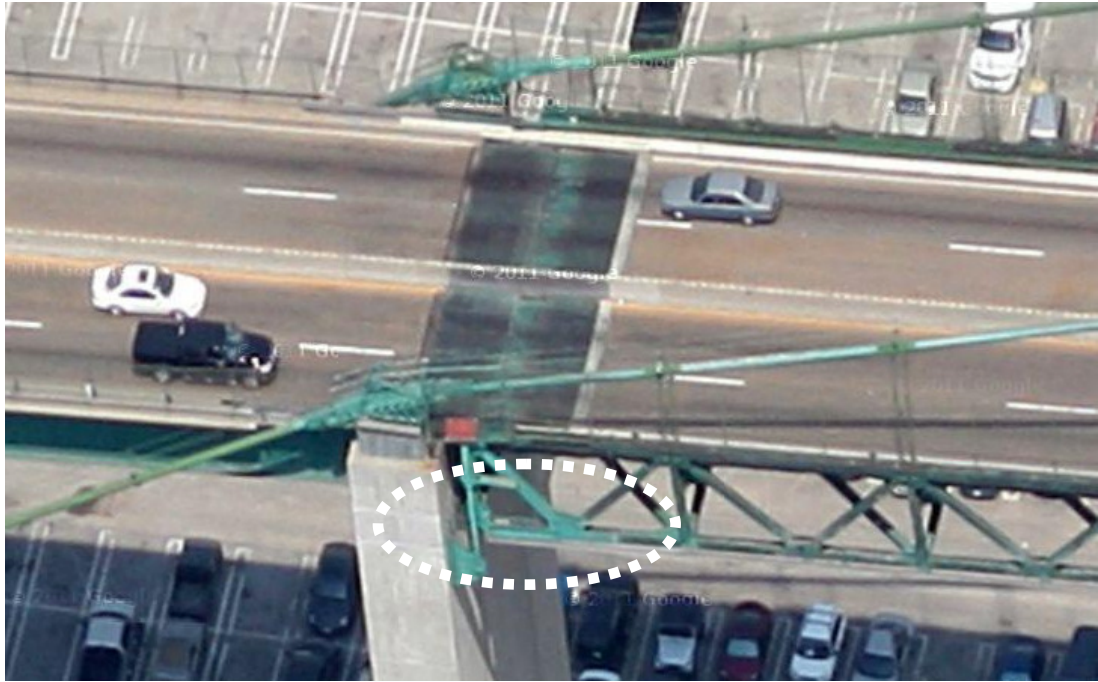


(a) At Cable Bent

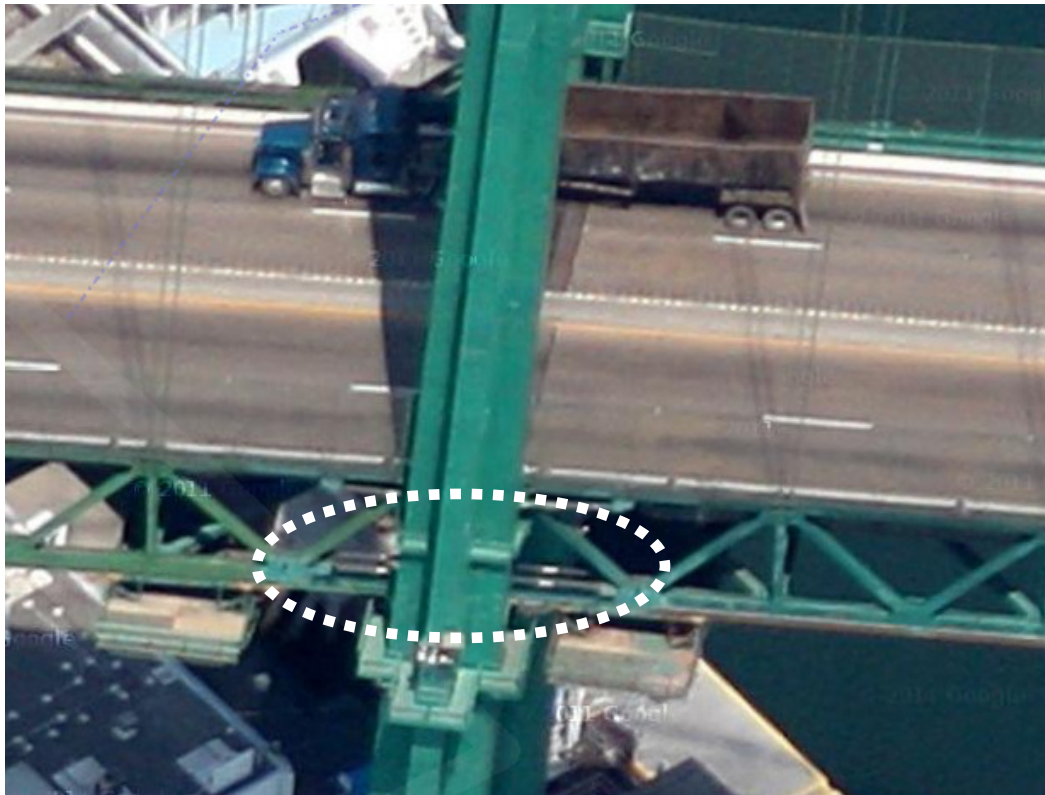


(b) At Towers

Figure 1.2 Schematic of Existing Structural Configuration (VTB Retrofit As-Built Drawings 1996)



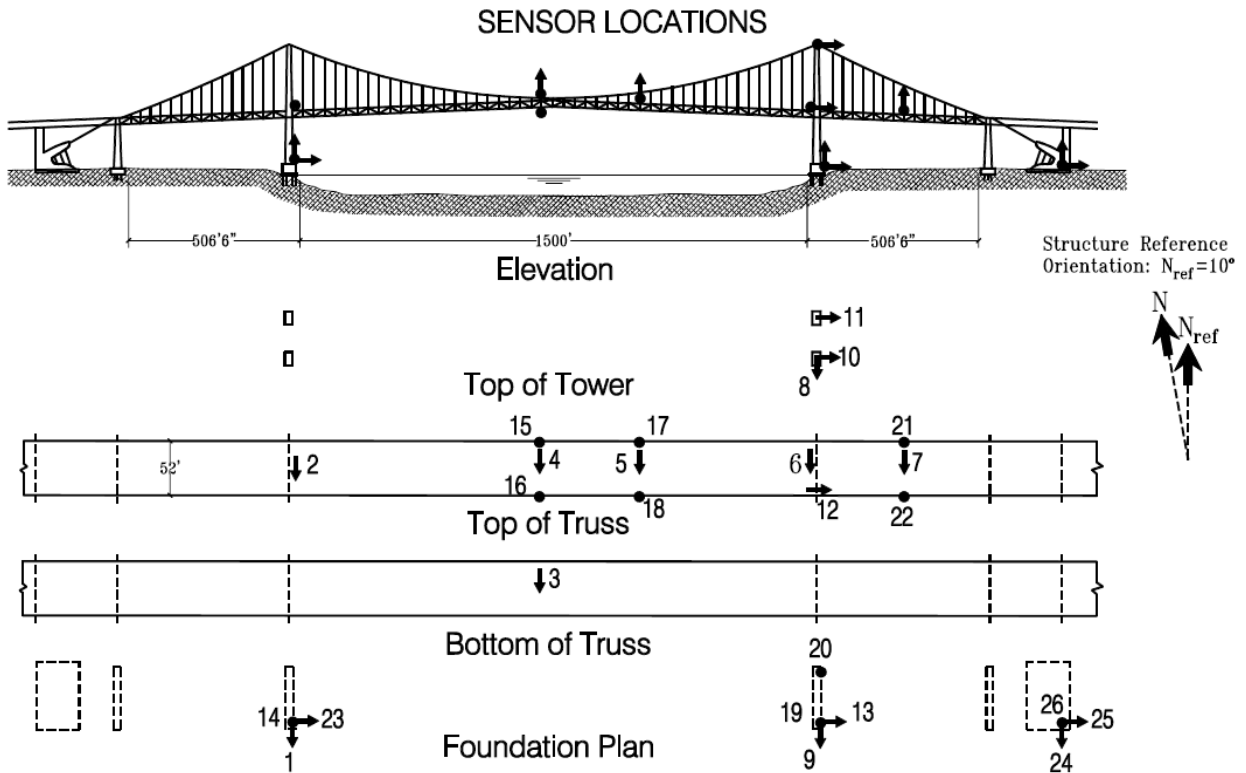
(a) Cable Bent to Side Span



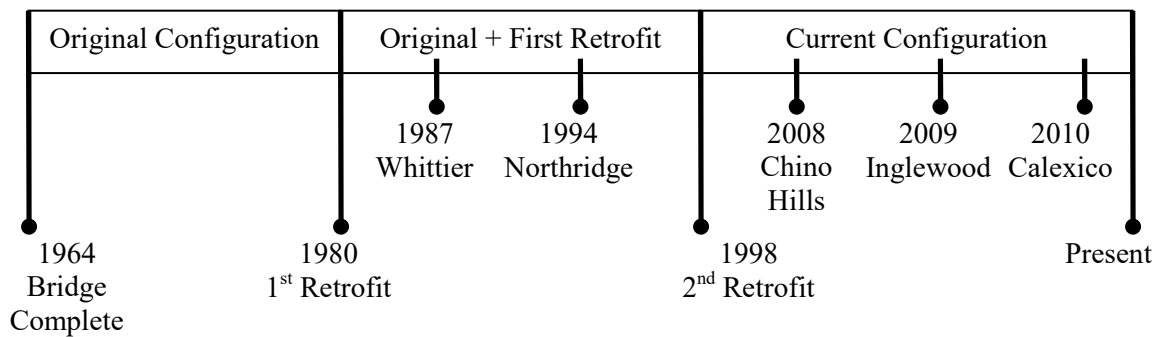
(b) Tower to Side and Main Spans

Figure 1.3 Photos of Viscous Dampers
(Google Maps 2011)

Los Angeles - Vincent Thomas Bridge
 Caltrans Bridge No. 53-1471 (07-LA-47-0.86)
 CSMIP Station No. 14406



(a) Instrumentation Layout



(b) Structural Configurations and Recorded Events Timeline

Figure 1.4 VTB Instrumentation Layout and Recorded Event Timeline
 (CESMD 2011)



Figure 1.5 Photos of VTB Damper Disassembly and Internal Damage (Graziotti 2010)

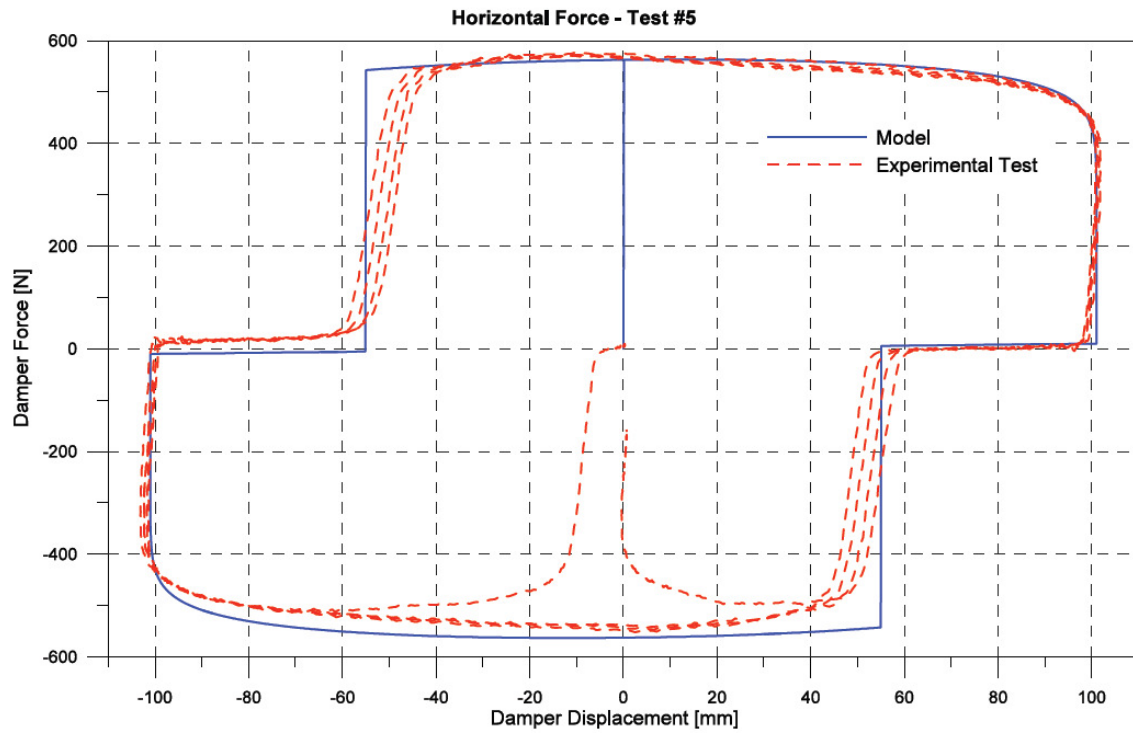


Figure 1.6 Damaged Viscous Damper Hysteretic Behavior (Benzoni et al. 2008)

2. BUCKLING-RESTRAINED BRACES

2.1 Device Description

Although pioneered in the 1970's, buckling-restrained braces (BRBs) received little attention until the mid-nineties after the 1994 Northridge and 1995 Kobe earthquakes. These events fueled research and consequent code provisions which allowed buckling-restrained braces to become better known and understood by structural engineers. Their excellent energy dissipation capacity has been more widely used in Japan; an increasing number of proprietary devices are also being developed and used in the United States (Uang et al. 2004).

Although many BRB designs have been developed and tested, their general anatomy remains fairly consistent, and is shown in Figure 2.1. Typically a steel plate, or core plate, is housed within a steel restraining tube that is filled with mortar. A gap and de-bonding agent are provided between the steel core and mortar, which account for Poisson expansion and decouple the restraining tube from the brace axial forces, respectively. Since compressive loads induce buckling behavior, the core is supported against lateral deformation by the mortar and restraining tube, thereby allowing it to undergo yielding in both tension and compression. This produces excellent energy dissipation with stable and fairly symmetrical hysteretic behavior. Black et al. (2004) have tested many Unbonded Braces™ which are manufactured by Nippon Steel Corporation of Japan, and have been implemented in the designs of many buildings in the United States (Black et al. 2004). CoreBrace and Star Seismic, two Utah based U.S. companies, have submitted many proprietary specimens for testing at the SRMD laboratory at UCSD (Merritt et al. 2003; Newell et al. 2006; Benzoni et al. 2007). These three companies represent almost the entire U.S. market for BRB and are constructed in the manner described above.

BRBs can be constructed in many different ways ranging from sand filled steel tubes as the restraining members (Palazzo et al. 2009) to many varieties of all-steel BRBs which utilize built up steel sections as restraining members (Zhao et al. 2010). Examples of various all-steel BRB cross sections are provided in Figure 2.2.

2.2 Structural Performance and Testing of Proprietary Devices

The performance of proprietary BRBs is fairly uniform as observed in a number of test reports. Almost exclusively, the braces are tested for implementation in buildings and, therefore, have a somewhat different performance expectation as compared to bridges.

Since BRBs were originally developed for use in building structures, qualification tests are usually conducted in accordance with Appendix T of the AISC *Seismic Provisions* 2005 (Sabelli et al. 2004) which requires the following loading sequence (graphically depicted in Figure 2.3) to be applied to the test specimen:

- (1) 2 cycles of loading at the deformation corresponding to $\Delta_b = 1.0 \Delta_{by}$
- (2) 2 cycles of loading at the deformation corresponding to $\Delta_b = 0.5 \Delta_{bm}$
- (3) 2 cycles of loading at the deformation corresponding to $\Delta_b = 1.0 \Delta_{bm}$
- (4) 2 cycles of loading at the deformation corresponding to $\Delta_b = 1.5 \Delta_{bm}$
- (5) 2 cycles of loading at the deformation corresponding to $\Delta_b = 2.0 \Delta_{bm}$
- (6) Additional complete cycles of loading at the deformation corresponding to $\Delta_b = 1.5 \Delta_{bm}$ as required for the brace test specimen to achieve a cumulative inelastic axial deformation of at least 200 times the yield deformation.

where the deformation Δ_b is the steel core axial deformation of the test specimen. Note that Δ_{by} corresponds to the axial deformation at first significant yield, and Δ_{bm} is the axial deformation which corresponds to the design story drift of the building structure. This is not directly applicable to the current research as will be discussed in Section 4.7.

After steps (1) through (5), the cumulative ductility of 200 is required in step (6). This alone provides a reference for just how resilient BRBs are, especially as is relevant to the demands exposed through the parametric study for application to the VTB. As will be later referenced, this bodes well for the idea that BRB members are perhaps capable of much more taxing, but shorter, demand time histories similar to those found in the current research.

A few examples of some basic BRB performance results are displayed in Table 2.1, and show that the AISC Standard Loading Protocol is by far the lower bound of acceptable BRB performance. Especially noticeable is the maximum cumulative ductility achieved compared to that obtained from the standard protocol. Furthermore, a representative example of BRB performance beyond the standard loading protocol is provided in Figure 2.4.

Maximum strains achieved in the specimens shown in Table 2.1 are observed to be in the range of approximately 2 to 4%. The loading protocol is, as previously mentioned, generally dependent on the design story drift which directly influences the tested axial strain. More recent research has shown all-steel BRB is capable of satisfactory low-cycle fatigue cumulative ductility at constant strain amplitudes of 4.5%. Other researchers have reported constant strain amplitude testing of BRB in the range of $\pm 2.4\%$, or peak amplitude of 4.5%, achieving cumulative ductility factors much higher than that required by AISC Seismic Provisions (Nakamura et al. 2000). Additionally, larger strains have been imposed through increasing strain amplitude tests which reached upwards of $\pm 5.2\%$ (Takeuchi et al. 2005). Moreover, tests from shake table earthquake simulations exhibited a half-cycle pulse of 7% maximum strain amplitude, while still achieving very large cumulative ductility measures (Yamaguchi et al. 2004). The aforementioned testing, however, has been conducted in Japan and is reported only in Japanese references but are summarized by Takeuchi et al. 2008. Some of these results are shown in Figure 2.7, along with the cumulative ductility factors reportedly obtained from increasing strain amplitude testing which more closely resembles the AISC Standard Loading Protocol. This is provided as a check to the very large cumulative ductility values. Additionally, the tests conducted through shake table excitation, which exhibited some pulse-like strain demands, are shown in Figure 4.26.

Table 2.1 shows that the proprietary BRB devices tested exhibit a wide range of yield forces, especially as this list is not comprehensive. Many yielding core configurations have been produced and tested, some with multiple cores which allows for a very wide range of yielding force.

Finally, the overstrength of BRBs is typically closely monitored as it is an important design consideration in building frames. Since BRB are currently designed as axially

loaded structural fuses in US buildings, the nominal and expected tension and compression forces are required to properly design the surrounding structural elements that are intended to remain elastic during a seismic event. The tension strength adjustment factor provides a measure of the maximum tension force in each cycle compared to the nominal yield force, and is defined as:

$$\omega = \frac{T_{\max}}{P_{yn}} = \frac{T_{\max}}{F_{yn} A_{sc}} \quad (2.1)$$

where F_{yn} = nominal yield strength, and A_{sc} = area of the yielding core. The compression strength adjustment factor, β , is defined as:

$$\beta = \frac{P_{\max}}{T_{\max}} \quad (2.2)$$

where P_{\max} is the maximum compressive force, and T_{\max} is the maximum tension force corresponding to a brace deformation of 1.5 the design story drift. It is observed that a typical value of the BRB overstrength, defined by the product of β and ω , is about 1.67. However, as the strain increases this value rises as is noticed in all BRB testing reports.

2.3 Finite Element Modeling

The finite element used to model the BRB members was fairly simple, yet still retained a significant level of similarity to the hysteretic behavior observed in testing (Black et al. 2004). This is a common technique in the approximation of BRB in building frames and other computer modeling of structural systems containing nonlinear BRB finite elements, as found in Kim et al. (2003); Black et al. (2004); Kim et al. (2004); Ravi et al. (2007), among others.

A bilinear BRB model contains an initial elastic stiffness up to a yield force and a post-yield stiffness afterwards, as opposed to an elastic perfectly plastic bilinear model. Figure 2.5(a) provides a depiction of the bilinear BRB model used in the current study (also see Section 4.2 for the varied parameters affecting this model). Figure 2.5(b) also provides one of three examples exhibiting the validity of using a bilinear BRB model as compared to a more sophisticated model. In this figure, Black et al. (2004) shows the results from many single-degree-of-freedom nonlinear dynamic analyses using both a Wen-Bouc nonlinear hysteretic model (which is based on experimental results) and a

compatible bilinear model BRB. The two curves shown in the figure are very nearly identical in drift, ductility and base shear coefficient. Additionally, Figure 2.6(a) presents results obtained by Usami et al. (2005) of experimental, beam model, and bilinear-truss model BRB behavior. This study focused on the analysis behind a seismic retrofitting of a steel arch bridge with BRB, and modeling of the BRB elements was determined sufficiently accurate using the bilinear-truss model based on the plots shown in Figure 2.6(a). Finally, Figure 2.6(b) shows a typical BRB hysteresis history from physical testing. The behavior is observed to be very nearly bilinear. However, the bilinear approximation could be less accurate given many variables such as loading rate and strain magnitude. Nonetheless, it is reasonable to assume the bilinear model fairly accurate up to an axial strain of about 3 to 4%, as this is the typical range tested.

The variety of yield forces available in BRB devices is amenable to the parametric study discussed in Section 4.2. This is one aspect of the bilinear model that allowed for straightforward implementation into the required parametric study for BRB on the VTB model.

The post-yield stiffness of the bilinear model demands attention to the proper overstrength attained by the element and the level of strain expected in the BRB. Several values of post-yield stiffness are found in the literature, and a range of overstrength is observed in test reports. Some examples of values used or reported are provided in Table 2.2. Some researchers have used values of post-yield stiffness that match well with test results with respect to the amount of energy dissipated (Usami et al. 2005). Other values shown in the table are calculated from test report values. It is notable that the two do not necessarily agree. This is not surprising, as secondary stiffness is highly dependent on the loading history due to strain hardening (Black et al. 2004). The overstrength is also affected by the loading history, as well as the magnitude of the strain achieved. This is evident in the BRB test report results where the reported values in Table 2.1 are significantly smaller than the maximum values achieved of about 2.0. These discrepancies led to the eventual variation of the post-yield stiffness in the parametric study, discussed further in Section 4.2.

Table 2.1 Examples of Tested Proprietary BRB Properties and Performance

Source / Specimen	Length	P_y (kips)	$\beta\omega$ *	Max. Axial Strain Tested (%)	Cumulative Ductility	
					Standard Protocol	Max. Achieved
(Merritt et al. 2003a)						
1D, 2D	18'	388	1.67	2.3	460	1100
3D, 4D	18'	712	1.70	2.4	375	700
5D, 6D	19'	897.3	1.63	2.3	345	1400
(Black et al. 2004)						
99-2	12'	364.2	N/R	2.00	243.5	636.5
00-11	12'	453.7	1.49		243.5	699.6
(Newell et al. 2005)						
1F	19'	1012.5	1.56	3.92	161	759
2F	19'	1012.5	1.51	3.67	149	632
(Newell et al. 2006)						
1G, 2G	22'	450	1.59	3.51	246	1143
3G, 4G	21'	1012.5	1.51	3.68	247	758

* Observed at the $1.5\Delta_{bm}$ AISC Standard Loading Protocol step

Table 2.2 Examples Post-yield Stiffnesses

Source	ϵ_y (%)	T_y (kip)	ϵ_{max} (%)	T_{max} (kip)	K_1 (kip/in)	K_2^* (% K_1)
(Merritt et al. 2003a)	0.13	388	2.4	1049	2697	3.47
(Black et al. 2004)						2.00
(Usami et al. 2005)						1.67
(Newell et al. 2006)	0.16	1012.5	3.86	1819	4219	3.76

* Either reported value or calculated from envelope of testing results

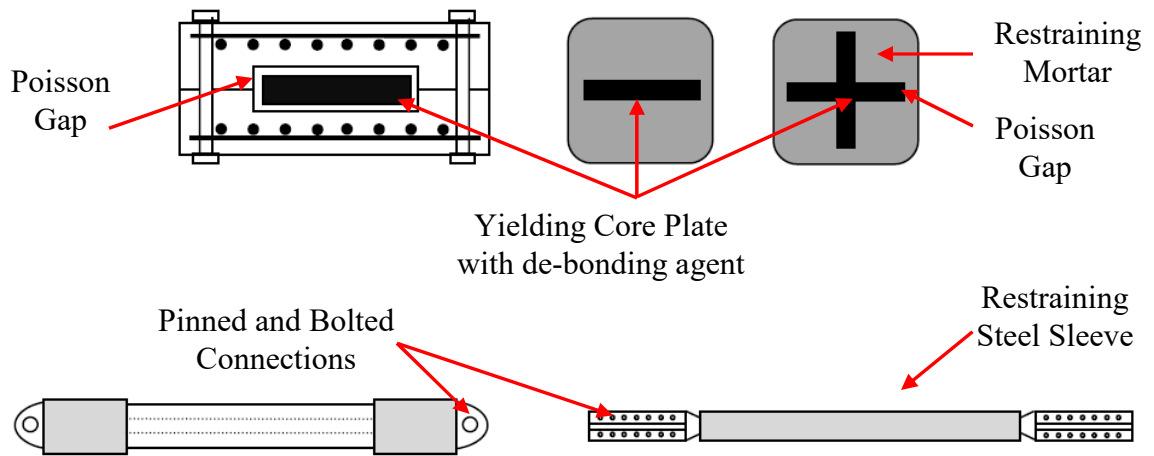


Figure 2.1 Examples of Typical Buckling-Restrained Brace Anatomy

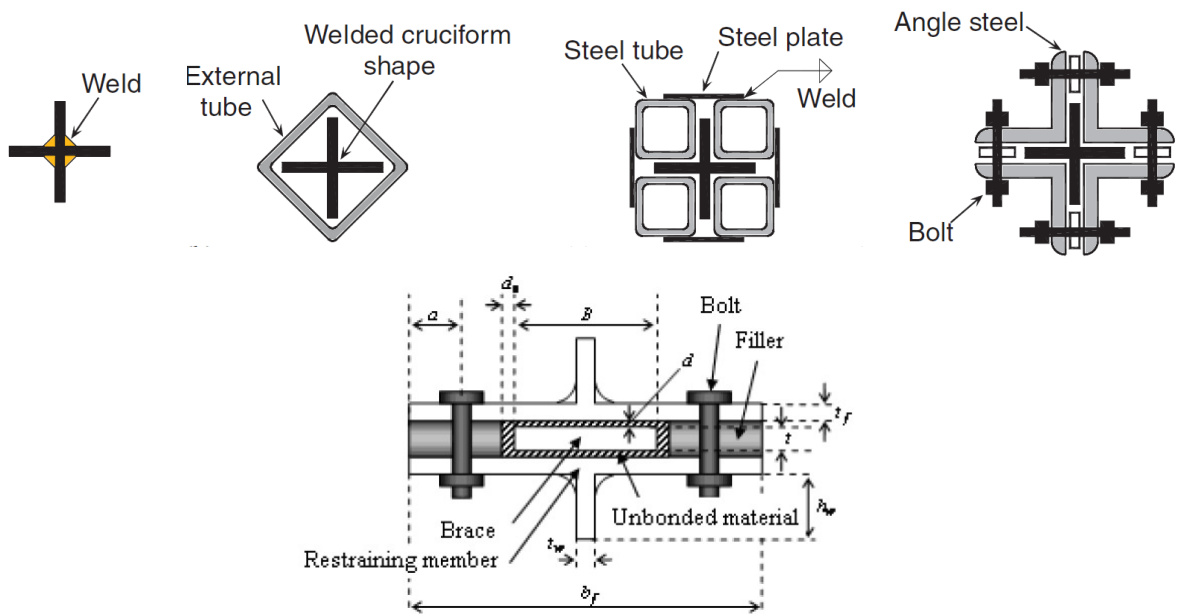


Figure 2.2 Examples of All-Steel Buckling-Restrained Braces (Zhao et al. 2010 and Usami et al. 2009)

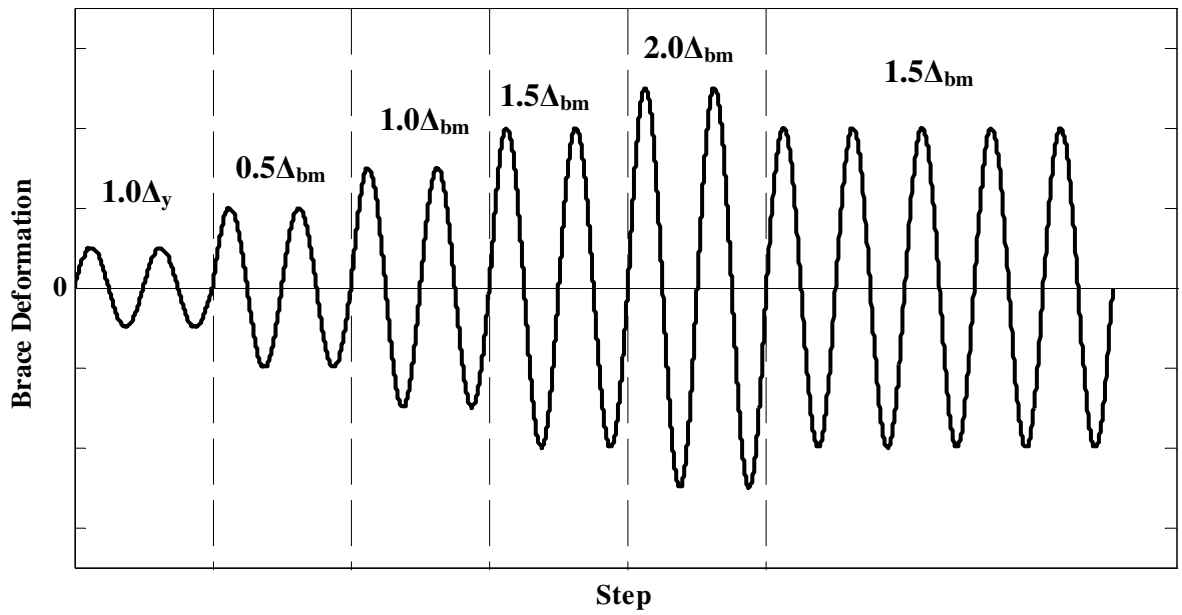


Figure 2.3 AISC Standard Loading Protocol for Buckling-Restrained Braces

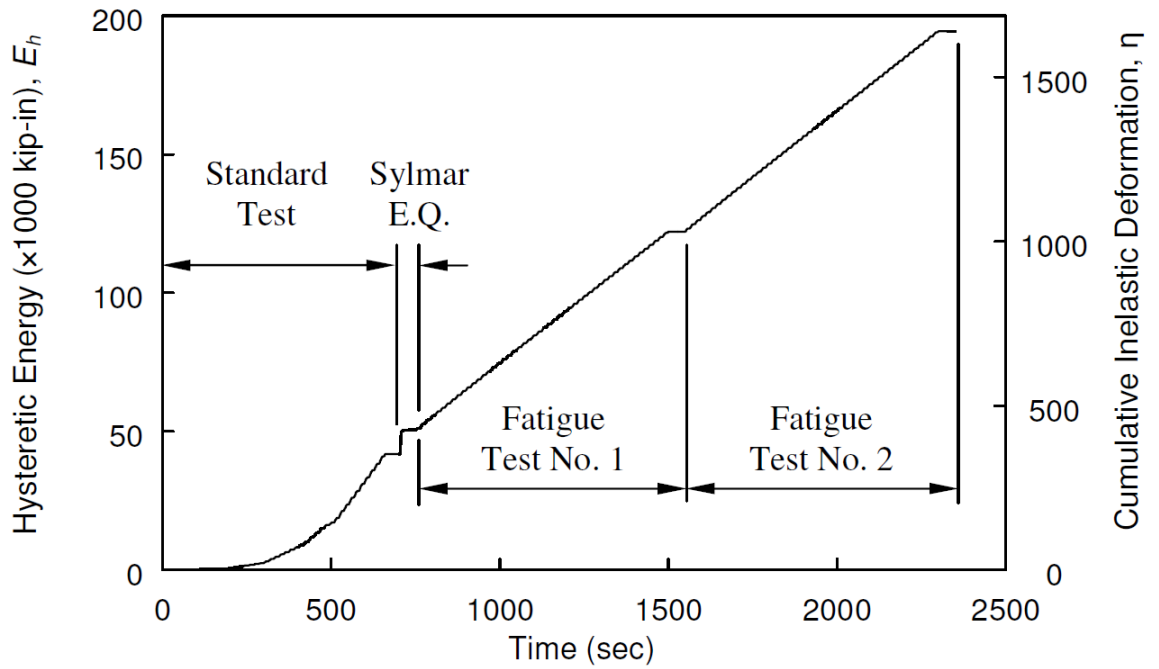
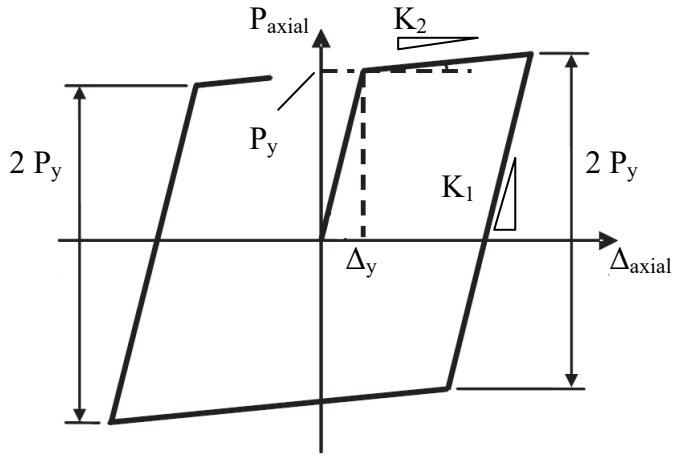
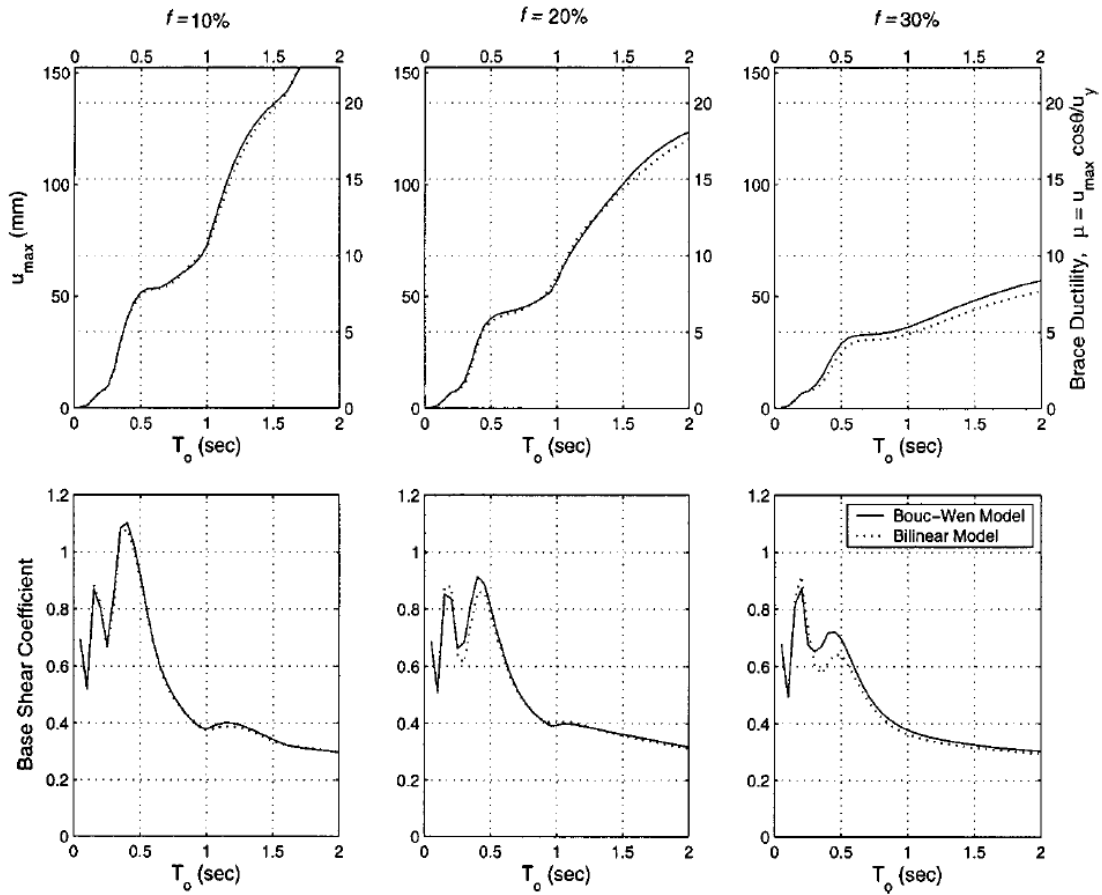


Figure 2.4 Example of Resilient BRB Performance (Merritt et al. 2003b)

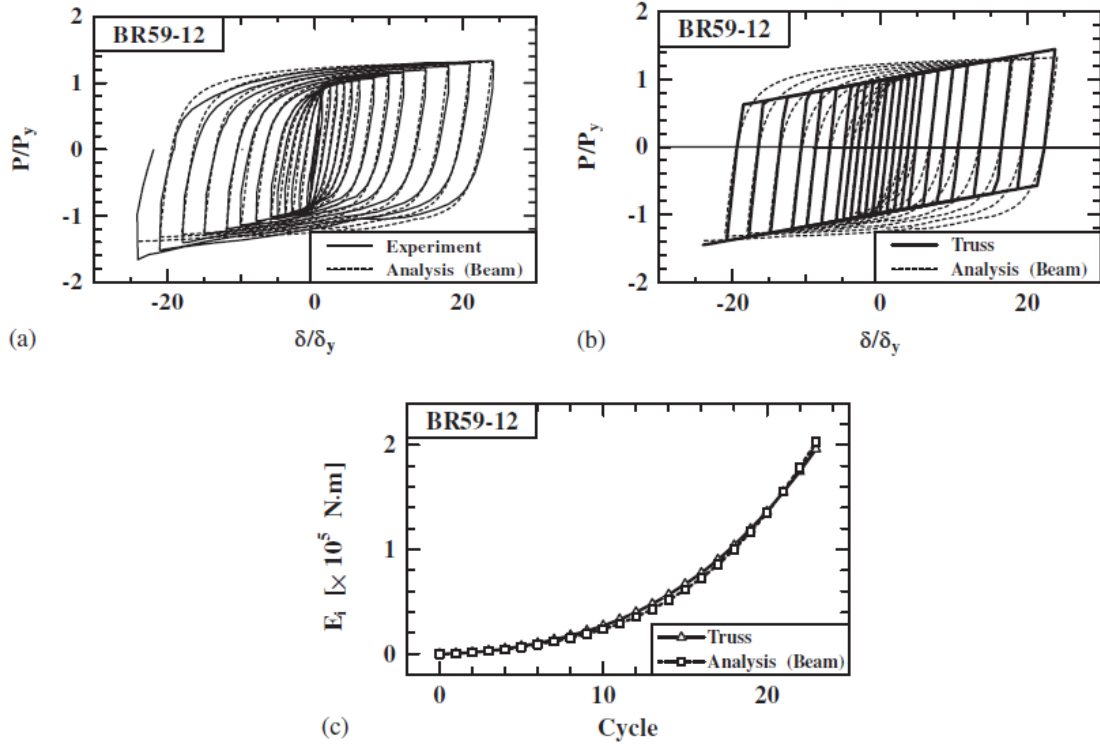


(a) Bilinear BRB Model with Kinematic Hardening Rule

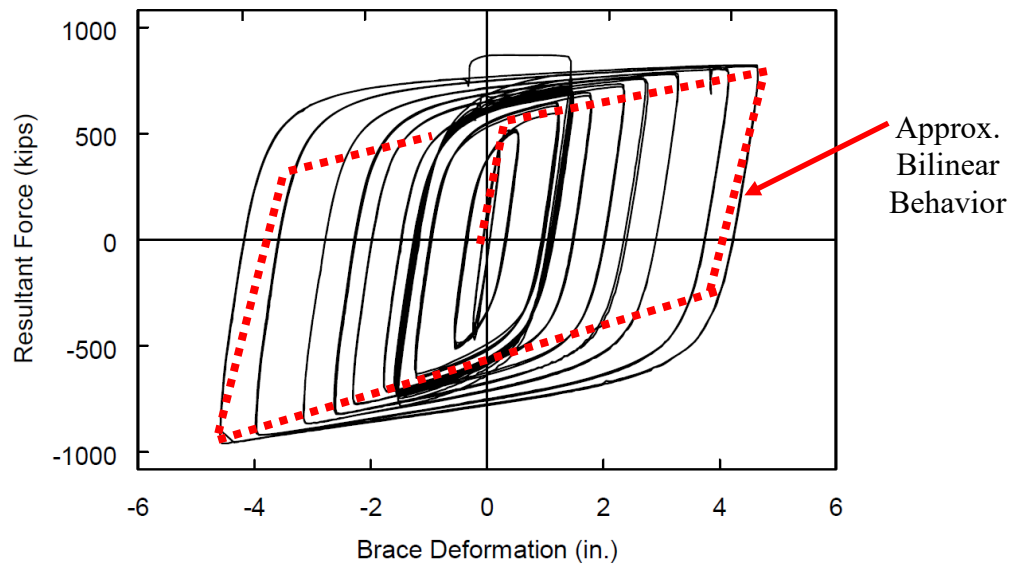


(b) BRB Models Result Comparison
(Black et al. 2004)

Figure 2.5 BRB Bilinear Model and Justification



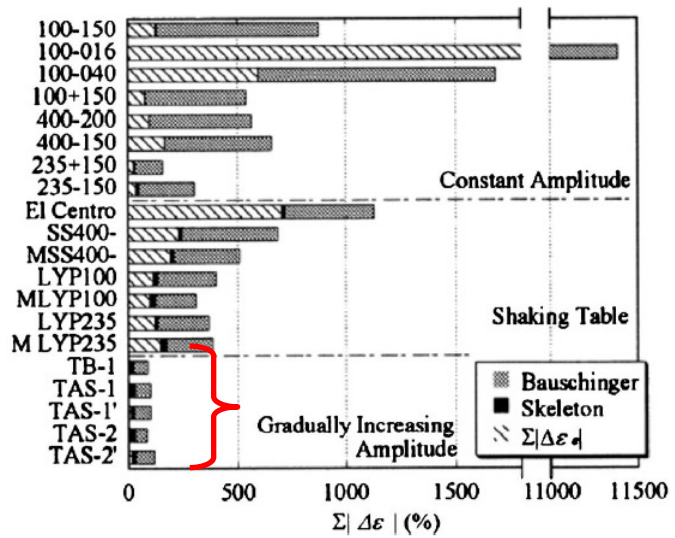
(a) Bilinear BRB Model with Kinematic Hardening Rule (Usami et al. 2005)



(b) Typical BRB Hysteretic Behavior from Testing (Newell et al. 2006)

Figure 2.6 Additional Bilinear BRB Model Justification

Maximum Strain Amplitude (%)	Approx. Cumulative Ductility
4.40	1136
3.94	1515
3.60	1515
3.31	947
4.12	1439



Maximum Strain Amplitude (%)	Approx. Cumulative Ductility
6.93	5300
6.55	6060
5.46	4168
5.47	6484
5.30	4544
6.89	3032
7.04	3032

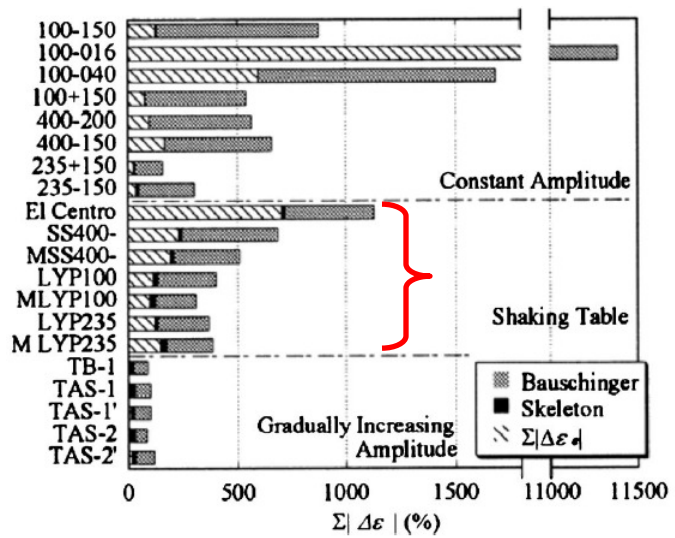


Figure 2.7 Examples of Tested BRB Cumulative Ductility and Maximum Strain (Takeuchi et al. 2008)

3. MODELING OF THE VINCENT THOMASE BRIDGE

3.1 Structural Analysis Software

Structural analysis of the VTB has been performed using two finite element software packages, ADINA (ADINA 2003) and Perform-3D (CSI 2006). Both are widely used in finite element analysis and have many similar capabilities.

ADINA (Automatic Dynamic Incremental Nonlinear Analysis) is a general-purpose finite element analysis package that can perform dynamic nonlinear analysis using 3D truss, beam, and shell elements commonly used in structural finite element analysis. Nonlinear dynamic analysis permits ground excitation time history input to models with nonlinear features such as large displacements and nonlinear material properties.

Perform-3D is a nonlinear analysis finite element software that is somewhat tailored to structural engineering in particular, and is widely used in the industry for nonlinear analysis of buildings. Nonlinear dynamic analysis is supported which allows seismic ground excitation time history input. Many nonlinear elements are readily available and include large displacement formulation and P-delta effects.

The following sections will provide a description of both models that have been used in the current study.

3.1.1 ADINA Model

The ADINA model currently being used was developed during the most recent seismic retrofit. This detailed model consists of over 20,000 degrees of freedom and considers nonlinear geometry and nonlinear material properties (Moffatt and Nichol 1996; Ingham et al. 1997). Foundation elements have been included to capture the flexibility of the tower foundation piles and pile cap. Additionally, this model has been modified to accommodate multiple support excitations in order to subject the bridge to the various ground motions described in subsequent sections.

The nonlinear spring and dashpot elements available in ADINA provide the capability to model both the existing viscous dampers and the proposed BRB members. Other notable nonlinearities are represented in the ADINA model including material

nonlinearity of the steel in the towers, tension-only behavior of the suspender ropes, and contact conditions between the towers and the span structures.

3.1.2 Perform-3D Model

Almost all of the details contained in the ADINA model were retained for the Perform-3D model as all of the necessary finite elements are available, including viscous dampers and nonlinear truss elements for BRBs. Additionally, the geometry for all of the elements was directly importable from ADINA to Perform-3D. This gave way to a very similar model.

However, several important simplifications were assumed to reduce the complexity of the model. First, shell elements were used in the ADINA model for the concrete deck. These elements add many degrees of freedom and were replaced with a system of beam elements in such a way to mimic the shell behavior observed in the ADINA model. Secondly, the bridge material properties were assigned as linear elastic (except for viscous dampers and BRBs), as it was assumed that any plastic behavior would be limited and not critical to the identifying the BRB properties required for desired structural performance. Secondly, the foundation modeling was neglected for similar reasons. The foundation flexibility was assumed to be of little importance to the BRB response. Finally, many of the analyses carried out with the simplified model are only subjected to the longitudinal component of the input motions. As, it has been observed that the longitudinal component is the most influential portion of the base excitation with respect to the longitudinal relative displacement between the spans and their adjacent supports. Even so, care was taken throughout the project to occasionally produce a reference data point with the ADINA model to reaffirm the conclusions obtained from the simplified model.

Motivation behind the construction of a simplified VTB model in Perform-3D was to speed computational time required for many analyses required for parametric study. With very little reduction in model detail, the number of degrees of freedom was reduced by approximately an order of magnitude simply by a coarser discretization of the structure's mass. Having about 2,400 degrees of freedom, the Perform-3D model provided a reduced

run-time and allowed simple implementation of parametric changes for a large portion of the study.

3.1.3 Correlation

As the ADINA model has been very skillfully developed (Ingham et al. 1997) and widely used for multiple studies of the VTB, using any simplified model requires some validation and correlation with this original model. Effort has been made to ensure sufficient structural similarity between the simplified Perform-3D model and the ADINA model. These efforts are documented in detail in Appendix A. Section 4 provides a comparison of the Perform-3D BRB parametric study analysis results with those obtained with the ADINA model, and the comparison is deemed acceptable.

3.2 Seismic Input Motions

Three levels of seismic intensities are considered for the BRB feasibility study, and are referred to as design-level, moderate-level, and low-level. The next two sections provide a description of the various seismic input ground motions for the VTB models. An organized layout of the input motion names, which earthquake they represent, and information regarding their intensities is provided in Table 3.1. The site specific design-level earthquake represents the expected maximum seismic demands that the VTB is likely to experience in its remaining lifespan (Moffat and Nichol 1997). The moderate-level and low-level earthquakes are considered for two main reasons. First, these records are site- and structure-specific because they were directly recorded at the base of the bridge towers. Therefore, convenient model correlation as well as a high level of confidence in the proposed retrofitted bridge model responses is attainable. This permits realization of the benefits of the proposed BRB retrofit scheme over the existing retrofitted configuration. Secondly, the highly nonlinear nature of the VTB and its model necessitate the use of multiple input records as nonlinear structural analysis results are highly sensitive to input.

3.2.1 Site Specific Design-Level Earthquake

The ground motions considered as design level for the VTB, as it pertains to the current research, have been obtained using information from the Caltrans Strategy Report

(Moffatt and Nichol 1996) together with the digital records provided by Earth Mechanics, Inc. (2011).

The previous seismic retrofit study of the VTB was performed in the mid-1990's by Moffatt and Nichol and a group of other structural and geotechnical engineering firms. One major product of this study was the Caltrans Strategy Report for the Toll Road Seismic Retrofit Project for the Vincent Thomas Bridge. As part of this study, a site-specific seismic hazard and geotechnical parameter analysis was performed by Earth Mechanics, which led to the development of a set of design motions appropriate for the VTB seismic retrofit. The following describes the methodology and reasoning used to implement these ground motions, given the available information and data, for use in this research project.

Site-specific seismic hazard analysis produces a site-specific ground motion from recorded local bedrock excitation by applying the effects of detailed geotechnical features such as subsurface conditions, fault proximity, and fault characteristics. The site response analyses for this study produced motions suitable for multi-direction, multiple support excitation analyses of the VTB models. A total of six support locations along the bridge are given, each with three orthogonal directional components of ground excitation. Support locations and bridge local directions are displayed in Figure 3.1. The design motions are reported in Appendix C of the Strategy Report, and two examples are provided in Figure 3.2 and Figure 3.3.

Given the length of time between the previous retrofit and the current research, these original ground motions were not readily available for implementation in the as-built ADINA model. Correspondence between Caltrans, UCSD, and Earth Mechanics yielded digital ground displacement data, via Earth Mechanics, which were thought to be the original motions reported in the Strategy Report. Only digital ground displacement time histories were provided, and therefore the corresponding ground accelerations were obtained via double differentiation. Examples of these ground motions are displayed in Figure 3.4 and Figure 3.5. However, these movements were not able to be well correlated with those in the report. Comparison of Figure 3.2 and Figure 3.4 as well as Figure 3.3 and Figure 3.5 makes clear the differences in wave form, especially in peak ground acceleration and pseudo-acceleration response spectra between the two sources of ground

motion. To highlight these disparities, the pseudo-acceleration response spectra from the Strategy Report were manually digitized and compared to those computed using the Earth Mechanics motions. Some important examples of this comparison are shown in Figure 3.7 through Figure 3.12. It is evident that the eastern motions compared fairly well with those provided in the Strategy Report, but still exhibited some differences. The west side records were fairly poorly correlated.

The Strategy Report describes the geographical layout of the bridge with respect to the underlying fault orientation, and discusses consideration of rotating the fault normal and fault parallel directions of the seismic hazard analysis derived motions. This rotation would produce motions which are aligned with the bridge local longitudinal and transverse directions. However, the report later states that rotation did not provide strongest shaking intensities and was ultimately not considered. Care was taken to ensure that this was not the source of the inconsistency; nonetheless better correlation was not able to be achieved even when the effect of rotation was considered.

The exact source of the inconsistency in the data is not clear. Instead a method for adjusting the given digital ground motions was used. Although the Earth Mechanics digital ground displacement time histories are different than those in the Strategy Report, the wave forms are sufficiently similar to safely assume that they are closely related to the original design motions. Therefore, the proper modification technique could provide slight changes to the time histories while maintaining the site-specific characteristics specific to the VTB. In so doing, the modified records could be considered “corrected” to better match the original design motions, and be appropriate for use as the design motions for this research project.

The proposed correction method utilizes a wavelet-based acceleration time history generation algorithm called WavGen (Mukherjee et al. 2002). The algorithm decomposes an acceleration time history into a number of separate histories containing energy in select bands of frequencies. These are iteratively scaled to closely match corresponding portions of a given target spectrum, and then are reassembled to form a modified time history. The resulting adjusted acceleration time history yields a pseudo-acceleration response spectrum which very closely matches the target spectrum (Mukherjee and Gupta 2002). Therefore, it is reasonable to use the given Strategy Report design pseudo-

acceleration response spectra as the target spectra for modifying the Earth Mechanics data. This should provide an adjusted time history that maintains the features of the site-specific motions, while ensuring that the design spectral content is present within the time histories.

To apply this algorithm, the pseudo-acceleration response spectra given in the Strategy report were first manually digitized. Each original design pseudo-acceleration response spectrum was then used as a target spectrum for the algorithm, which modified the corresponding Earth Mechanics derived acceleration time history record. Original and modified ground displacements, accelerations, and pseudo-acceleration response spectra are presented in Figure 3.7 through Figure 3.12. Note that proper baseline correction was performed for the displacement time histories. This is not immediately evident, as the full length of the records is not plotted to better display the adjustments made in the acceleration time histories.

Six support locations, three for the west side and three for the east side, along with three directional components results in 18 ground excitation records. Although computer model implementation of this complex loading history is achievable, it is considered appropriate to subject either side of the main span to the same excitation. One longitudinal, transverse, and vertical component should be selected as a reasonable representative of the collective motion of each side. This will allow for two important simplifications.

First, as the BRB parametric study will use this newly obtained design-level ground displacement scheme, it seems appropriate to avoid excessively complex loading to aid in both computational time and response data processing. The pseudo-acceleration response spectra, from the original Strategy Report, are displayed in Figure 3.6. It is clear that the records at each location exhibit very similar spectral content, varying somewhat between east and west support locations. These can reasonably be assumed as the same record (in each respective direction). Therefore, it appears permissible to proceed, as described, using only 3 motions on each side of the main span of the bridge, rather than 18 total.

Secondly, through the process of the above described time history modification, the ground motions have been modified individually. Although the process very closely achieves the target pseudo-acceleration response spectrum for a given time history, there

is no consideration for the similarities in motion of adjacent supports and their different levels of similarity to the target spectra. For example, Figure 3.13 displays the difference between the west side longitudinal ground displacements, provided by Earth Mechanics, and the respective modified displacements, via the wavelet-based algorithm. The raw records have very little relative differences throughout much of the time history, while the modified records are adjusted to meet the differences between the raw pseudo-acceleration response spectra and the target pseudo-acceleration response spectra (from the Strategy Report motions). Therefore, it became apparent that in order to avoid large unrealistic relative displacements between adjacent support motions, judgment would be required in using the “least modified” records to represent each side of the bridge motion appropriately.

This process led to the matrix of design input ground motions for multiple support excitation provided in Table 3.2. The vertical components provided by Earth Mechanics were essentially identical to those in the Strategy Report, so the vertical components of the supports used for modified transverse components were used for continuity. The complete set of site specific design-level motions used in the current research is presented in Figure 3.7 through Figure 3.12. For direction and location orientations refer to Figure 3.1.

3.2.2 Site Recorded Earthquakes

After the bridge was instrumented with seismic sensors in 1980, several significant earthquakes have occurred which were recorded at the VTB site. The recorded data are made available via the Center for Engineering Strong Motion Data (CESMD) website. The recorded acceleration and displacement time histories, along with the corresponding pseudo-acceleration response spectra, are provided in Figure B.1 through Figure B.8. The location and direction descriptions used in these figures correspond to the appropriate instrument channels and directions as displayed in Figure 1.4 and Figure 3.1, respectively.

As mentioned in Section 3.2, the Northridge and Whittier records are considered moderate-level seismic events for the bridge, while the Inglewood and Chino Hills records are provided as low-level events representing fairly commonly occurring seismic

demand. This distinction is evident upon inspection of the input peak ground accelerations as well as the responses provided in Section 4.

3.2.3 Ambient Bridge Motion

A valuable result of placing seismic sensors on the VTB is the availability of ambient motion of the flexible suspension bridge. Numerous studies have utilized readings taken from these sensors to carry out system identification and verification studies (Benzoni et al. 2008; Grazioti 2010).

Several sets of such data are available which were recorded in April 2003, June 2006, and December 2006. The recorded channels correspond to various directions of motion along different locations of the bridge as shown in Figure 1.4. These recordings can aid in predicting ambient demands for the existing bridge and retrofit options including the use of BRB.

3.3 Existing Bridge Model Design-Level Response

In order to highlight the need for any seismic response mitigation system, the existing model response is compared to that of the model with completely ineffective viscous dampers. This is carried out by changing the damping coefficient, C , to close to zero in (Eq. 1.1).

Table 3.3 shows the maximum responses obtained from the two models. Maximum impact displacements are compared to distance available between the decks and their respective adjacent supports. For instance, the main span rests approximately 39 inches away from the nearest face of the tower. Therefore, a relative displacement between the two that is greater than 39 inches would indicate impact.

It is evident from Table 3.3 that the model having no active dampers does permit such an impact at both the side to tower and main to tower locations. This is very undesirable given the cellular-steel makeup of the main towers. However, the model with fully effective dampers shows greatly reduced maximum displacements. This verifies the original seismic retrofit intent, and provides a benchmark for the following BRB retrofit parametric study.

Table 3.1 Input Ground Motion Information

Seismic Event	Peak Ground Acceleration, <i>g</i>			Level of Intensity
	Longitudinal	Transverse	Vertical	
Site Specific*	0.686	0.850	1.021	Design-Level
Northridge 1994	0.227	0.173	0.034	Moderate-level
Whittier 1987	0.072	0.047	0.016	Moderate-level
Chino Hills 2008	0.039	0.035	0.007	Low-Level
Inglewood 2009	0.063	0.089	0.015	Low-Level
Calexico 2010	0.015	0.016	0.005	Low-Level

* See Section 3.2.1

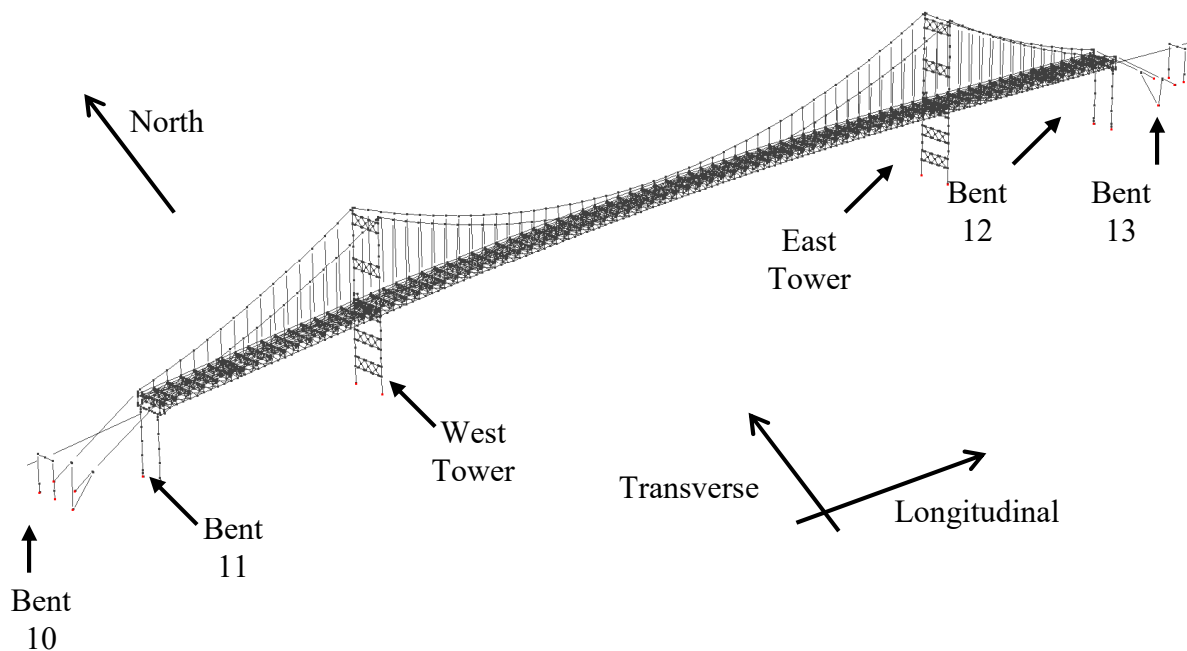
Table 3.2 Modified Earth Mechanics Records Used as Design-Level Input Motion

Side	Longitudinal	Transverse	Vertical
West	Bent 10	Bent 11	Bent 10
East	Bent 13	East Tower	East Tower

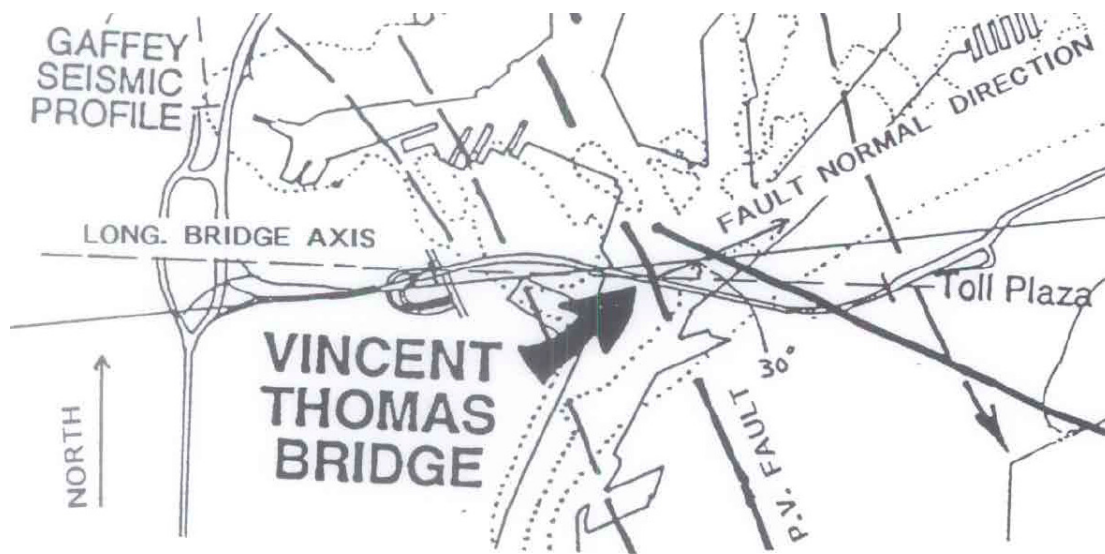
Table 3.3 Response of Existing Bridge Model with Fully Effective and Ineffective Viscous Dampers

Model	Device Location	Max. Impact Displacement* (in)	Max. Axial Force (kips)
Fully effective dampers	Side/Cable Bent	18.5 (30)	445
	Side/Tower	17.3 (21)	131
	Main/Tower	22.7 (39)	364
Fully ineffective dampers	Side/Cable Bent	22.3 (30)	N/A
	Side/Tower	30.8 (21)	N/A
	Main/Tower	42.6 (39)	N/A

* Values in parentheses are the displacement at which impact occurs



(a) Support Locations and Bridge Local Directions



(b) Bridge Geographical Orientation

Figure 3.1 Seismic Site Overview of VTB

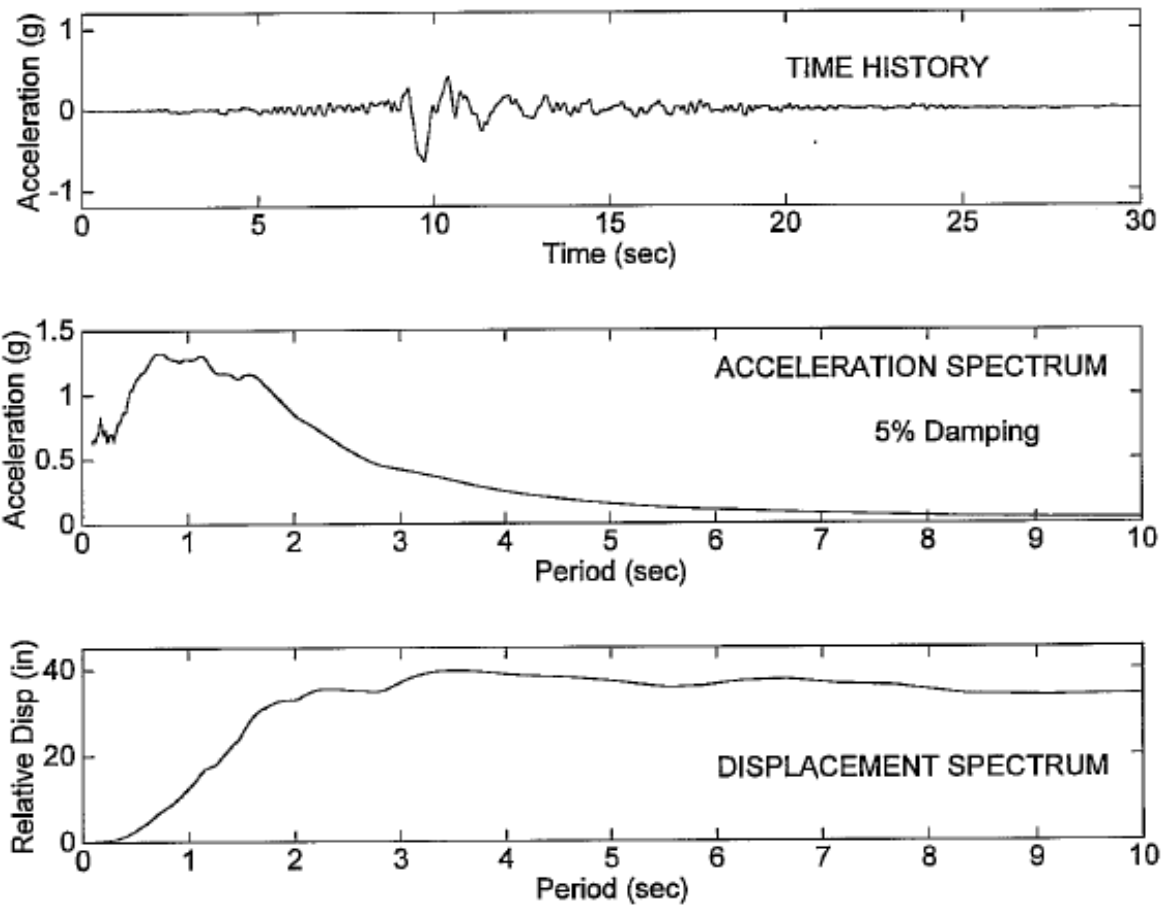


Figure 3.2 Bent 10 Longitudinal Ground Motion (Moffatt and Nichol 1996)

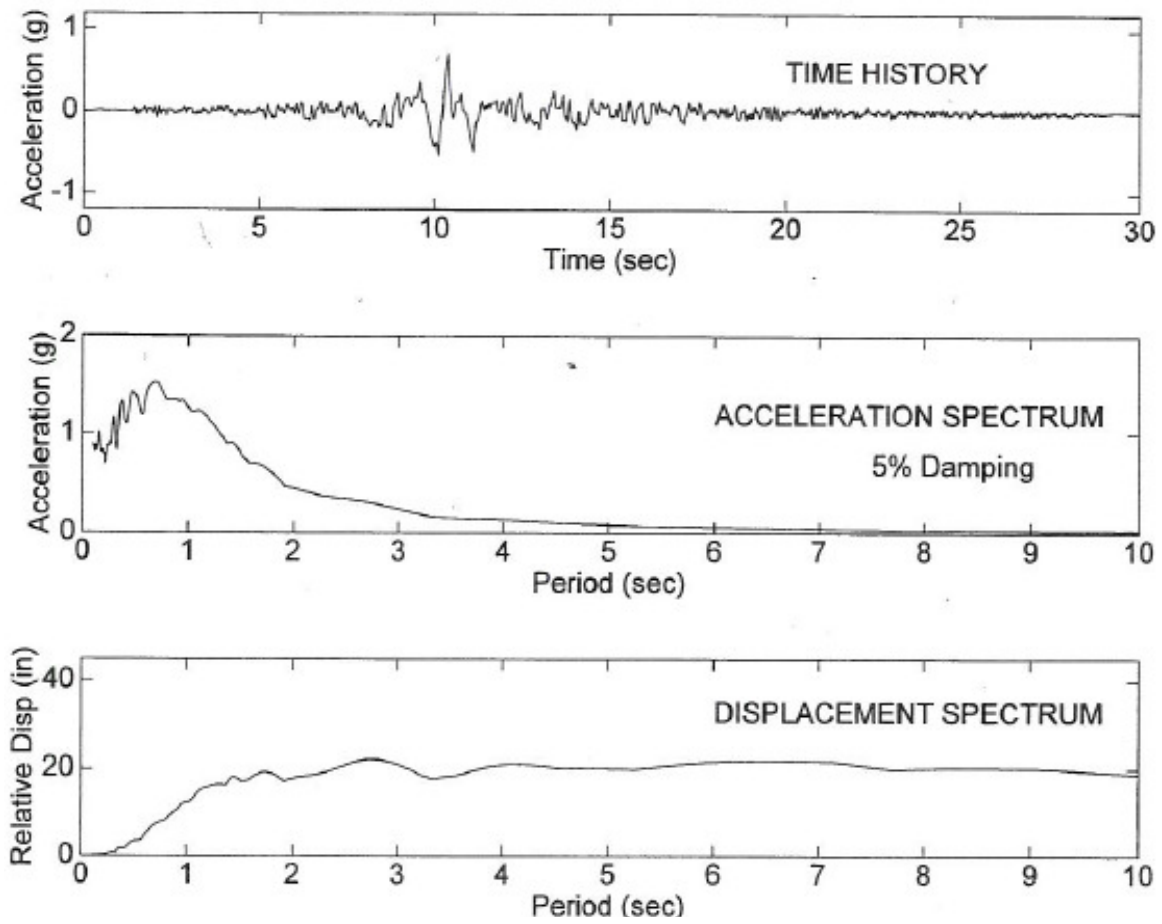
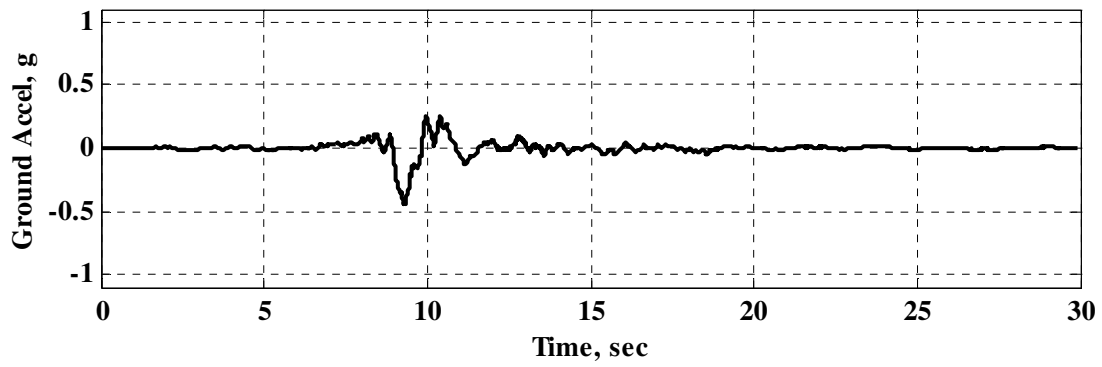
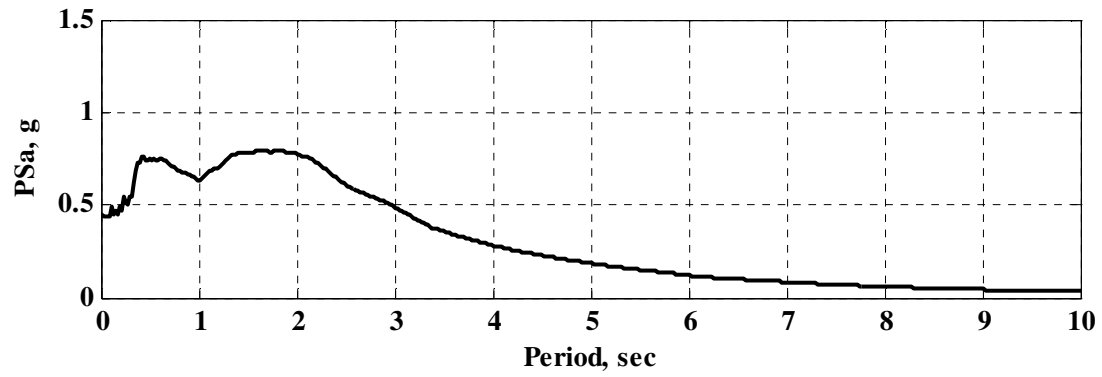


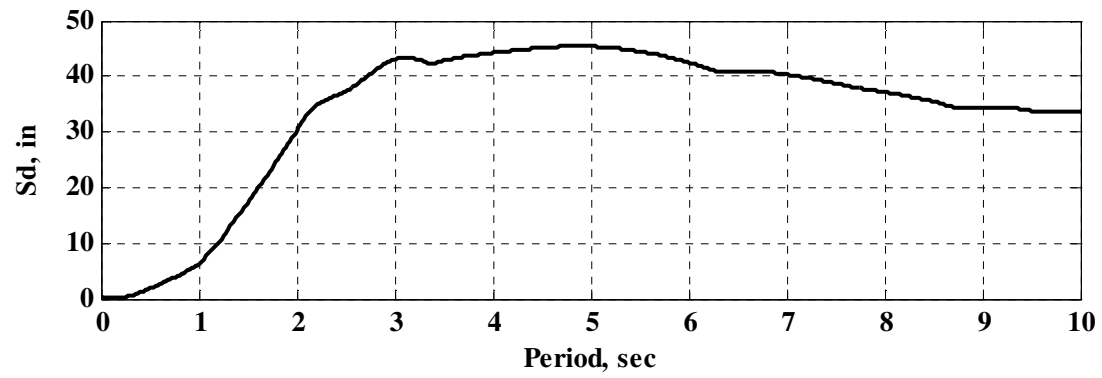
Figure 3.3 East Tower Transverse Ground Motion (Moffatt and Nichol 1996)



(a) Ground Acceleration Time History

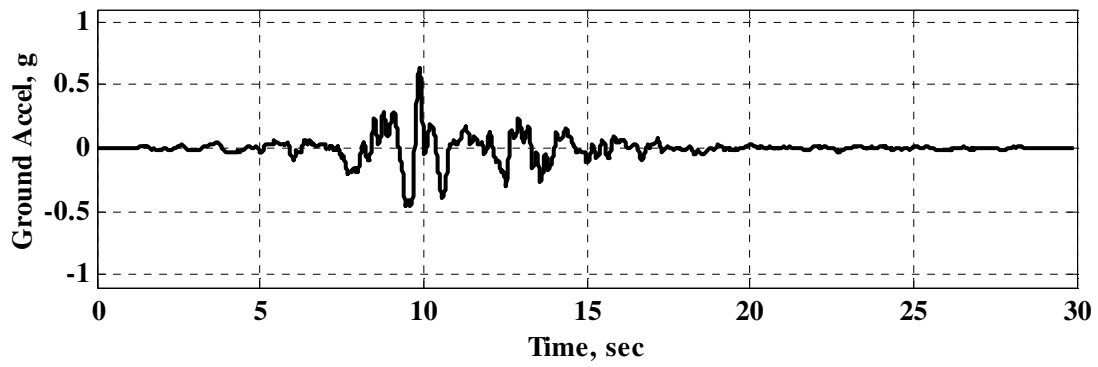


(b) Pseudo-acceleration Response Spectrum ($\zeta=5\%$)

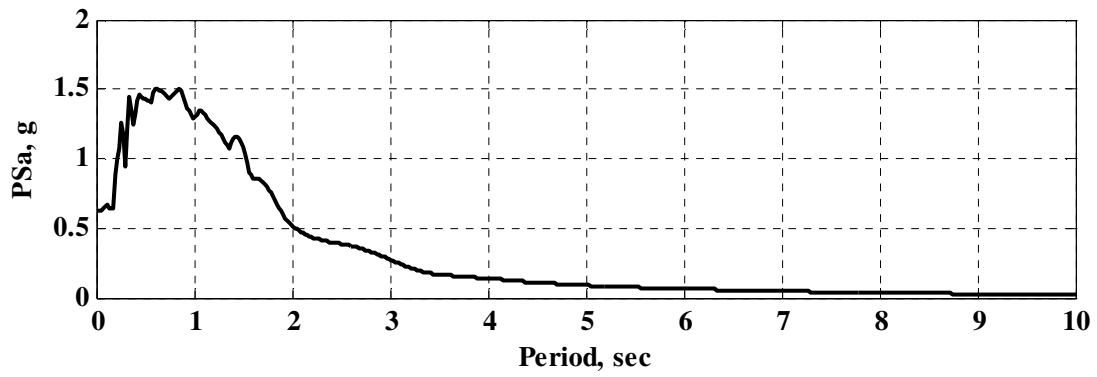


(c) Spectral Displacement ($\zeta=5\%$)

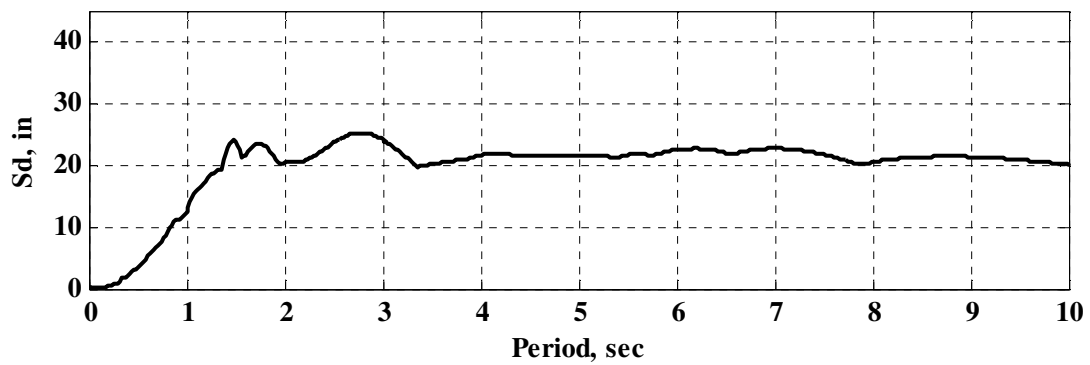
Figure 3.4 Bent 10 Longitudinal Ground Motion (Earth Mechanics 2011)



(a) Ground Acceleration Time History

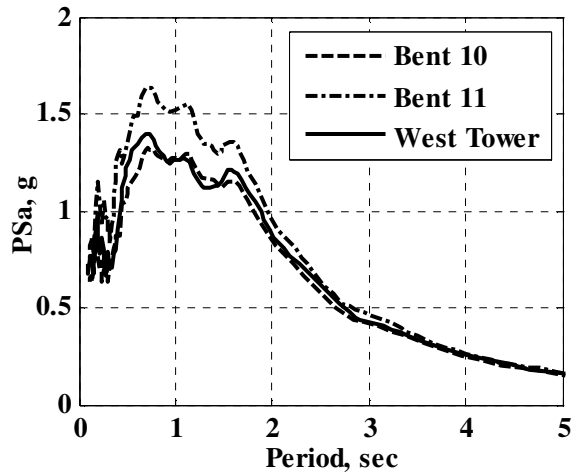


(b) Pseudo-acceleration Response Spectrum ($\zeta=5\%$)

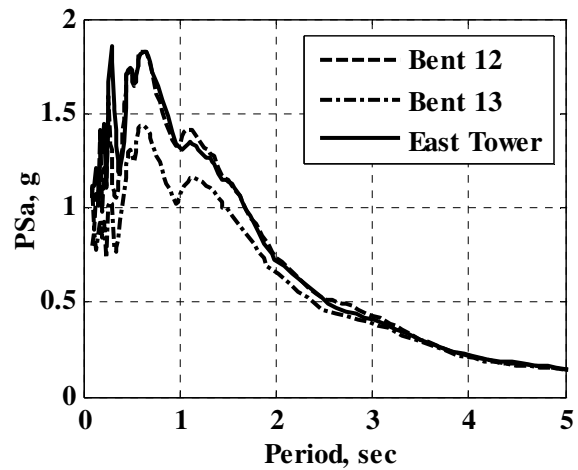


(c) Spectral Displacement ($\zeta=5\%$)

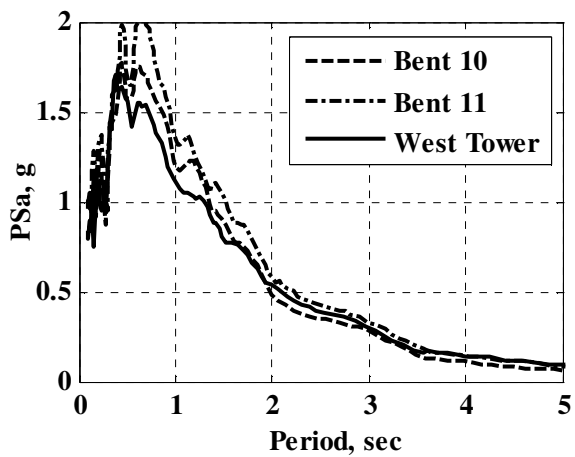
Figure 3.5 East Tower Transverse Ground Motion (Earth Mechanics 2011)



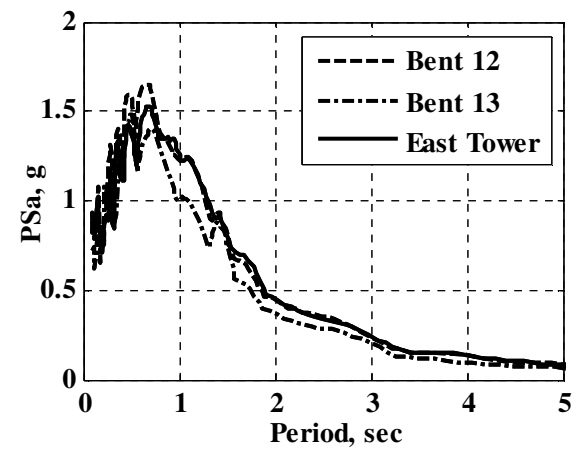
(a) West Supports, Longitudinal Direction



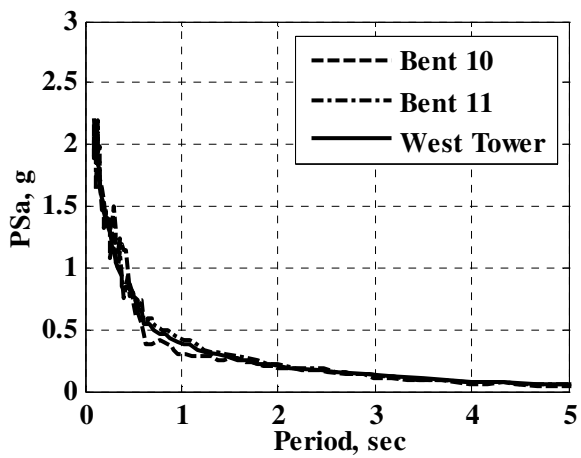
(b) East Supports, Longitudinal Direction



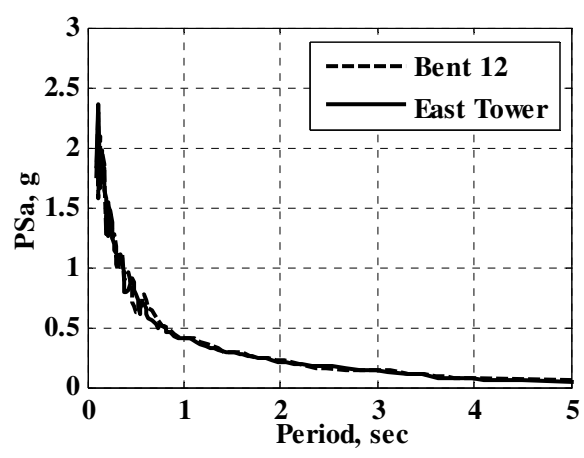
(c) West Supports, Transverse Direction



(d) East Supports, Transverse Direction

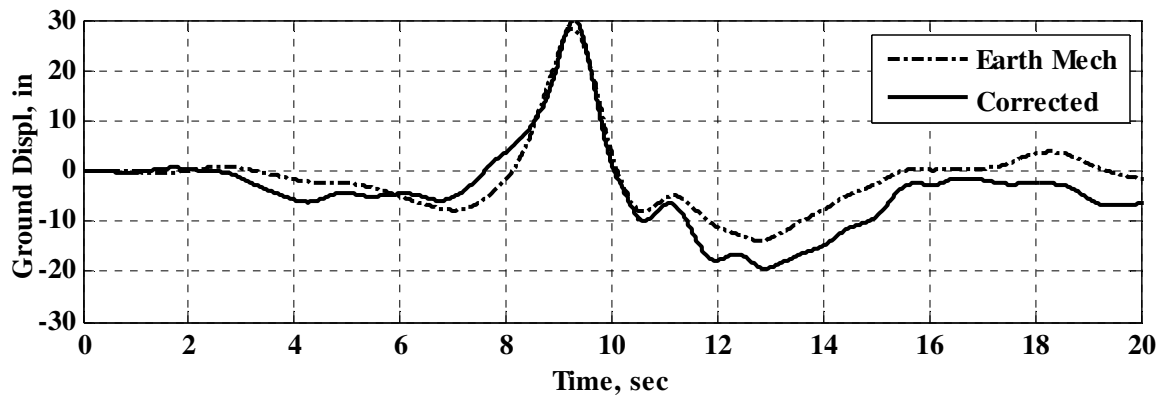


(e) West Supports, Vertical Direction

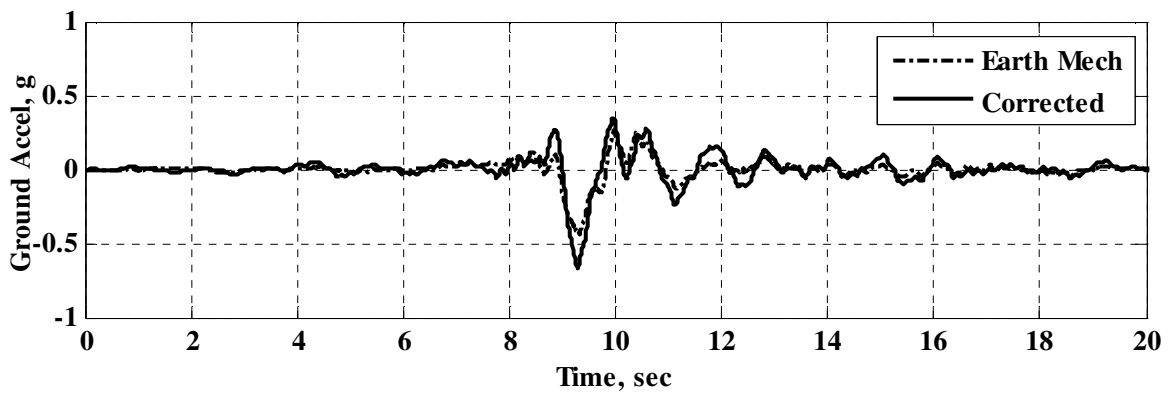


(f) East Supports, Vertical Direction

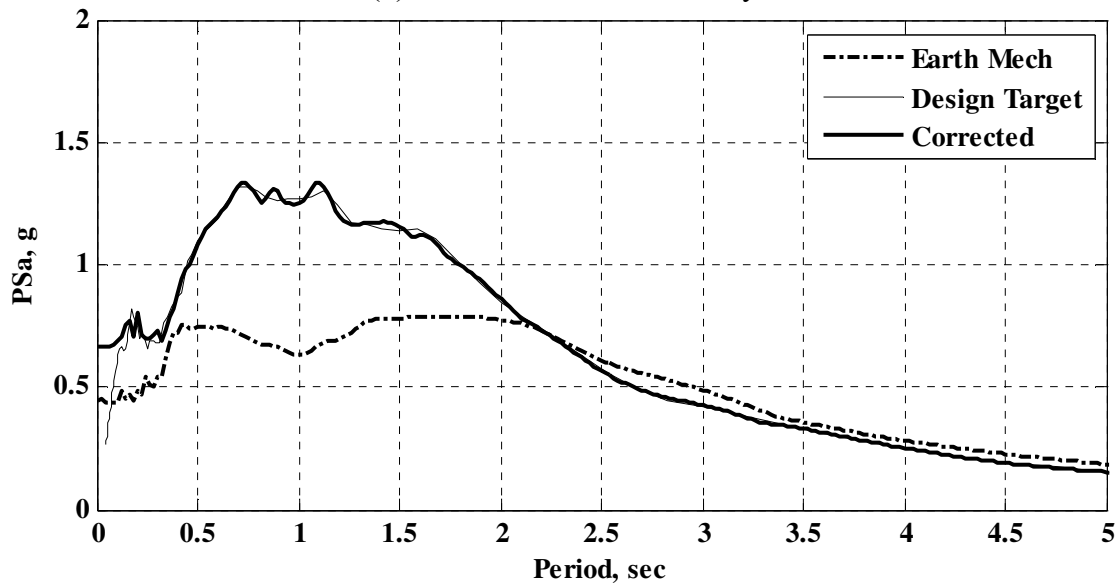
Figure 3.6 Design-Level Earthquake Pseudo-Acceleration Response Spectra ($\zeta=5\%$)



(a) Displacement Time History

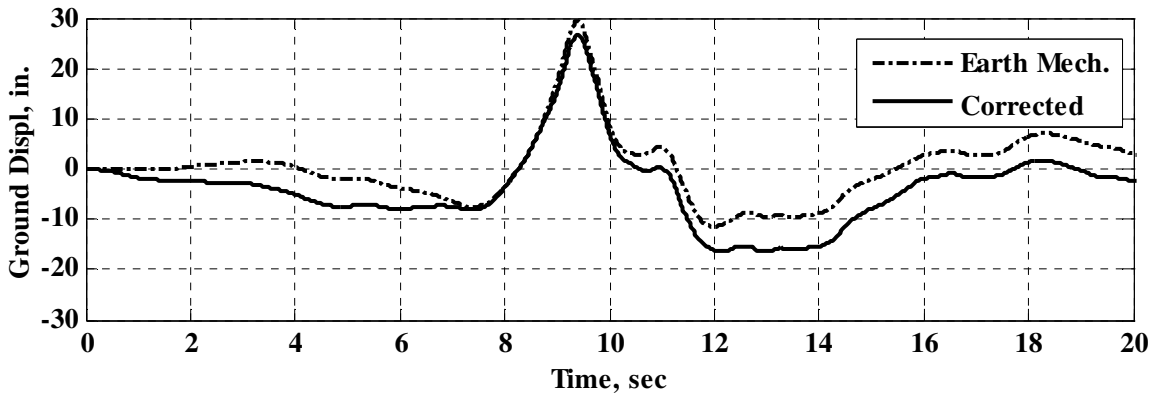


(b) Acceleration Time History

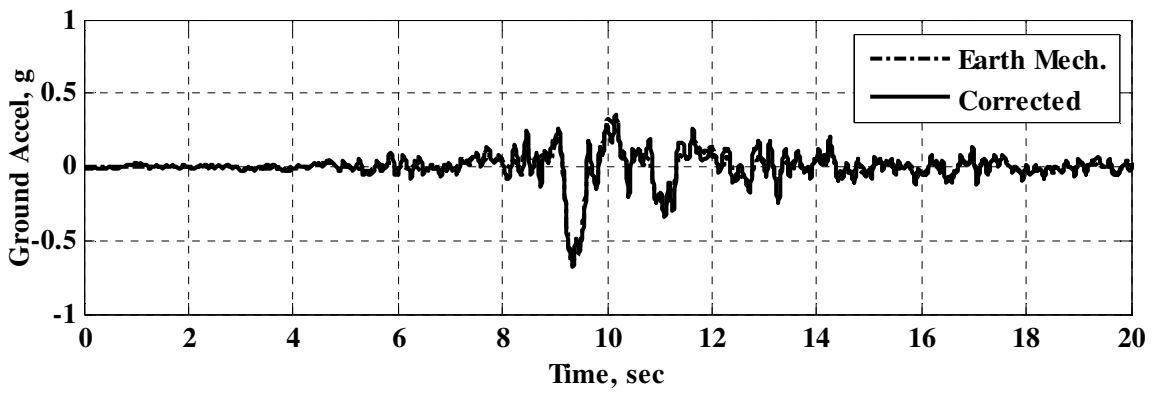


(c) Pseudo-Acceleration Response Spectrum ($\zeta=5\%$)

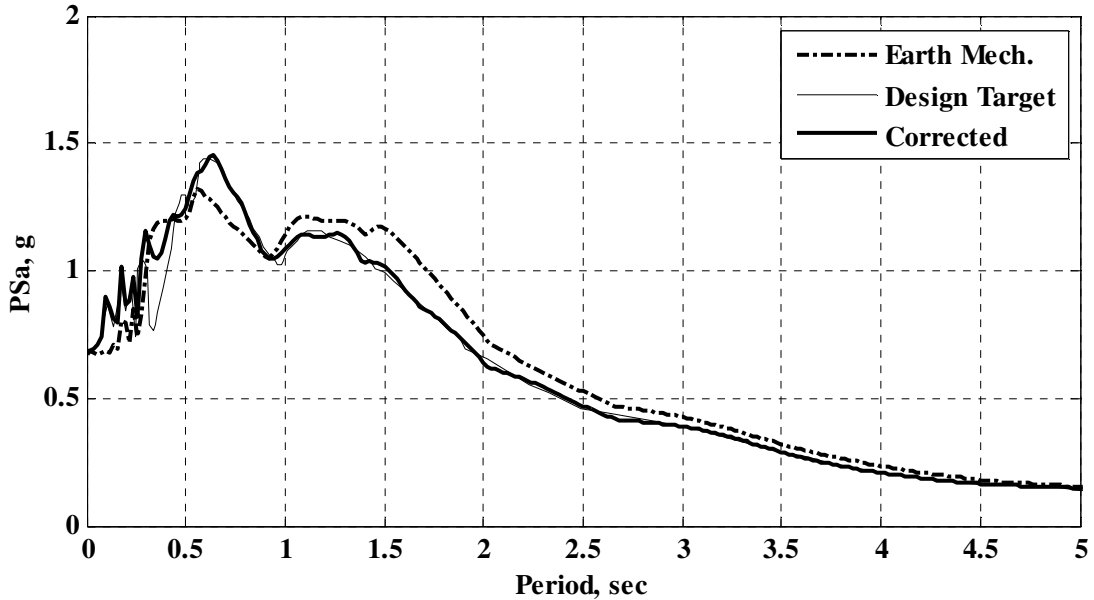
Figure 3.7 Design-Level Earthquake, West Side Longitudinal



(a) Displacement Time History

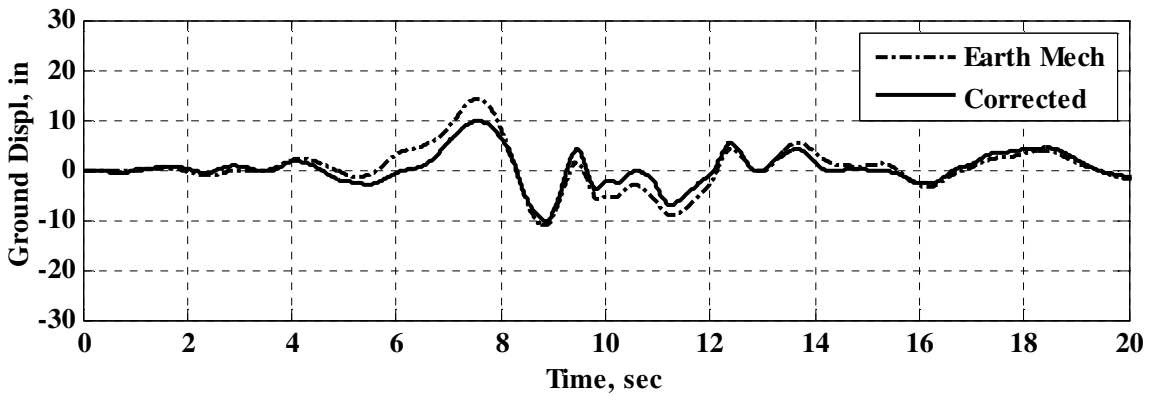


(b) Acceleration Time History

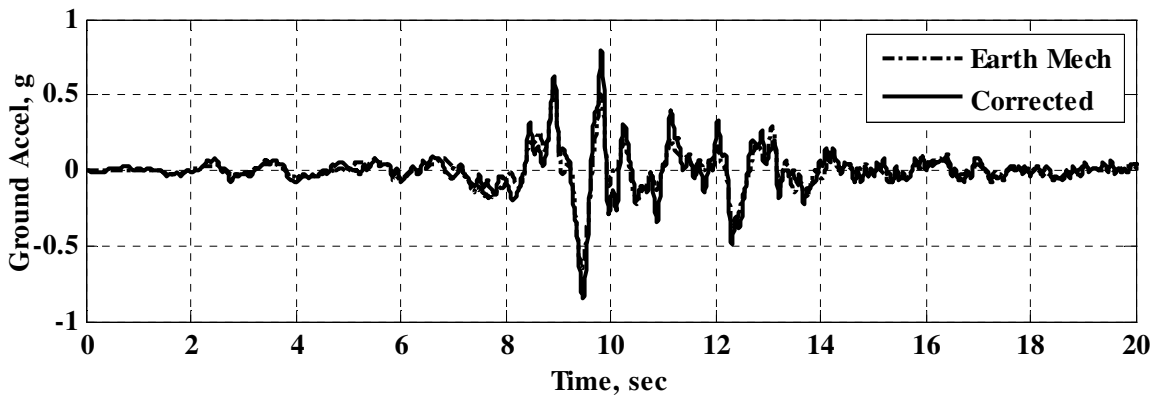


(c) Pseudo-Acceleration Response Spectrum ($\zeta=5\%$)

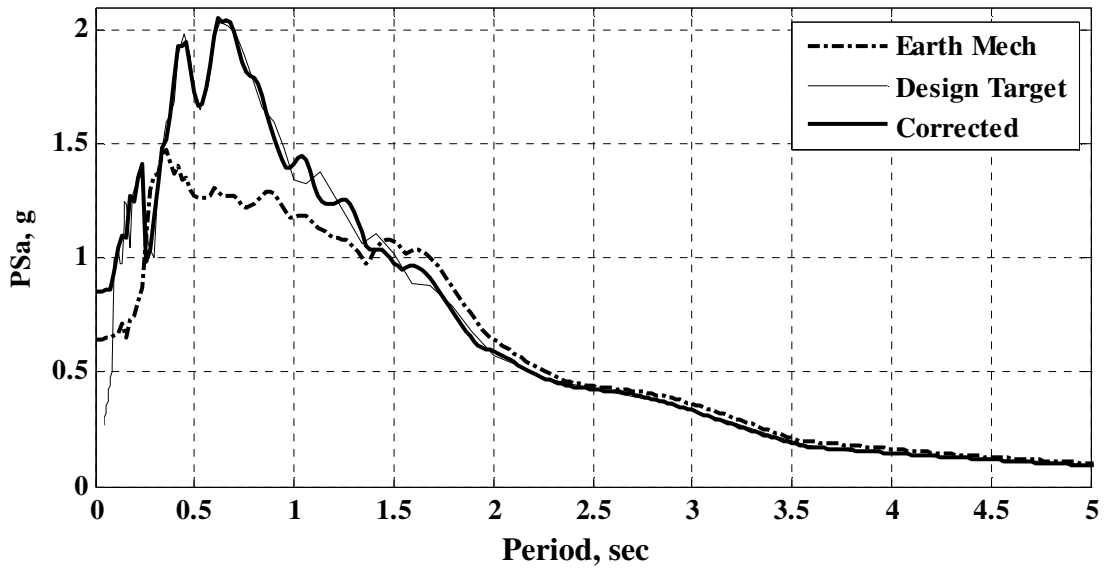
Figure 3.8 Design-Level Earthquake, East Side Longitudinal



(a) Displacement Time History

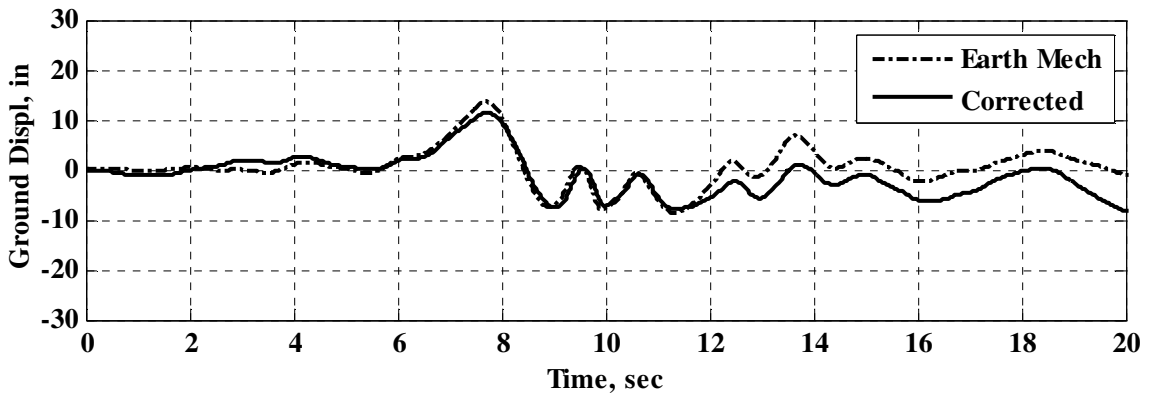


(b) Acceleration Time History

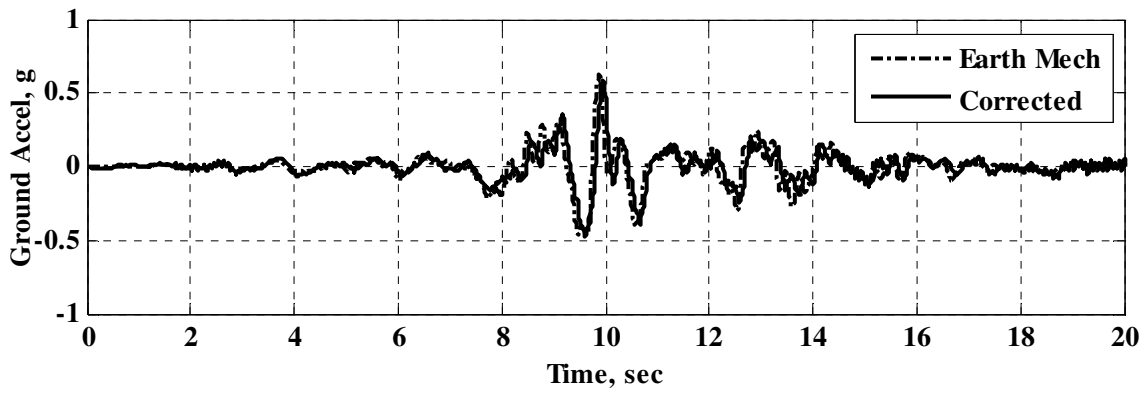


(c) Pseudo-Acceleration Response Spectrum ($\zeta=5\%$)

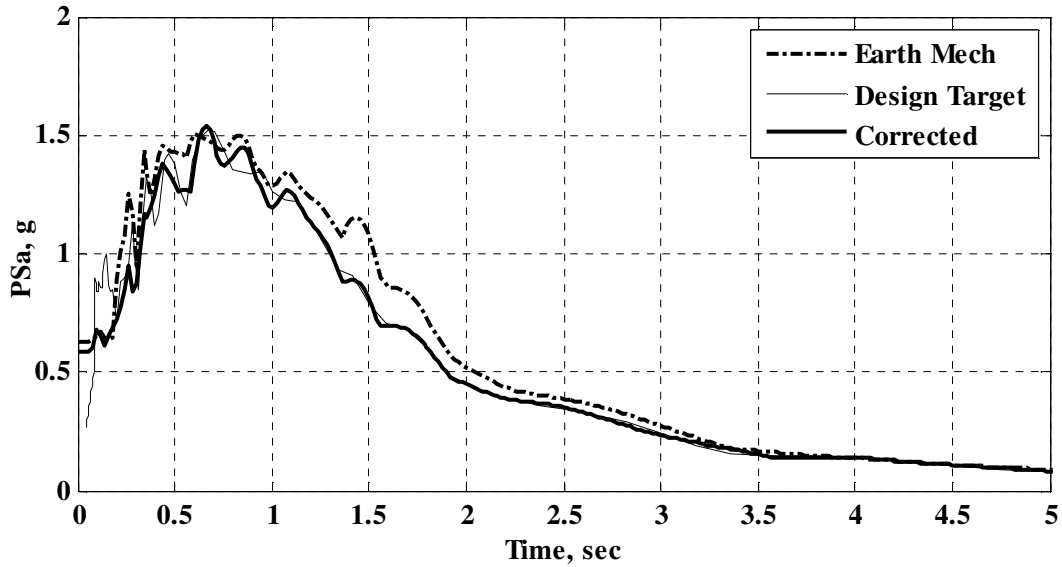
Figure 3.9 Design-Level Earthquake, West Side Transverse



(a) Displacement Time History

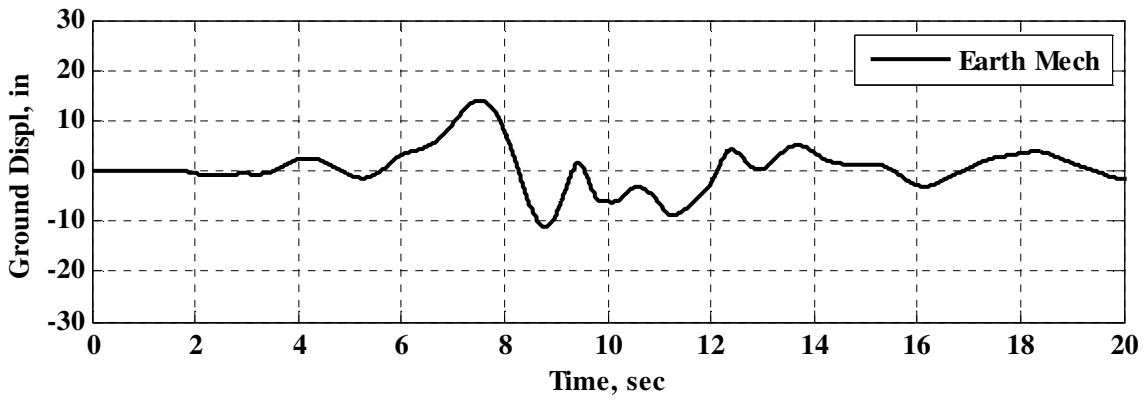


(b) Acceleration Time History

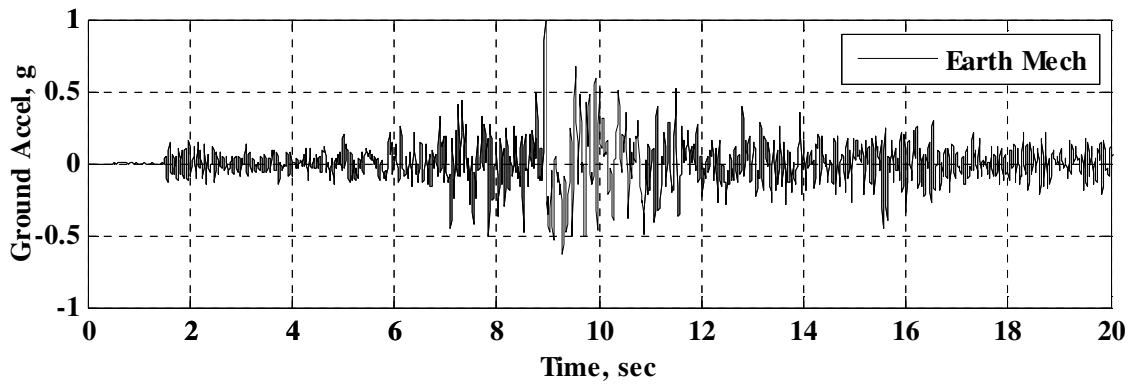


(c) Pseudo-Acceleration Response Spectrum ($\zeta=5\%$)

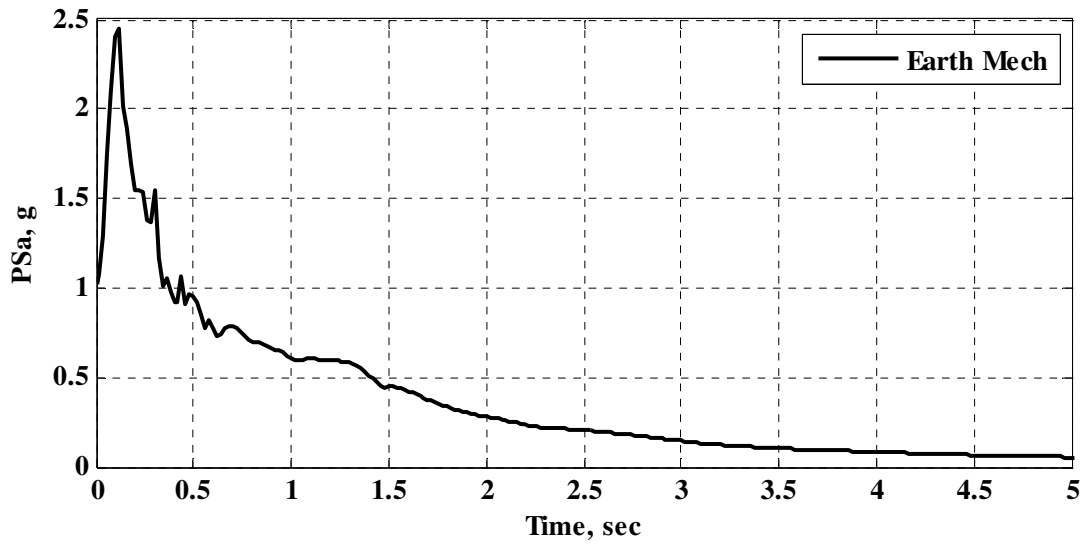
Figure 3.10 Design-Level Earthquake, East Side Transverse



(a) Displacement Time History

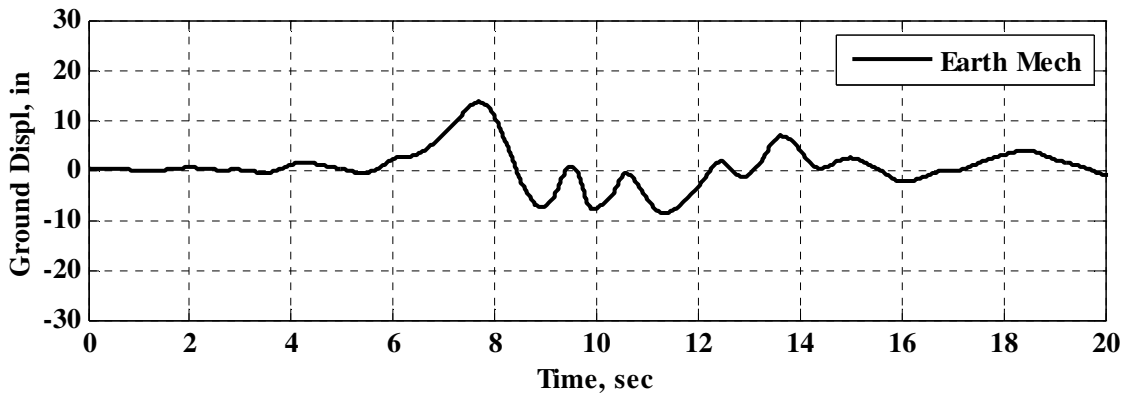


(b) Acceleration Time History

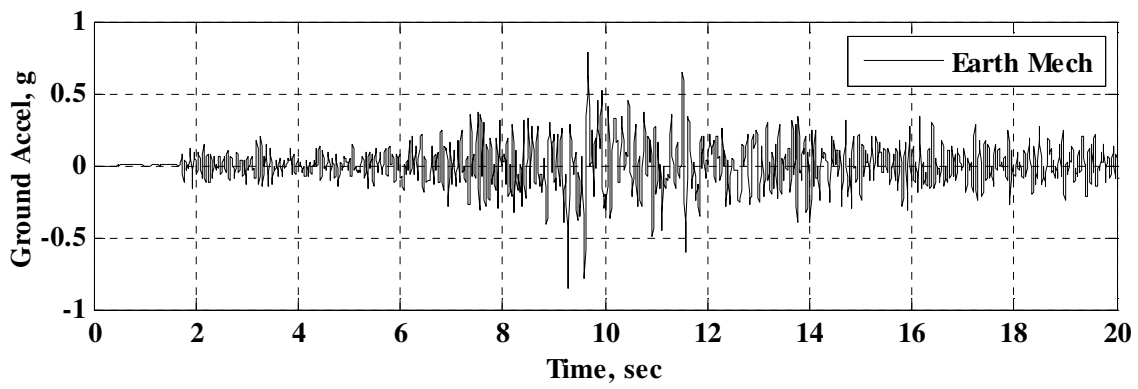


(c) Pseudo-Acceleration Response Spectrum ($\zeta=5\%$)

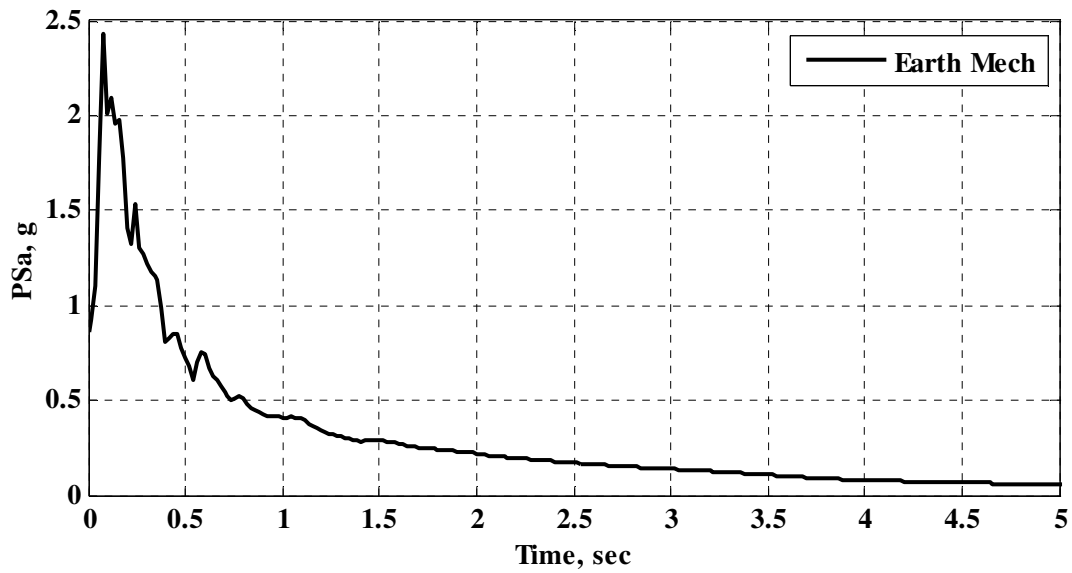
Figure 3.11 Design-Level Earthquake, West Side Vertical



(a) Displacement Time History

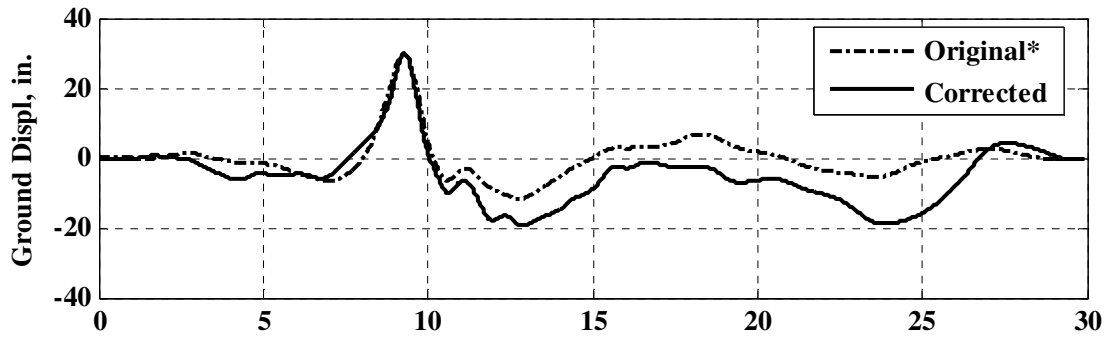


(b) Acceleration Time History

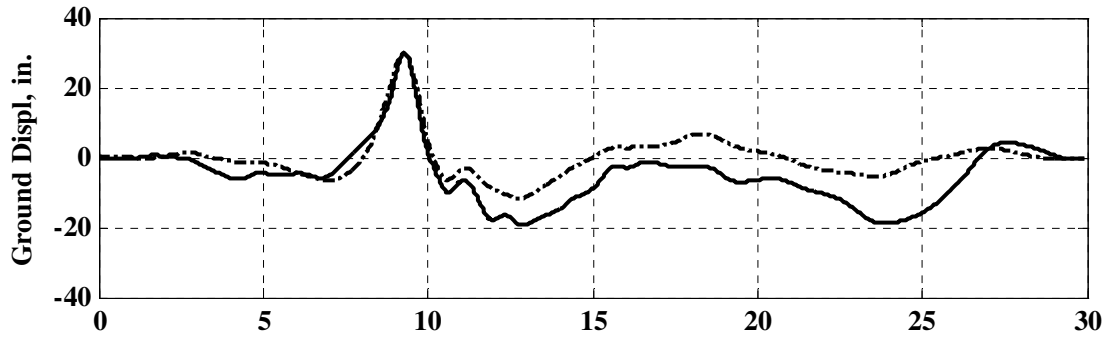


(c) Pseudo-Acceleration Response Spectrum ($\zeta=5\%$)

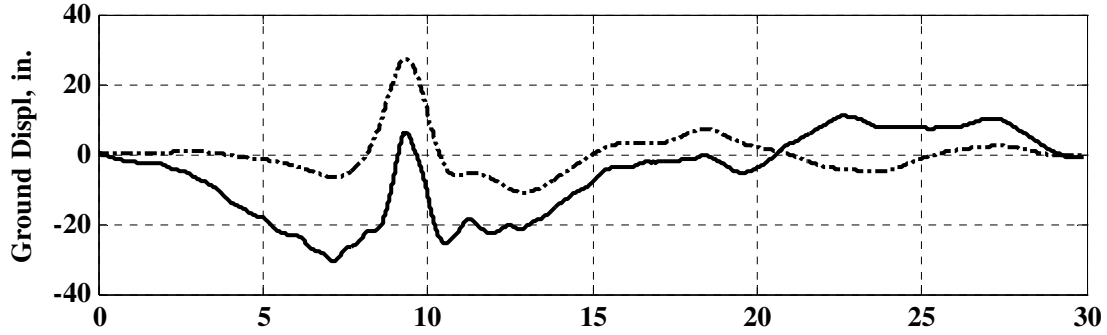
Figure 3.12 Design-Level Earthquake, East Side Vertical



(a) Bent 10



(b) Bent 11



(c) West Tower

Figure 3.13 Original* and Modified Longitudinal West Side Ground Displacements

(*Earth Mechanics 2011)

4. SEISMIC RESPONSE EVALUATION OF BRB-RETROFIT OF VTB: A PARAMETRIC STUDY

4.1 Introduction

The primary goal of this research is to assess the feasibility of using BRBs to mitigate the seismic response of long-span bridges. The VTB was considered as a case study to demonstrate the feasibility through a parametric study aimed at determining the BRB characteristics required to provide sufficiently mitigated seismic response.

A finite element model of the VTB, which included BRB elements, was subjected to a near-fault pulse-type ground motion simulating the bridge design-level earthquake. The bridge model response thereby dictated the deformational demands required of the BRB elements for seismic response mitigation. Several BRB element parameters, which define the primary characteristics of BRBs, were investigated and varied to determine a combination of reasonable BRB parameters and mitigated bridge response.

In order to be assessed as feasible, the BRB characteristics need to be reasonably similar to those which are commercially available, and likewise the deformational demands reasonably similar to those which have been imposed in physical testing, or are considered physically possible. In other words, if the parametric study results in BRBs fairly similar to those that are currently commercially available, and the required deformational demands are deemed physically possible, then the concept will be judged as feasible.

Recalling from the discussion in Section 2.3, only a limited number of factors are required for BRB finite element representation: a yield force, post-yield stiffness, and a member length. Further detail of these parameters is provided in the following sections. The parametric study aims to strike a balance between these parameters and the resulting mitigation seismic response of the bridge, as described above.

The study has been organized into stages which progressively tune the BRB properties to a somewhat optimized solution. The first is a global stage and aims to provide a first-order account of the required BRB properties, where each BRB parameter is held constant over all BRB locations. In so doing, a better understanding is developed for how the bridge and BRB work together. The parameters are then varied at a single

BRB location at a time in the localized parametric study. In each case the results are analyzed and discussed, and finally a retrofit solution is proposed based on the best possible combination of bridge response and BRB demand.

The parametric study considers the bridge response to the design-level earthquake described in Section 3.2.1. This base excitation is used so as to consider the maximum demands for both the BRB elements and their respective demands of the bridge structure. The simplified Perform-3D model was first used throughout preliminary studies as well as the global parametric study. The remaining stages are conducted using the ADINA model, which includes the proposed feasible solution. As will be discussed in the subsequent sections, correlation will be ensured validating the assumptions simplifying the Perform-3D model and analyses.

4.2 BRB Design Parameters

Three variables (BRB length, yield force, and post-yield stiffness) are considered in the parametric study. These three variables control, or directly represent, the three main values that characterize BRB structural behavior. The parameters controlling the characteristics are chosen as α , γ , and BRB Scheme. In addition to the following discussion, Figure 4.1 and Figure 4.2 provide a visual description. This figure shows how the combined variation of yield force and member length allow for the parameter study to explore a large BRB design space.

Defining the non-dimensional post-yield stiffness as:

$$\alpha = \frac{K_2}{K_1} \quad (4.1)$$

where K_1 = elastic axial stiffness, and K_2 = post-yield axial stiffness. This parameter gives the BRB element a bilinear force-displacement relationship, which is assumed to have kinematic hardening (see Section 2.3). The use of this type of bilinear element has been shown to provide a good representation of BRB behavior (Usami et al. 2005; Black et al. 2004), and α is varied within a practical range to explore sensitivity of the VTB response to post-yield stiffness. Table 4.1(a) displays the matrix of cases considered for α .

BRBs are axial members whose axial stiffness is controlled by the cross-sectional area, material young's modulus, and member length. However, the member yield force is

also controlled by the cross-sectional area. This results in interplay between the stiffness and yield force, thereby requiring a choice of how to proceed for parametric variation.

$$\text{Axial Stiffness:} \quad K = \frac{EA}{L} \quad (4.2)$$

$$\text{Yield Force:} \quad P_y = F_y A \quad (4.3)$$

Selecting to vary the yield force proves useful for this study. The strength of each BRB can be related to the existing viscous damper design capacity

$$\text{Yield Force Variation:} \quad \gamma = \frac{P_y}{P_{n,damper}} \quad (4.4)$$

This facilitates a reference between proposed BRB members and the existing bridge construction. Additionally, this allows both the variation of member length and yield force, thereby covering a large BRB design space (see Figure 4.1). It is also critical to vary the BRB length, as will be observed throughout the parametric analysis, due to the importance of BRB axial strain response. Blindly investigating only various stiffness values would make difficult the identification of the effects of changing the yield force as compared to changing the length, since both affect the BRB stiffness. By including yield force and length as variables, these relationships can be readily observed and utilized to inform a more optimized solution. The reference yield force was somewhat arbitrarily chosen to be set to 70% of the damper capacity, which corresponds to $\gamma = 0.7$.

Finally, the member length can be varied by means of considering three primary BRB Schemes. Figure 4.2 displays three schemes investigated, along with their respective BRB member lengths at each location. Scheme 1 represents a one-to-one replacement of existing viscous dampers with BRBs, meaning that the BRBs utilize the same connection points where the viscous dampers are attached. Scheme 2 is a somewhat arbitrary member length resulting from assuming the existing damper tower connection location and extending to the middle of the first stiffening truss panel. Lastly, Scheme 3 extends the BRB to attach around the end of the first stiffening truss panel. As shown in Figure 4.2, these schemes represent a fairly large variation in BRB length.

4.3 Global Parametric Study

The first set of the parametric study (see Table 4.1) is primarily used to obtain a general understanding of how the VTB structure responds to the replacement of viscous damper elements with BRB elements with fairly large elastic stiffness. This is important as the existing viscous damper elements do not exhibit any elastic stiffness, and such a modification changes the natural periods of the structure. Additionally, this parametric study aims to qualitatively identify the VTB model response sensitivity to the three varied parameters.

The first varied parameter is α , while the yield force is held constant with $\gamma = 0.7$ at all BRB locations. Likewise, when the BRB yield force is varied with γ , the post-yield stiffness value, α , is held constant at 0.02. The BRB length is varied simultaneously in both cases so as to cover a larger parameter space. Finally, correlation between ADINA and Perform-3D models, with longitudinal only and 3-D input motions, is presented. This correlation is to ensure similar trends and responses provided by the design-level earthquake are obtained, since the simplified model is subjected to only longitudinal excitation.

4.3.1 Effect of BRB Post-Yield Stiffness

The response sensitivity to the post-yield stiffness is investigated through various plausible ratios of elastic to post-yield stiffness. The values were chosen to correspond to slightly less than the lowest and higher than the maximum found in the reviewed literature. The results suggest that the bridge response is least sensitive to α and therefore only one plot is presented which is representative of the general trend for this parameter. In Figure 4.3, it can be observed that the response curves are fairly horizontal for each scheme. Compare this figure with, for example, Figure 4.6 which show the responses are more sensitive to other parameters. Particularly important is the lack of sensitivity for the impact-direction relative displacement and the maximum BRB axial strain responses. The purpose of varying α was to ensure that post-yield stiffness sensitivity was not being overlooked. However, these results permitted the decision to set α to a well reasoned intermediate value, as described below, which is used for the remainder of the parametric study beginning at Section 4.4.

As discussed in Section 2.2, the overstrength of many BRBs is observed to be in a range from about 1.5 to 1.8 (see Table 2.1). By assuming an intermediate value of the post-yield stiffness, from the literature, and an intermediate value of the overstrength, a set of parameters can be used to describe a typical BRB post-yield behavior for finite element representation. A secondary stiffness with $\alpha = 0.0325$ was selected which provides an overstrength of 1.67 at an axial strain of 3%. This represents a best estimate at an intermediate value for any given BRB element, and is not intended to provide a tuned parameter. Such a value should be evaluated by testing with a specific BRB and configuration under consideration. However, this post-yield stiffness and overstrength agree with the reviewed literature with respect to modeling the BRB as a bilinear finite element.

4.3.2 Effect of BRB Yield Strength

Figure 4.4 shows the bridge responses by varying the BRB yield strength. For comparison purposes, the responses of the existing bridge model with fully effective viscous dampers are also shown. Figure 4.4(b) shows impact-direction relative displacement for the side span-to-cable bent location (S-C). The plot clearly shows that small γ values do not provide a benefit over the existing damper response, while also producing very large BRB axial strains [Figure 4.4(c)]; these strains for $\gamma < 1.05$ are very far from the typical BRB cyclic strain capacity range. Furthermore, looking back to the impact measure, $\gamma \geq 1.05$ do present a response below that observed from the existing viscous damper model. Moving to Figure 4.4(d), the maximum axial force is very evidently much higher than that of the damper capacity for $\gamma \geq 1.05$. With these forces reaching more than twice the damper design capacity, this is obviously a concern because it implies a much larger seismic force will be imposed to the existing structure. Finally, the cumulative ductility demand is calculated for each case in Figure 4.4(e). It is apparent that all but Scheme 3 with $\gamma < 0.7$ have cumulative ductility demands that are in line with typical BRB cumulative ductility capacity (see Section 2.2).

The side span-to-tower location (S-T) is observed in Figure 4.5. With the exception of Scheme 3 with $\gamma = 0.35$, all configurations show better impact response than the viscous

damper model as well as acceptable BRB axial strain and cumulative ductility values. However, the increased axial force is again observed.

The main span-to-tower location (M-T) shows very similar trends as the S-C. However, the responses presented in Figure 4.6 exhibit a much greater sensitivity to BRB yield force in almost every criterion. Impact displacement is drastically reduced as γ increases, and almost every case shows lower response than that of the viscous damper model. Turning again to the BRB axial strain, however, it is evident that the cases of Schemes 2 and 3 with $\gamma \geq 1.05$ are within the typical BRB cyclic strain capacity range. Cumulative ductility demands are relatively low for these cases.

4.3.3 Perform-3D and ADINA Global Response Comparison

The preliminary portion of the parametric study was performed using the Perform-3D model. In an effort to expedite the many analyses required for parameter study, the Perform-3D model with input ground motion in the longitudinal direction was used for the analyses presented above. This was deemed an acceptable assumption for the initial phases of the study, as the longitudinal component has been observed to produce the majority of the seismic demand upon the dampers and BRB elements. Nevertheless, it was necessary to ensure that these simplified analyses were capable of capturing similar trends and responses as the 3-D excitation of the more comprehensive ADINA model. Therefore, the ADINA model analyses were conducted to provide a few data points relating the two models.

Figure 4.7 through Figure 4.9 show Scheme 2 with γ varied from 0.35 to 1.4 as in the initial γ variation, in addition to four data points produced from ADINA model analyses. As is stated in the figure, one set is the result of exactly the same model conditions as the Perform-3D model. This means that the ADINA model foundation finite elements are restrained, fixed, and is subjected to longitudinal excitation only. It is evident that these data points (solid diamonds) correlate very well with a majority of their Perform-3D counterparts. This is strong evidence that the Perform-3D provided trends that are fairly accurate, and the results thus far are valid. Additionally, the ADINA model responses due to 3D excitation provided some mild disparities. The main differences are observed in the cumulative ductility demands. Of course, the 3D excitation adds a certain amount of

increased demand; however the longitudinal-only input also demonstrates some areas of increased demand. This is most likely due to some additional flexibility inherent in the ADINA model which is not perfectly represented in the Perform-3D model. However, some cumulative ductility values are observed to be significantly different. This is of little concern as even the larger ADINA values are still very low compared to the cumulative ductility capacities typically achieved by BRBs in performance testing (as discussed in Section 2.2). Without cumulative ductility demands that are drastically greater than that ($= 200$) required by the AISC Seismic Provisions, the most important indicators of BRB feasibility are the peak axial strain demands and the impact-direction relative displacements. Moreover, most of the results are in fair agreement and both the global and preliminary analyses are deemed to be valid.

4.3.4 Concluding Remarks

Based on the results presented in Figure 4.4 through Figure 4.6, it is clear that a preliminarily feasible solution is Scheme 2 with $\gamma = 1.05$. Given the reduced impact displacement, acceptable strain values, and relatively low cumulative ductility demands, this retrofit scheme is attractive. The primary problem that is yet to be addressed is the significant increase in force imparted to the bridge structure by each of the six BRBs. This issue is investigated in Section 4.6.

4.4 Parametric Study with Local Adjustment of BRB Parameters

First, it is reminded that the parameter analyses in Section 4.3 were conducted with a globally constant γ value for varying the BRB yield forces. The next step recognizes the results from the initial parametric study and refines the preliminarily feasible solution by seeking out local adjustments to the BRB property parameters. This is accomplished through local variation of γ , by way of the variables γ_{S-C} , γ_{S-T} , and γ_{M-T} , where the subscript designates the BRB location as used above. At each location the case of $\gamma = 0$ is considered as it is rational to explore this extreme in the parameter space. This process yields an understanding of how each BRB location affects the others. Results of the localized parametric study are analyzed in more depth as these relations demand increased attention.

After noting the effects of local γ variation, the local BRB length will also be considered for parametric study. Similarly, the location under consideration will be the only BRB to exhibit a varied length. Cases of interest from the localized γ cases will all be compared simultaneously with varied length to readily identify the best combination of variables for each location. Again, the main variable will be accompanied by a subscript which designates the location of the BRB it affects, such as L_{S-T} for length of the side-to-tower BRB. The range of length used are those of Scheme 2 increased to a maximum of Scheme 2 plus two-thirds the difference between Scheme 3 and Scheme 2. For instance, L_{S-C} for Scheme 2 is 29 ft and Scheme 3 is 44 ft. Therefore, Scheme 2.1 is used to designate a length of $29 + (44-29)(1/3) = 34$ ft, while Scheme 2.2 would produce 39 ft. These increased lengths obviously decrease the BRB stiffness if the yield force is unchanged. However, the responses are not entirely dependent on the stiffness as the yield force must be reached before post-yield stiffness is effective.

4.4.1 Effect of γ_{S-C} on Bridge Response

In Figure 4.10 the yield force for the γ_{S-C} BRB is varied while γ_{S-T} and γ_{M-T} set to 1.05 as a basic value. Inspecting Figure 4.10(b), the extreme case of no cable bent BRB, where $\gamma_{S-C} = 0$, shows that the side span nearly impacts the cable bent support. This is obviously not desired, however the influence on the S-T and M-T impact-direction displacements is notably reduced from the other extreme $\gamma_{S-C} = 1.25$. A slight inverse relationship is present between γ_{S-C} , γ_{S-T} , and γ_{M-T} BRB locations respectively. Additionally, it is interesting to note the BRB maximum strain, maximum axial force, and cumulative ductility demands for S-T and M-T locations are also reduced. Conversely, the S-T and M-T BRBs show a modest increase in axial strain with an increase in S-C BRB stiffness. For the S-T location, this can be visualized as the cable bent pushing the side span into and pulling it away from the tower. Essentially, the S-C BRB is a much more stiff spring than the S-T BRB, and the suspended span has little other longitudinal stiffness other than these two springs. This relationship is important for further refinement of the BRB retrofit solution.

The cases which present the most promising responses are $\gamma_{S-C} = 0.7, 1.05$, and 1.25 . These three scenarios present, first and foremost, impact-direction displacements which

are either less than or equal to that of the damper model. Furthermore, the displacements are roughly one half the impact displacement. This suggests that these BRBs are adequately, if not overly, stiff. Inspection of the maximum axial force, of course, shows large increases with increasing γ_{S-C} . However, the axial strain values are fairly high, and is prohibitively so in the $\gamma_{S-C} = 0.70$ case. Given the combination of overly stiff and large axial strain, the logical action would be to increase the BRB length. Increasing the length without changing the stiffness resolves excessive strains, but does take advantage of the available impact relative displacement due to relatively small responses. Therefore, increasing the BRB length while the yield force (i.e., the cross-sectional area via γ_{S-C}) remains unchanged satisfies both concerns. Hence, an additional localized parameter refining stage should explore $\gamma_{S-C} = 0.7, 1.05$ and 1.25 with various increased lengths. See Section 4.4.4 for further discussion.

4.4.2 Effect of γ_{S-T} on Bridge Response

Once again, in Figure 4.11, for the case considering $\gamma_{S-T} = 0$ results in a displacement that constitutes impact to the support. However, with the variation of only γ_{S-T} it is evident that the S-C BRB is fairly insensitive with respect to maximum axial strain, while the M-T BRB is somewhat inversely affected. Due to the complex nature of the VTB model and the multiple support excitations, it is difficult to reconcile the observation that the S-C is fairly independent of the S-T BRB stiffness with respect to the maximum strain while the impact-direction displacement is modestly influenced [Figure 4.11(b) and (c)]. However, it is likely due to the single large impulse in one longitudinal direction, which is present in the design-level input ground motion. The ground displacements pulse from West to East and then abruptly back towards the West. This causes the West-facing BRBs to be subjected to very large compression forces, and East-facing BRB to be subjected to large tension forces, upon the pulse back towards the west.

The difference in compression and tension demands could be a result of the delayed motion of the suspended spans, which causes different compression and tension relative displacements. In other words, the tower is moving much faster due to the ground pulsing while the spans swing about the suspension cables, which causes a delay in their response. This initially causes a compression and tension in BRB on either side of the

span. Afterwards, the towers pulse back toward the initial position while the spans' inertia force carries them in the opposite direction again causing a tension and compression on either side. See Figure 4.12, which displays the two displacement time histories to further illustrate this behavior. The respective differences in these two events could possibly account for the difference in relationship between S-C and S-T BRB strain and impact-direction responses, as maximum strain is observed to occur in tension as well as the large difference in strength between the two.

Note the S-T displacement is larger than the impact displacement, indicated by the solid line in Figure 4.11. This is explained by the fact that the finite elements which account for impact of the spans to the supports are only located at the centerline of the bridge together with the transverse motion resisting wind shoe configuration. This creates a pinned condition, in the transverse direction, for each of the spans. Therefore, it was important to monitor each BRB element's change in length in order to capture a case such as this where either transverse side of the bridge is displaced more in the longitudinal direction than is the center, due to transverse rotation about the wind shoe.

A similar conclusion, to that in the γ_{S-C} variation step, can be reached for γ_{S-T} variation. The $\gamma_{S-T} = 1.05$ case yields an impact-direction relative displacement roughly one-half the impact value. Therefore, this configuration will be subjected to changes in length in an attempt to reduce the strain demand, utilize the excess displacement available, and reduce the maximum force imparted on the bridge structure.

4.4.3 Effect of γ_{M-T} on Bridge Response

From Figure 4.13 similar response relationships can be observed between the three locations. With $\gamma_{M-T} = 0$, yet again the demand is reduced on both S-C and S-T while permitting the main span to become very near the impact level displacement. However, with $\gamma_{M-T} = 0.7, 1.05,$ and 1.25 the results are much more revealing and helpful. For example, there is a very clear increase in S-T impact displacement response with a decrease in M-T impact displacement (due to an increased M-T stiffness). Additionally, the drastic drop in maximum strain demand between $\gamma_{M-T} = 0.525$ and $\gamma_{M-T} = 0.70$. Obviously, the structure is sensitive to this range of stiffness as $\gamma_{M-T} > 0.70$ only shows modest decreases in maximum strain. For $\gamma_{M-T} = 1.25$, the benefits of a larger yield force

are realized in a reduced strain demand well within the typical BRB performance range. Furthermore, the impact-direction displacements for $\gamma_{M-T} > 0.525$ exhibit some available displacement that could provide some parameter flexibility, which will be explored in Section 4.4.6.

4.4.4 Effect of L_{S-C} on Bridge Response

In Figure 4.14 the variation of L_{S-C} is explored, while the others are held to $L =$ Scheme 2 and $\gamma = 1.05$. The plot in Figure 4.14(a) shows only a slight increase of impact-direction displacement, which displays the fact that the responses are not entirely dependent on the stiffness. Most significant is the decrease in maximum strain for the $\gamma_{S-C} = 1.25$ case, which is shown to be just over 4% decreased from over 5%. Again, the initially uncertain relationship between the responses and the stiffness is exhibited in the fact that the maximum strain does not change from $L_{S-C} =$ Scheme 2.1 to $L_{S-C} =$ Scheme 2.2. Furthermore, the trend would also be expected for $\gamma_{S-C} = 0.7$ and 1.05 cases. Additionally, in Figure 4.14 (d), the maximum force is shown to be decreased and almost equal to that of the $\gamma_{S-C} = 1.05$ with $L_{S-C} =$ Scheme 2.1 case. Therefore, from these results the S-C BRB with $\gamma_{S-C} = 1.25$ and $L_{S-C} =$ Scheme 2.1 (or approximately 34 ft) is selected as the best observed solution for the location. Section 4.4.7 will validate the use of this BRB configuration despite the parameters being unchanged, in this step, for the other locations.

4.4.5 Effect of L_{S-T} on Bridge Response

The L_{S-T} variation presents a more straightforward trend of decreasing maximum strain, slightly increasing impact displacement, and slight decrease in maximum force (see Figure 4.15). With $L_{S-T} =$ Scheme 2.2 corresponding to a length of only 30 ft, Scheme 2.2 is chosen as the best candidate. Even though the strain value for $L_{S-T} =$ Scheme 2.1 is within the desired range, past steps show that a decrease in S-C BRB maximum strain yields an increase in S-T maximum strain. The same has been observed for the M-T location. Therefore, the lowest possible S-T strain should be selected in an effort to hold it within the desired range after modifications are implemented at the other locations.

4.4.6 Effect of L_{M-T} on Bridge Response

An interesting similarity to the S-C BRB local refinement results is present in the M-T refinement, and is observable in Figure 4.16. The linear trends are found for the $\gamma_{M-T} = 0.70$ and 1.05 cases, while the same response flattening occurs between $\gamma_{M-T} = 1.25$ between $L_{M-T} =$ Scheme 2.1 and Scheme 2.2. However, for this location two options appear to be feasible. The $\gamma_{M-T} = 1.25$ Scheme 2.1 case provides the least M-T BRB maximum strain, while approximately the same maximum force. However, the $\gamma_{M-T} = 1.05$ with $L_{M-T} =$ Scheme 2.2 case produces a mid-range maximum strain and very slightly less maximum force. All the while, the impact displacements are both very low as compared to the damper model response. With some ambiguity regarding which BRB is the best choice, both $\gamma = 1.05$ with Scheme 2.2 and $\gamma = 1.05$ will be considered for a final solution study in Section 4.5.

4.4.7 Insensitivity of Length Variation on Adjacent BRBs

The choices made in the previous three sections have seemingly been based on only the responses of the BRB at the location under variation. This is not the case, and would not be the proper way to make such a decision. Therefore, Figure 4.17 provides the plots of the maximum axial strain for the remaining two locations for each portion of the localized parameter refinement study. These show the very small, if not complete lack, of sensitivity for the strain responses at the adjacent BRB locations. Besides this fact, the greatest sensitivity is observed to in Figure 4.17(a). The S-T BRB strain demand actually decreases more than 0.5% with a S-C BRB of $\gamma = 1.25$ and length corresponding to Scheme 2.1. This did not directly influence the choice for the S-C BRB, however it was noted. The location-to-location relationships observed from the global γ , along with the benefits realized in the refined γ local variation, were the major factors for choosing a configuration with which to proceed.

4.5 Final Parametric Refinement and Concluding Remarks

From Section 4.4, two configurations are chosen for a finalized feasible BRB retrofit solution. The two cases have $\gamma_{S-C} = 1.25$, $\gamma_{S-T} = 1.05$, $L_{M-T} =$ Scheme 2.1, and $L_{S-T} =$ Scheme 2.2 in common while $\gamma_{M-T} = 1.05$ and $\gamma_{M-T} = 1.25$ with lengths of $L_{M-T} =$ Scheme 2.2 and Scheme 2.1 are parametrically investigated. This leads to the two plots presented

in Figure 4.18, which are taken as the two most feasible cases found in the present study. With the impact displacement responses of each configuration being less than that of the damper model, they are much less than the impact displacements. Most importantly, for the BRB performance consideration, the maximum strains are all within the desired range between 3% and 5%. The S-C location is roughly 5%, however this could possibly be further tuned to be somewhat reduced.

The final solution is selected to be $\gamma_{M-T} = 1.05$ with length $L_{M-T} = \text{Scheme 2.2}$. This conclusion is due to the lower strain demands for M-T and S-T BRBs as well as the decreased impact displacement at the S-T location. Two main issues affect the feasibility of the final configuration. The axial strains of 4 and 5% are not typically acceptable operating values for BRB. However, the seismic demand is presented in a single pulse, while the remainder of the demand is well within the normally tested strain range of 1 to 3%. Additionally, the maximum forces imparted to the tower and cable bent are larger than those presented by the dampers. Yet, the damper forces are likely not indicative of the support structure capacity. Further discussion of the BRB, BRB demand, and support demand is provided in Section 4.7.

A summary of the 3-D excitation design-level responses from the ADINA model is provided in Table 4.4. Maximum responses due to the recorded seismic events described in Section 3.2.2, are provided in Table 4.5 through Table 4.8. It is evident that the BRB retrofit drastically reduces the impact displacement demands for these ground motions. Additionally, the lower level events do not yield the BRB, indicating that the BRBs would be capable of sustaining no damage from yielding due to somewhat frequent events.

Attention has been paid to the changes in the bridge fundamental dynamics. The periods of the first few modes are reported in Table 4.9 for the damper model and Table 4.10 for the proposed BRB retrofit model. It is observed that the first longitudinal mode in the damper model has been shifted, or entirely changed. These modes are very clear in the damper model but are not well represented in the BRB model per the model effective mass fractions reported in the table. Additionally, the first transverse and the first few vertical modes are also shifted moderately. Higher modes are not affected as much, which may help explain the lack of increased shear demand observed in the towers. This

is not typically the goal in a seismic retrofit; however the very different nature of the BRB and damper elements makes this shift unavoidable. This obviously would cause the bridge to attract higher response accelerations given a totally elastic system; however the ductility of the braces actually provides a decreased acceleration along parts of the response, as observed in Figure 4.19.

The result of the parametric study is the VTB equipped with $\gamma_{S-C} = 1.25$, $\gamma_{S-T} = 1.05$, and $\gamma_{M-T} = 1.05$ with lengths $L_{S-C} = \text{Scheme 2.1}$, $L_{S-T} = \text{Scheme 2.2}$, and $L_{M-T} = \text{Scheme 2.2}$, which corresponds to approximately 34, 30 and 32 ft, respectively. This configuration provides greatly reduced impact-direction relative displacements between the supports and the spans for all seismic events, as compared to the viscous damper model, while providing an elastic response under low level earthquakes.

Additionally, the energy dissipation provided by the BRB as compared to the viscous dampers is notable. Figure 4.20 displays some examples of the cumulative energy dissipation time histories from each BRB location, with the corresponding cumulative energy dissipated by the viscous damper. Figure 4.21 provides a global comparison of the amount of energy dissipated by each device. Most all locations experience a significant increase in dissipated energy with BRBs.

4.6 Bridge Superstructure Demands and Capacities

From the parametric study, a feasible solution for BRB implementation has been developed. To implement this solution, it is highly desirable that the capacity of existing support structures such as the towers and the cable bents is sufficient to resist the BRB reaction forces such that expensive strengthening is unnecessary. In this section, the seismic demands are presented and a preliminary assessment of the superstructure capacities is presented.

4.6.1 Tower

The towers provide a connection point for the BRBs attached to the main and side spans. The viscous damper axial force capacities, as well as the design-level damper maximum force responses, are notably lower than the proposed BRB reactions and, therefore, the ability of the tower to withstand these forces should be evaluated. The

towers are constructed of primarily $\frac{3}{4}$ -in steel plates built-up to form a crucifix type cross-section with steel plate diaphragms spaced along the height.

Figure 4.22 displays the comparison of the tower seismic force demand results from the damper and final BRB solution models; ADINA models with 3D input motion were used in the analysis. Regardless of the large increase in maximum axial force delivered by the BRBs over the dampers, the tower longitudinal shear and moment demands are only slightly larger. The mechanics are not initially apparent until the axial force phase-relationship between the S-T and M-T BRB members is considered. As shown in Figure 4.23, the adjacent BRBs are in tension and compression in-phase with each other. Therefore, in spite of the larger seismic forces the two act opposite one another, thereby limiting the increased shear and moment demand on the tower. Also shown in Figure 4.23 is the damper force phase relation. The opposite behavior is found, and therefore the dampers actually act together to produce shear, and consequently moment, to the tower. This phase relation is also observed in the moderate-level and low-level earthquake responses. The phase relation is plotted for the 1994 Northridge earthquake in Figure 4.24 for reference.

The strength of pin-plate connection that currently connects the viscous dampers to the towers was evaluated. Limit states of tensile rupture, shear rupture, bearing, and yielding were checked for the $1\frac{1}{2}$ -in thick pin-plates that receive the damper pin. The welds and bolted connection that attaches the pin-plates to the tower wall were also evaluated for weld rupture and bolt tension capacities. The resulting strengths are displayed in Table 4.12, and show that the proposed BRB retrofit exhibits a force just slightly over the design strength. Moreover, the damper forces are much less than the capacity found. This provides an indication that the tower and stiffening truss members are likely capable of similar levels of reaction force. This is an encouraging finding as it suggests that the BRB retrofit may not require significant strengthening of the existing superstructure. However, further evaluation of tower strength would be required for actual BRB implementation.

The somewhat small increase in longitudinal moment did not motivate a more global check of the tower capacity, as the geometry and construction require detailed attention. However, past studies have shown demand-to-capacity ratios of approximately 2 for the

existing retrofit performance (Moffatt and Nichol 1996; Ingham et al. 1997). Therefore, with this small increase, the ratio will increase somewhat. Despite the increased ductility required, the global capability of the tower shafts to resist the BRB reaction forces is deemed adequate for feasibility considerations.

4.6.2 Cable Bent

Cable bent longitudinal moment demands are displayed in Figure 4.25. Due to the lack of changes observed in the tower transverse demands, it is obvious that the BRBs do not contribute to this direction; therefore only the longitudinal moment has been presented for the cable bents. The damper and BRB models exhibit very similar moment time histories, and do not motivate any further consideration at this point. The cable bents are deemed fully capable of withstanding the changes in force due to the addition of the BRBs.

4.6.3 Span Trusses

The BRB attach to the main and side spans via the stiffening trusses. Since the maximum axial forces observed in the BRBs are higher than those of the dampers, it is obvious that the force demands are higher for the stiffening truss members. The tower-to-main span BRBs as well as the cable bent-to-side span BRBs exhibit larger forces than the side span BRBs while the trusses have similar sections. Therefore, additional strengthening may be limited to only those two locations. For feasibility considerations, this is a secondary concern even some portions are likely to require minor strengthening to accommodate the BRB forces.

4.7 BRB Demands and Capacities

The parametric study produced maximum axial strain demands for the BRBs that are somewhat higher than those typically considered during component testing, but within the range of those tests discussed in Section 2.2. This section addresses this issue and gives way to the testing plan presented in a later section.

The maximum strain demands on the BRB elements are shown in Table 4.5. They are no greater than 5% and occur only in the design-level earthquake during a single pulse. Although this level of strain is slightly higher than that typically tested (Merritt 2003;

Newell 2005; Newell 2006) among others, the maximum tested strain values are generally applied in a low-cycle fatigue loading step. This loading consists of fairly large strain amplitudes which are repeated many times, usually around 5-10 cycles. Therefore, the direct comparison of the test strain values and the demand is not a clear one. Takeuchi et al. (2008) report BRB testing results from various loadings some of which are shake table BRB frame results, and others which are BRB component tests under random amplitude loading. The maximum strains reported are upwards of 7%, and some time histories appear to have similar characteristics in loading history to those observed from the VTB design-level earthquake, as seen in Figure 4.26. The strain time histories of BRBs with the largest, and also pulse-like, strain demands are shown in Figure 4.27. It is evident that the strain demand has one distinct large peak, while the remainder of the time history has small-amplitude strains that are much more typical values observed in BRB performance testing. Furthermore, the other lower strain demands occur over slightly more cycles but are very much in the typically tested strain range for BRBs. This supports the feasibility for using the BRB for the VTB retrofit. The main difference between the BRB in the feasible solution and those reported on by Takeuchi et al. is the lengths of the BRBs. Those reported are much shorter than the proposed BRB, however the strain amplitudes are still very high in the report. Additionally, the BRB and damper hysteresis plots are provided in Figure 4.28 for reference. The pulse is visible in the hysteresis plots as well.

The BRB capacity as it relates to yield force is of little concern, as many BRB have been produced and tested with much larger yield forces than have been investigated in this study. For example, the highest considered yield force considered in the entire parametric study is that of the S-C BRB with $\gamma = 1.25$. This corresponds to a yield force of only 662.5 kips which is well below the maximum reviewed in Section 2.2. Therefore, the capability of BRB to supply the required yield force is known to be available. Additionally, the maximum axial forces should also be considered achievable as the post-yield stiffness was selected using the overstrength and post-yield stiffness values observed from the literature and test results shown in Section 2.2.

The demands on the BRB due to the lower level events do not pose any feasibility questions (see Table 4.5) aside from, perhaps, a fatigue question which is addressed in

Section 5 and should be verified through physical testing before BRB retrofit implementation.

4.8 Feasibility and Required Data

This BRB retrofit parametric study has yielded a solution that does appear feasible for further implementation after some additional and more detailed investigation. The benefits in seismic response mitigation are marked with respect to the impact displacement responses for design-level, moderate-level, and low-level earthquakes. These results are summarized in Table 4.4 through Table 4.8. The reduction in impact-direction displacement is typically no less than one half that of the damper model. As will be discussed in the next section, the ambient motion is also reduced in a similar fashion, which is considered very beneficial considering the reports of excessive bridge movement. The primary challenge for BRB use on long-span bridges is the large core strain demand. The large pulse-like strain demand on the BRB should be included in a component test plan to verify the adequacy of the braces.

The challenges facing actual implementation of the proposed solution are few, but critical. Tower capacity should be evaluated in detail and truss members likely will require reinforcement and relocated attachment locations for BRBs with lengths different from the lengths of the viscous dampers. Overall, actual implantation would require a detailed design-oriented evaluation of the bridge superstructure considering the expected forces imparted to the bridge by BRBs.

Table 4.1 Parametric Matrices for Global Adjustment of BRB Mechanical Properties

(a) Variation of Post-Yield Stiffness and Member Length

α	γ	Scheme 1*			Scheme 2			Scheme 3		
		S-C	S-T	M-T	S-C	S-T	M-T	S-C	S-T	M-T
0.01	0.70	Response Parameter Investigated: Maximum Impact-direction Relative Displacement Absolute Maximum BRB Axial Strain Absolute Maximum BRB Axial Force Cumulative Ductility Demand Goal: Determine response sensitivity								
0.02										
0.03										
0.04										
0.05										

* See Figure 4.2 for scheme designation

(b) Variation of Yield Force and Member Length

α	γ	Scheme 1			Scheme 2			Scheme 3		
		Cable -Bent	Side	Main	Cable -Bent	Side	Main	Cable -Bent	Side	Main
0.0325	0.35	Response Parameter Investigated: Maximum Impact-direction Relative Displacement Absolute Maximum BRB Axial Strain Absolute Maximum BRB Axial Force Cumulative Ductility Demand Goal: Determine response sensitivities and preliminary feasibility								
	0.525									
	0.70									
	1.05									
	1.40									

(c) Correlation between Perform-3D and ADINA

α	γ	Scheme 2		
		Cable-Bent	Side	Main
0.0325	0.525	Response Parameter Investigated: Same as Global α and γ Variation Studies Goal: Produce crucial data points verifying Perform-3D and ADINA models providing similar trends and values		
	1.05			

Table 4.2 Parametric Matrices for Local Adjustment of BRB Mechanical Properties

(a) Effect of Yield Force Variation

γ_{S-C}	γ_{S-T}	γ_{M-T}		γ_{S-C}	γ_{S-T}	γ_{M-T}		γ_{S-C}	γ_{S-T}	γ_{M-T}
0	1.05	1.05		1.05	0	1.05		1.05	1.05	0
0.525					0.35					0.525
0.70					0.525					0.70
1.05					0.70					1.05
1.25					1.05					1.25

Note: All BRB lengths correspond to Scheme 2

(b) Effect of Yield Force and Length Variation

Location	S-C			S-T	M-T		
γ	0.70	1.05	1.25	1.05	0.70	1.05	1.25
L	Scheme 2, Scheme2.1, Scheme 2.2 (each location together with γ)						

Note: All $\gamma = 1.05$ and $L =$ Scheme 2 unless noted otherwise

Table 4.3 Examples of Varied Characteristic Values

Dampers		Buckling-Restrained Braces						
Location	P_u (kips)	γ	P_y (kips)	Area* (in ²)	Length	K_1 (kip/in)	α	K_2 (kip/in)
S-C	530	0.70	371	9.37	Scheme 1 14 ft	1617.4	0.02	32.35
		1.05	556.5	14.1		2426.0	0.0325	78.85
S-T	150	0.70	105.0	2.65	Scheme 2 20 ft	320.2	0.02	6.40
		1.05	157.5	3.98		480.9	0.0325	15.63
M-T	400	0.70	280.0	7.07	Scheme 3 37 ft	461.8	0.02	9.24
		1.05	420	10.6		693.0	0.0325	22.53

*Assuming $F_y = 36(1.1) = 39.6$ ksi

Table 4.4 BRB Final Retrofit and Damper Model Design-Level Earthquake

Model	Location	Final Retrofit Parameters	Max Impact Displacement* (in)	Max Axial Force (kips)	Max Axial Strain (%)	Cumulative Ductility Demand
BRB	S-C	$\gamma = 1.25$ $L = \text{Sch. 2.1}$	13.8 (30)	1408	4.86	133
	S-T	$\gamma = 1.05$ $L = \text{Sch. 2.2}$	15.1 (21)	311	4.21	250
	M-T	$\gamma = 1.05$ $L = \text{Sch. 2.2}$	9.5 (39)	818	4.11	113
Damper	S-C		18.5 (30)	445		
	S-T		17.3 (21)	131		
	M-T		22.7 (39)	364		

* Values in parentheses are the displacement at which impact occurs

Table 4.5 BRB Retrofit and Damper Model 1994 Northridge Responses

Model	Location	Final Retrofit Parameters	Max Impact Displacement* (in)	Max Axial Force (kips)	Max Axial Strain (%)	Cumulative Ductility Demand
BRB	S-C	$\gamma = 1.25$ $L = \text{Sch. 2.1}$	0.28 (30)	354	0.07	0
	S-T	$\gamma = 1.05$ $L = \text{Sch. 2.2}$	1.20 (21)	168	0.40	23.5
	M-T	$\gamma = 1.05$ $L = \text{Sch. 2.2}$	0.42 (39)	346	0.11	16.5
Damper	S-C		2.64 (30)	76		
	S-T		0.62 (21)	19		
	M-T		1.40 (39)	53		

* Values in parentheses are the displacement at which impact occurs

Table 4.6 BRB Retrofit and Damper Model 1987 Whittier Responses

Model	Location	Final Retrofit Parameters	Max Impact Displacement* (in)	Max Axial Force (kips)	Max Axial Strain (%)	Cumulative Ductility Demand
BRB	S-C	$\gamma = 1.25$ $L = \text{Sch. 2.1}$	0.15 (30)	184	0.04	0
	S-T	$\gamma = 1.05$ $L = \text{Sch. 2.2}$	0.56 (21)	161	0.21	16.2
	M-T	$\gamma = 1.05$ $L = \text{Sch. 2.2}$	0.30 (39)	268	0.09	0
Damper	S-C		1.27 (30)	45		
	S-T		0.59 (21)	12		
	M-T		1.10 (39)	40		

* Values in parentheses are the displacement at which impact occurs

Table 4.7 BRB Retrofit and Damper Model 2008 Inglewood Responses

Model	Location	Final Retrofit Parameters	Max Impact Displacement* (in)	Max Axial Force (kips)	Max Axial Strain (%)	Cumulative Ductility Demand
BRB	S-C	$\gamma = 1.25$ $L = \text{Sch. 2.1}$	0.06 (30)	83	0.02	0
	S-T	$\gamma = 1.05$ $L = \text{Sch. 2.2}$	0.13 (21)	50	0.04	0
	M-T	$\gamma = 1.05$ $L = \text{Sch. 2.2}$	0.07 (39)	56	0.02	0
Damper	S-C		0.37 (30)	7.84		
	S-T		0.94 (21)	8.83		
	M-T		0.94 (39)	7.49		

* Values in parentheses are the displacement at which impact occurs

Table 4.8 BRB Retrofit and Damper Model 2009 Chino Hills Responses

Model	Location	Final Retrofit Parameters	Max Impact Displacement* (in)	Max Axial Force (kips)	Max Axial Strain (%)	Cumulative Ductility Demand
BRB	S-C	$\gamma = 1.25$ $L = \text{Sch. 2.1}$	0.07 (30)	79	0.02	0
	S-T	$\gamma = 1.05$ $L = \text{Sch. 2.2}$	0.25 (21)	80	0.07	0
	M-T	$\gamma = 1.05$ $L = \text{Sch. 2.2}$	0.12 (39)	106	0.03	0
Damper	S-C		0.34 (30)	6		
	S-T		0.80 (21)	8		
	M-T		0.81 (39)	11		

* Values in parentheses are the displacement at which impact occurs

Table 4.9 Damper Model Natural Periods and Modal Effective Mass Fractions

Mode	Period (sec)	MEMF Longitudinal (%)	MEMF Transverse (%)	MEMF Vertical (%)	Description
1	7.71	0	5.78	0	Main trans., symm.
2	5.55	4.36	0	0	Main longt.
4	4.43	0.07	0	1.40	Vert both, symm.
6	4.34	2.12	0	0	Main longt. and vert side, symm.
7	2.78	0.04	0	0	Vert sides, symm.
8	2.75	0	0	0.01	Vert both, symm.
9	2.44	0	0.01	0	Sec main trans., symm.
12	2.19	0	0	7.75	Vert both, symm.

Table 4.10 BRB Retrofit Model Natural Periods and Modal Effective Mass Fractions

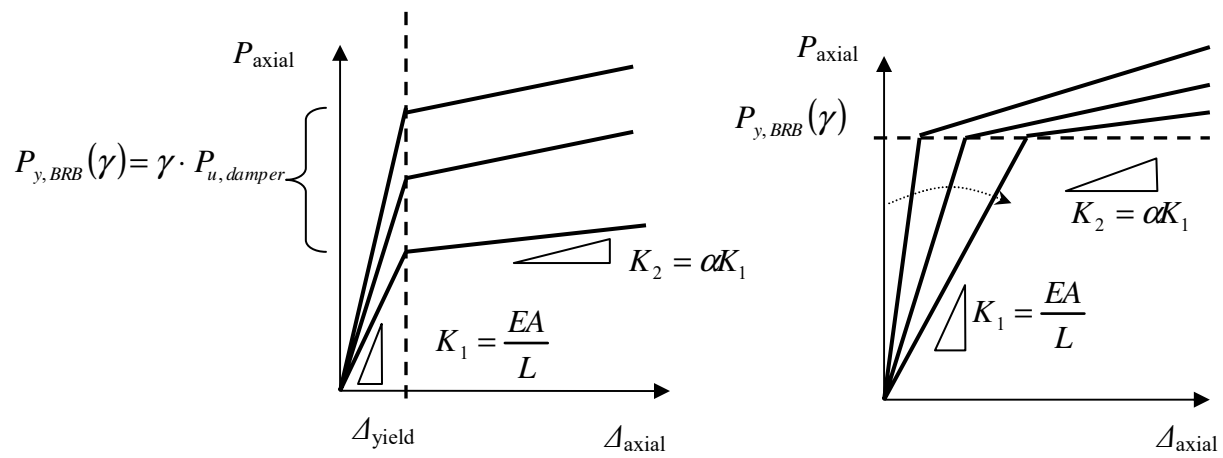
Mode	Period (sec)	MEMF Longitudinal (%)	MEMF Transverse (%)	MEMF Vertical (%)	Description
1	6.32	0	5.53	0	Similar to Damper 1
4	4.32	4.0×10^{-4}	0	1.0×10^{-4}	Similar to Damper 2
5	4.19	0	0	1.77	Similar to Damper 4
6	2.58	0	0	1.4×10^{-2}	Similar to Damper 8
8	2.51	1.7×10^{-3}	0	0	Similar to Damper 7
10	2.30	1.7×10^{-4}	9.7×10^{-3}	0	Similar to Damper 9
11	2.04	0	0	7.33	Similar to Damper 12
23	1.44	0	0	0	Whole bridge longt.

Table 4.11 Comparison of BRB Axial Force Demands

Design-Level Earthquake	Axial Force At Pulse		% Difference
	BRB (kips)	Damper (kips)	
Main Span BRB	817.9	362.3	225.7 %
Side Span BRB	268.8	-50.5	532.3 %
Net Contribution to Tower Shear	549.1	412.8	133.0 %

Table 4.12 Damper to Tower Connection Capacities and Demands

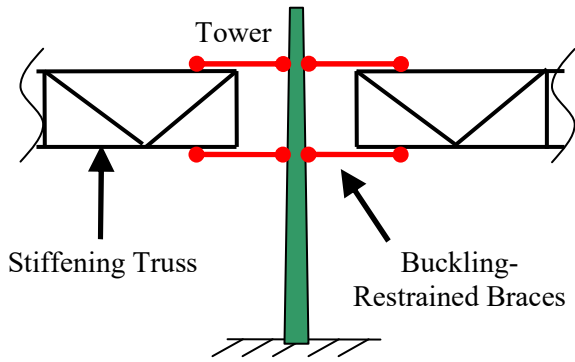
Component	Design Strength, (kips)		Design-Level Seismic Force Demand (kips)			
			Side Span		Main Span	
	Side Span	Main Span	Damper	BRB	Damper	BRB
Pin Plate	492	810	161	311	364	818
Bolted Connection to Tower Wall	2332	2332				



(a) Effect of Varying Steel Core Area

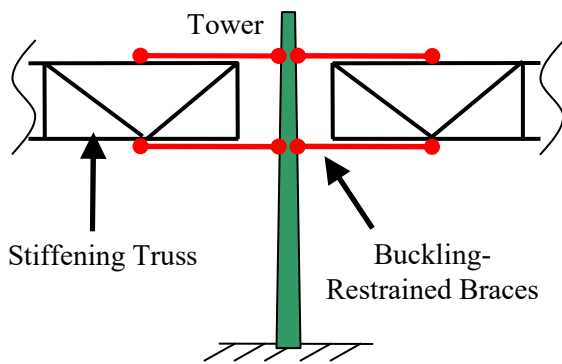
(b) Effect of Varying Brace Length

Figure 4.1 Depiction of BRB Stiffness and Strength Space



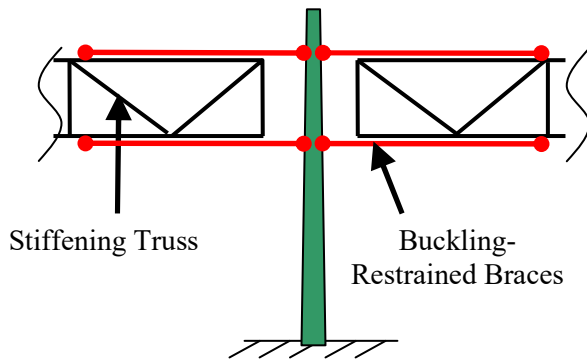
Location	BRB Length
Side/Cable Bent	14 ft
Side/Tower	13 ft
Main/Tower	15 ft

(a) Scheme 1



Location	BRB Length
Side/Cable Bent	29 ft
Side/Tower	20 ft
Main/Tower	21 ft

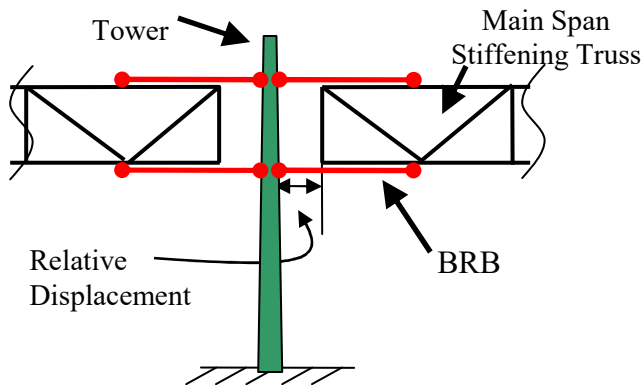
(a) Scheme 2



Location	BRB Length
Side/Cable Bent	44 ft
Side/Tower	35 ft
Main/Tower	37 ft

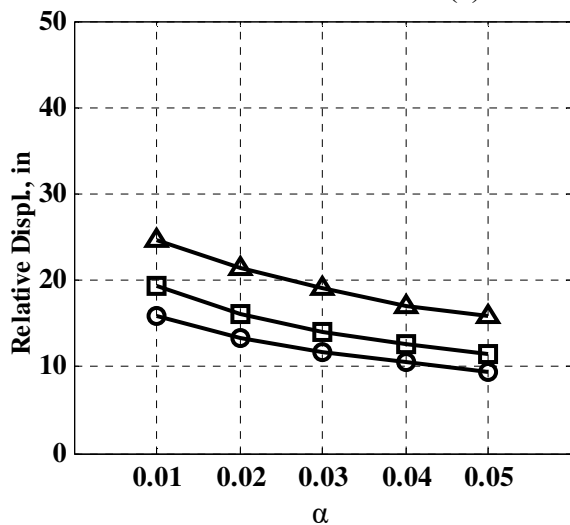
(c) Scheme 3

Figure 4.2 BRB Schemes and Length Variation

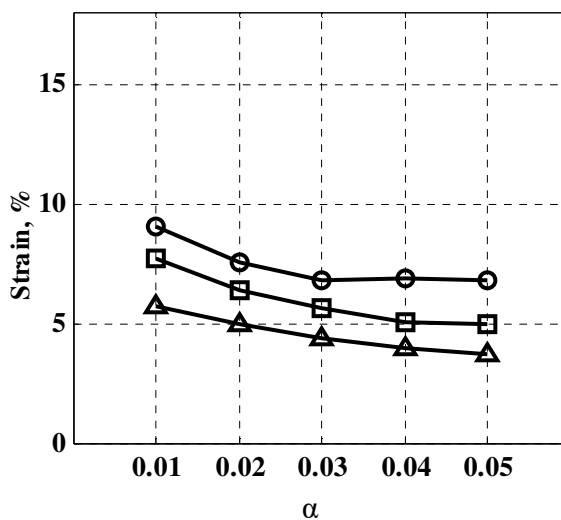


Scheme	BRB Length	Marker
1	15 ft	○
2	21 ft	□
3	37 ft	△

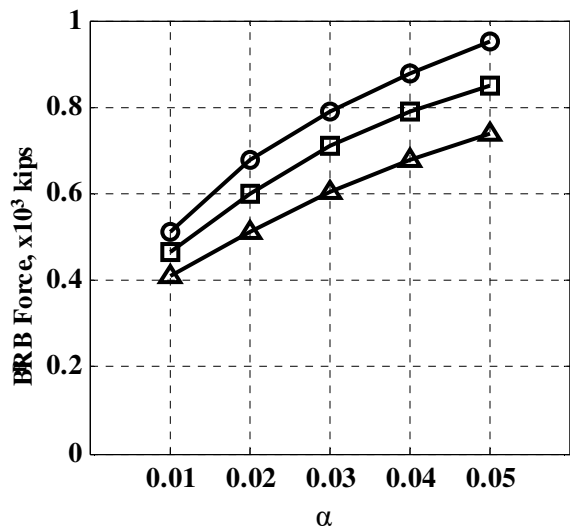
(a) Main / Tower Location



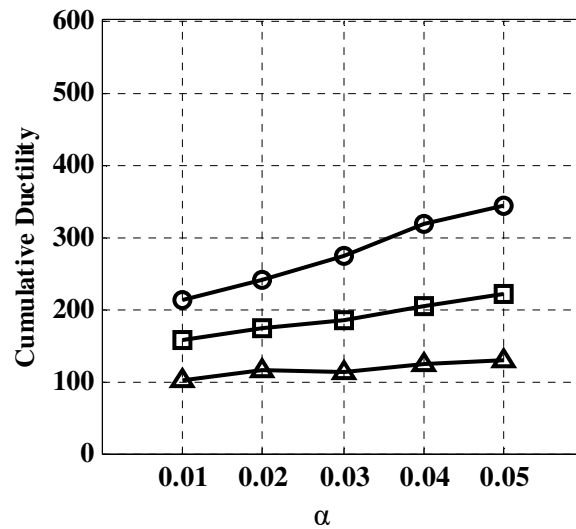
(b) Impact-direction Relative Displacement



(c) Absolute Maximum Strain

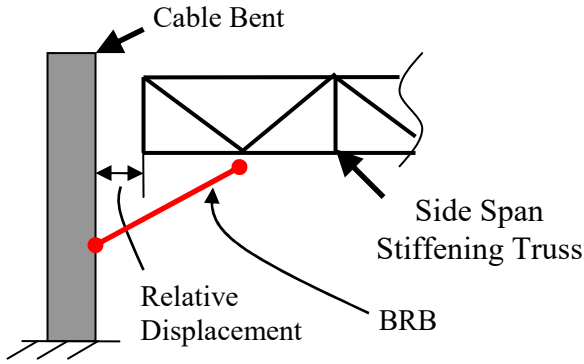


(d) BRB Axial Force



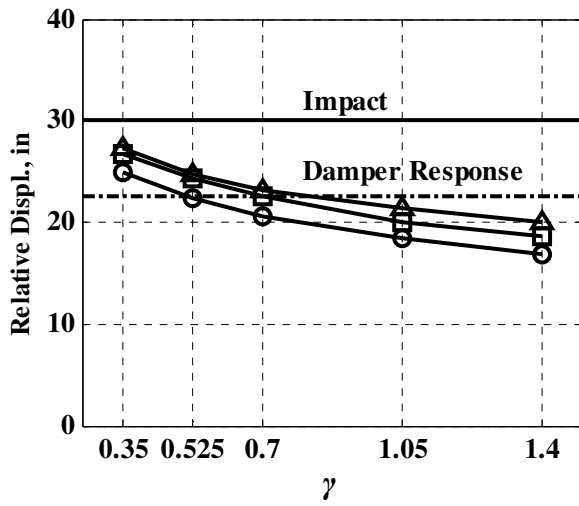
(e) Cumulative Ductility

Figure 4.3 Effect of BRB Post-Yield Stiffness, α , on VTB Response: Main/Tower

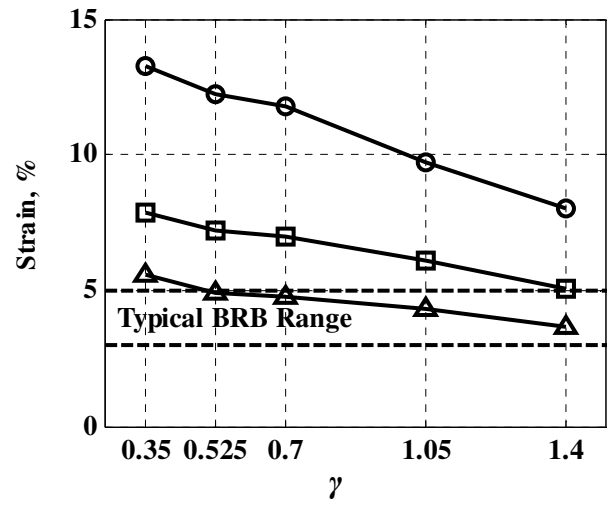


Scheme	BRB Length	Marker
1	14 ft	○
2	29 ft	□
3	44 ft	△

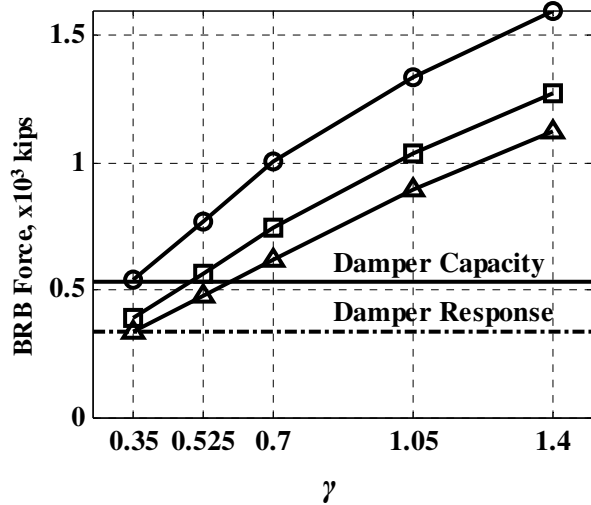
(a) Side / Cable Bent Location



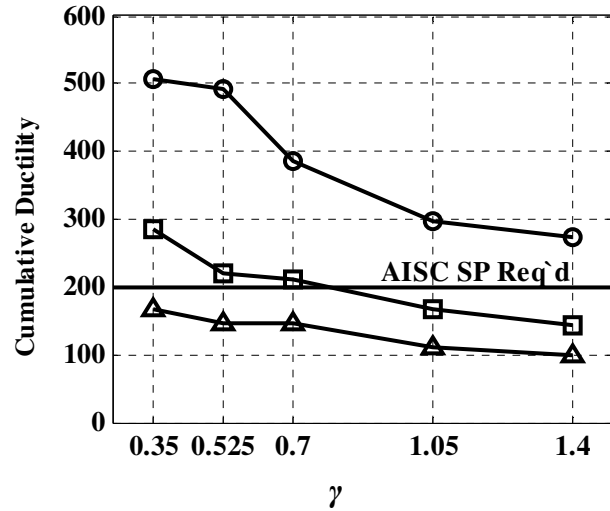
(b) Impact-direction Relative Displacement



(c) Absolute Maximum Strain

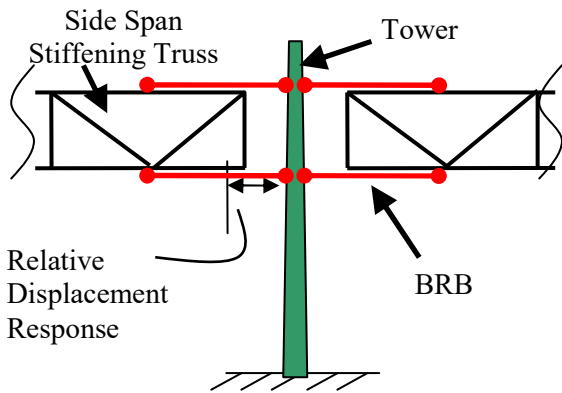


(d) Maximum Axial Force



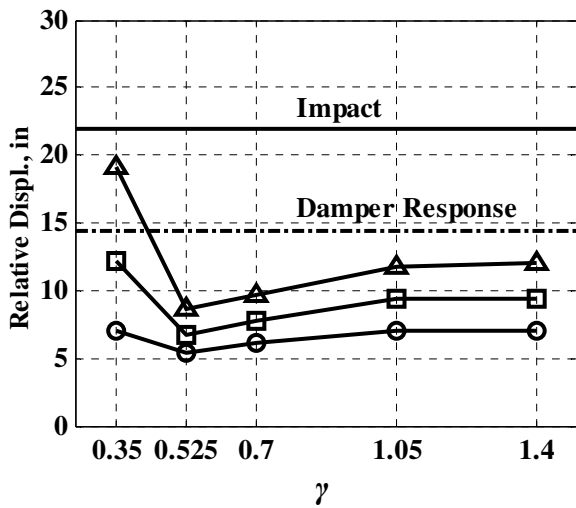
(e) Cumulative Ductility

Figure 4.4 Effect of BRB Yield Strength, γ , on VTB Response: Side/Cable Bent

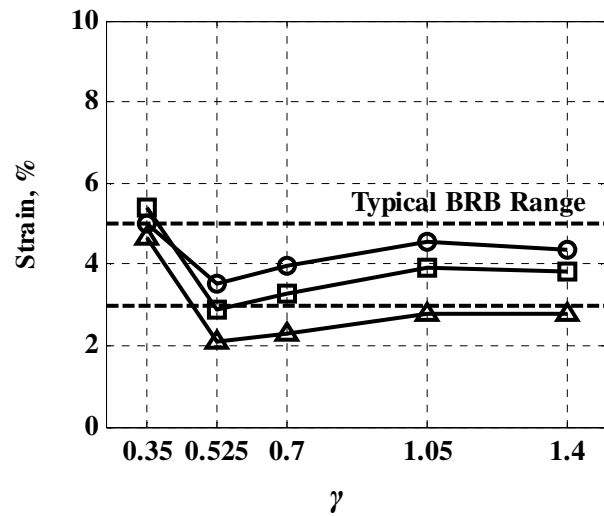


Scheme	BRB Length	Marker
1	13 ft	
2	20 ft	
3	35 ft	

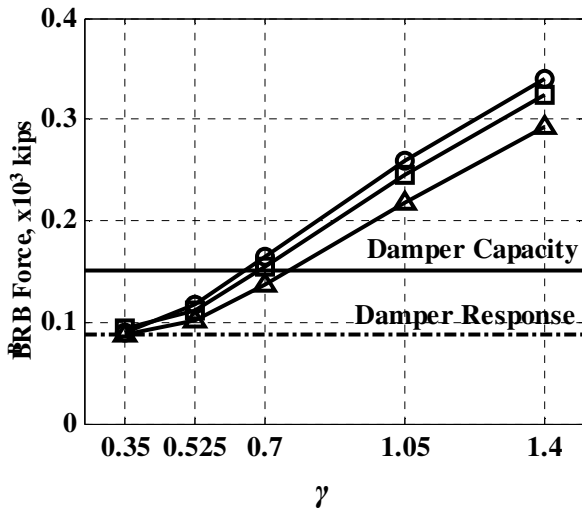
(a) Side / Tower Location



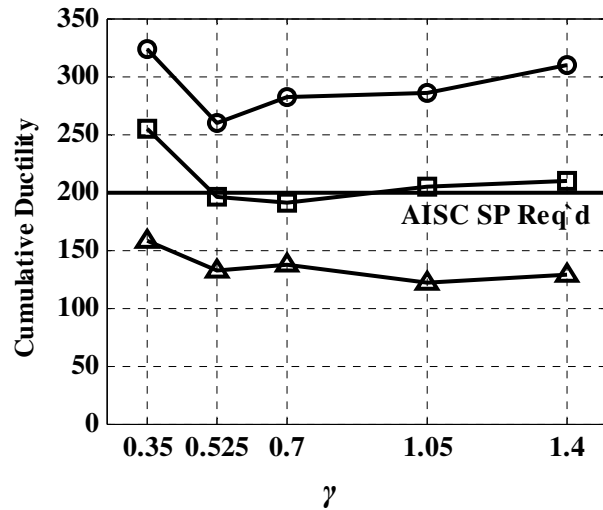
(b) Impact-direction Relative Displacement



(c) Absolute Maximum Strain

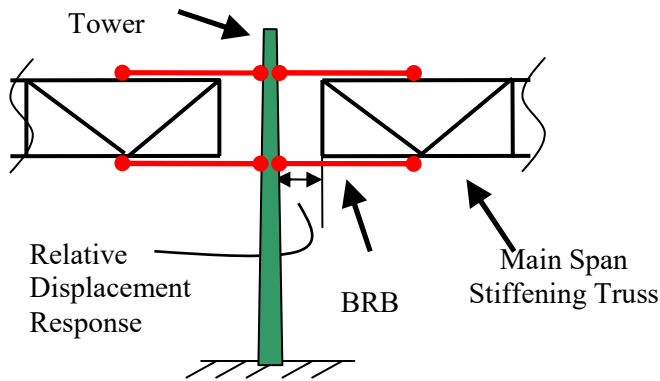


(d) Maximum Axial Force



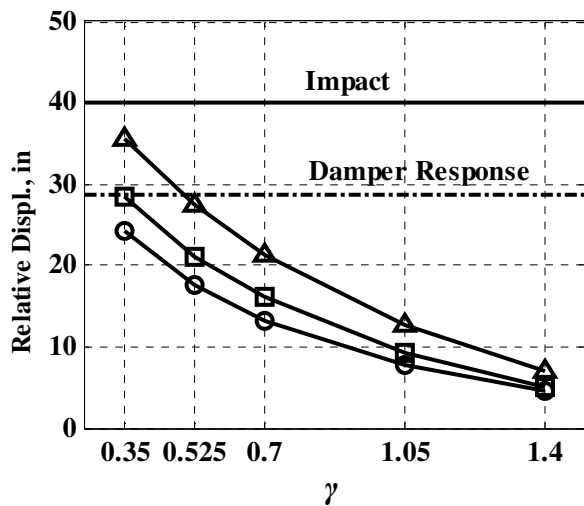
(e) Cumulative Ductility

Figure 4.5 Effect of BRB Yield Strength, γ , on VTB Response: Side/Tower

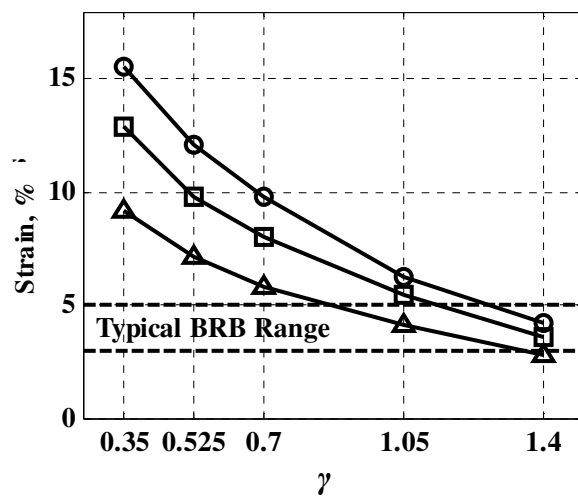


Scheme	BRB Length	Marker
1	15 ft	
2	21 ft	
3	37 ft	

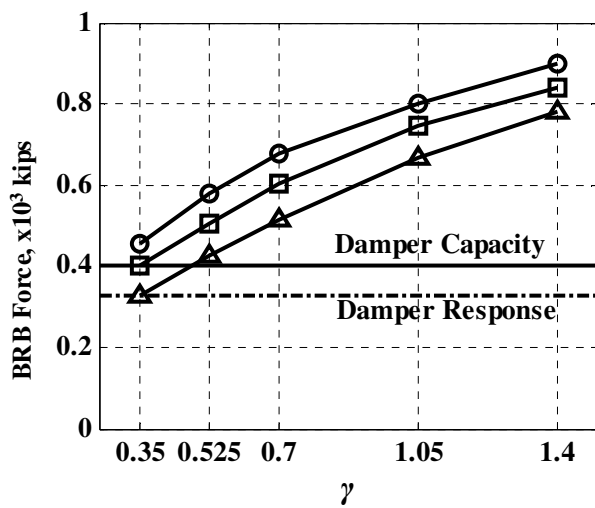
(a) Main / Tower Location



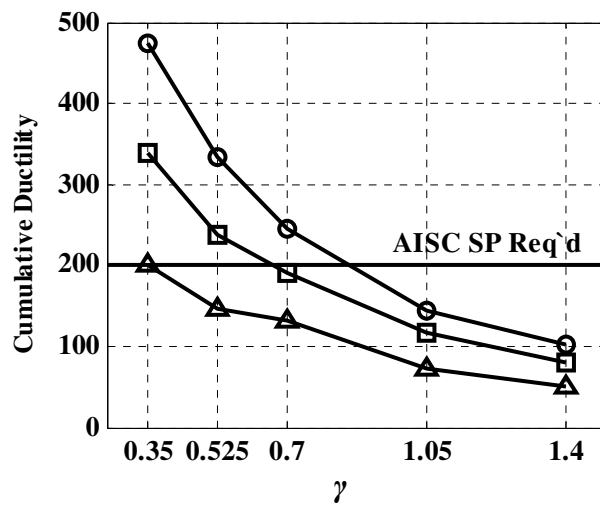
(b) Impact-direction Relative Displacement



(c) Absolute Maximum Strain

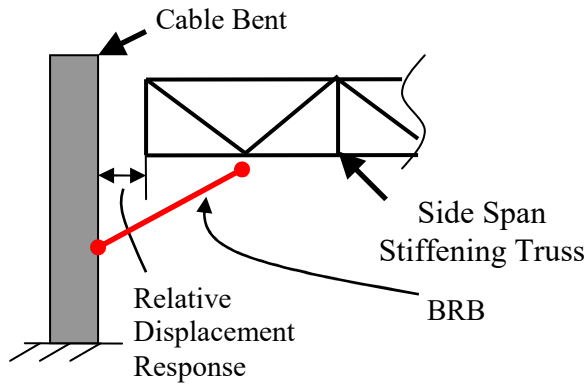


(d) Maximum Axial Force



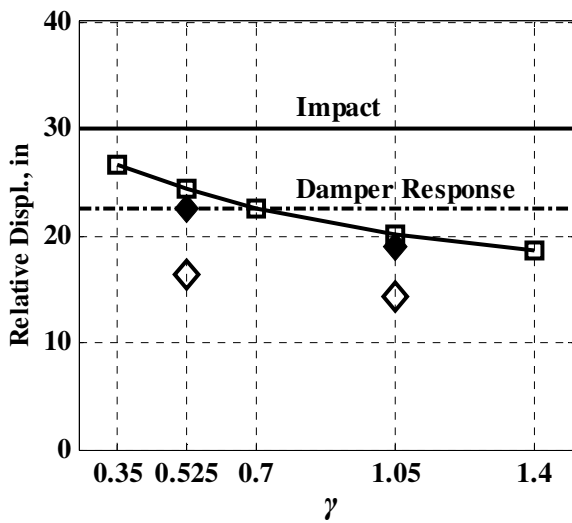
(e) Cumulative Ductility

Figure 4.6 Effect of BRB Yield Strength, γ , on VTB Response: Main/Tower

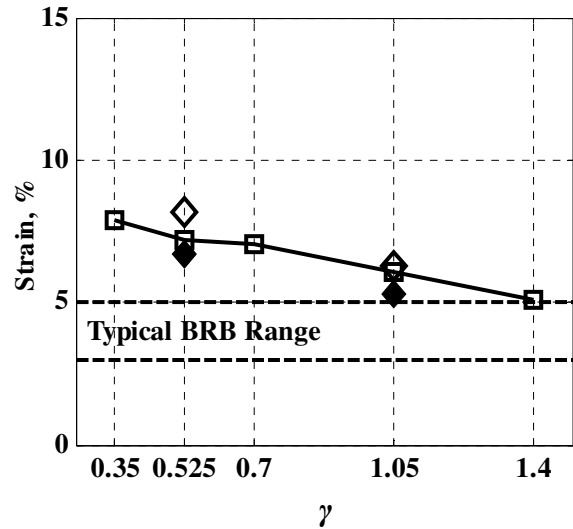


Model	Input Excitation	Marker
Perform-3D	Longitudinal	—□—
ADINA	Longitudinal	◆
ADINA	All Directions	◇

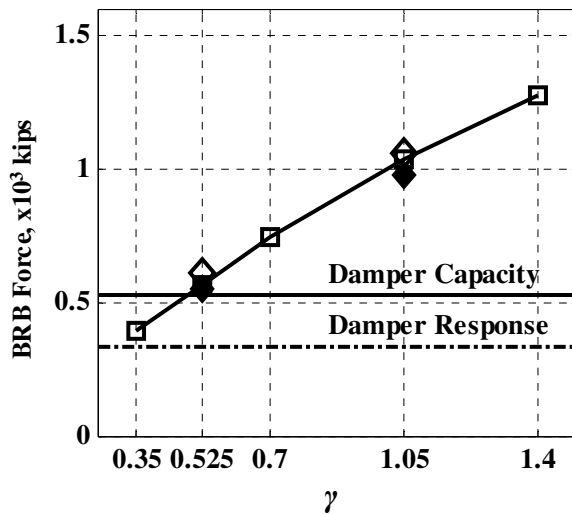
(a) Side / Cable Bent Location



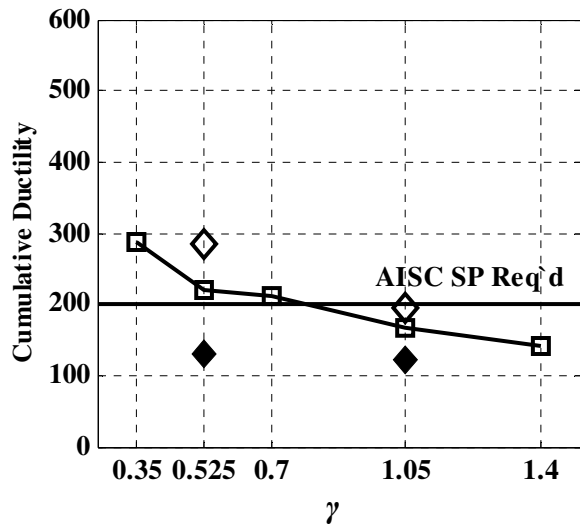
(b) Impact-direction Relative Displacement



(c) Absolute Maximum Strain

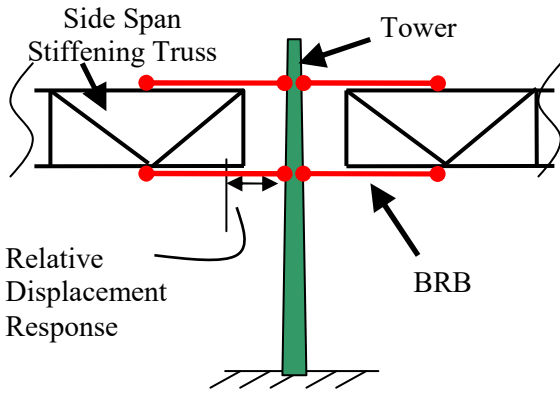


(d) Maximum Axial Force



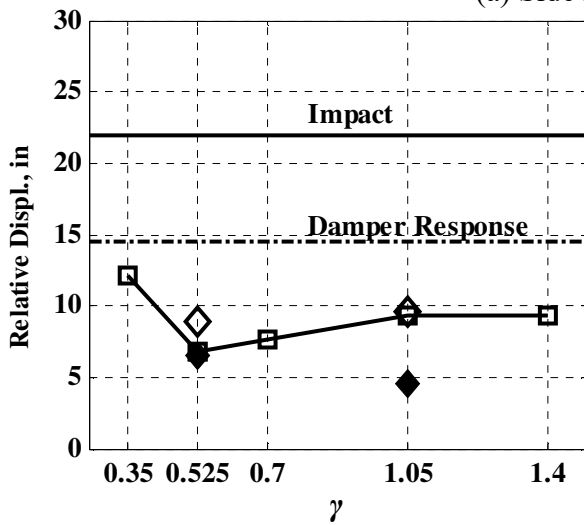
(e) Cumulative Ductility

Figure 4.7 Comparison of Perform-3D and ADINA Responses: Side/Cable Bent

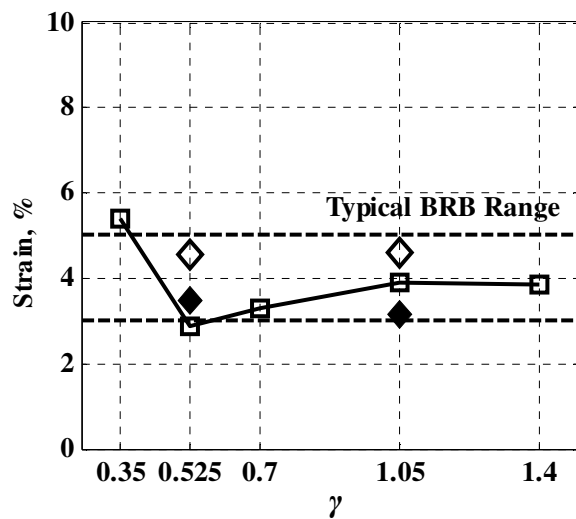


Model	Input Excitation	Marker
Perform-3D	Longitudinal	—□—
ADINA	Longitudinal	◆
ADINA	All Directions	◇

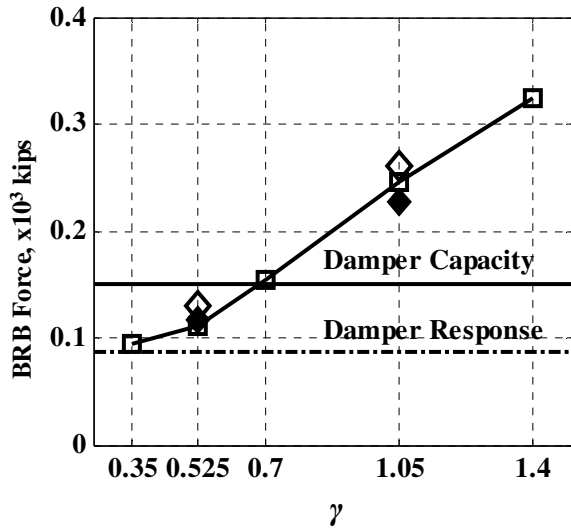
(a) Side / Tower Location



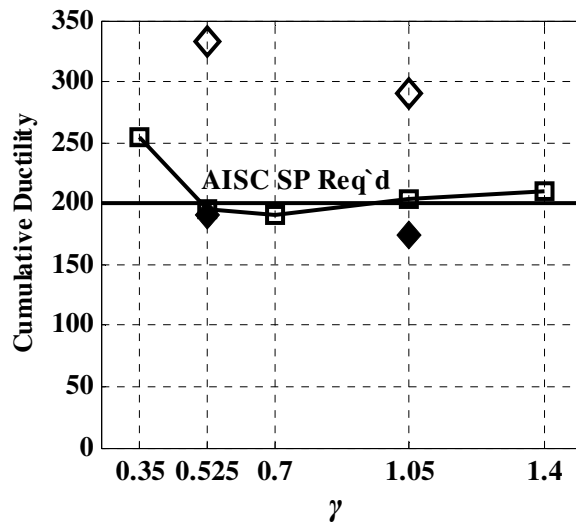
(b) Impact-direction Relative Displacement



(c) Absolute Maximum Strain

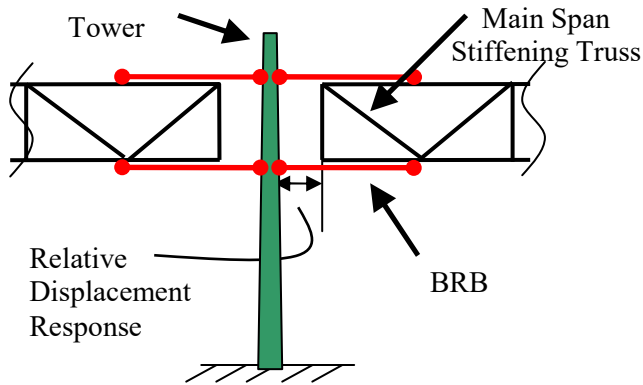


(d) Maximum Axial Force



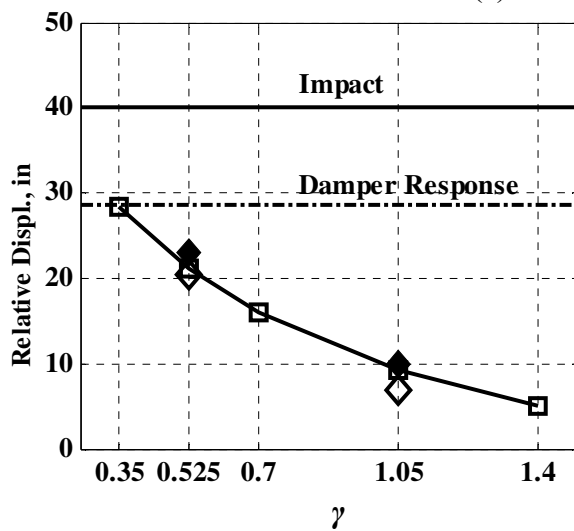
(e) Cumulative Ductility

Figure 4.8 Comparison of Perform-3D and ADINA Responses: Side/Tower

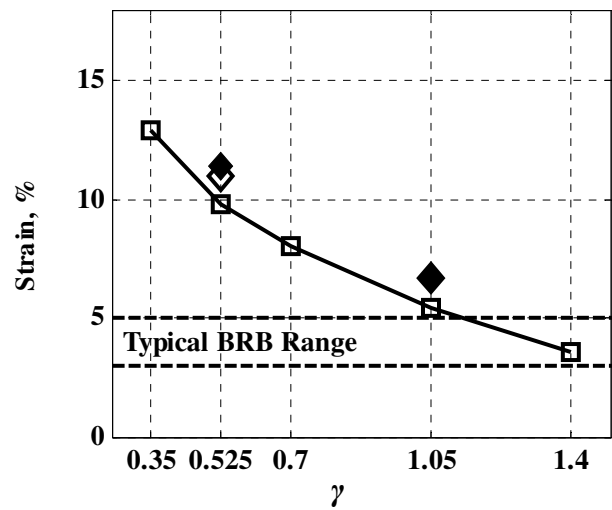


Model	Input Excitation	Marker
Perform-3D	Longitudinal	—□—
ADINA	Longitudinal	◆
ADINA	All Directions	◇

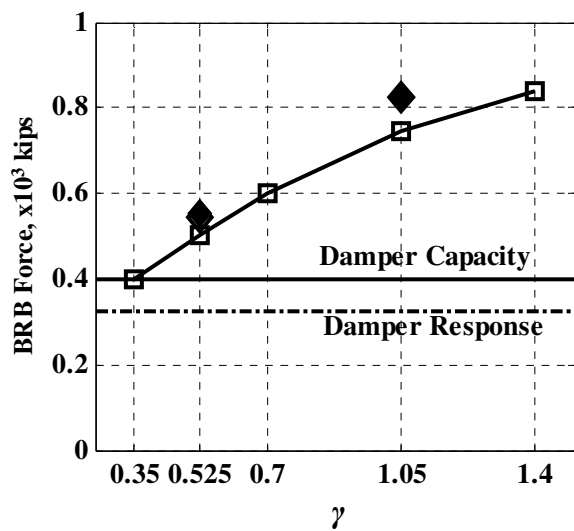
(a) Main / Tower Location



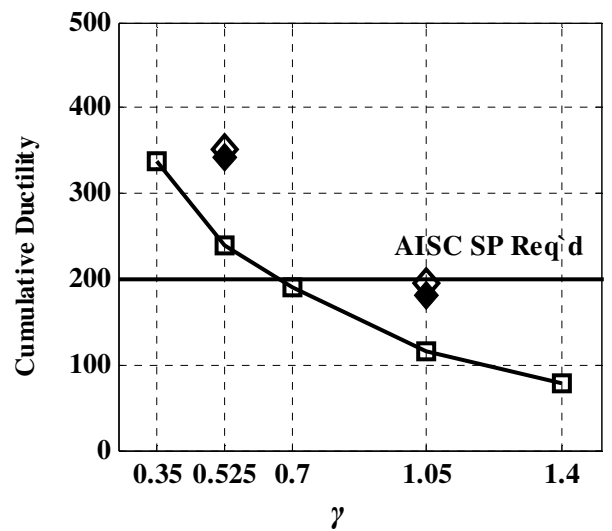
(b) Impact-direction Relative Displacement



(c) Absolute Maximum Strain



(d) Maximum Axial Force



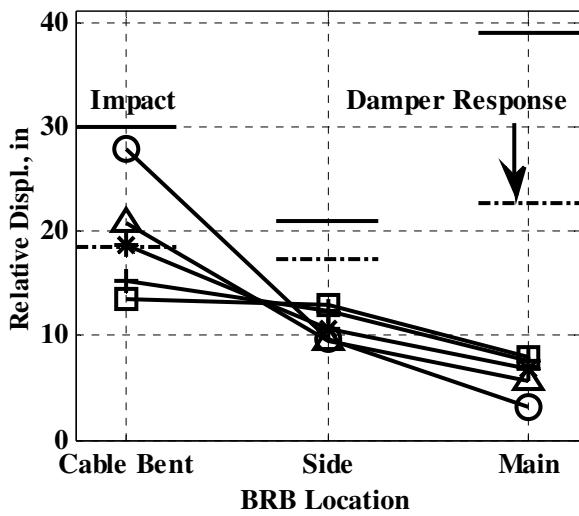
(e) Cumulative Ductility

Figure 4.9 Comparison of Perform-3D and ADINA Responses: Main/Tower

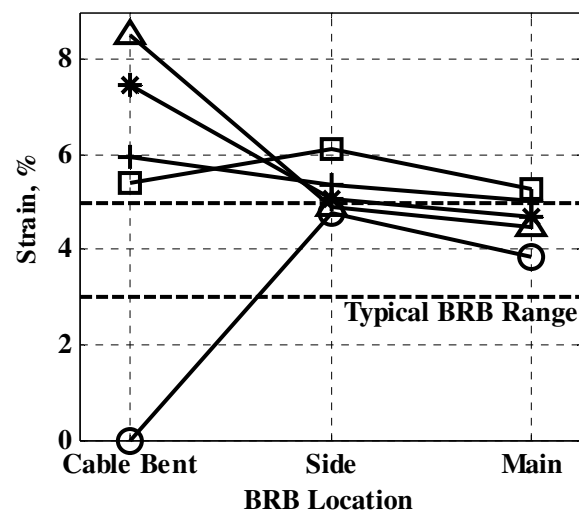
Location	γ				
	0	0.525	0.70	1.05	1.25
S-C	0	0.525	0.70	1.05	1.25
S-T	1.05				
M-T	1.05				

γ_{s-c}	Marker
0	○
0.525	△
0.7	*
1.05	+
1.25	□

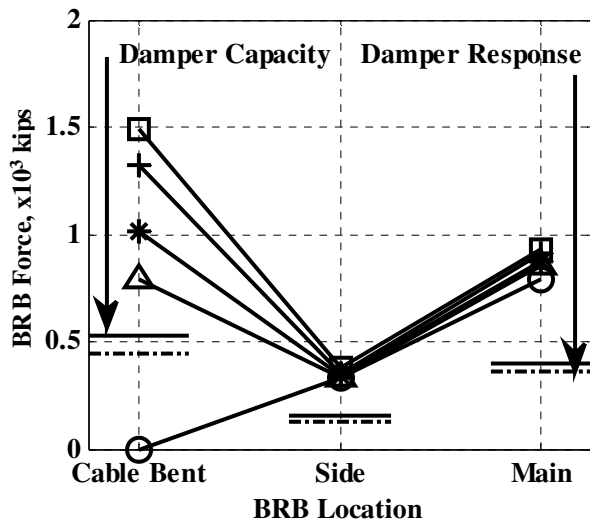
(a) Parameter Information



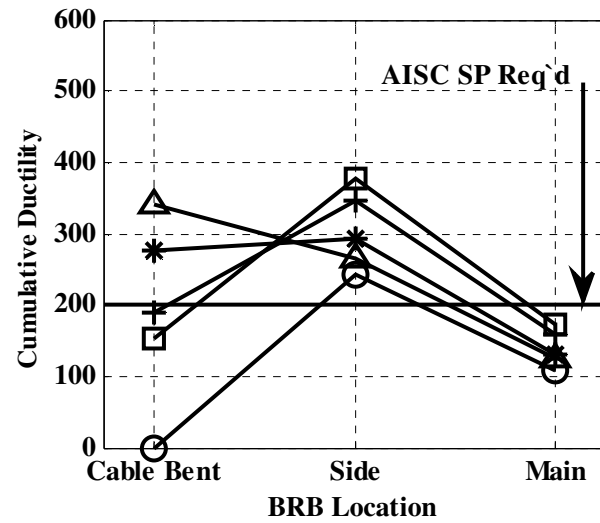
(b) Impact-direction Relative Displacement



(c) Absolute Maximum Strain



(d) Maximum Axial Force



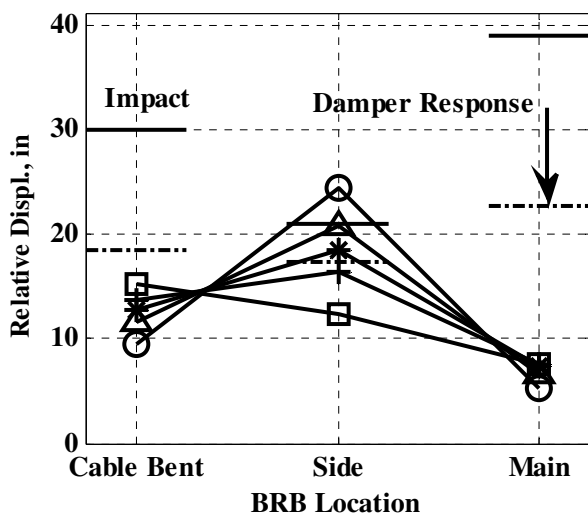
(e) Cumulative Ductility

Figure 4.10 Effect of Local BRB Yield Strength, γ , on VTB Response: Side/CableBent

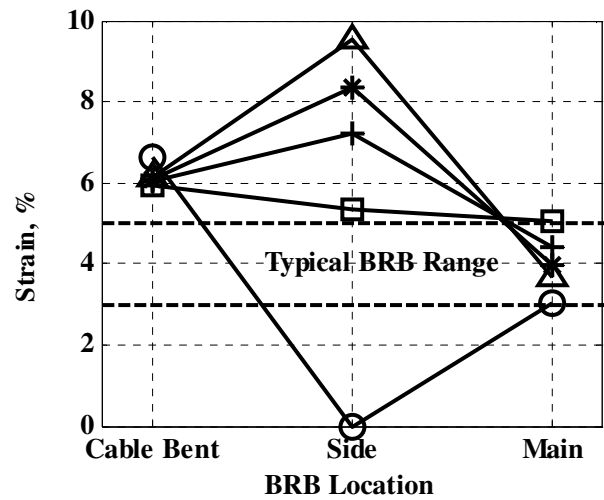
Location	γ				
S-C	1.05				
S-T	0	0.35	0.525	0.70	1.05
S-C	1.05				

γ_{S-T}	Marker
0	○
0.35	△
0.525	*
0.7	+
1.05	□

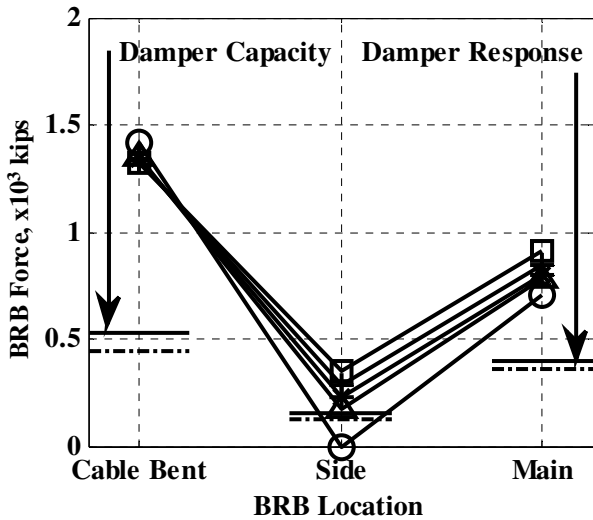
(a) Parameter Information



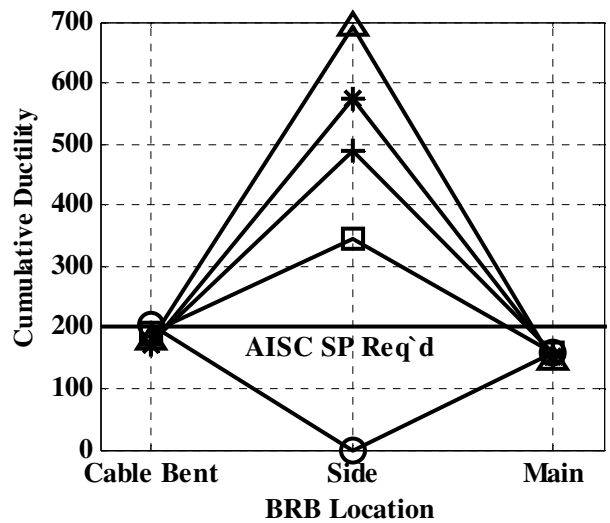
(b) Impact-direction Relative Displacement



(c) Absolute Maximum Strain



(d) Maximum Axial Force



(e) Cumulative Ductility

Figure 4.11 Effect of Local BRB Yield Strength, γ , on VTB Response: Side/Tower

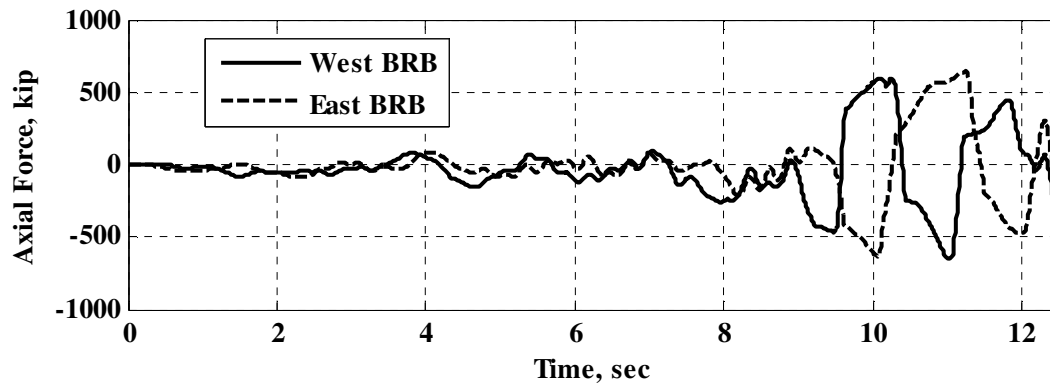
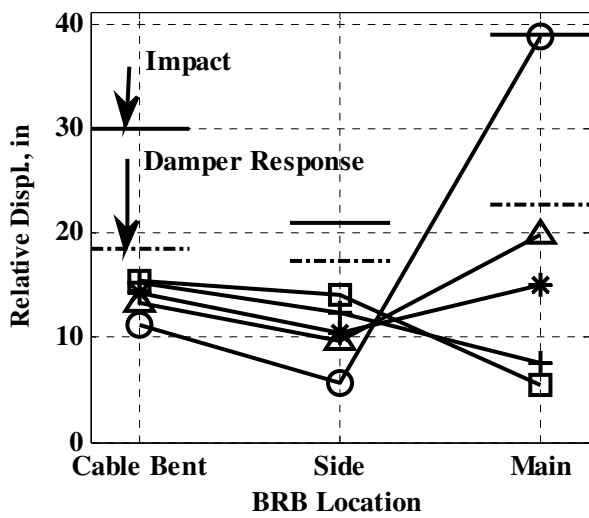


Figure 4.12 Example of Main Span BRB East and West Out of Phase

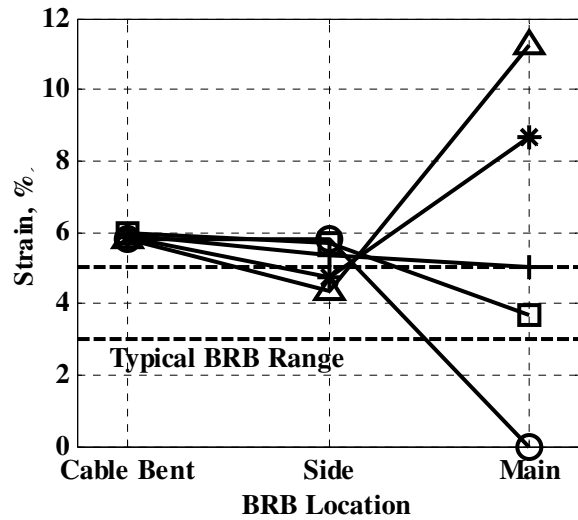
Location	γ				
S-C	1.05				
S-T	1.05				
M-T	0	0.525	0.70	1.05	1.25

γ_{M-T}	Marker
0	○
0.525	△
0.7	*
1.05	+
1.25	□

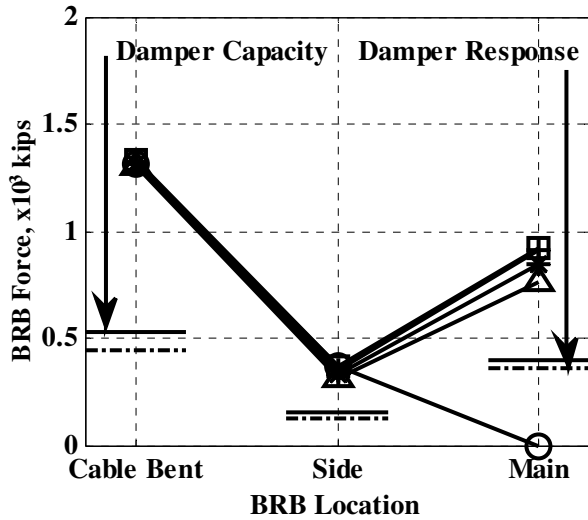
(a) Parameter Information



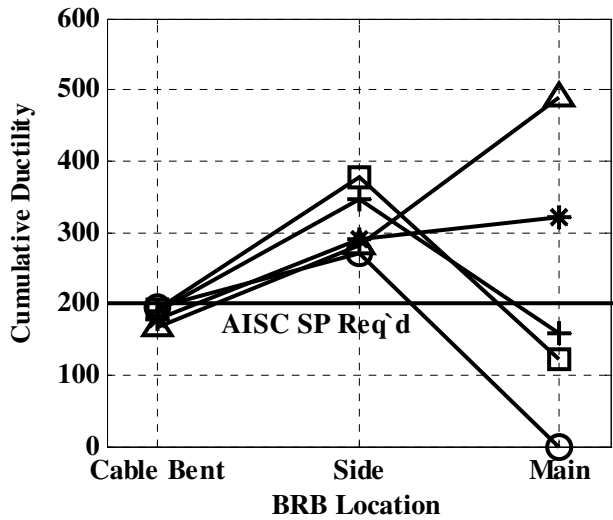
(b) Impact-direction Relative Displacement



(c) Absolute Maximum Strain



(d) Maximum Axial Force



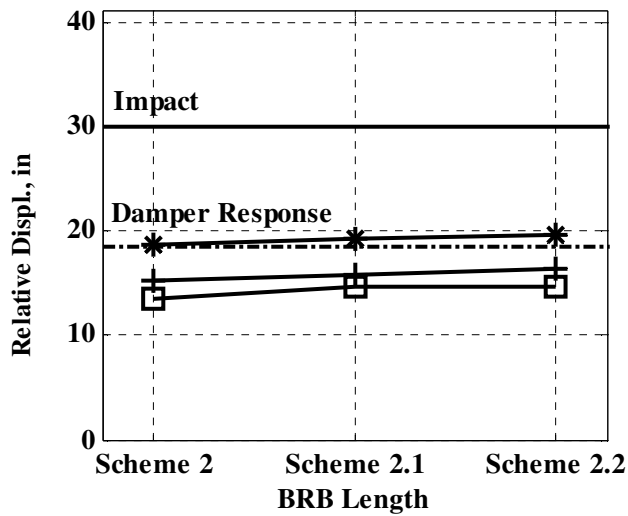
(e) Cumulative Ductility

Figure 4.13 Effect of Local BRB Yield Strength, γ , on VTB Response: Main/Tower

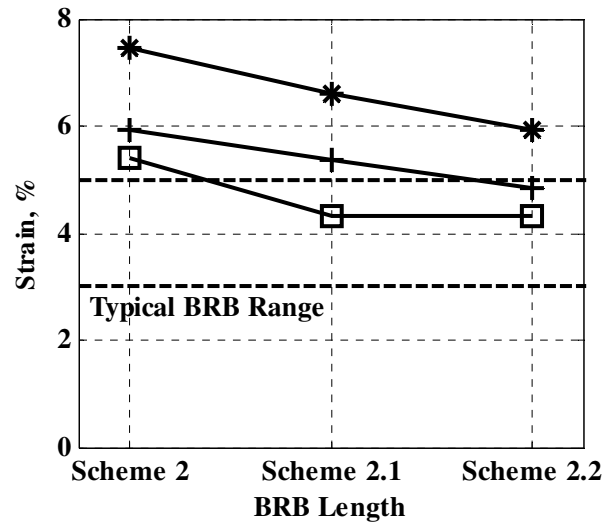
Location	Parameters			
	S-C	γ	0.70	1.05
L		Sch2 = 29 ft	Sch2.1 = 34 ft	Sch2.2 = 39 ft
S-T	$\gamma = 1.05$ $L = \text{Scheme 2}$			
M-T	$\gamma = 1.05$ $L = \text{Scheme 2}$			

γ_{s-c}	Marker
0.70	—*
1.05	—+
1.25	—□

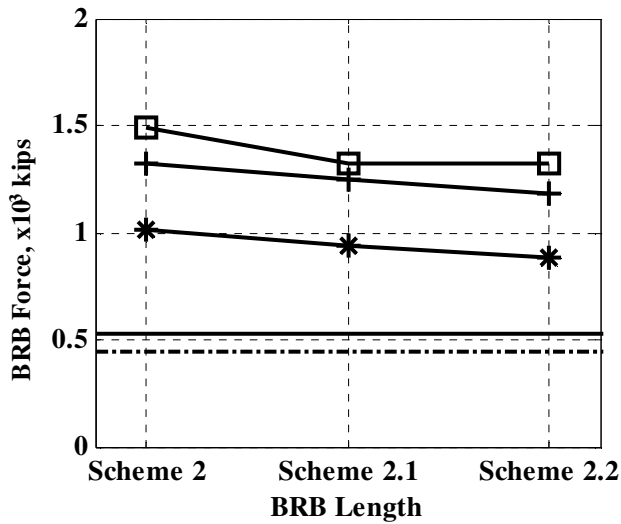
(a) Parameter Information



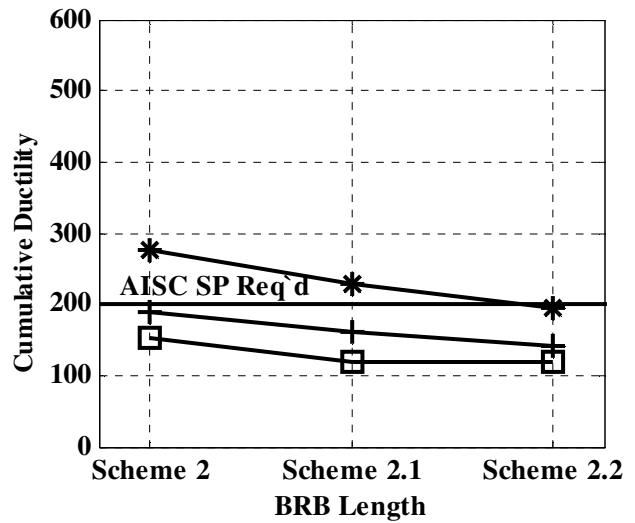
(b) Impact-direction Relative Displacement



(c) Absolute Maximum Strain



(d) Maximum Axial Force



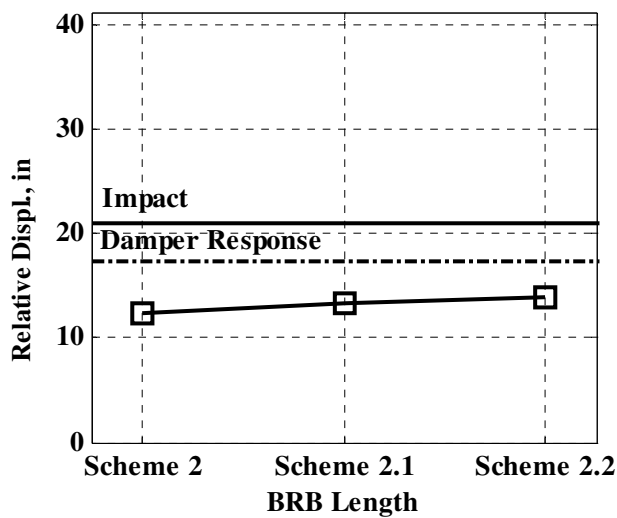
(e) Cumulative Ductility

Figure 4.14 Local Parameter Refinement: Side/Cable Bent

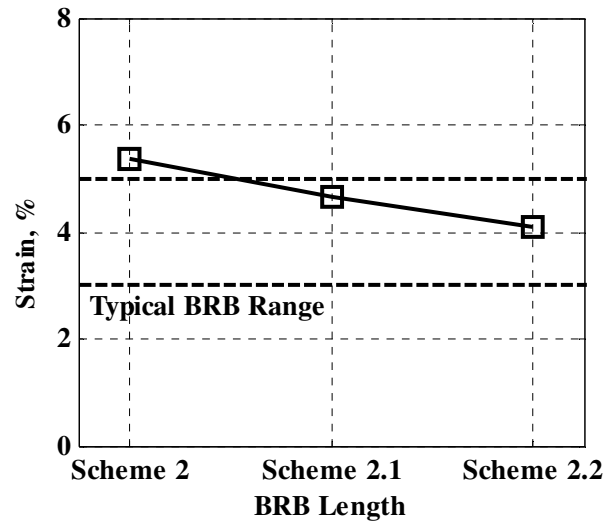
Location	Parameters			
S-C	$\gamma = 1.05$ $L = \text{Scheme 2}$			
S-T	γ	1.05		
	L	Sch2 = 21 ft	Sch2.1 = 25 ft	Sch2.2 = 30 ft
S-C	$\gamma = 1.05$ $L = \text{Scheme 2}$			

γ_{S-T}	Marker
1.05	

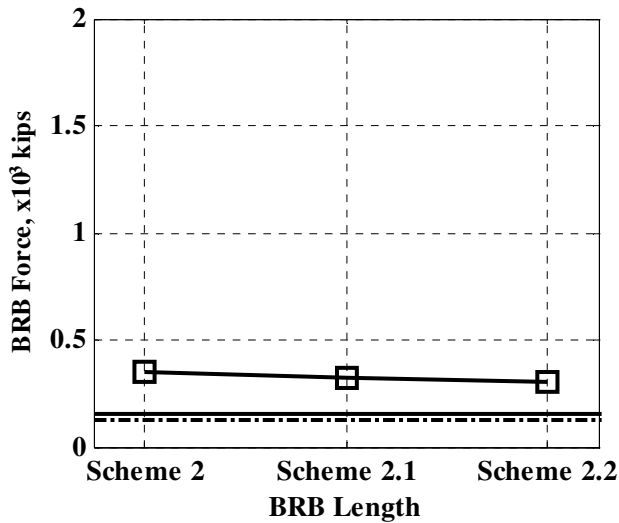
(a) Parameter Information



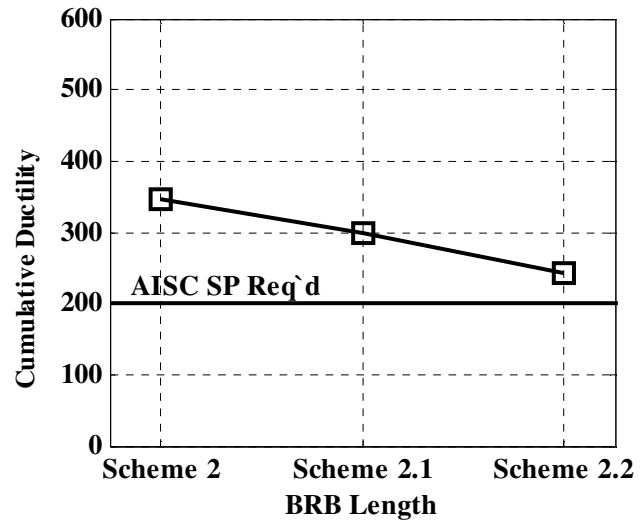
(b) Impact-direction Relative Displacement



(c) Absolute Maximum Strain



(d) Maximum Axial Force



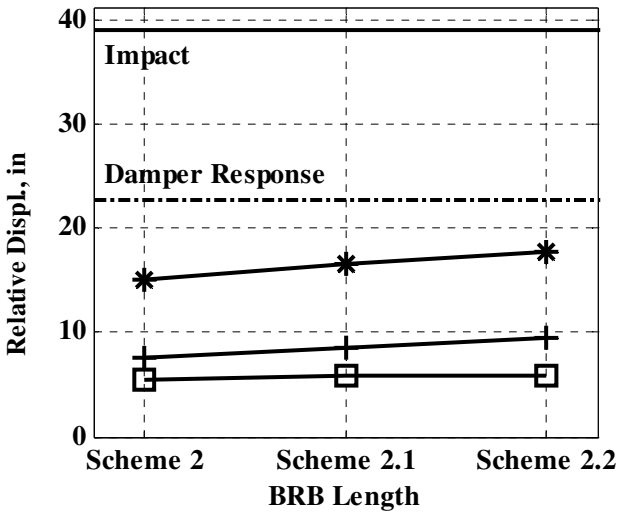
(e) Cumulative Ductility

Figure 4.15 Localized Parameter Refinement: Side/Tower

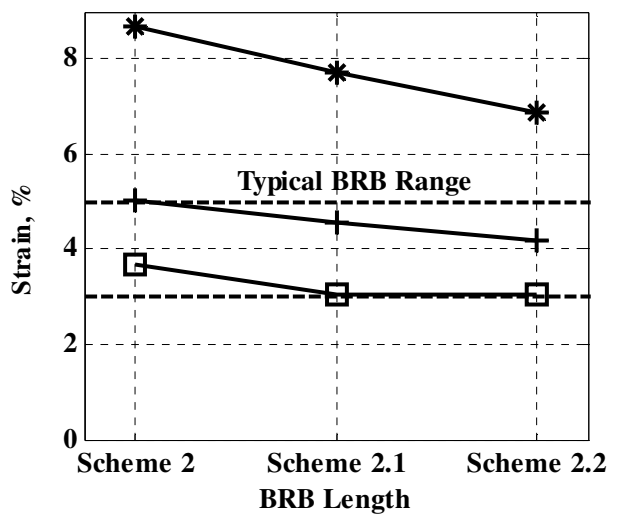
Location	Parameters			
S-C	$\gamma = 1.05$ $L = \text{Scheme 2}$			
S-T	$\gamma = 1.05$ $L = \text{Scheme 2}$			
M-T	γ	0.70	1.05	1.25
	L	Sch2 = 21 ft	Sch2.1 = 25 ft	Sch2.2 = 30 ft

γ_{M-T}	Marker
0.7	—*—
1.05	—+—
1.25	—□—

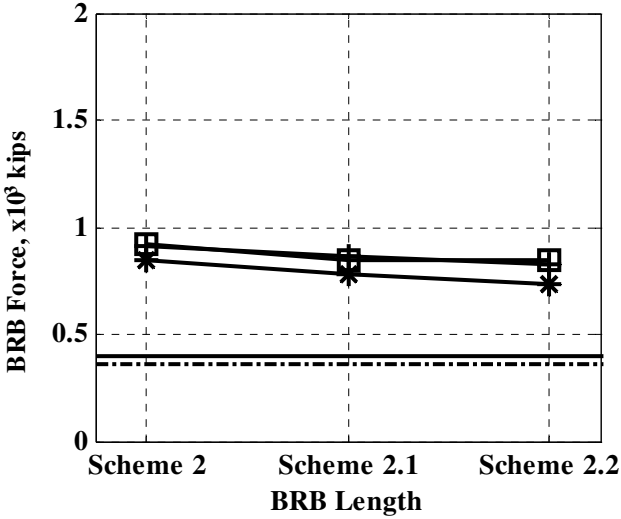
(a) Parameter Information



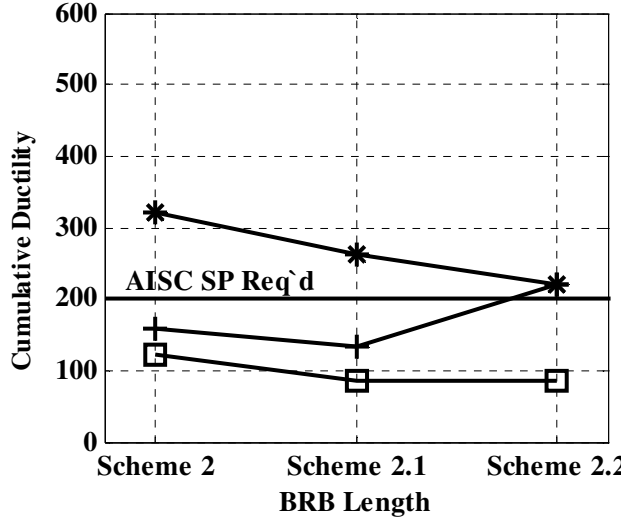
(b) Impact-direction Relative Displacement



(c) Absolute Maximum Strain

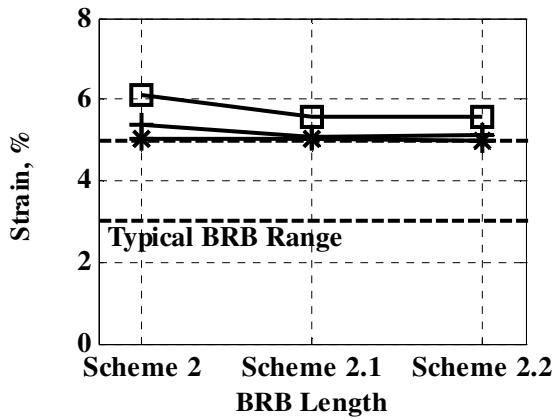


(d) Maximum Axial Force

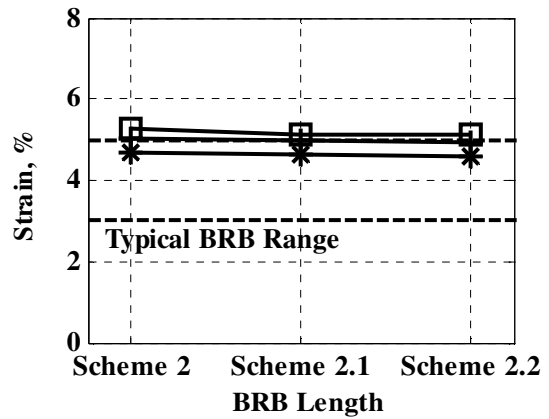


(e) Cumulative Ductility

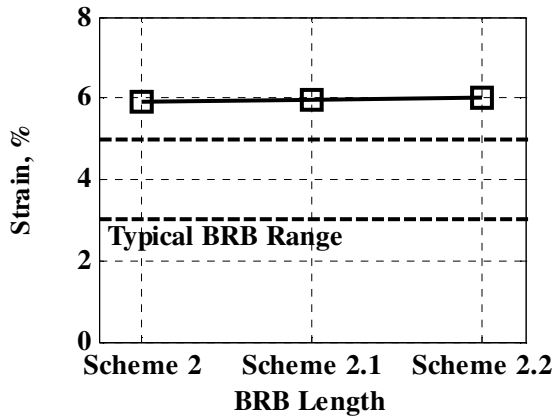
Figure 4.16 Localized Parameter Refinement: Main/Tower



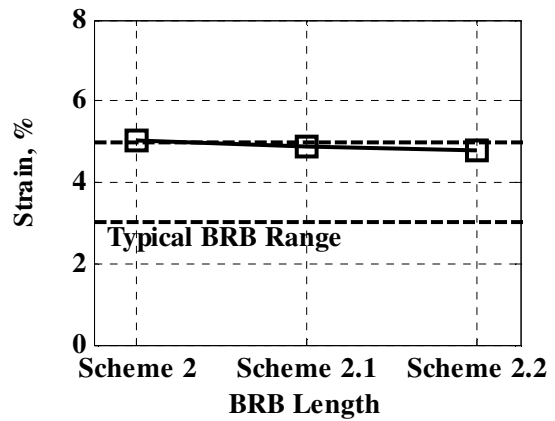
(a) Step 3.1 Side/Tower Max Strain



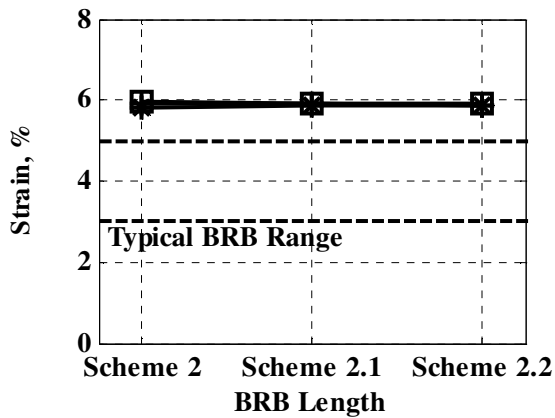
(b) Step 3.1, Main/Tower Max Strain



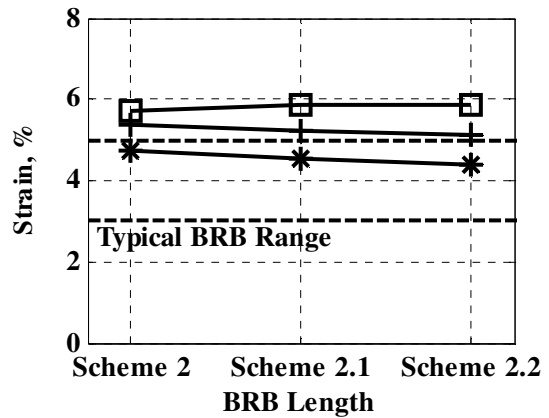
(c) Step 3.2, Cable Bent Max Strain.



(d) Step 3.2, Main/Tower Max Strain



(e) Step 3.3, Cable Bent Max Strain



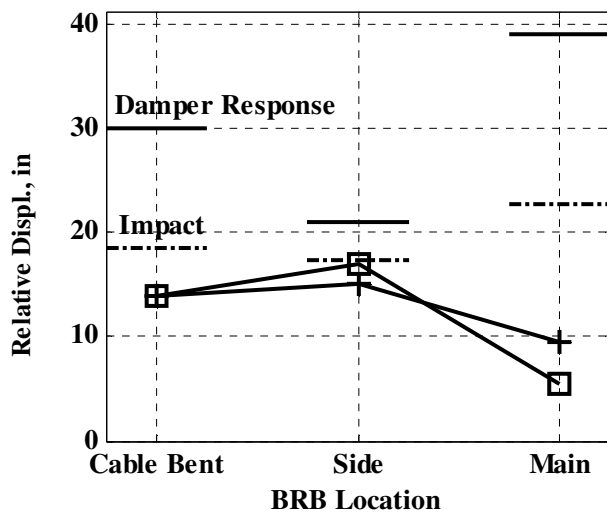
(f) Step 3.3, Side/Tower Max Strain

Figure 4.17 Local Parameter Refinement: Adjacent Location Insensitivities
(For legend see Figure 4.14, 4.15, and 4.16, respectively)

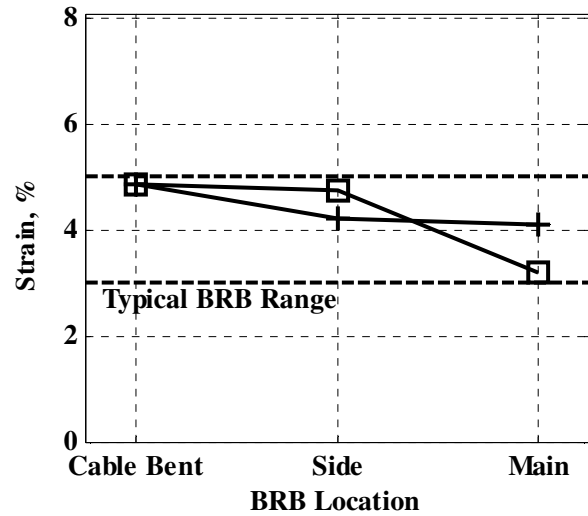
Location	Parameters		
S-C	$\gamma = 1.25$ $L = \text{Scheme 2.1}$		
S-T	$\gamma = 1.05$ $L = \text{Scheme 2.2}$		
M-T	γ	1.05	1.25
	L	Scheme 2.1	Scheme 2.2

γ_{M-T}	Marker
1.05	+
1.25	□

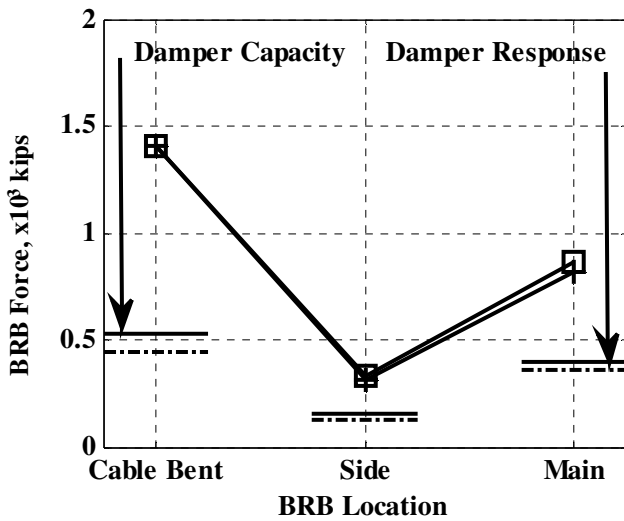
(a) Parameter Information



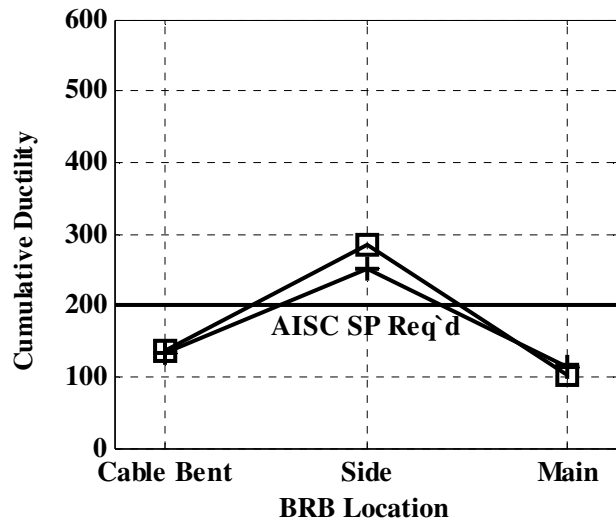
(b) Impact-direction Relative Displacement



(c) Absolute Maximum Strain



(d) Maximum Axial Force



(e) Cumulative Ductility

Figure 4.18 Final Feasible BRB Solutions

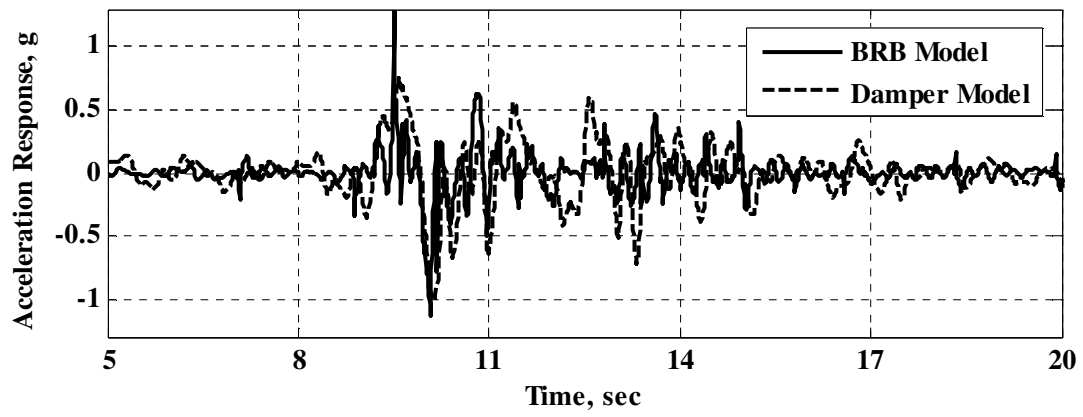
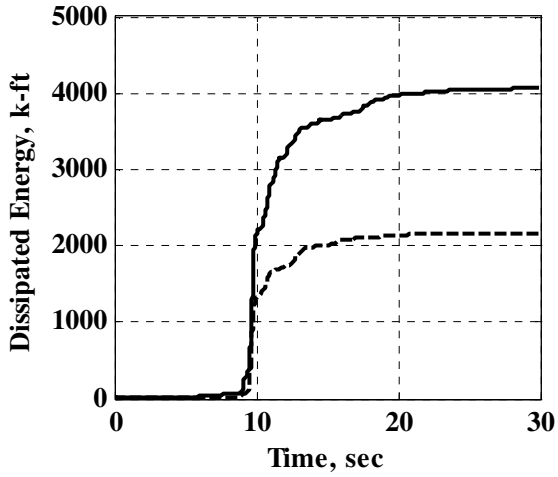
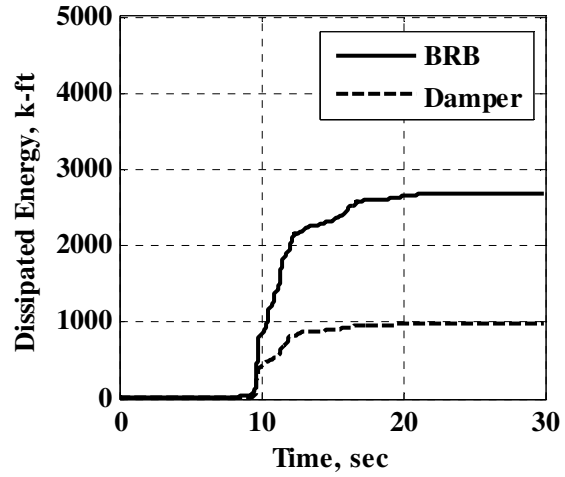


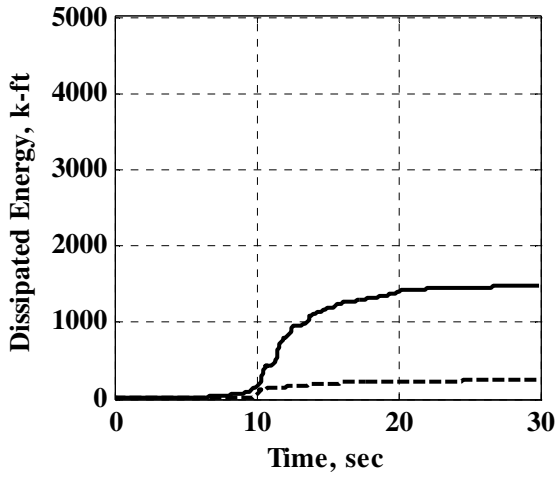
Figure 4.19 Design-Level Earthquake Main Span Acceleration Response



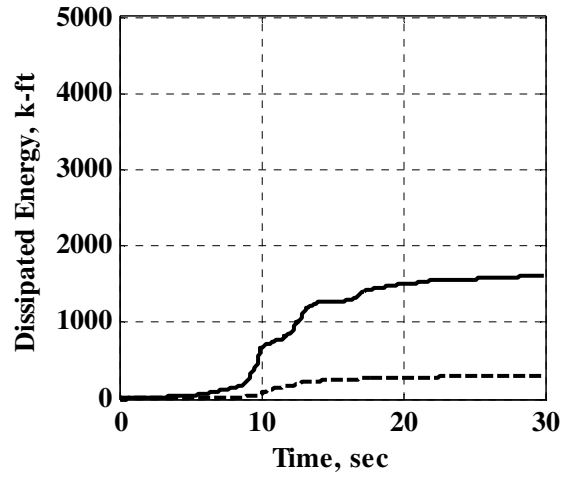
(a) Side to Cable Bent No. 2



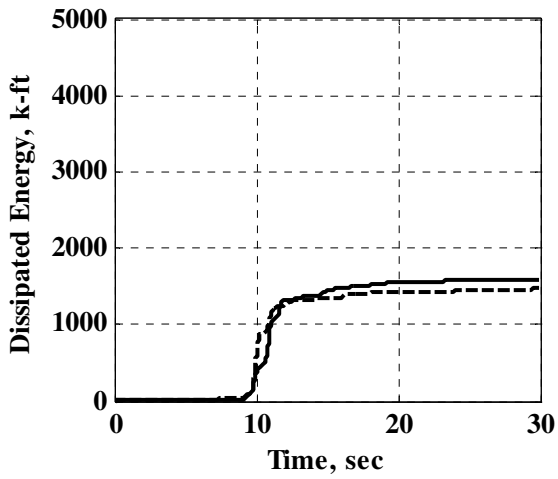
(b) Side to Cable Bent No. 19



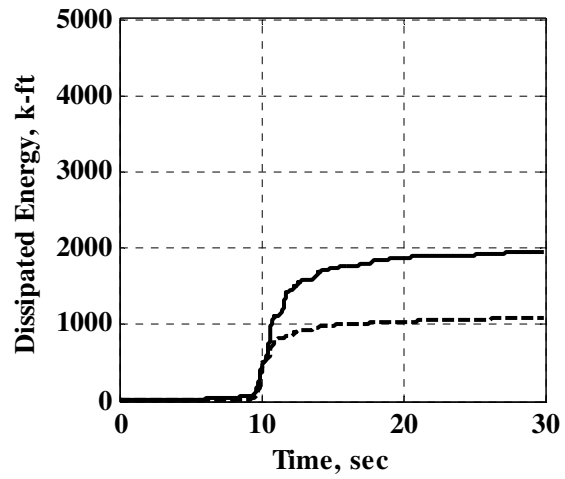
(c) Side to Tower No. 6



(d) Side to Tower No. 16



(e) Main to Tower No. 7



(f) Main to Tower No. 12

Figure 4.20 Example Cumulative Energy Dissipation Time Histories

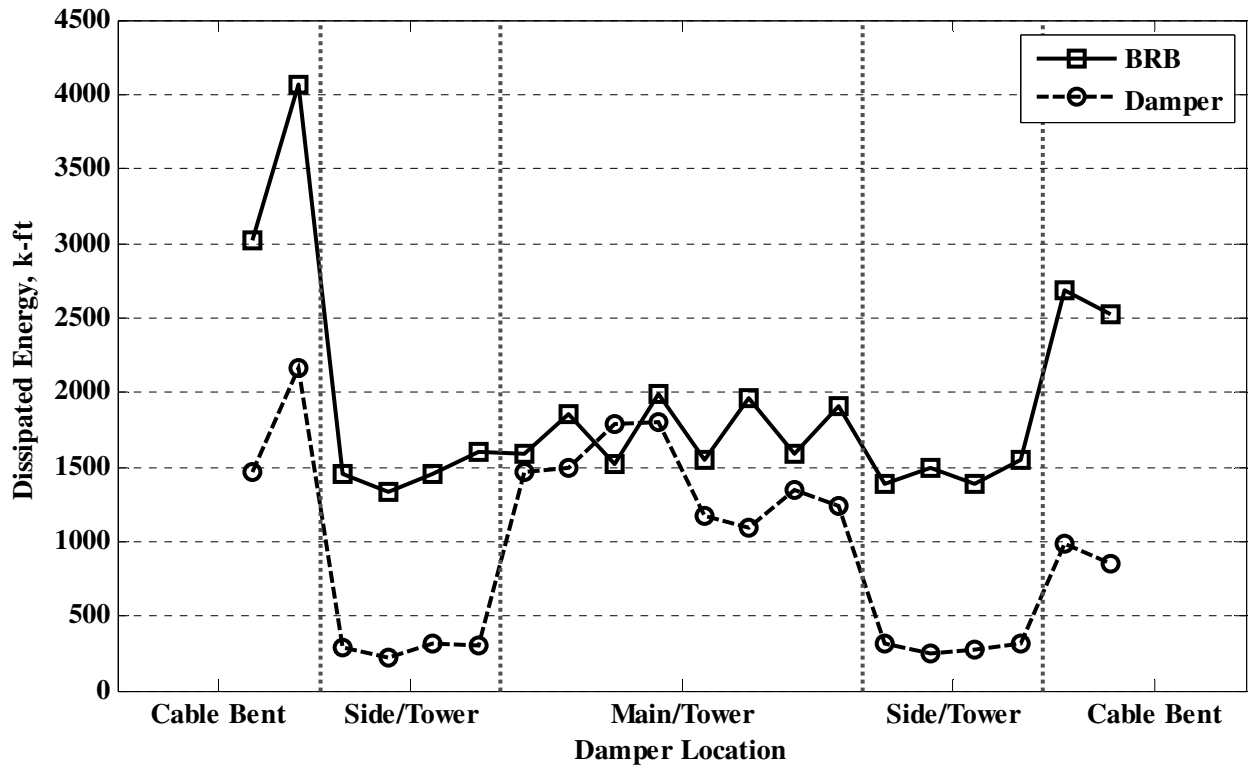
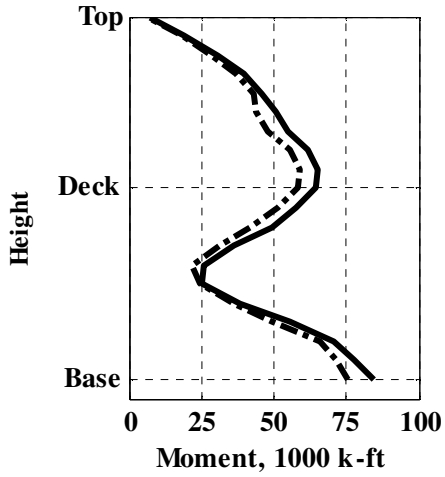
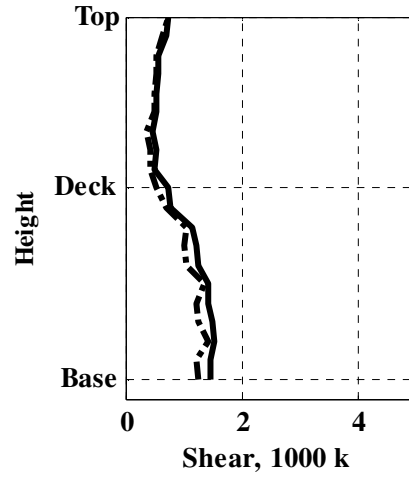


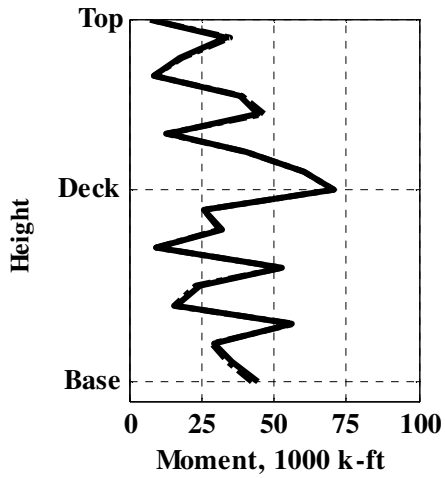
Figure 4.21 BRB and Damper Energy Dissipation Comparison by Location



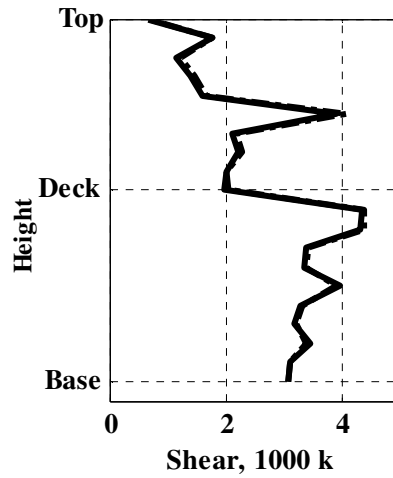
(a) Longitudinal Moment



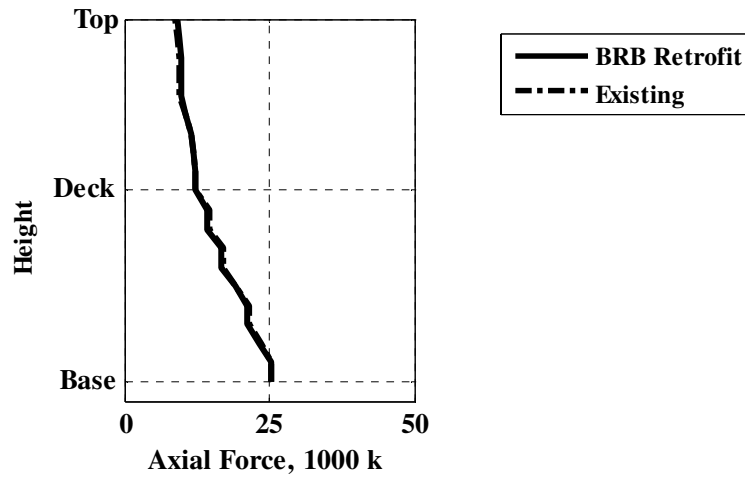
(b) Longitudinal Shear



(c) Transverse Moment

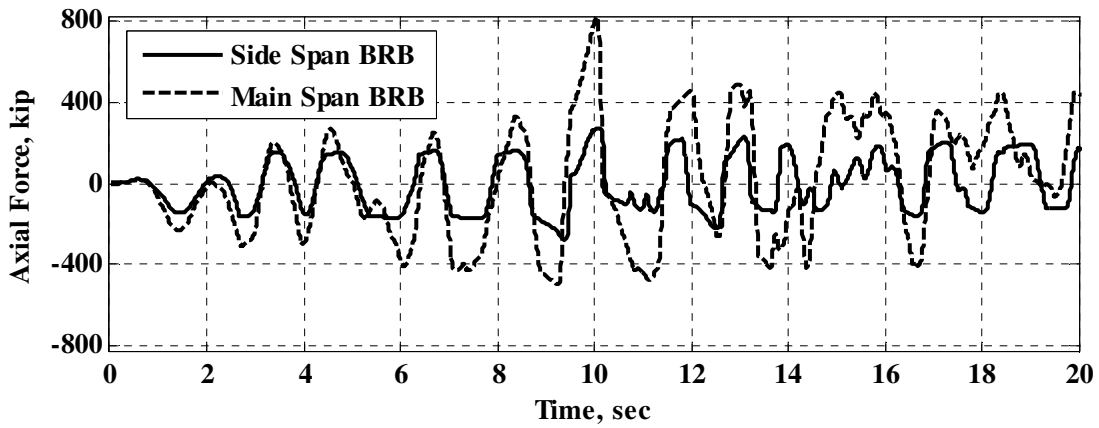


(d) Transverse Shear

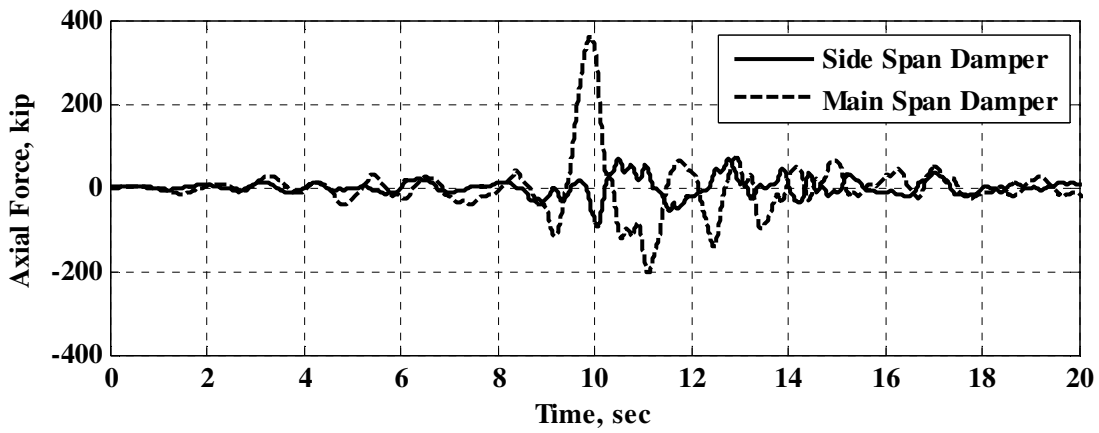


(e) Axial Force

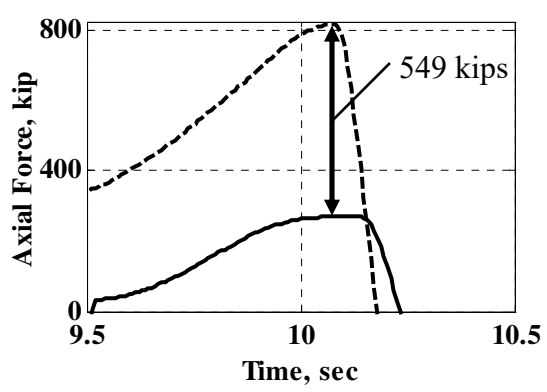
Figure 4.22 Tower Seismic Force Demand Envelopes: Design-Level Earthquake



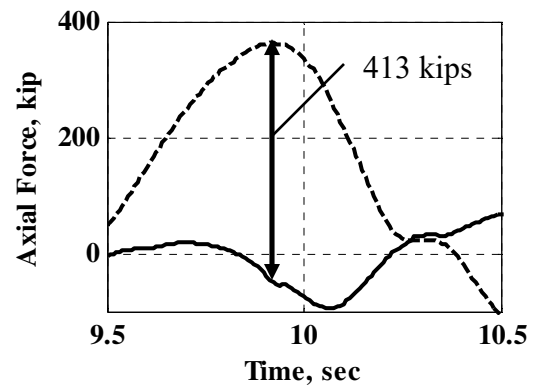
(a) VTB with BRBs



(b) VTB with Viscous Dampers



(c) BRB In-Phase



(d) Damper Out-of-Phase

Figure 4.23 Design-Level Earthquake BRB and Damper Axial Force Phase Relation

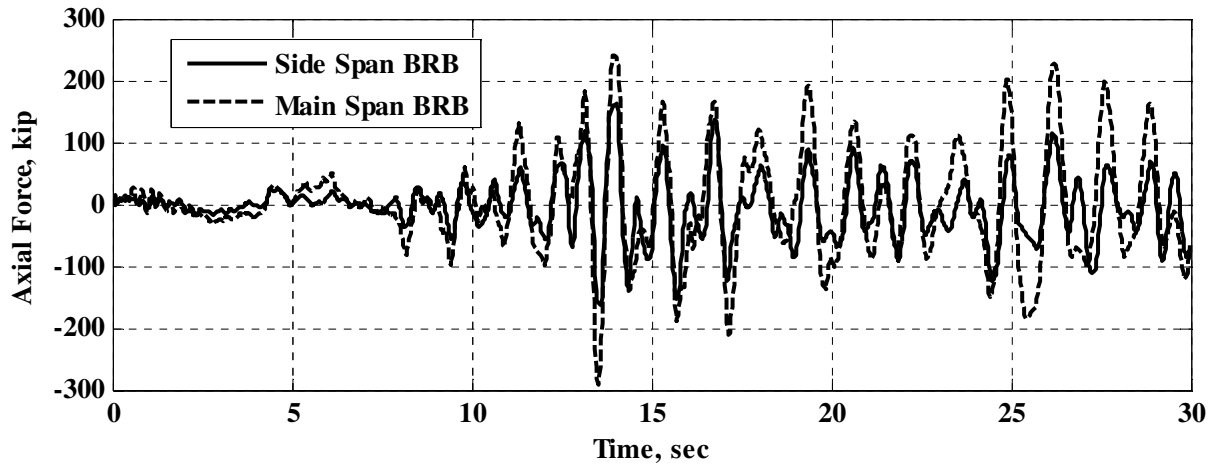
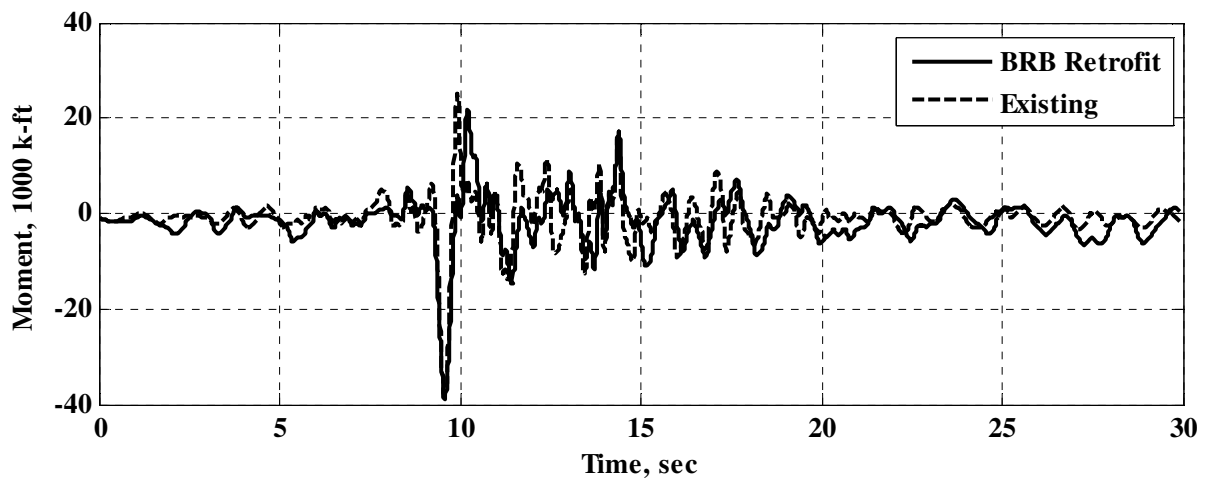
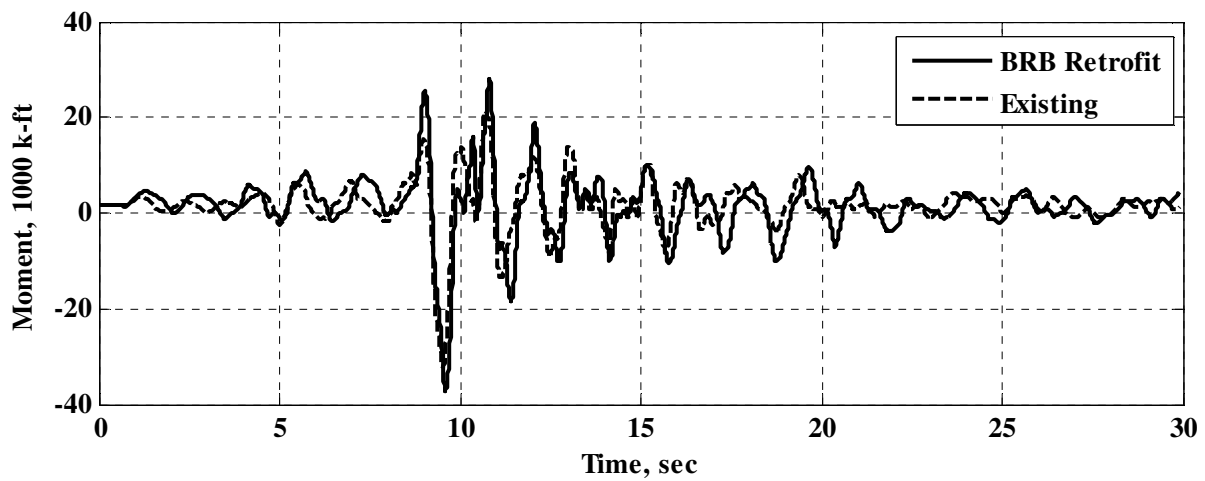


Figure 4.24 1994 Northridge Earthquake BRB Axial Force Phase Relation

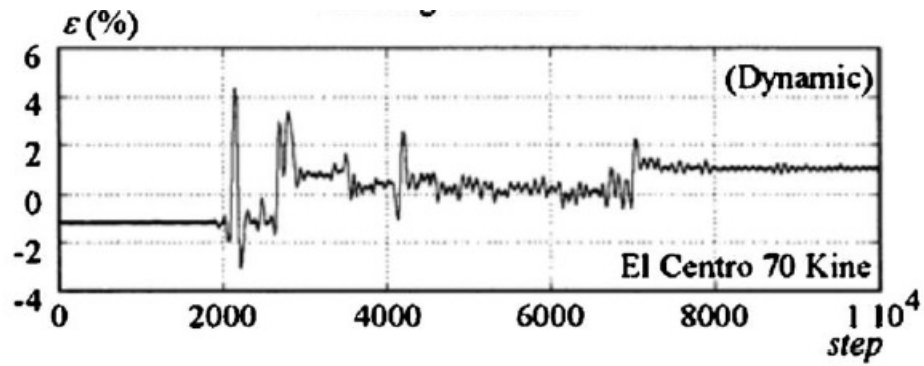


(a) Longitudinal Moment

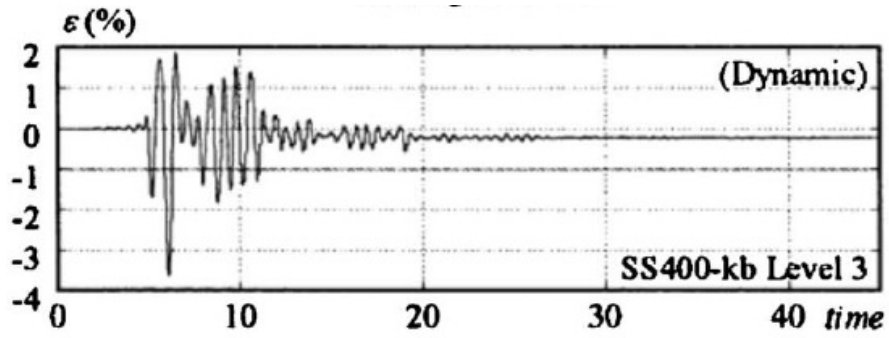


(b) Transverse Moment

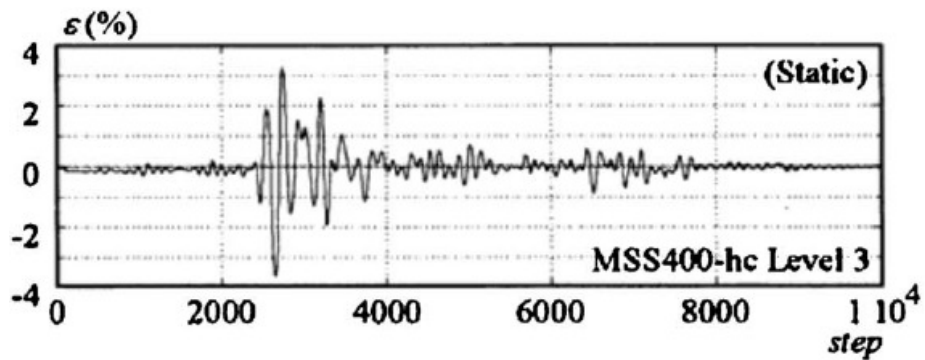
Figure 4.25 Cable Bent Seismic Force Demand Envelopes: Design-Level Earthquake



(a) Hasegawa et al. 1999

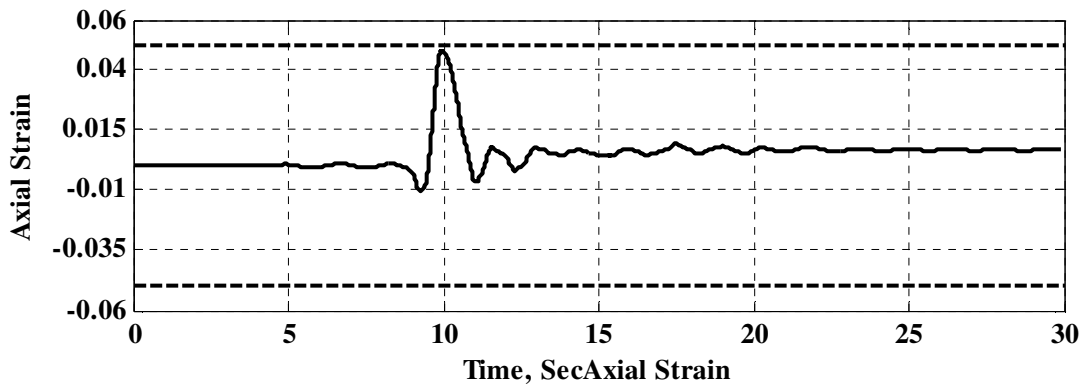


(b) Yamaguchi et al. 2002

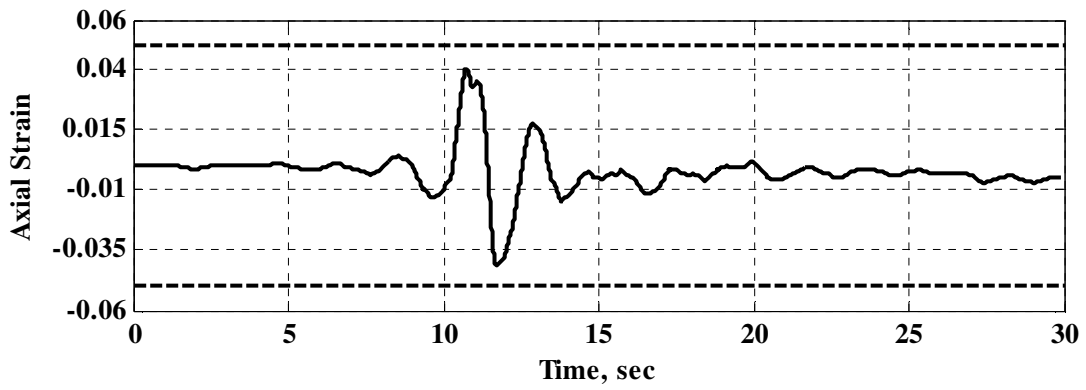


(c) Yamaguchi et al. 2004

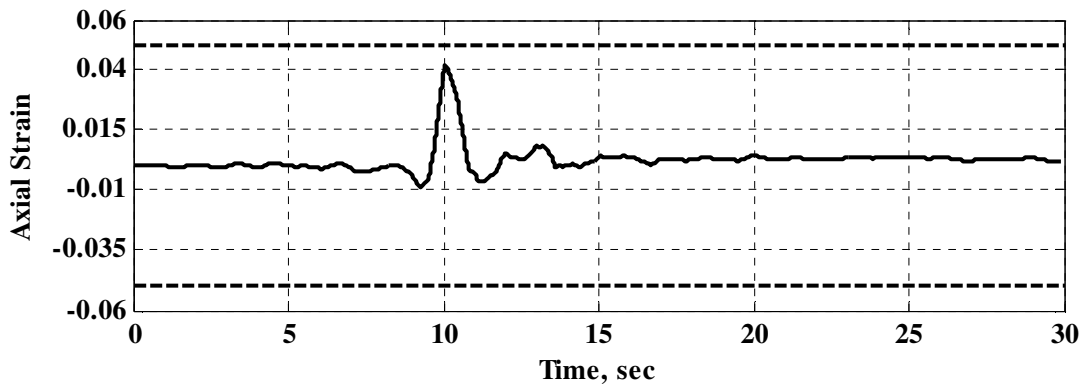
Figure 4.26 Example BRB Results As Reported by Takeuchi et al. (2008)



(a) Side to Cable Bent BRB

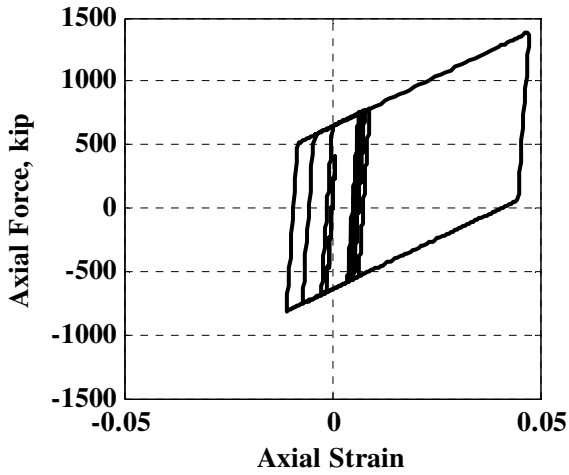


(b) Side to Tower BRB

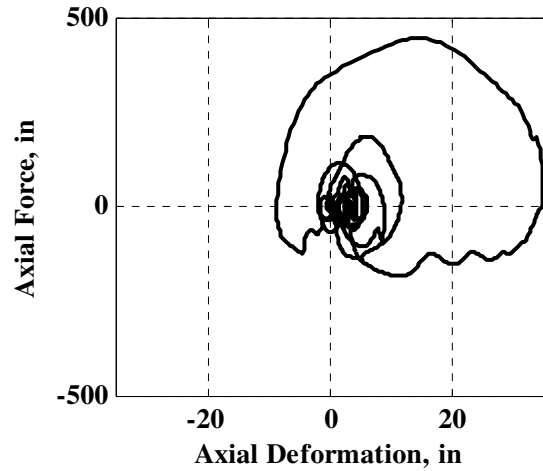


(c) Main to Tower BRB

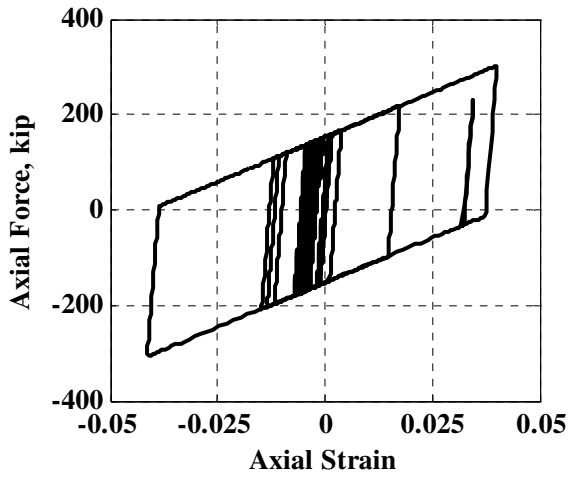
Figure 4.27 BRB Retrofit Design-Level Earthquake Axial Strain Time Histories



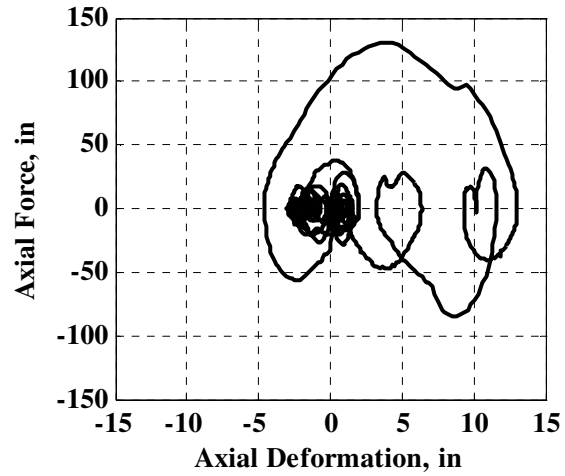
(a) Side to Cable Bent BRB



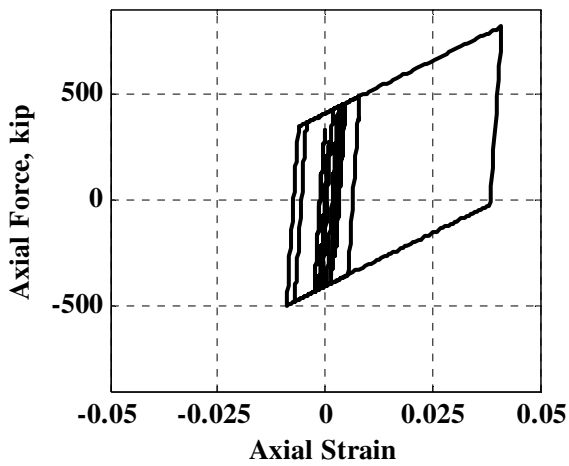
(b) Side to Cable Bent Damper



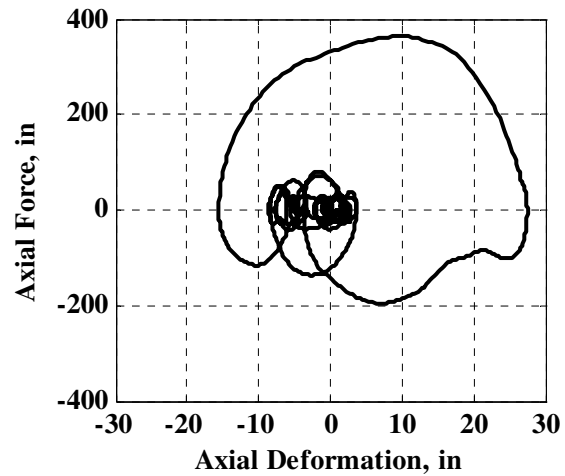
(c) Side to Tower BRB



(d) Side to Tower Damper



(e) Main to Tower BRB



(f) Main to Tower Damper

Figure 4.28 Design-Level Earthquake BRB and Damper Hysteretic Behavior

5. SERVICEABILITY EVALUATION

5.1 Introduction

Since damage of the existing viscous dampers has been observed to be a result of serviceability loading, or ambient conditions such as excitation from wind and traffic, it is necessary to investigate the serviceability performance of the BRBs. However, this condition is more difficult to recreate in the model as a result of the nonlinear nature of both the system and the real physical input forces. Analyses have been performed basing all input on several ambient condition response recordings, which were taken by the in-place accelerometers on the VTB. Difficulty arises from the fact that these motions are not induced as a base excitation, like earthquake responses; rather the excitation is from forces due to wind and traffic loading applied to the structure. In other words, the recorded ambient data is structural response and not appropriate as model input excitation time history. Additionally, the responses were recorded from the existing bridge configuration with viscous dampers, therefore it is also not appropriate to use the record as direct input to the BRB equipped model. In the following, an alternate method, which uses the recorded responses, is utilized to estimate the BRB ambient response.

5.2 Method Used to Obtain BRB Serviceability Demand

A conservative assumption will be made in order to arrive at a reasonable estimate for the ambient demands for the BRB retrofit solution. The relative displacement between the tower and the main span, calculated via the recorded data, will be directly applied to the proposed M-T BRB. This essentially assumes that the motion recorded from the existing bridge with viscous dampers would also be experienced given installation of BRBs on the bridge. This is, of course, not likely to be the case as viscous dampers theoretically have zero elastic stiffness while BRBs possess quite large elastic stiffness. Therefore, this is a conservative approach.

Note, however, in Figure 1.4 that the bridge has accelerometers installed in limited locations throughout the structure. The relevant sensors for this method are channels 10, 13, and 12, which represent the top and base of the east tower and a tower-adjacent point

on the main bridge span. These recordings are in the longitudinal direction, which will provide the great majority of axial deformation in the energy dissipation members.

Furthermore, an interpolation assumption must also be made for the tower displacement time history as the recordings are only present at the top and base while the location of interest is at the deck level. This will be accomplished by identifying the dominating natural period the top-of-tower displacement response and assuming that a corresponding mode shape will provide a reasonable tower deformation shape, which can be used as a guide for deck-level interpolation.

The recorded motions of the top and base of the southeast tower are displayed in Figure 5.1(a). From this record an approximate natural period of 4.5 seconds is observed, which aligns well with mode 4 of the bridge model ($T_4 = 4.43$ sec, see Table 4.9). A picture of this mode shape is provided in Figure 5.1(b), along with a schematic depiction of the interpolation used in Figure 5.1(c). Finally, in Figure 5.1(d) the interpolated tower displacement at deck level is provided. Note that these motions are very small.

In Figure 5.2, the interpolated tower displacement at deck-level and recorded deck motions are provided, along with the relative displacement between the two and resulting BRB stress. This stress is calculated by multiplying the relative displacement by the stiffness to obtain the corresponding force in the BRB, and then dividing by the area used for the M-T BRB. This stress history is provided in Figure 5.2(c).

5.2.1 Demands and Performance

Despite the two conservative assumptions made in the above procedure, the responses obtained are low, with a maximum BRB stress of 4 ksi [Figure 5.2(c)].

From Section 6 of AASHTO Specification (2007), fatigue design is based on the following relations:

$$\gamma(\Delta f) \leq (\Delta F)_n \quad (5.1)$$

where $\gamma = 0.75$, is the fatigue load factor

$$(\Delta F)_n = \left(\frac{A}{N}\right)^{\frac{1}{3}} \geq \frac{1}{2}(\Delta F)_{TH} \quad (5.2)$$

and: $A =$ Constant Based on Detail Configuration

$$= 250(10^8), \text{ ksi, constant for Detail Category A}$$

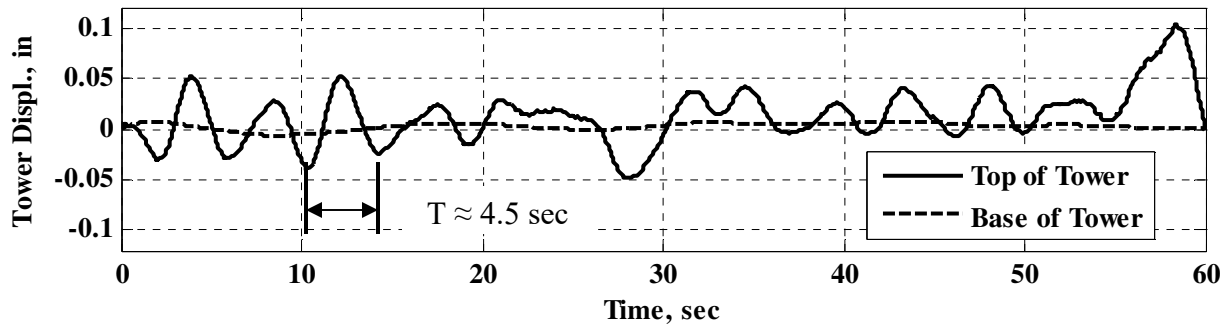
N = Number of Cycles

$$(\Delta F)_{TH} = \text{Constant-Amplitude Fatigue Threshold Stress}$$

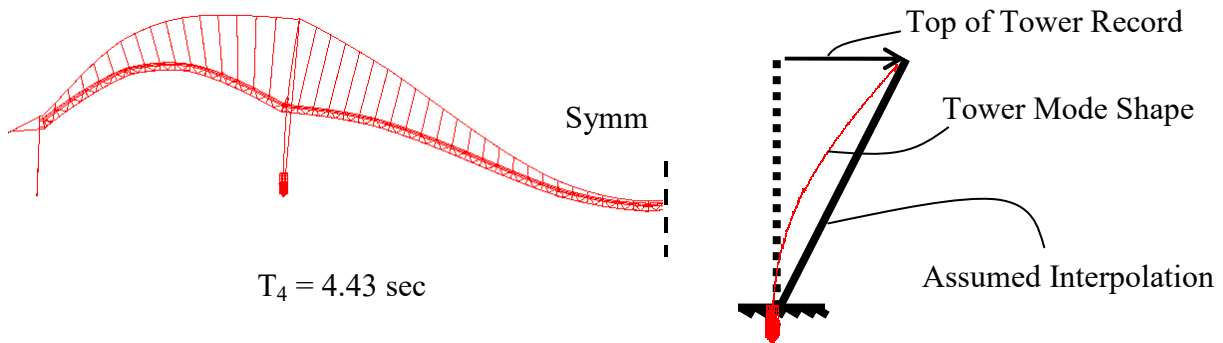
$$= 24 \text{ ksi, Detail Category A}$$

The fatigue load factor is neglected due to the fact that the analyses do not obtain the stress range from the typically assumed values calculated based on the number of expected design truck passages. The constant A is provided for details described by plain members undergoing the fatigue loading over the base metal. This condition closely represents that of the BRB core element which assumes the above reported A value.

The most important portion of the above equation is the constant-amplitude fatigue threshold stress, which is shown to be 24 ksi. This stress range corresponds to ± 12 ksi, and therefore the maximum stress ($=\pm 4$ ksi) shown in Figure 5.2(c) provides a theoretical infinite life span.

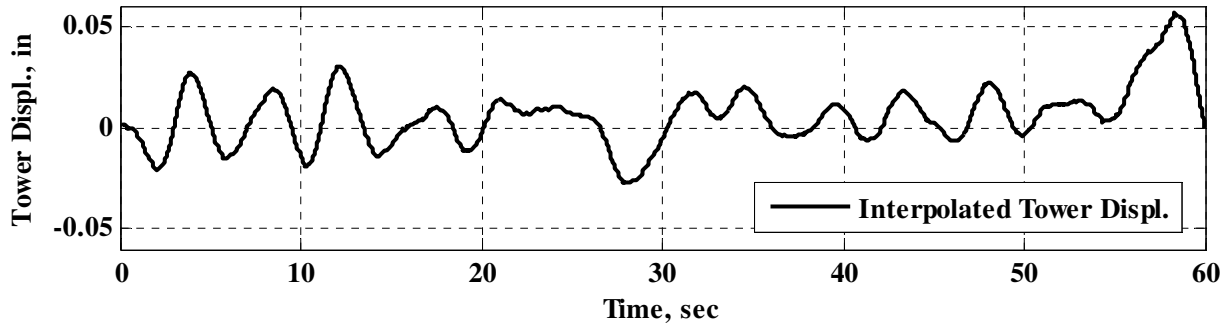


(a) Recorded Tower Displacement



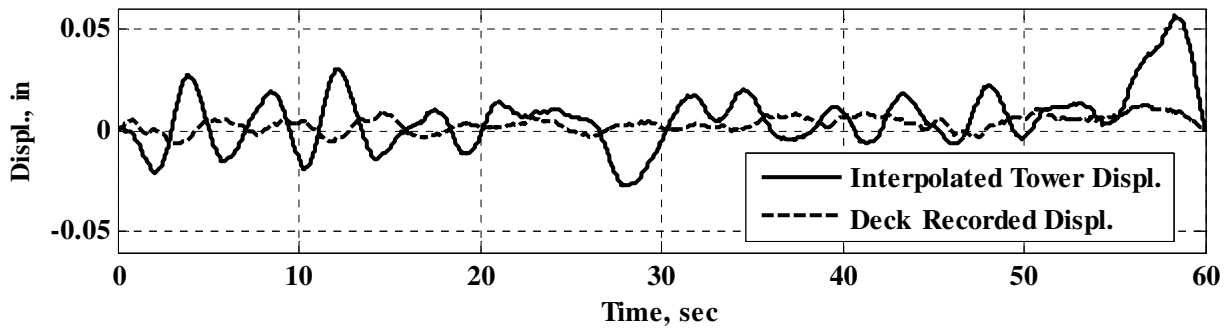
(b) Mode 4 Deformation

(c) Linear Interpolation

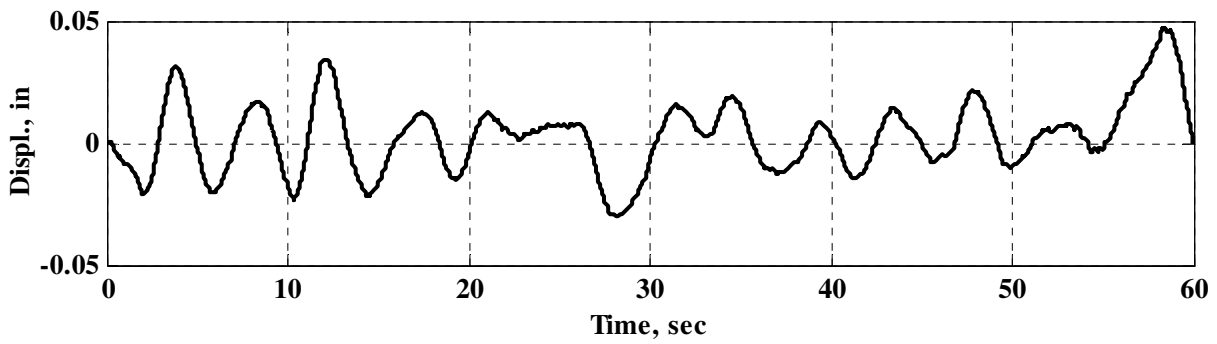


(d) Interpolated Tower Deck-Level Displacement

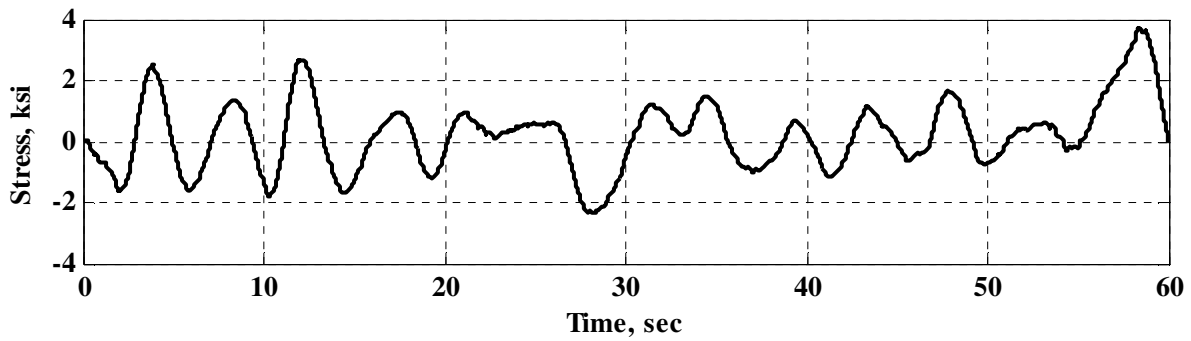
Figure 5.1 Recorded and Interpolated Ambient Motion of VTB Southeast Tower



(a) Deck-Level Displacements



(b) Relative Deck-to-Tower Displacements



(c) Resulting BRB Stress Time History

Figure 5.2 Deck-to-Tower Relative Displacement due to Ambient Vibration

6. SUMMARY, CONCLUSIONS, AND RECOMMENDATIONS

6.1 Summary

The Vincent Thomas Bridge is currently equipped with viscous dampers acting as a seismic response mitigation system between the cable bents and towers and the adjacent bridge deck structures, respectively. A replacement plan is desired due to damage of the dampers, characterized as the loss of viscous fluid, from excessive ambient motion. From this situation arose the opportunity to conduct research which explores the feasibility of using buckling-restrained braces on long-span bridges. In particular, this case study has investigated BRBs as a replacement for the viscous dampers for bridge seismic response mitigation. A parametric study was conducted, in Chapter 4, which produced a feasible solution that provides improvement in seismic response compared to the current configuration. Additionally some efforts have been presented in an effort to preliminarily address serviceability concerns regarding BRB on the VTB. This topic is addressed in Chapter 5. The serviceability stress on the BRB is estimated to be very low with respect to the threshold stress that is considered to have an infinite fatigue life. Furthermore, the displacement of the bridge under ambient loading conditions is likely to be reduced due to the elastic stiffness provided by the BRB in lieu of the viscous damper, which has very little elastic stiffness. Overall, the relative displacements between suspended spans and the towers is reduced with the use of BRB while demands on the BRBs remain within a feasible range.

6.2 Conclusions

The results of the parametric study on VTB ADINA model, with bilinear BRB structural characteristics, show that the response of both the BRB and bridge structure is feasible and beneficial, respectively. For design-level seismic mitigation, the VTB experiences on average a 32% reduction in impact-direction relative displacement, with the maximum being 59% between the main span and the towers (Table 4.4) as compared to fully functional viscous dampers. This reduced displacement response, however, is dependent upon the ability of BRBs to sustain the predicted 5% axial core strain pulse present in the simulated design-level earthquake BRB demand (Figure 4.27).

Furthermore, the force demands imparted to the bridge structure are observed as only slightly increased due to design-level input ground motion (Figure 4.22).

Moderate-level and low-level earthquakes recorded at the VTB site, and used as finite element model input, result in decreased span motion (Table 4.5 through Table 4.8), as compared with the model equipped with viscous dampers. Additionally, the BRB exhibit little or no yielding due to these recorded motions. This shows that the use of BRB as a replacement for the existing viscous dampers is very beneficial with respect to their originally intended purpose of limiting the displacement between the towers and the span structures.

Despite the difficulties of proper modeling of ambient bridge motion, the proposed method (Chapter 5) using two conservative assumptions provides acceptable estimated BRB performance. The considered method suggests that the BRB are subjected to a fatigue stress range of roughly one-third the threshold stress range that corresponds to a theoretically infinite service life.

The use of BRB on the VTB model is beneficial, although actual implantation would require a detailed design-oriented evaluation of the bridge superstructure considering the expected forces imparted to the bridge by BRBs, and serviceability demands imparted to the braces.

Ultimately, the results of this study suggest that the use of buckling-restrained braces on long-span bridges near fault lines for seismic response mitigation is feasible upon verifying the ability to sustain pulse-type demands of 5% axial core strain.

6.3 Recommendations

The current work has produced promising results through finite element model predictions of the performance of both the BRB and the VTB. However, some additional questions remain, some of which can only be answered through physical testing and subsequent correlated model implementation. The physical testing would begin with a number of reduced scale braces, to identify any adjustments that may be required for larger/full-scale specimens.

First, the strong pulse-type ground motion that dominates the design-level earthquake for the VTB creates a large half or single cycle of strain demand for the BRBs. These strains are at maximum 5% which is significantly larger than the levels to which BRBs are typically subjected. After some limited additional refinements, a number of devices that correspond to those modeled in the bridge should be subjected to physical testing to verify their acceptable performance for implementation.

Secondly, the uncertainty of the proper ambient motion input for the bridge finite element model should be clarified, possibly by new ambient data being collected from the bridge. The latest ambient recordings are nearly 4 years old, and fresh data should be gathered from the bridge site. This data could include wind speeds and traffic counts which may lead to development of an actual dynamic forcing function that would more accurately portray the actual service loading of this bridge. As such, any input motion that relies on recorded data from the as-built bridge necessarily includes the contribution of the dampers and makes implementation to a modified model automatically incorrect.

Third, further high-cycle fatigue testing on BRB devices would be required. The limited data available in the literature and in the BRB proprietary industry necessitates the generation of new test data. The degradation of the possible BRB hysteretic behavior is unknown as it relates to high-cycle fatigue. This fact, combined with the design-level earthquake pulse-like demand, makes for a very unique important BRB loading sequence. The device should be shown to possess the ability to provide the expected service life and then satisfactorily perform during the design-level demand. This would provide a great deal of useful information for both the VTB project and the general body of knowledge of BRB performance.

There are currently three main companies in the U.S. manufacturing BRBs, and all would be contacted to participate in the testing program. After some additional limited adjustments to the desired BRB properties, which have been proposed in this report, the manufacturers would be provided with a range of acceptable BRB design properties. In addition, all-steel BRBs should be included as the proposed BRB members are somewhat long in comparison with braces typically used in building applications. The all-steel BRB configuration could address self-weight issues that may be present with conventional mortar-filled steel tube BRBs. However, all-steel BRBs are not currently produced by the

three manufacturers in the U.S., therefore the braces would be developed by UCSD in keeping with Phase 4 of the project proposal. Furthermore, other BRB variations found to be promising should be investigated as part of this testing plan in order to ensure a beneficial solution for the bridge is not overlooked. However, no single-source BRB is expected to be required for adequate performance. With adequate industry participation, a competitive environment should yield a general specification for appropriate BRB properties for implementation on the VTB.

Finally, the use of BRB for other long-span bridges should be investigated. Many other bridge designs exhibit much less complicated structural behavior as compared to the VTB. Therefore, BRB implementation is likely much more straightforward and equally beneficial, if not more so. An example of such would be the Coronado Bridge in San Diego, CA, whose study has been discussed in the project proposal. Any potential BRB demands, additional to those identified through analysis of the VTB, should be identified from analyses of all considered bridges before physical testing plans are finalized. This will allow for a comprehensive demand envelope and loading protocol to be developed. This will cause the physical testing program to be very attractive for manufacturer participation, to further their product development in parallel with the completion of the current research objectives.

REFERENCES

- AASHTO. (2007). "LRFD Bridge Design Specifications." *American Association of State Highway and Transportation Officials*, 4th Edition Washington D.C.
- ADINA: *Automatic Dynamic Incremental Nonlinear Analysis*. ADINA R&D, Inc., Watertown, Massachusetts.
- AISC (2005). "Seismic Provisions for Structural Steel Buildings". *American Institute of Steel Construction*, Chicago, Illinois.
- Benzoni, G., Amaddeo, C., DiCesare, A., Palermo, G., (2008). "A damage identification procedure for bridge structures with energy dissipation devices" *Report No. SRMD-2007/09*. Department of Structural Engineering, University of California, San Diego, La Jolla, Calif.
- Benzoni, G., Innamorato, D., (2007). "Star Seismic brace tests Mercy San Juan hospital project" *Rep. No. SRMD 2007/05*. Department of Structural Engineering, University of California San Diego, La Jolla, Calif.
- Black, C., Makris, N., Aiken, D. (2004). "Component testing, seismic evaluation and characterization of buckling-restrained braces" *J. Struct. Eng., ASCE*, 130(6), 880-894.
- CESMD - Information for Strong-Motion Station, Los Angeles–Vincent Thomas Bridge, CGS–CSMIP Station 14406, www.strongmotioncenter.org
- Earth Mechanics (2011). *Personal communication*, May 27 2011.
- El-Tawil, S., Ekiz, E., (2009). "Inhibiting steel brace buckling using carbon fiber-reinforced polymers: Large-scale tests" *J. Struct Eng. ASCE*, 135(5), 530-538.
- Graziotti, F (2010). "Seismic bridge response modification due to degradation of viscous dampers". *Thesis*. Department of Structural Engineering, University of California San Diego, La Jolla, Calif.
- Hasegawa, H., Takeuchi, T., Iwata, M., Yamada, S., and Akiyama, H. (1999). "Dynamic performances of unbonded braces." *AIJ Technical Rep. No. 9.*, Architecture Institute of Japan
- Ingham, T J., Rodriguez, S., Nader, M. (1997). "Nonlinear analysis of the Vincent Thomas Bridge for seismic retrofit." *Computers and Structures*, 64(5), 1221-1238.
- Kim, J., Choi, H., (2004). "Behavior and design of structures with buckling-restrained braces" *Eng. Struct.*, 26(6), 693-706.

- Merritt, S., Uang, C.M., Benzoni, G. (2003a). "Subassemblage testing of CoreBrace buckling-restrained braces." *Rep. No. TR-2003/01*. Department of Structural Engineering, University of California San Diego, La Jolla, Calif.
- Merritt, S., Uang, C. M., and Benzoni, G. (2003b). "Subassemblage testing of Star Seismic buckling-restrained braces." *Rep. No. TR-2003/04*, Department of Structural Engineering, University of California San Diego, La Jolla, Calif.
- Moffatt and Nichol Engineers (1996). "Toll road seismic retrofit project Vincent Thomas Bridge, strategy report." *Report to Caltrans*, May 1996.
- Mukherjee, S., Gupta, V.K. (2002). "Wavelet-based generation of spectrum-compatible time-histories" *Soil Dynamics and Earthquake Engineering*, 22(9), 799-804.
- Nakamura, H., et al. (2000). "Fatigue properties of practical-scale un-bonded braces." *Nippon Steel Technical Rep. No. 82*, 51-57.
- Newell, J., Uang, C.M., Benzoni, G., (2005). "Subassemblage testing of CoreBrace buckling-restrained braces (F Series)." *Rep. No. TR-2005/01*. Department of Structural Engineering, University of California San Diego, La Jolla, Calif.
- Newell, J., Uang, C.M., Benzoni, G., (2006). "Subassemblage testing of CoreBrace buckling-restrained braces (G Series)." *Rep. No. TR-2006/01*. Department of Structural Engineering, University of California San Diego, La Jolla, Calif.
- Palazzo, G., Lopez-Almansa, F., Cahis, X., Crisafulli, F., (2009). "A low-tech dissipative buckling restrained brace. Design, analysis, production, and testing" *Eng. Structure*, 31(9), 2152-2161.
- Perform-3D: Nonlinear Analysis and Performance Assessment for 3D Structures*. Computers & Structures, Inc., Berkeley, Calif.
- Ravi Kumar, G., Satish, S.R., Kalyanaraman, V., (2007). "Behaviour of frames with non-buckling bracings under earthquake loading." *J. Constructional Steel Research*. 63(2), 254-262.
- Sabelli, R. (2004). "Recommended provisions for buckling-restrained braced frames" *Engineering Journal*, AISC. 41(4), 155-175.
- Satellite Image of Vincent Thomas Bridge, www.maps.google.com
- Takeuchi, T., Ida, M., Yamada, S., Suzuki, K., (2008). "Estimation of cumulative deformation capacity of buckling restrained braces" *J. Struct. Eng.*, ASCE, 134(5), 822-831.

- Ren, W., Blanford, G., Harik, I. (2004). "Roebing suspension bridge. I: Finite-element model and free vibration response." *J. Bridge Eng.*, 9(2), 110-118.
- Uang, CM., Nakashima, M., Tsai, KC,. (2004). "Research and application of buckling restrained baced-fames" *Steel Structures*, 4, 301-313.
- Usami, T., Lu, Z., Ge, H., (2005). "A seismic upgrading method for steel arch bridges using buckling-restrained braces" *Earhquake Eng Struct. Dyn.*, 34(4-5), 471-496.
- Usami, T., Ge, H., Luo, X.Q., (2009). "Experimental and analytical study on high-performance buckling restrained brace dampers for bridge engineering", *Proc. 3rd International Confr. on Advances in Experimental Struct. Eng.* 2009.
- WavGen*. Wavelet-Based Generation of Spectrum-Compatible Ground Motion. Dr. Vinay K. Gupta, Department of Civil Engineering, Indian Institute of Technology, Kanpur, India, <http://home.iitk.ac.in/~vinaykg/wavgen.htm>
- Yamaguchi, M., et al (2002). "Shaking table test of damage controlled frame with buckling restrained braces." *J. Struct. Constr. Eng.*, 558, 189-196. (in Japanese)
- Yamaguchi, M., Yamada, S., Takeuchi, T., Wada, A. (2004). "Seismic performance of buckling resistant brace within a steel frame in the case of ultimate earthquake." *J. Constructional Steel*, 12 207-210. (in Japanese)
- Zhao, J., Wu, B., Ou, J., (2010). "A novel type of angle steel buckling-restrained brace: Cyclic behavior and failure mechanism" *Earthquake Eng. Struct. Dyn.*, 40(10), 1083-1102.

Appendix A – ADINA/Perform-3D Model Correlation Study

The ADINA model of the VTB provided by Caltrans is a very detailed model (Moffat and Nichol 1996; Ingham et al. 1997). However, parametric BRB study does not necessarily warrant such a finely discretized model, as global response is the general focus for much of the analyses. The ADINA model applies a lumped mass at every element connection node, resulting in approximately 22,000 degrees of freedom (Ingham et al. 1997).

Perform-3D was chosen for construction of a simplified model. This program offers a few very attractive features with respect to parametric study for use of BRB on the VTB. Perform-3D is design oriented and contains detailed templates for BRB members, viscous dampers, and many other nonlinear structural elements. With the parameters of typical BRB members well organized within the software, the program is amenable to parametric analyses.

There were four main simplifications made to the Perform-3D bridge model. The first, and most important, is the coarser discretization of mass. The Perform-3D model has approximately 2,400 degrees of freedom. This should allow for faster solution times, as there are, roughly, an order of magnitude less degrees of freedom. Second, some averaging assumptions were made with respect to cross sectional properties, as these were not importable in Perform. Third, in ADINA the bridge deck is modeled with membrane and shell elements, which possess many degrees of freedom and integration points requiring added solution time and memory size. These have been replaced by a system of beam and truss elements, thereby eliminating these complex finite elements. Finally, the extensive modeling of the towers' foundations was excluded from the Perform-3D model. This study is most interested in the global response of the structure, and therefore the foundation elements were deemed to be unnecessary to investigate the feasibility of replacing the viscous dampers with BRB.

A.1 ADINA Foundation Elements

As stated above, one of the major simplifications made to the Perform-3D model is the exclusion of the tower foundation finite element modeling. In order to verify that this assumption is not eliminating any major response features, dynamic analyses of the ADINA model are compared. A “locked-foundation” and an “unlocked-foundation” model are subjected to a dynamic time history, the design ground motion, and the responses are compared.

Each component of the Northridge event was investigated separately, along with the respective span displacement response. The results are displayed in Figure 3.1. It is evident that there is only a slight difference in longitudinal response of the side span. Attention was paid to ensure that boundary conditions were correct in locked model, and they should closely represent those used in the Perform-3D model. The comparison in Figure 3.1(a)-(f) shows insignificant differences at almost all of the checked points. Figure 3.1(d) shows only a slight variation in the side span longitudinal response.

This comparison was deemed sufficient evidence, and verified that there is not a major response feature being overlooked by neglecting the foundation discretizations in Perform-3D.

A.2 Perform-3D/ADINA Model Correlation

A.2.1 Eigenvalue Analyses

A good measure for comparing dynamic similarity between two models is the eigenvalue analysis. The eigen solution is obtained independently in both programs and the results are compared. However, due to the suspension construction of the bridge, it is necessary to include the pre-tension present in the cables as the nonlinear geometric stiffness is extremely significant for the bridge. Perform-3D does not currently offer analysis options for including any member loads in the eigenvalue analysis. Therefore, in order to gain correlation between ADINA and Perform-3D modes, some temporary modifications were required of the ADINA model. The cable strain was “turned-off” in ADINA, so as to match the conditions of the Perform-3D model. See Figure 3.2(a) for a depiction of the initial strain in the cables.

One additional modification was required concerning the cables. With each cable modeled with truss elements, the nodes connecting the suspension and hanger cables have near zero transverse stiffness since it contains only 3 truss elements in one plane. Figure 3.2(b) shows a closer view to aid in visualization. This near zero stiffness results in failure of the eigen solution, and thereby required modification. These nodes were slaved, in the transverse direction only, to the corresponding nodes on the stiffening truss. This allows the eigenvalue problem to be solved by adding a constraint that does not significantly deviate from how the bridge deforms in reality (Ren et al. 2004). This change was required in both models as the geometry and element types are equivalent, while they are also the cause of the problem.

A.2.2 Span Modes

Table 3.1 provides a summary of the periods of the span mode and the differences between the ADINA and Perform-3D models. Figure 3.3 displays the mode shapes with the eigenvectors scaled to be equal in magnitude. The correlation is observed to be very good with all model to model periods within 5%, and all mode shapes comparing well. Perform-3D mode 1 is tuned slightly by making the initial elastic stiffness of the damper element equal to 1.2 times that ($= 1.2 \text{ kip/in}$) of the ADINA model. The first longitudinal mode is not what one typically expects from a bridge eigen solution and warrants some discussion. This mode is the result of the exclusion of the suspension cable initial strains. The effect is comparable to that base-isolation in a building, as typically the first mode is shifted due to the added flexibility in that mode shape. This is essentially what is causing this unexpected mode, as the only stiffness in the longitudinal rigid body motion of the main span is a component of the axial stiffness of the relatively flexible suspension cables and the very low initial axial stiffness of the damper elements. Once the cable initial strain is reinstated, as past studies have performed in ADINA, this mode is not as readily observed.

As a supplement to the comparison of the modified eigenvalue analysis results, a correlation is made utilizing the response due to excitation based on recorded ambient response. Ambient acceleration records from the bridge instrumentation are applied as acceleration input to the supports to provide response to be analyzed in the frequency

domain via Fourier Transform. Since Perform-3D is able to apply the cable strain prior to dynamic analyses this ambient response, transformed to the frequency domain, can allow identification of a few primary modes that should correlate with typically considered eigenvalue solutions from ADINA. The results are presented in Figure 3.4, and summarized in Table 3.2. The Fourier magnitude peaks appear to fall within a range that is deemed satisfactory and suggests that the strained Perform-3D model has very similar fundamental periods as the ADINA model.

A.2.3 Tower Modes

During preliminary analyses it became apparent that the tower response is a very important aspect of the behavior of the entire seismic mitigation system, and therefore additional analyses were conducted to ensure dynamic correlation for the towers.

The tower modes are at much higher frequencies, as the towers are very stiff and lightweight compared to the spans. The frequency domain is utilized, along with visual inspection of the eigenvector solutions, to more readily identify the tower modes. Table 3.3 summarizes the comparison between ADINA and Perform-3D tower modes. Figure 3.6 presents the ambient displacement response and corresponding Fourier spectra for various points along the height of the tower. This provided contrast crucial for distinguishing the tower modes amongst many very complicated, high frequency, mode shapes. Figure 3.7 displays a comparison of mode shapes. Some of the 3-dimensional rendered views are slightly different as the model discretization occasionally blocked a clean view of the tower shapes. It should also be noted that the low frequency observed in the longitudinal direction (see Figure 3.6) is due to a minor response artifact involving the transition of the Perform-3D model from nonlinear static to dynamic analysis. Given a record with a sufficient acceleration silence, this low frequency is attenuated. This was resolved in the dynamic analysis comparison. Nonetheless, all subsequent analyses show the artifact is not significant. The response characteristics correspond well with ADINA regardless of this disparity early in the time history response.

As the modes are of high frequency, and more easily coupled with other modes, the FFT correlation is somewhat coarse respectively. Despite this, the modes are identifiable by inspection of the FFT amplitude spectrum and mode shape results. The correlation

between the models' tower modes is deemed acceptable, as only small variations are observed.

A.2.4 Dynamic Analyses

A similar approach was taken to compare the response of each of the models to dynamic excitation, as that used for the ADINA locked and unlocked foundation model comparisons. Each model was subjected to the design ground motions' separate components, and the respective span response was inspected. Strong correlation between ADINA and Perform-3D model responses will provide convincing evidence of adequate model equivalence, since the nonlinear dynamic time history analysis utilizes all aspects of the finite elements in each mode (i.e. all nonlinearities participate). The directional components of the Northridge record were used separately to more easily distinguish possible misrepresentations in the Perform-3D model.

From Figure 3.8 it is clear that the response of the main and side spans is sufficiently equal between ADINA and Perform-3D models. One difference is observed in a small period shift in the main span vertical response, which is most likely due to combined effects from slight differences in tower stiffness and total deck mass. The side span transverse response is also somewhat ill matched at the end of the record; however this is likely a numerical issue and not a problem with the model discretization or configuration. Most notably both longitudinal span responses are nearly identical, which provides model correlation confidence, especially considering that the longitudinal response is the primary concern for the current study. These results are deemed to be strong evidence that the Perform-3D model is sufficient for carrying out the BRB parametric study.\

A.3 Conclusion

As discussed above, all model correlation efforts appear to show satisfactory similarity between the Perform-3D and ADINA VTB models. The Perform-3D model has been used for the BRB results presented in Section 2, and it is concluded that equivalent BRB elements used within the ADINA mode will provide very similar results. This will be the procedure once the full parametric study has highlighted the ideal BRB member for use on the VTB.

Table A.1 Summary of Modified Model Span Modes

Mode	Period (sec)		Difference from ADINA (%)	Description
	ADINA	Perform-3D		
1	9.51	10.58 (9.67)	11.1 (1.6)	1st Longitudinal
2	9.62	9.30	3.3	1st Transverse
3	8.53	8.20	3.9	1st Vertical
4	5.81	5.72	1.5	2nd Vertical
5	4.03	3.87	4.0	3rd Vertical
6	3.85	3.73	3.1	4th Vertical

Table A.2 Summary of Span Modes Obtained from Fourier Analysis

Mode	Period (sec)		Difference from ADINA (%)	Description
	ADINA	Perform-3D		
1	7.41	7.87	10.8	1 st Transverse
2	5.88	5.88	0.0	1 st Longitudinal
3	5.85	4.76	22.9	1 st Vertical Anti-symm.
3	4.36	4.17	4.4	1 st Vertical Symm

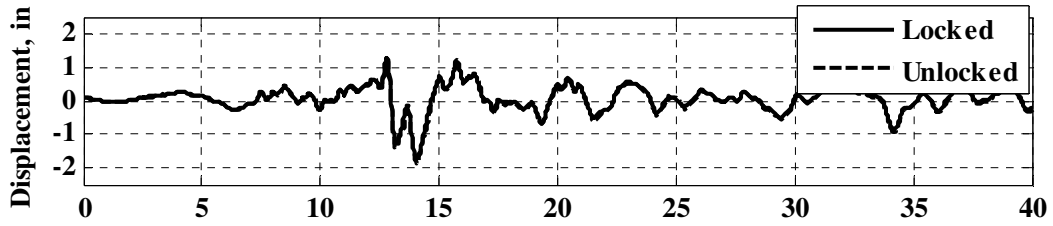
Table A.3 Summary of Tower Modal Analysis

(a) Longitudinal Tower Modes

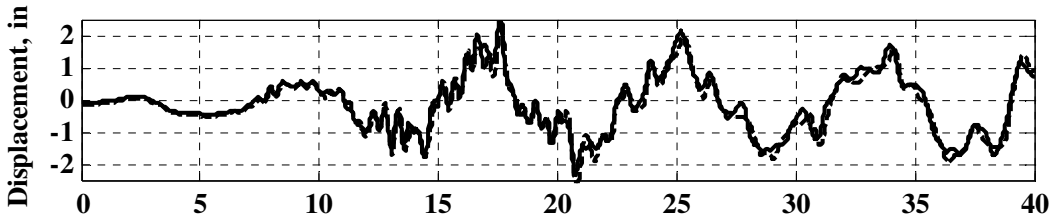
Tower Modes	ADINA Eigen / FFT (Hz)	%	Perform Eigen / FFT (Hz)	%	Adina vs Perform (%)	Description
L-1	1.02 / 1.05	2.9	1.00 / 1.05	5.0	2.0	Towers act in same direct.
L-2	1.05 / 1.10	4.8	1.07 / 1.10	2.8	1.9	Towers act in opp. direct
L-3	1.15 / 1.20	4.3	1.16 / 1.20	3.4	0.8	Towers act in opp. direct.
L-4	1.32 / 1.30	1.5	1.39 / 1.30	6.9	5.3	Torsional Tower action, spans displace vertically

(b) Transverse Tower Modes

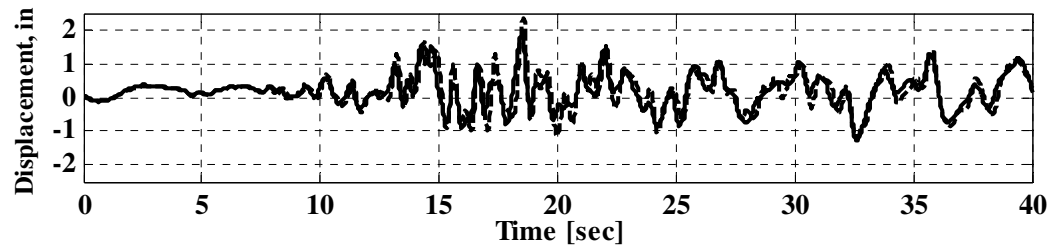
Tower Modes:	ADINA Eigen / FFT (Hz)	%	Perform Eigen / FFT (Hz)	%	Adina vs Perform (%)	Description
T-1	1.04 / 1.05	1.0	1.04 / 1.05	1.0	0.4	Minor Tower mode, spans particip.
T-2	1.13 / 1.10	2.7	1.2 / 1.15	4.2	5.8	Major Tower mode, sim. to SDOF 1st mode, towers same direction
T-3	1.18 / 1.20	1.7	1.26 / 1.2	5.0	6.8	Major Tower mode, sim. to SDOF 1st mode, towers opp. direction
T-4	1.29 / 1.30	0.8	1.50 / 1.50	0.0	16.3	Major Tower mode, slightly sim. to SDOF 2st mode, towers act in opp. dir.



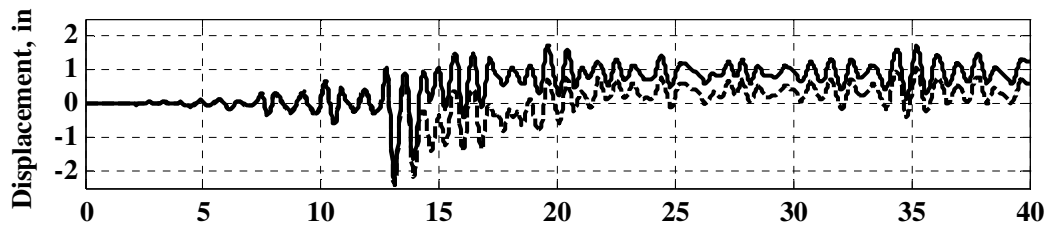
(a) Main Span Longitudinal Response



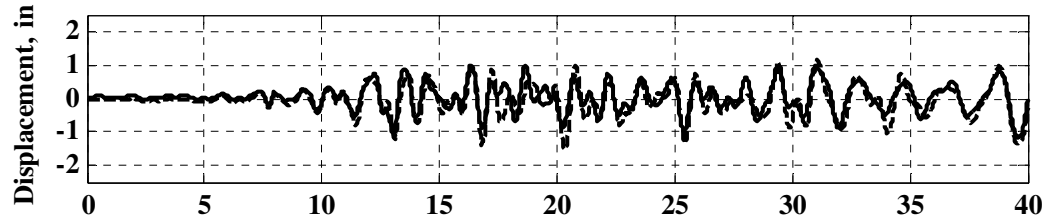
(b) Main Span Transverse Response



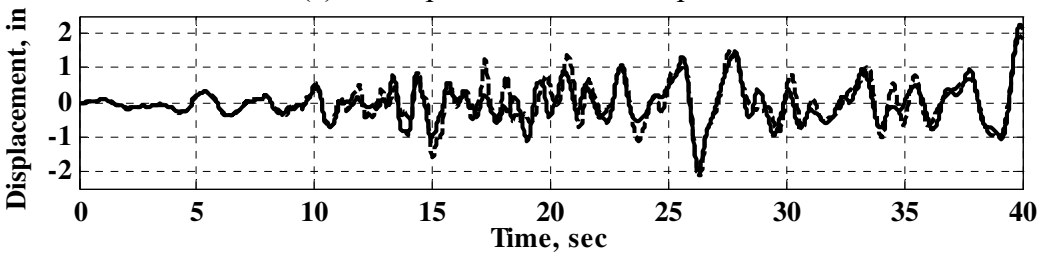
(c) Main Span Vertical Response



(d) Side Span Longitudinal Response

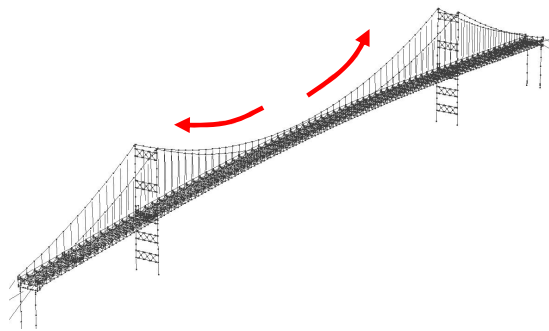


(e) Side Span Transverse Response

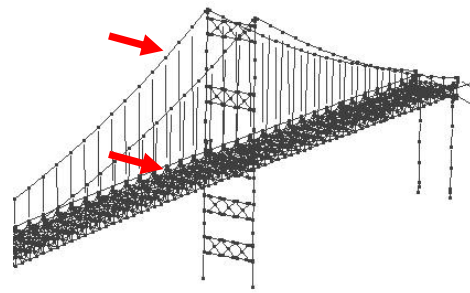


(f) Side Span Vertical Response

Figure A.1 ADINA Locked versus Unlocked Foundation Model Responses

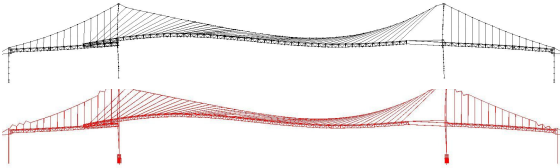


(a) Cable Initial Strain

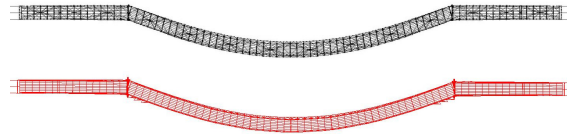


(b) Constrained Cable Nodes

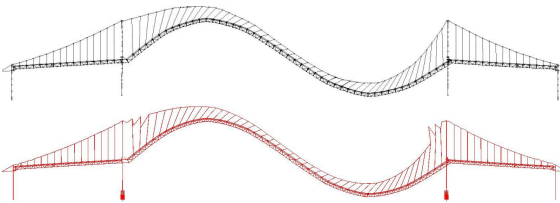
Figure A.2 Modification Required for Eigenvalue Analysis Comparison



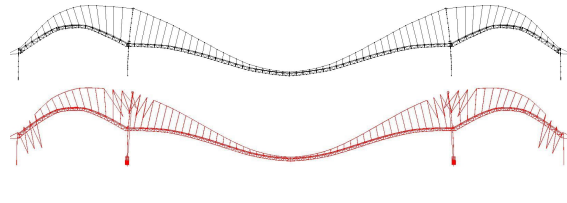
(a) Mode 1



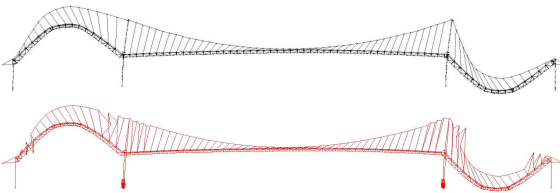
(b) Mode 2



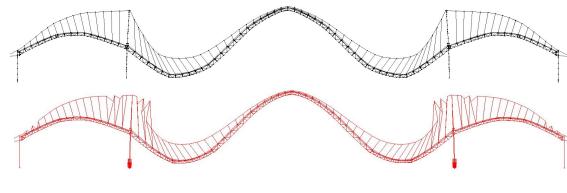
(c) Mode 3



(d) Mode 4



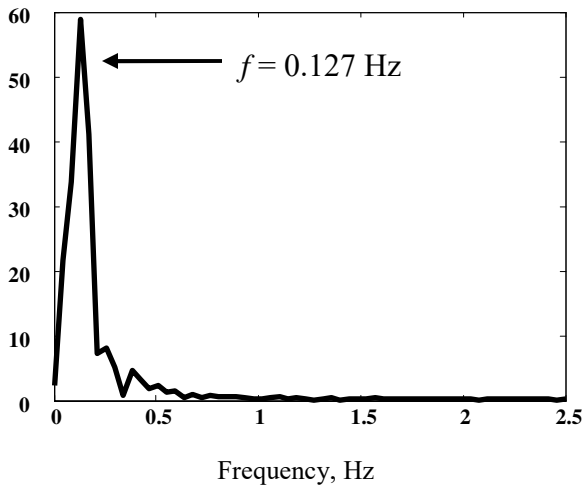
(e) Mode 5



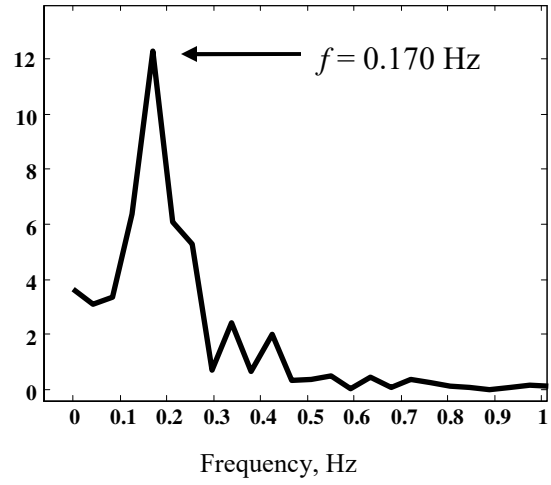
(f) Mode 6

Figure A.3 Modified Model Span Mode Shapes

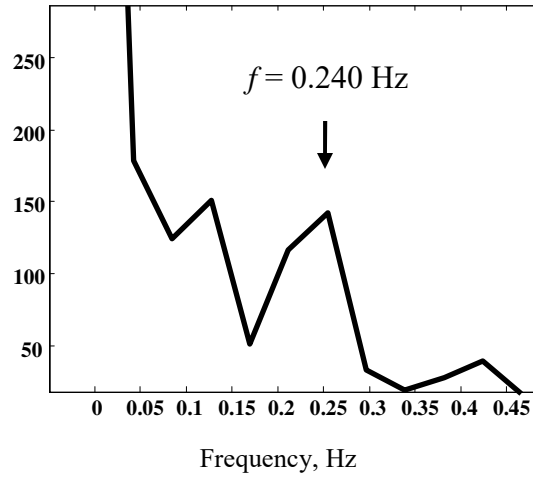
(Top: Perform-3D, Bottom: ADINA)



(a) Transverse Response



(b) Longitudinal Response



(c) Vertical Response

Figure A.4 Fourier Analysis of Ambient Deck Response

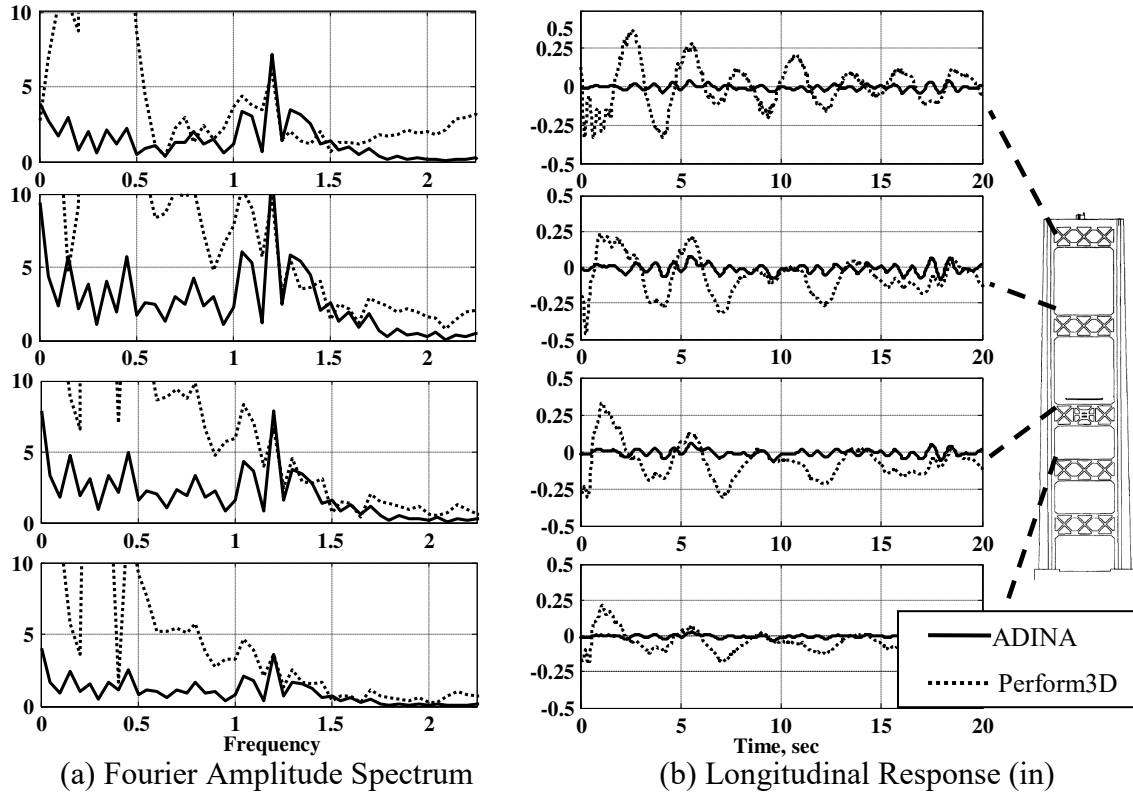


Figure A.5 Fourier Analysis of Tower Longitudinal Ambient Response

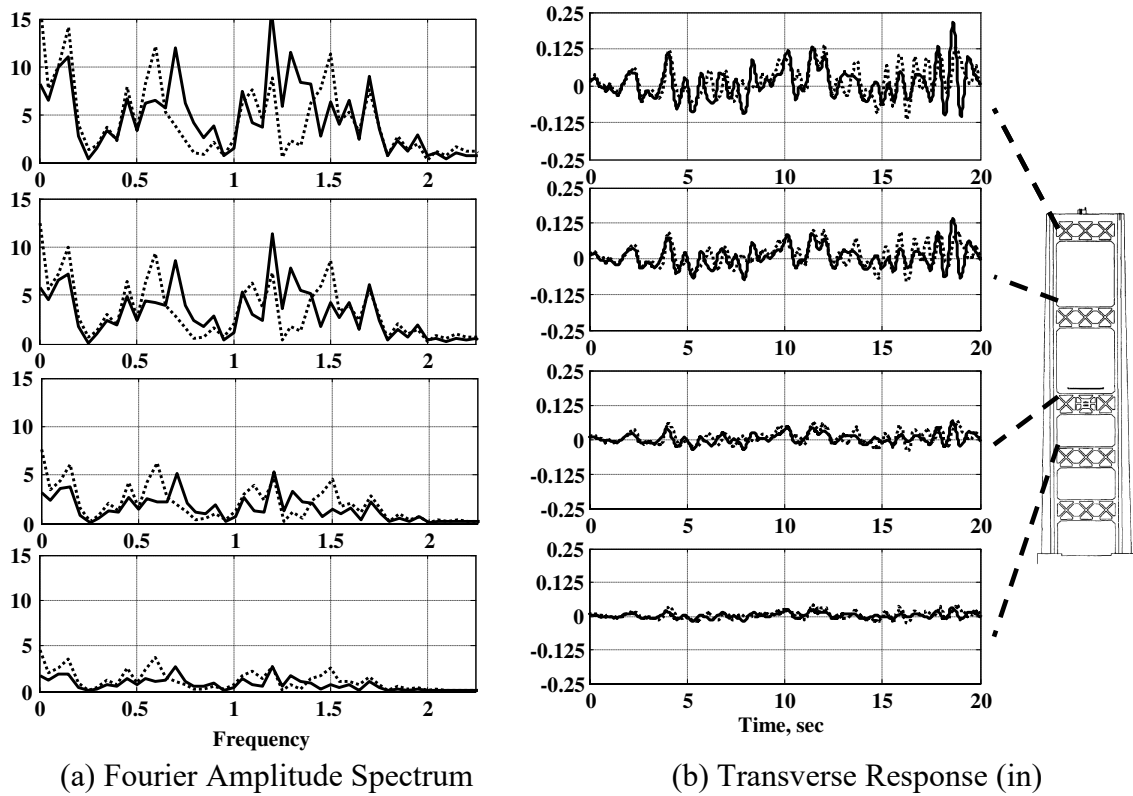
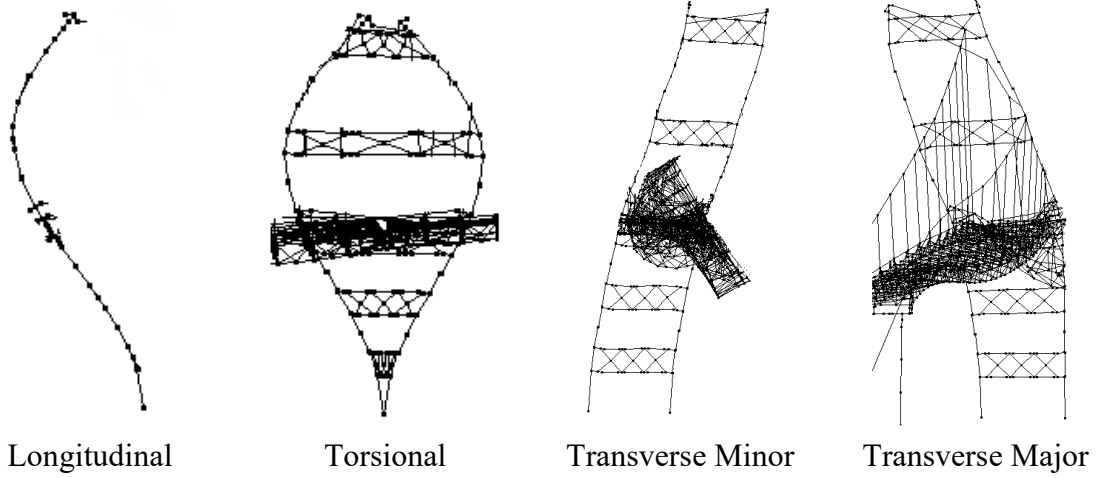
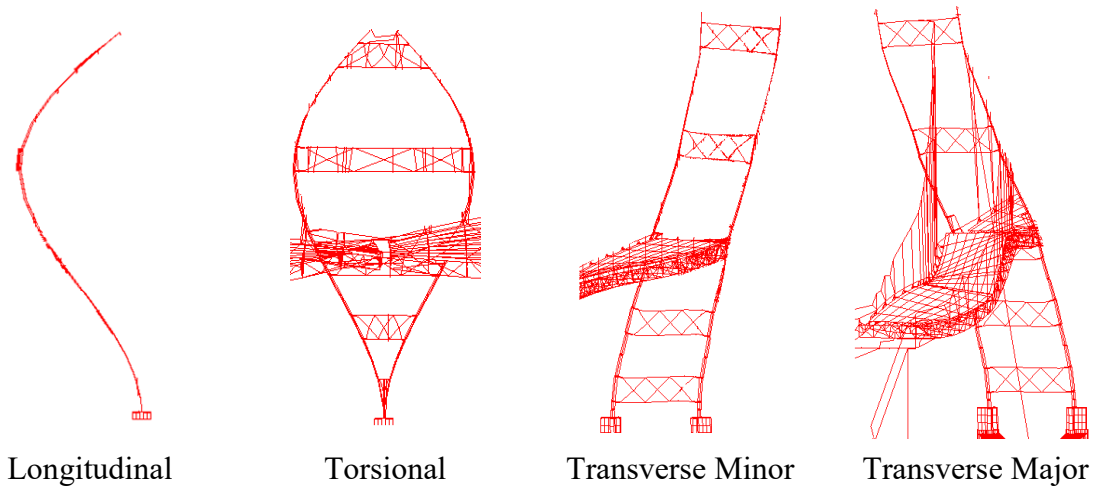


Figure A.6 Fourier Analysis of Tower Transverse Ambient Response



(a) Perform-3D Model



(b) ADINA Model

Figure A.7 Tower Mode Shapes

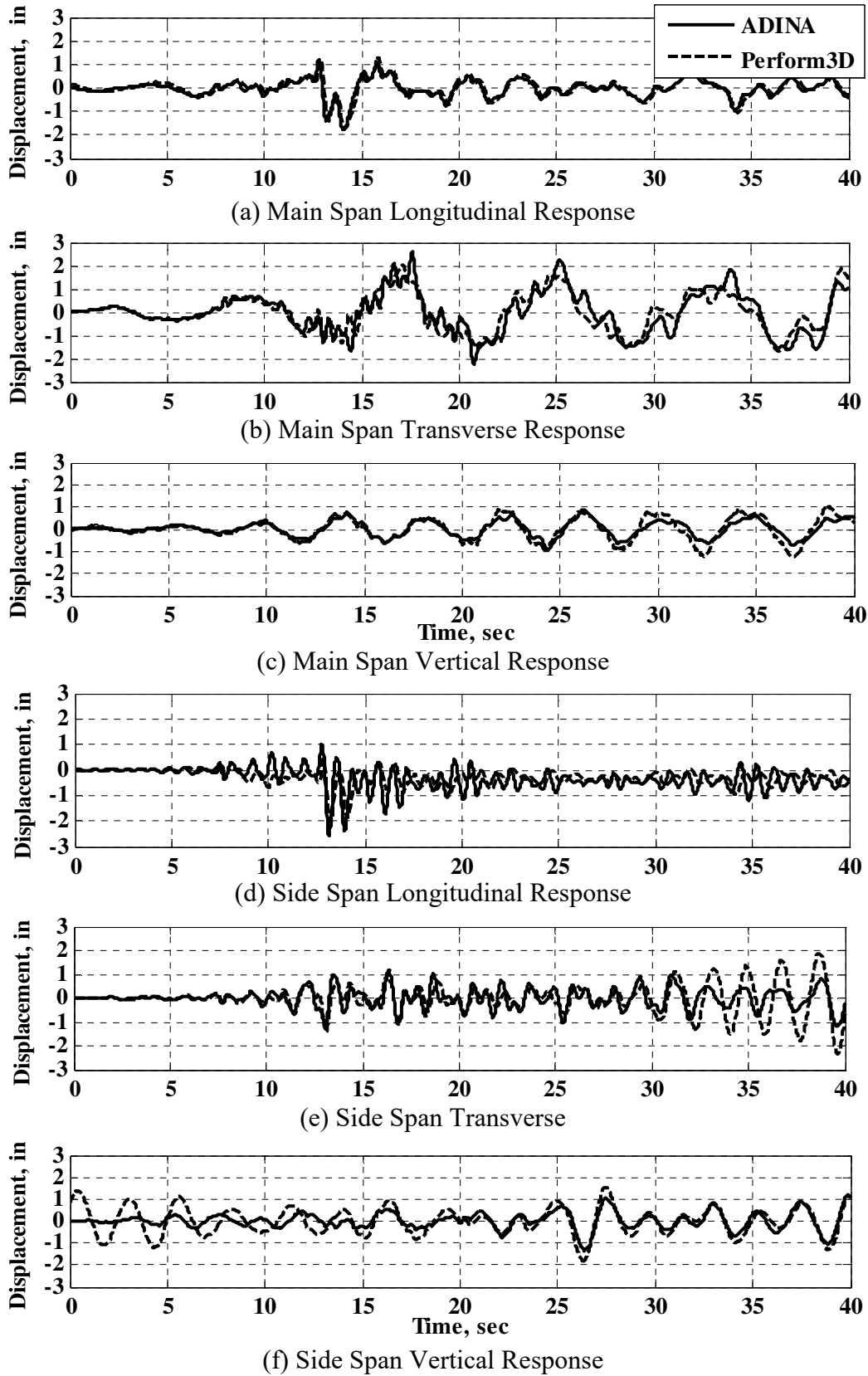
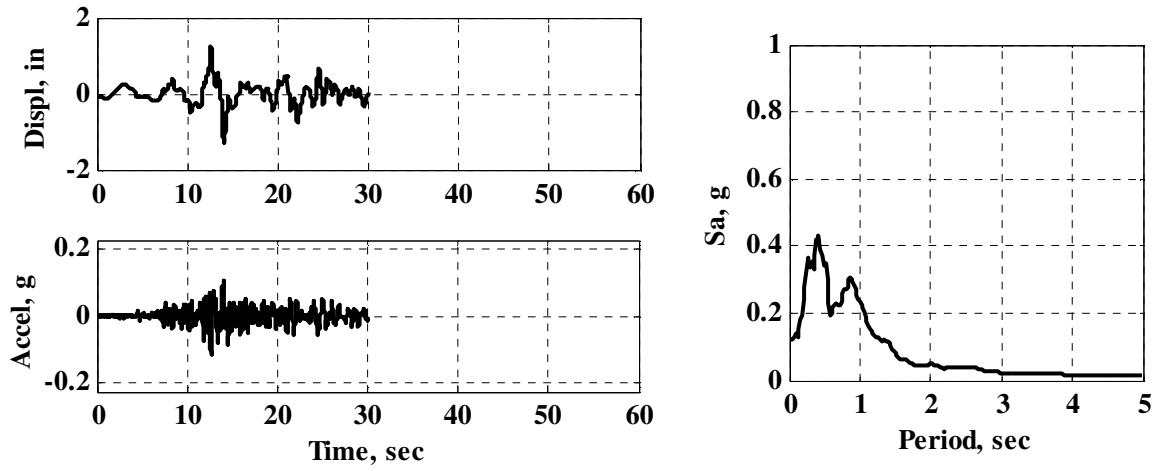
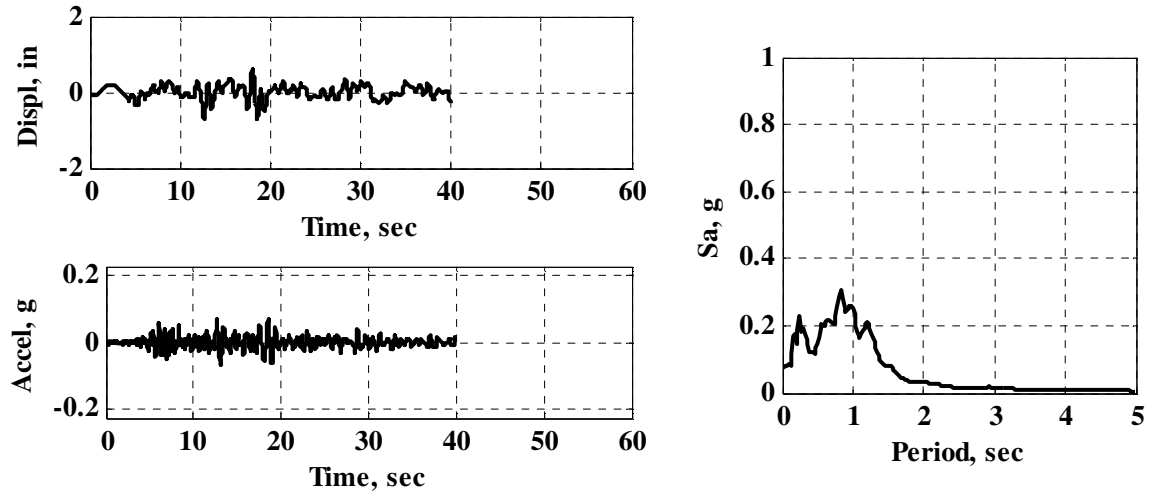


Figure A.8 ADINA versus Perform-3D Dynamic Time History Response Comparison

Appendix B – Seismic Ground Motion Recorded at VTB Site

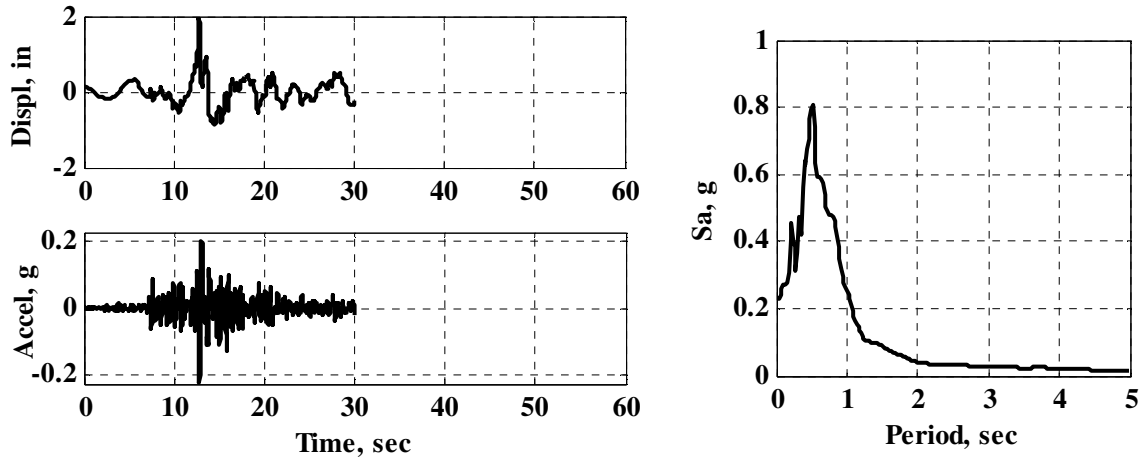


(a) 1994 Northridge Earthquake

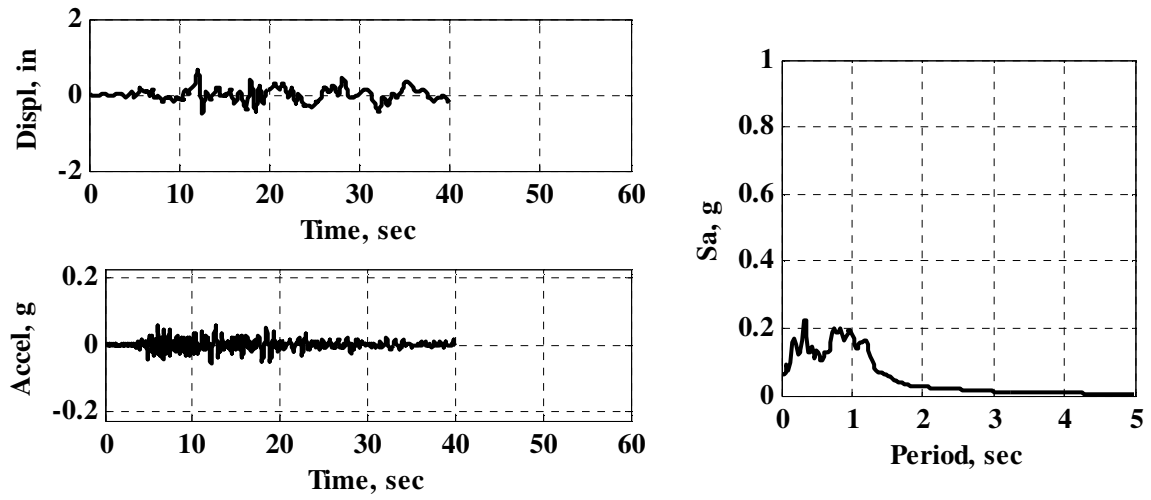


(b) 1987 Whittier Earthquake

Figure B.1 Moderate-level Site Recorded Earthquakes, West Longitudinal

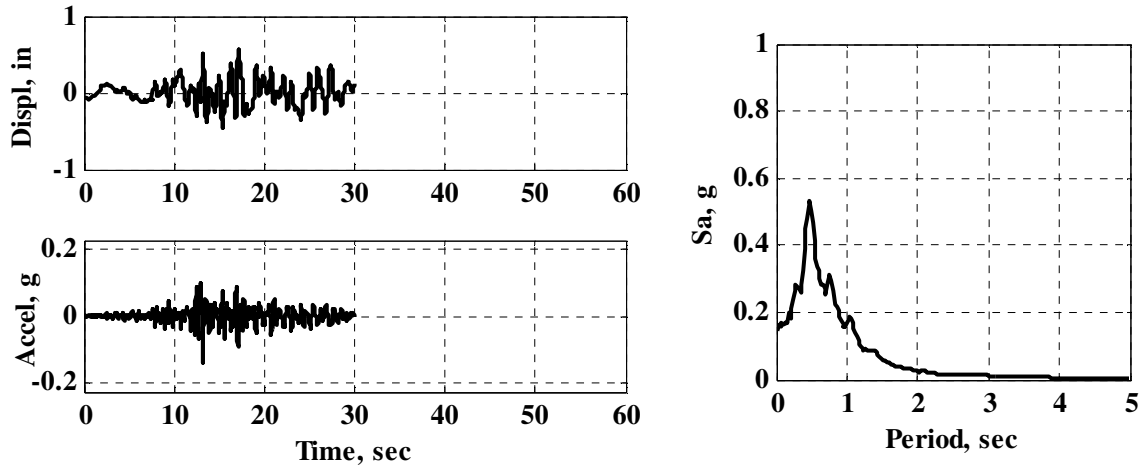


(a) 1994 Northridge Earthquake

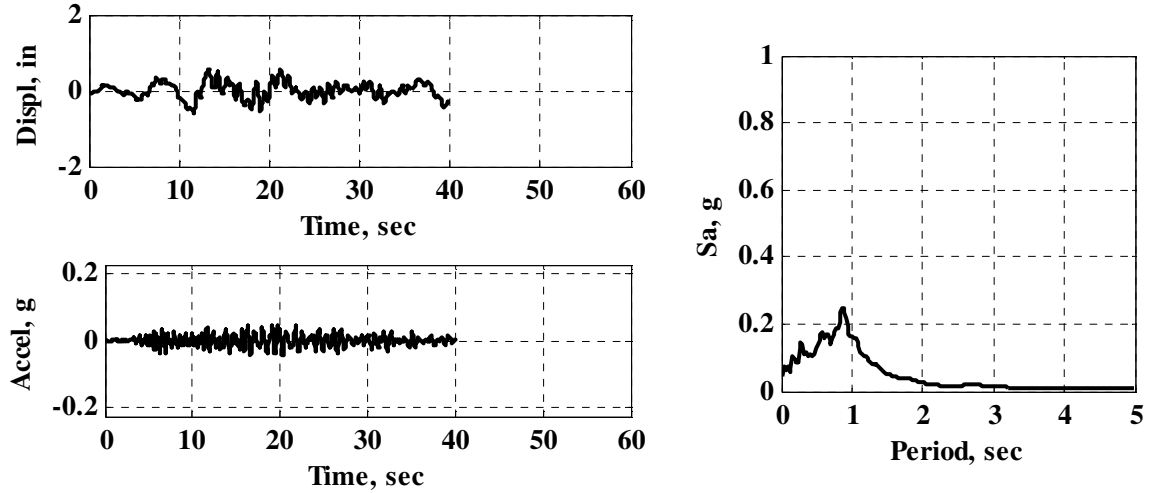


(b) 1987 Whittier Earthquake

Figure B.2 Moderate-level Site Recorded Earthquakes, East Longitudinal

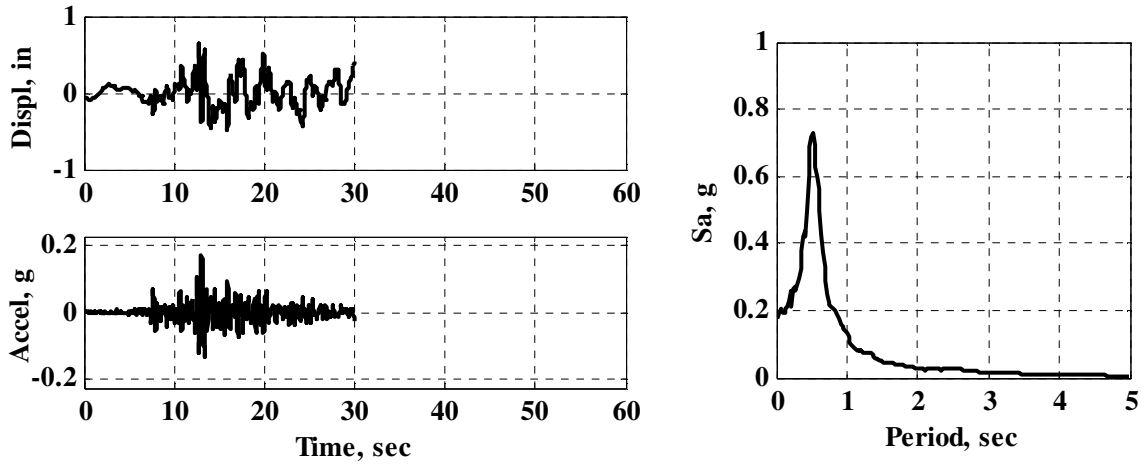


(a) 1994 Northridge Earthquake

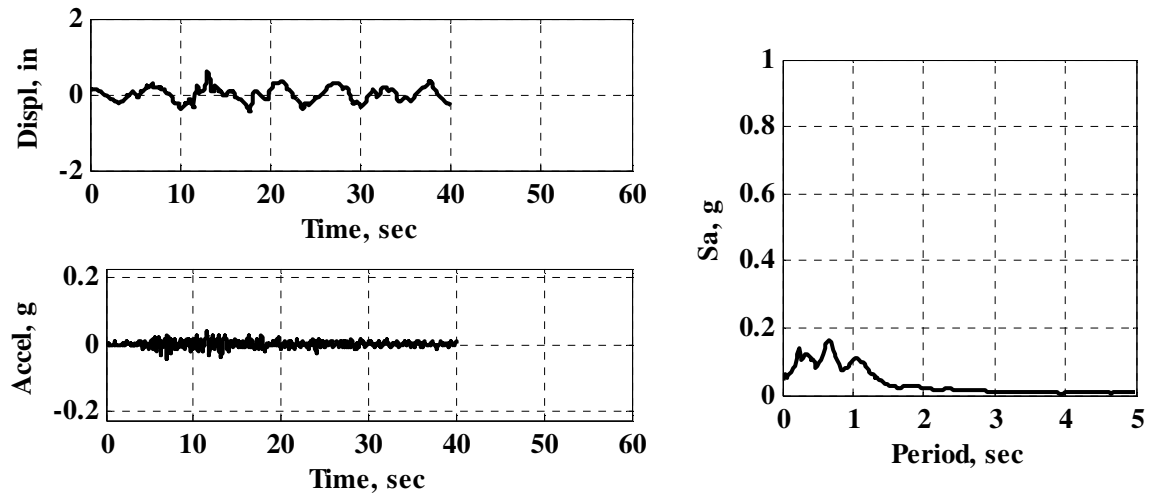


(b) 1987 Whittier Earthquake

Figure B.3 Moderate-level Site Recorded Earthquakes, West Transverse

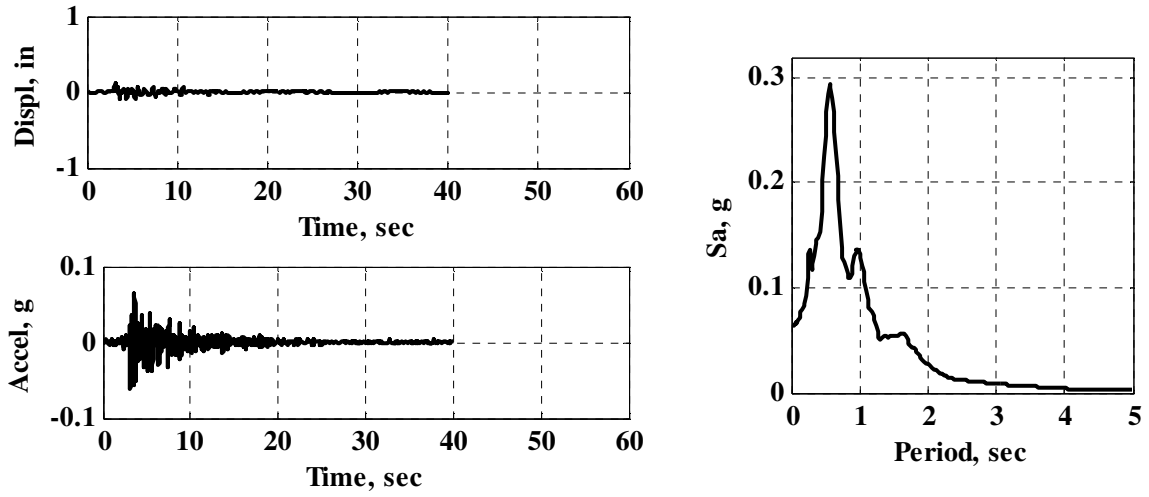


(a) 1994 Northridge Earthquake

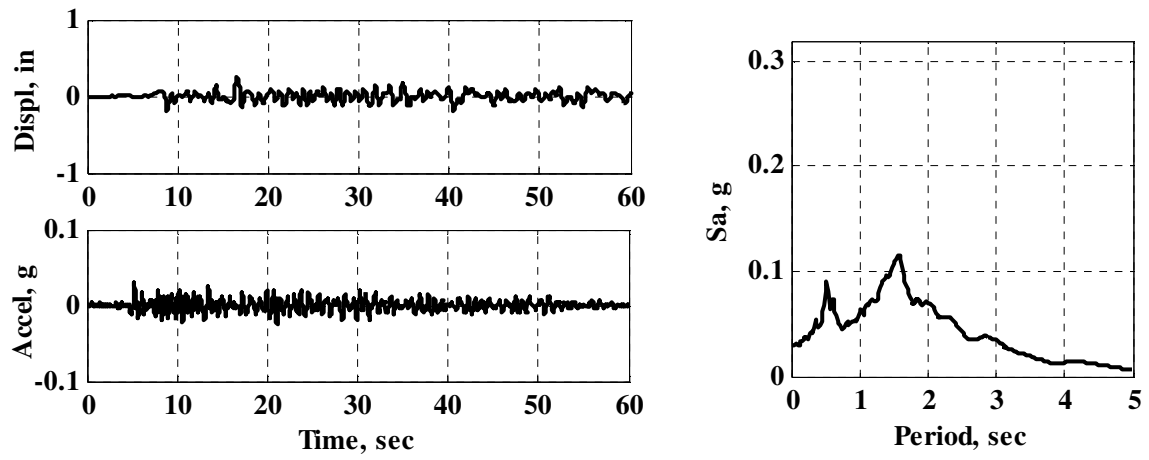


(b) 1987 Whittier Earthquake

Figure B.4 Moderate-level Site Recorded Earthquakes, East Transverse

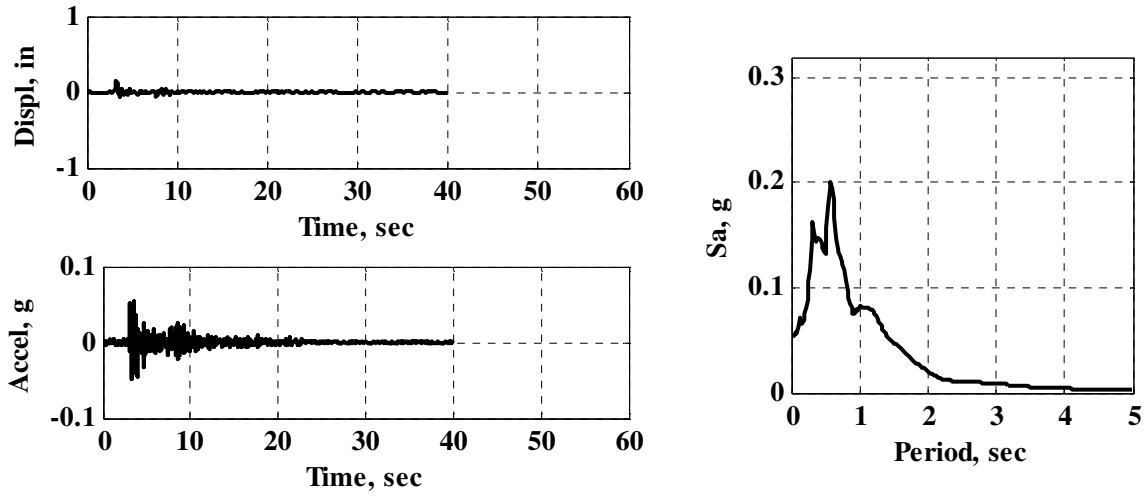


(a) 2009 Inglewood Earthquake

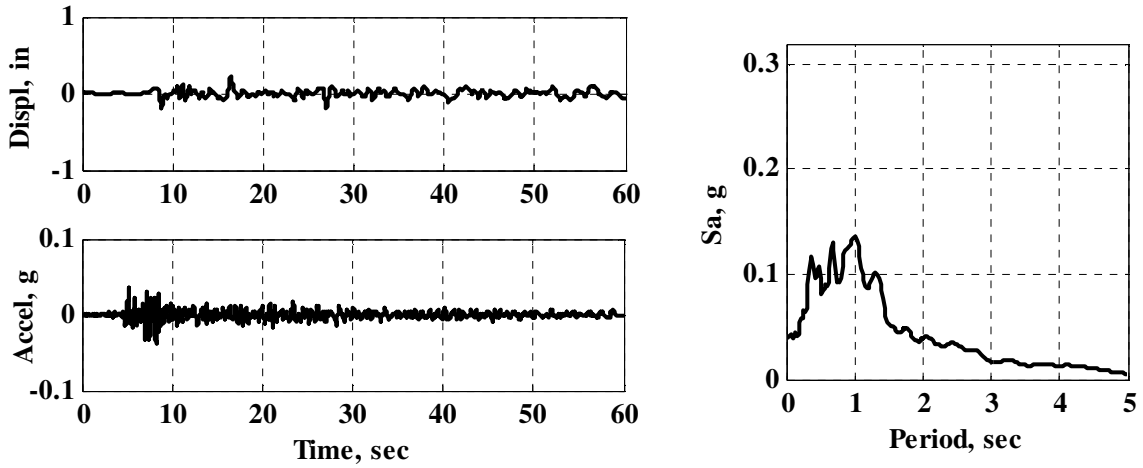


(b) 2008 Chino Hills Earthquake

Figure B.5 Low-Level Site Recorded Earthquakes, West Longitudinal

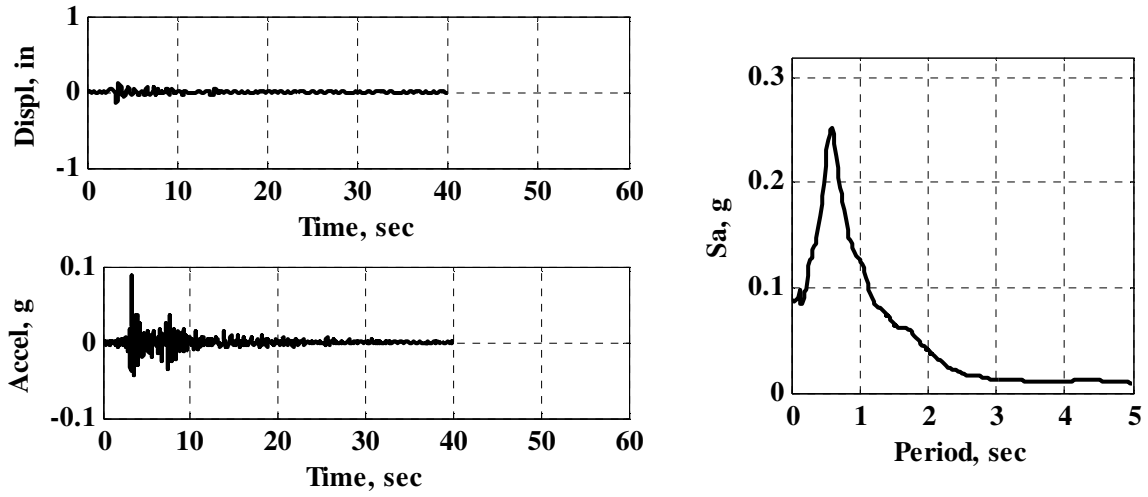


(a) 2009 Inglewood Earthquake

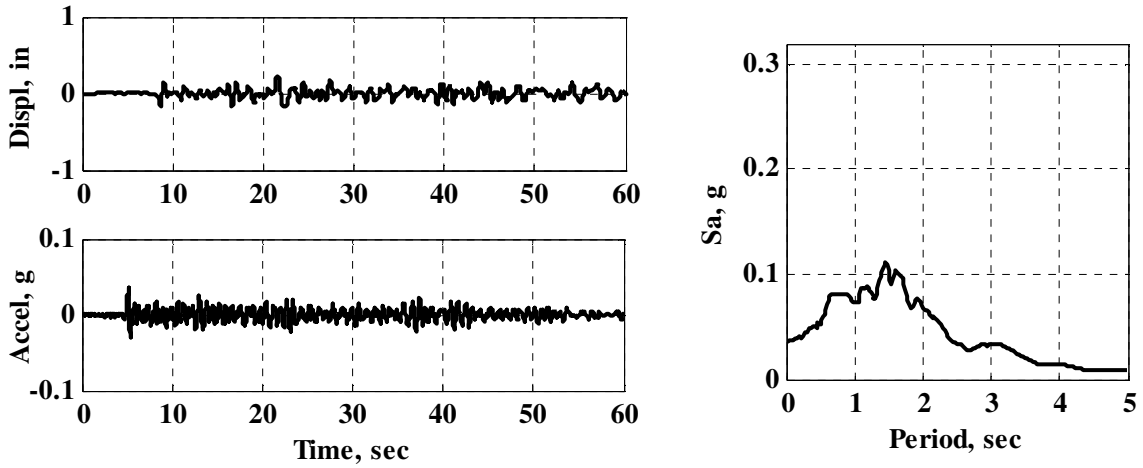


(b) 2008 Chino Hills Earthquake

Figure B.6 Low-Level Site Recorded Earthquakes, East Longitudinal

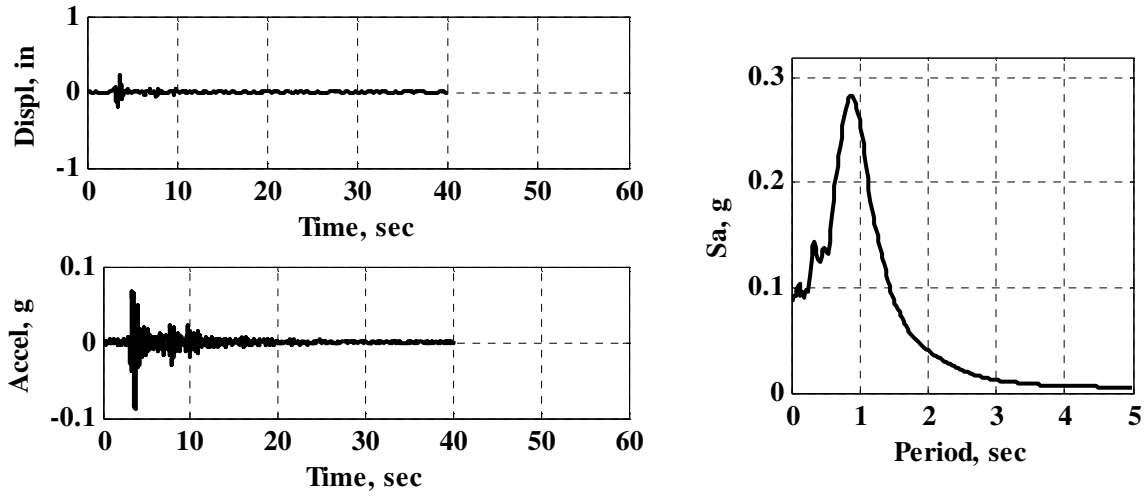


(a) 2009 Inglewood Earthquake

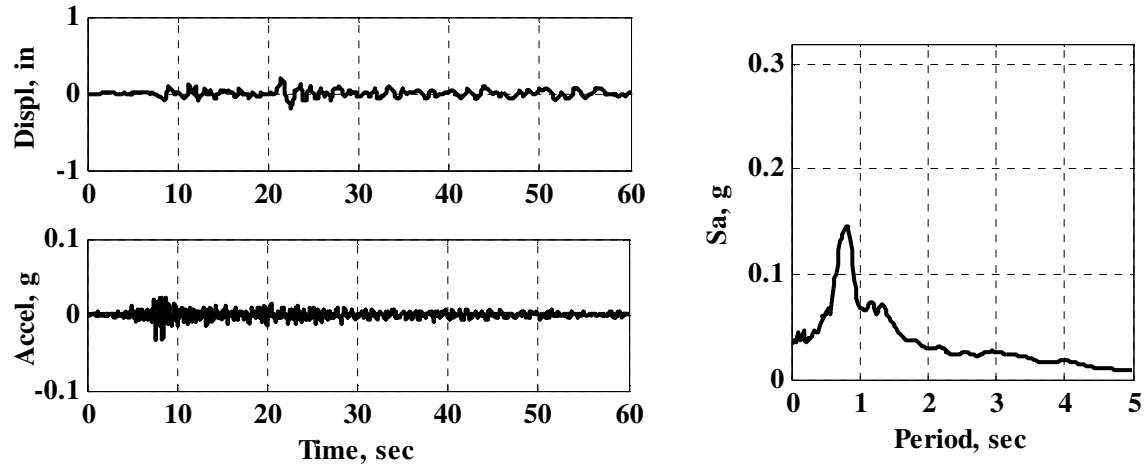


(b) 2008 Chino Hills Earthquake

Figure B.7 Low-Level Site Recorded Earthquakes, West Transverse



(a) 2009 Inglewood Earthquake



(b) 2008 Chino Hills Earthquake

Figure B.8 Low-Level Site Recorded Earthquakes, East Transverse

Appendix C – Additional Serviceability Considerations

C.1 Introduction

This appendix is provided as a supplement to the report “The Feasibility of Using Buckling-Restrained Braces for Long-Span Bridges: A Case Study”. The purpose of the addendum is to investigate the performance of the proposed BRBs due to vehicular live load applied to the bridge and to provide an additional fatigue analysis to complement the previous ambient demand analysis.

Since the live load conditions considered consist of transient traffic loading along the span of the bridge, influence lines allow a convenient method for evaluating the BRB response with loading at any location. In the VTB ADINA model a line load, of 1 kip total, positioned transversely across the bridge was used to create the axial stress influence lines for each BRB. Figure C.1 provides an illustration of the loading condition. Figure 2.C and Figure 3.C show the influence lines for the West and East BRB respectively. The axial stress due to a load at any point along the bridge can be estimated by multiplying the load by the stress value from the curve at the appropriate location. These curves also provide a clear way of identifying the most likely live load pattern to obtain the maximum axial stress.

C.2 AASHTO Fatigue Assessment

A fatigue assessment is presented in this appendix to supplement the one presented in the main body of the report. The primary assumption in the previous analysis is avoided with the use of the influence line diagrams, which allow for an estimate of BRB stress demands from ADINA model analysis rather than from uncorrelated field measurements.

The AASHTO procedure discussed in Section 5.2 of the report is followed with the fatigue force effect, Δf , found using the fatigue truck load described in Section 3.6.1.4.1 of the AASHTO Specifications. The fatigue truck is found as:

$$\text{Fatigue Truck} = 72 \text{ kips (IM)} (\gamma) \quad (\text{Eq. C2.1})$$

where IM = Dynamic Load Allowance

= 1.15 for Fatigue and Fracture Limit States

γ = Fatigue Load Factor

= 0.75

The above equation results in a fatigue truck load of 62.1 kips. The fatigue loading procedure in AASHTO requires the evaluation of only one fatigue truck passing.

In this simplified analysis the truck is assumed as a point load based on the fact that the truck is specified to be 44 ft, at the longest, which is less than 10% and less than 3% of the side and main span lengths, respectively. This simplification also represents a somewhat conservative assumption. Therefore, the truck point load can be applied directly to the influence lines to obtain an estimated BRB axial stress for each location. An estimate of the cyclic stress is found, then, by passing the point load over each influence line. The stress is found by multiplying the truck point load by the influence line stress value, since it was obtained from a unit load.

Table C.1 provides a summary of the maximum tensile and compressive stress which would result from the fatigue truck crossing the bridge. Each stress range is well below that of the 24 ksi threshold stress for base metal, and the BRB again is determined to possess a theoretical infinite fatigue life.

C.3 AASHTO Factored Live Load Assessment

The AASHTO Specification requires the consideration of many load combinations for the design of new bridge structures. These include strength and serviceability combinations, among others. The performance of the proposed BRB under the application of live load is important for their implementation.

This section discusses the application of the Service II load combination per AASHTO Section 3.4.1, which is aimed at limiting yielding in steel structures. The loading consists of dead load (DL) and transient vehicular live load (LL) which are then combined with a LL load factor of 1.3, resulting in a combination of DL + 1.3LL. The transient live load for Service II is vehicular loading on the lanes of the bridge. AASHTO Section 3.6.1.3 describes that the design vehicular live load shall be taken as the

application of the design truck in addition to the design lane load positioned along the traffic lanes to result in the maximum stress for each component under consideration.

The design truck is the HS20-44, which consists of one 8-kip and two 32-kip axels, which is applied on the lanes in any combination that results in the maximum stress for the components. Again, the design truck can reasonably be assumed as a point load, and directly applied at the point on the influence line diagram that results the greatest BRB stress. Furthermore, the design lane load is defined as 640 lbs/ft per lane and should be applied in any combination that results in the maximum stress for the components. In addition to applying the loads to yield the maximum stress demand, the number of loaded lanes loaded is also required to be considered.

All lanes are loaded to produce maximum demand in the analysis. This is the case despite the permitted multiple presence factors given in AASHTO Section 3.6.1.1.2. The force effect being evaluated is reduced by the multiple presence factor of up to 0.65 for 4 lanes of traffic. This factor was applied to both the design truck and design lane loads, in accordance with the AASHTO recommendations.

Finally, the design truck load is required to be increased by the dynamic load allowance factor of 1.33. This factor combined with the live load factor of 1.3, result in a 173% increase for the design truck load. This may represent a very conservative estimate for evaluation of an existing bridge.

The influence line diagrams provide a clear guide for loading combinations which are likely to cause maximum axial stress in each BRB. Figure C.4 displays the three considered cases. Figure C.4(a) and Figure C.4(b) contain the loading patterns that should yield the maximum stress values in both the S-C and S-T BRBs. Figure C.4(c) contains the same but for the M-T BRB. The loading patterns have been analyzed within the ADINA model as nonlinear static analyses. These are performed, in lieu of directly multiplying the loads by the influence line values, because of the nonlinearity of the BRB elements. If the stresses found via the influence lines exceed the yield stress of the BRB, the values would be based only on the BRB initial axial stiffness (as the influence line loading does not yield the BRB elements). This would result in very large values which would provide little useful information.

Table C.2 displays the resulting ultimate stress values obtained from the loading schemes in Figure C.4. For the maximum factored loading, all locations besides the S-C exhibit stresses slightly beyond that which would cause yielding in the BRB (the nominal yield stress for the considered BRB is 36 ksi). As mentioned above, the LL combination load factors and traffic positions are used in design to represent the ultimate stress demands for the bridge components. Therefore these are very conservative estimates of the likely conditions to actually occur on the bridge. Table C.2 also presents the results obtained without these load factors. A moderate decrease in the maximum stresses is observed, and perhaps provides a more realistic worst case loading scenario for live load stress in the BRBs. Furthermore, it is important to note the very limited ductility that these stress ranges represent. Table C.2 also shows the ductility demand for each maximum stress level. Recall the cumulative ductility achieved by test specimens, in Section 2 of the main report, is in the range of 200 to 1,000. Therefore, it is clear that the ultimate live load ductility demands are far lower than what is typically provided by BRBs.

C.3.1 Additional Live Load Considerations

Despite the low ductility demand due to the full Service II condition, AASHTO Section 3.4.1 , the live load effects have been further studied. Direct scaling of the design lane load, truck load, or both together has been considered to obtain the amount of live loading that allows the BRB to remain elastic. Scaling all Service II live load together in equation form can be represented as:

$$DL + \alpha_1 [\gamma_L \times \text{Lane} + \gamma_L \times (\text{IM}) \times \text{Truck}] \quad (\text{Eq. C3.1})$$

where α_1 = Service II Live load scale factor.

Recall that γ_L , Lane, IM, and Truck have all been previously defined, for Service II, in this Appendix.

In addition to using the patterned load (see Figure C.4), the case of design lane load over the entire length of the bridge was also considered (see Figure C.5). This was

performed to investigate the compensation effect of the positive influence line ordinates on the stresses obtained from the conservative patterned loading.

With the same design live loads considered in the previous section, the results from applying the live load scale factor are presented in Figure C.6 and Figure C.7, (a) and (b), for the patterned loading and full length lane loading, respective to (a) and (b). Even though the full Service II condition results in minor ductility demand, the BRB are elastic only up to a minimum of about $\alpha_1 = 40\%$, as seen in Figure C.6(a). If the full bridge length is considered loaded by the design lane load the BRB are elastic up to $\alpha_1 = 50\%$ approximately. These results are presented in Figures C.6(b) and Figure C.7(b). These analyses made evident the fact that the design lane loading was the dominate contributor to the BRB stress.

Another loading combination was explored which was motivated by AASHTO Section 3.6.1.3.2 which is titled “*Loading for Optional Live Load Deflection Evaluation*”. The commentary for this section explains that the live loads required in the current specifications are greater than in previous versions, particularly when considering live load deflections. Additionally, as Section C2.5.2.6.1 indicates, live load deflection is a service condition and does not appear to present adverse effects on bridges designed under previous AASHTO specifications. Therefore, a reduced loading is recommended, by AASHTO Section 3.6.1.3.2, for the evaluation of live load deflection. When the design lane load controls, which is the case for BRB stress evaluation, this load is suggested as the design lane plus 25% of the design truck. With this reduced design truck load, (Eq. C3.1) is:

$$DL + \alpha_2 [1.0 \times \text{Lane} + 1.0 (1.33) (0.25 \times \text{Truck})] \quad (\text{Eq. C3.2})$$

where α_2 = Live load deflection loading scale factor

There are several reasons that support the use of this reduced loading. Per AASHTO Section 2.5.2.6.2 Service I is considered as normal operation plus 55 mph wind loading. Service I uses a load factor for both dead and live load to 1.0, which matches the description in Section 3.6.1.3.2. It is also reasonable to consider the effect of wind on the

BRB as negligible for the current discussion. Additionally, the BRB are not intended to resist gravity loads and are intended only to provide energy dissipation from longitudinal motion of the bridge deck. The vehicular loading causes vertical deflection of the bridge spans which are essentially pinned at their ends, see Figure C.10. This photograph shows the hinge that allows the ends of these spans to act mostly as a pinned-pinned beam. Therefore, any vertical deflection along the span will create a rotation at the ends, where the BRB are attached, and translates into axial deformation in the BRB. Figure C.11 further illustrates this deformation relationship. The BRB are not sufficiently strong or stiff enough to appreciably resist this type of bridge deformation, as this is not their intended use. Therefore, the live load deflection is actually the mechanism driving the axial deformation demand in the BRB under live load service condition..

The results from this reduced loading scheme are provided in Figures C.8 and C.9. Figures C.8(a) and C.9(a) show the increase in elastic BRB live load to a minimum of about $\alpha_2 = 60\%$ under patterned loading. The corresponding analyses using the fully loaded bridge length provide a higher amount of live load around $\alpha_2 = 80\%$ for the S-T BRB and $\alpha_2 = 100\%$. This suggests that under more realistic (but still conservative, as all four lanes are fully loaded) live loading the BRBs are very close to remaining elastic.

C.3.2 Horizontal versus Inclined BRB

As discussed above, rotation of the stiffening trusses at their ends due to vertical deflection at mid-span causes longitudinal translation at the BRB connection. This motivates the investigation of inclining the BRB to force the longitudinal translation component to become less influential on the BRB axial deformation, as the vertical translation component is much smaller due to geometry (see Figure C.11).

One final consideration was investigated by slightly rotating the BRB orientation. This is schematically represented in Figure C.12. Currently the BRB are positioned completely parallel with the stiffening truss chords which causes the end rotation longitudinal translation component to be almost entirely equal to the axial deformation in the BRB. This can be alleviated by simply rotating the orientation of the BRB, such that the axial deformation will be oriented at an angle with the longitudinal component of the rotation. The S-T BRB is the worst case from the previous analyses, and was inclined

approximately 20 degrees to investigate the benefit. Figure C.13 shows the significant benefit, increasing α_2 from 40% to 60%. This is a consideration that could be further explored in efforts towards the BRBs actual implementation.

Table C.1 Fatigue Stress Demands Due to AASHTO Fatigue Truck

BRB	Max. Tensile Stress (ksi)	Max. Compressive Stress (ksi)	Stress Range* (ksi)
S-C	0.8	2.9	3.7
S-T	4.6	6.4	7.2
M-T	4.2	5.3	7.0

* Maximum tension and compression do not typically occur in the same BRB

Table C.2 Vehicular Live Load BRB Maximum Stress and Ductility Demands

BRB	Live Load LL (ksi)	Ductility ϵ	IM (γ LL) 1.33 (1.3 LL) (ksi)	Ductility ϵ
S-C	16.5(16.2)	0	17.5	0
S-T	43.3(42.8)	1.9	45.4	3.5
M-T	42.3(42.1)	1.1	44.0	2.4

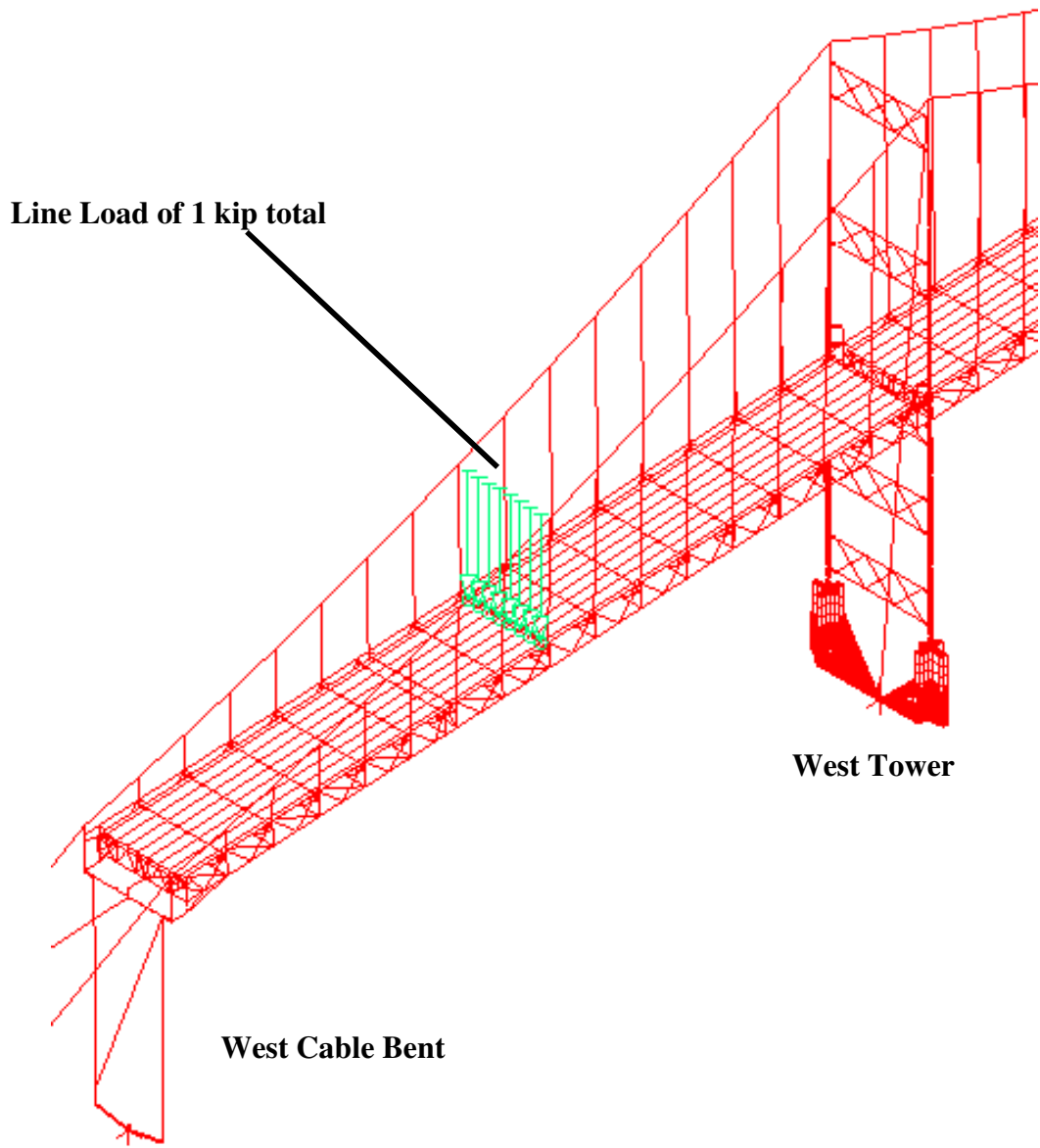
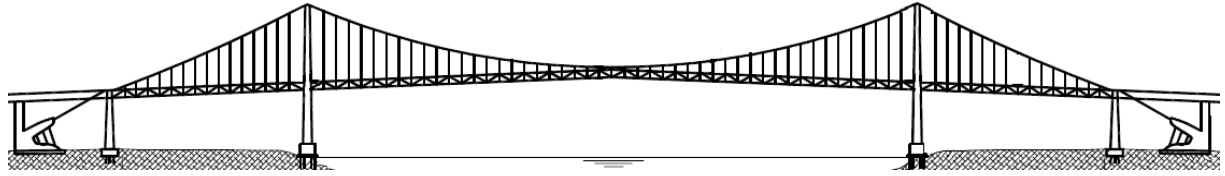


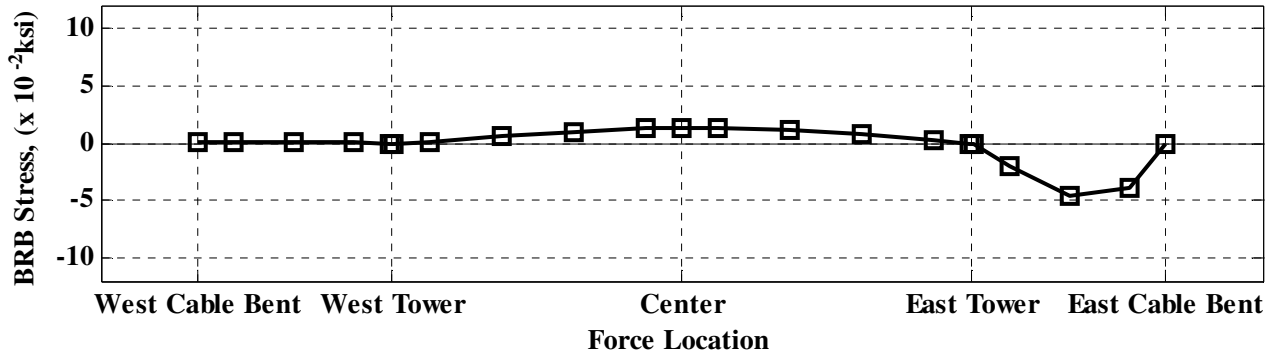
Figure C.1 VTB Influence Line Loading



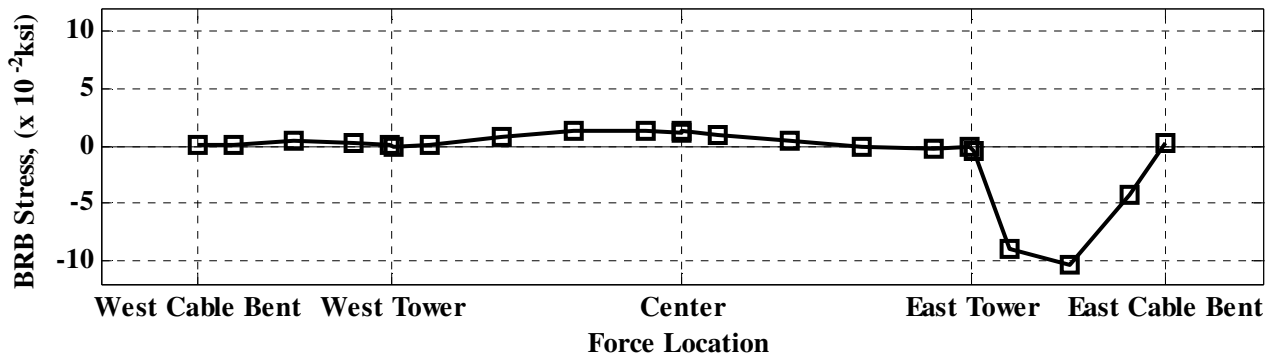
West Cable Bent West Tower

East Tower East Cable Bent

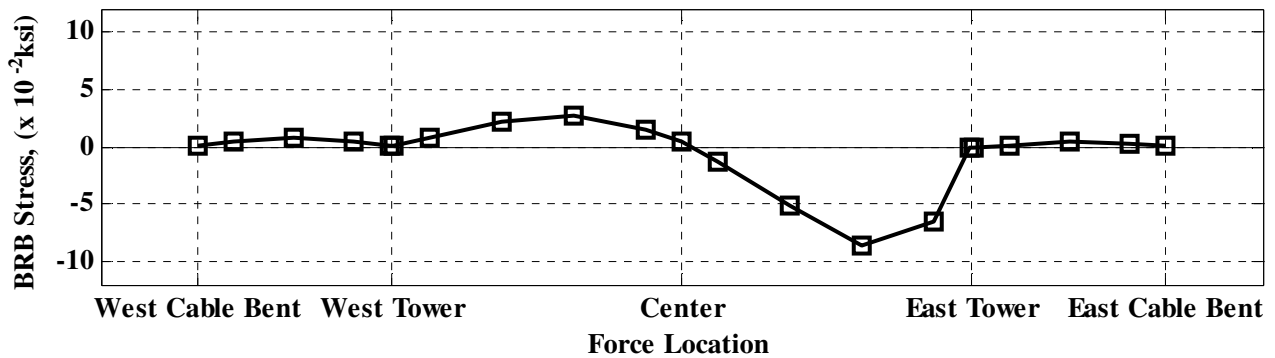
(a) VTB Elevation View



(b) East S-C BRB

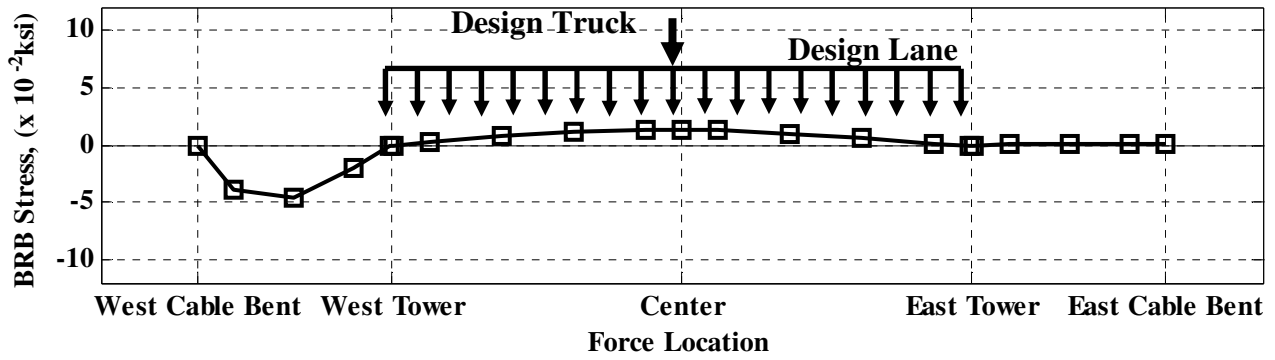


(c) East S-T BRB

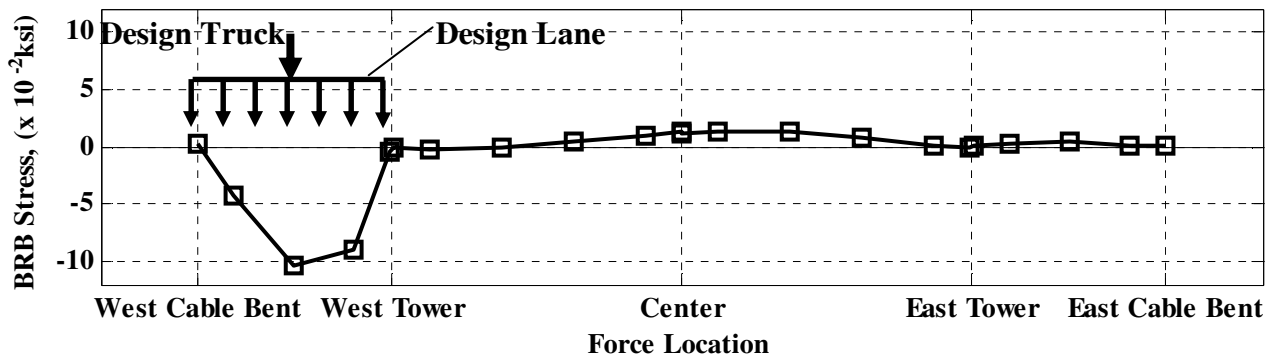


(d) East M-T BRB

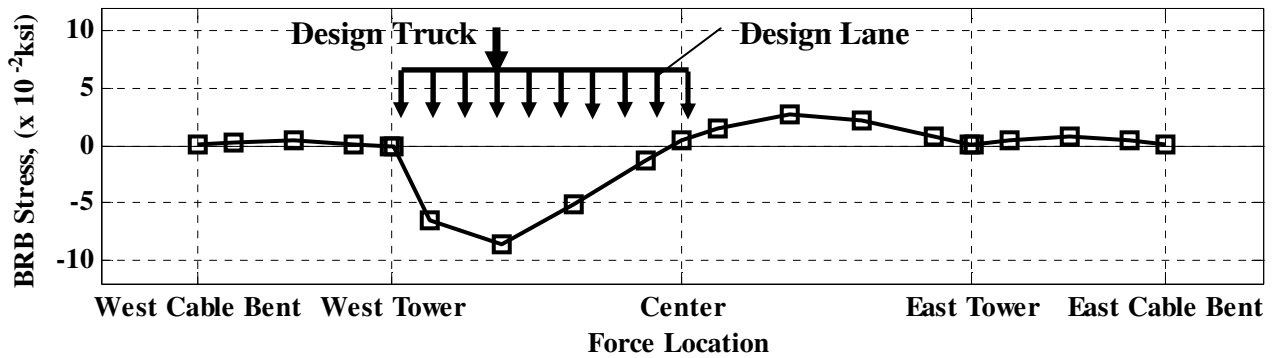
Figure C.3 East Side BRB Axial Stress Influence Lines, 1 kip Line Load



(a) S-C and S-T BRB Pattern 1

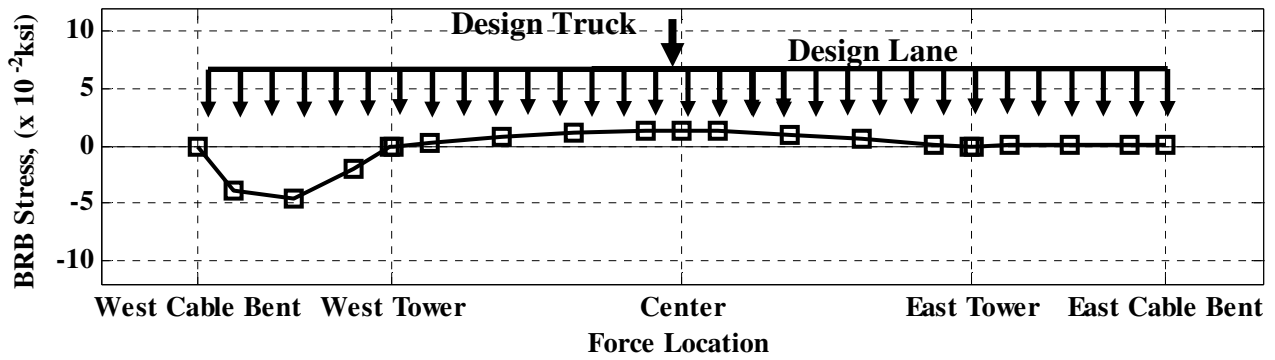


(b) S-C and S-T BRB Pattern 2

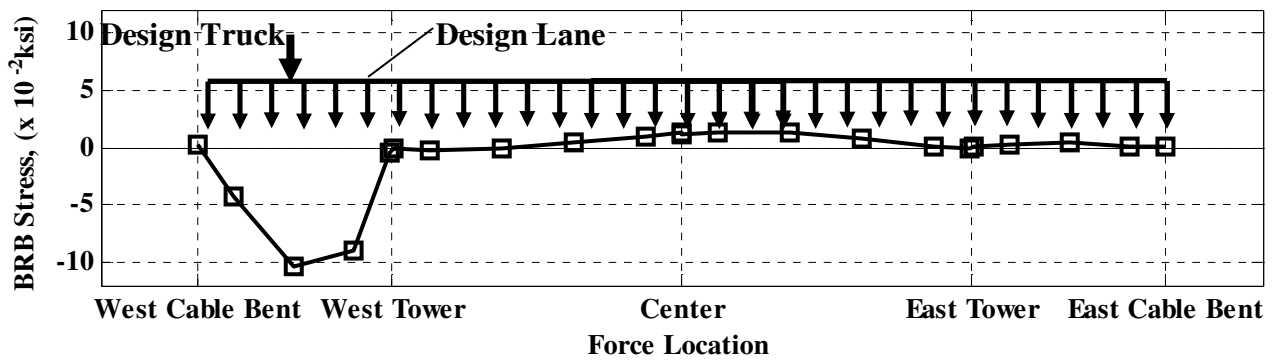


(c) M-T BRB Pattern

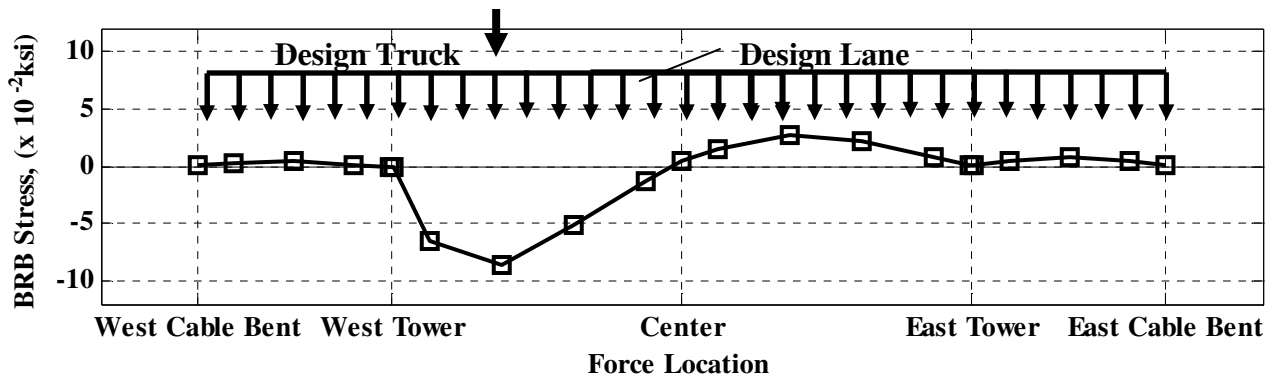
Figure C.4 Live Load Maximum Force Effect Patterns



(a) S-C and S-T BRB Pattern 1

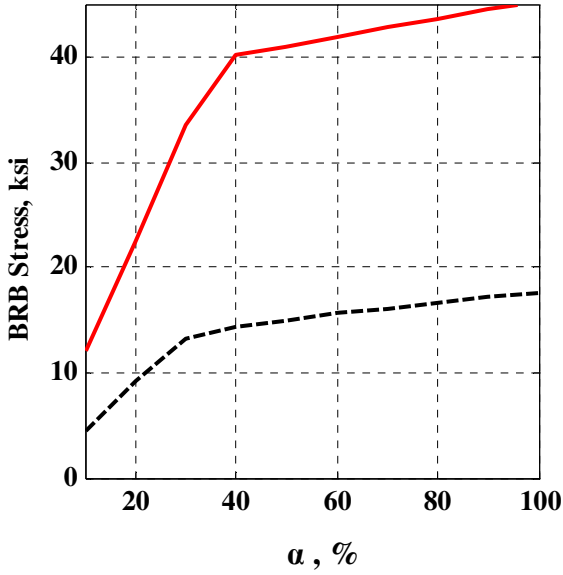


(b) S-C and S-T BRB Pattern 2

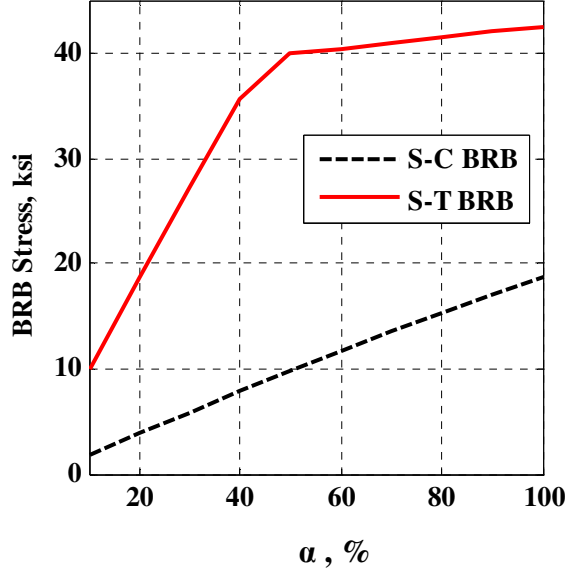


(c) M-T BRB Pattern

Figure C.5 Live Load Maximum Force Effect Continuous Lane Patterns

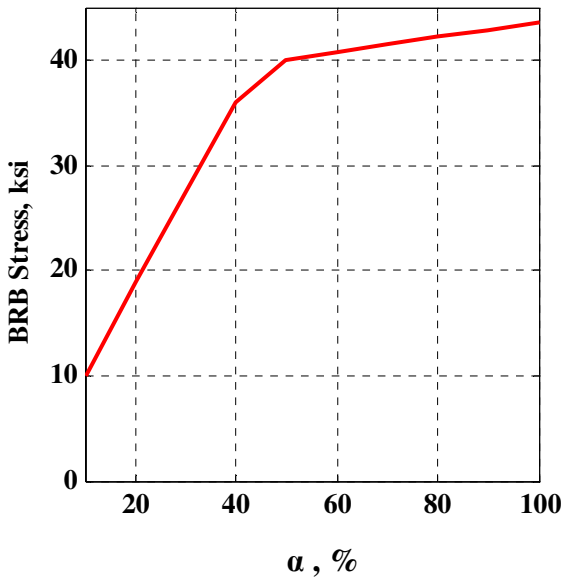


(a) Patterned Lane Loading
(see Figure C.4)

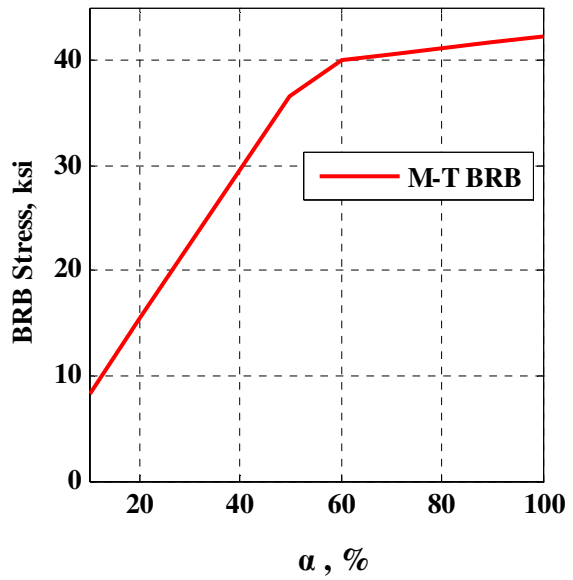


(b) Continuous Lane Loading
(see Figure C.5)

Figure C.6 BRB Stress with Live Load Scale Factor, Service II Load Pattern 2

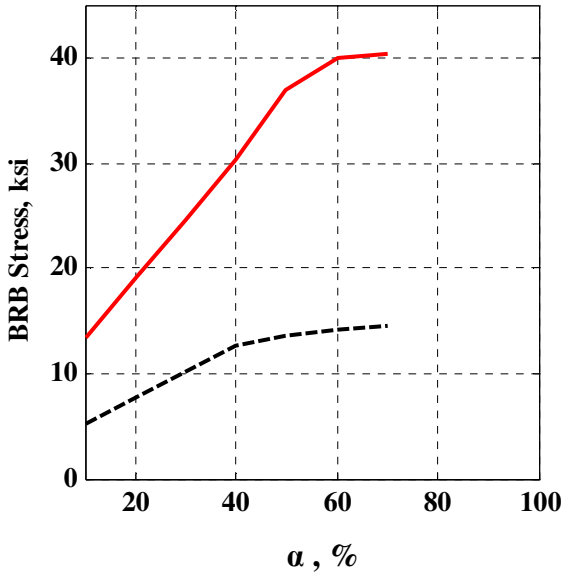


(a) Patterned Lane Loading
(see Figure C.4)

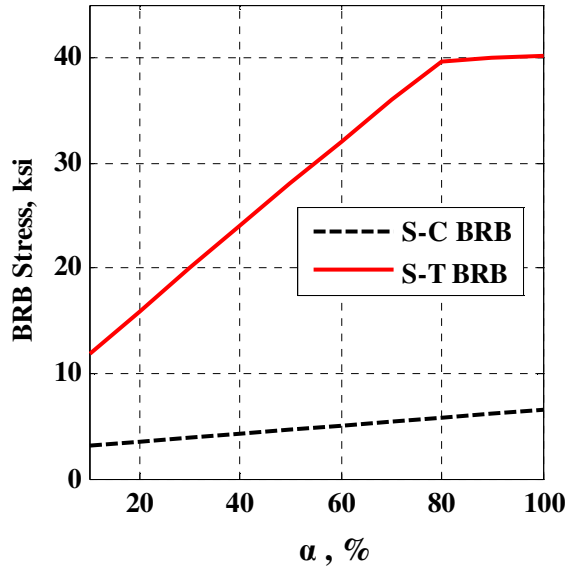


(b) Continuous Lane Loading
(see Figure C.5)

Figure C.7 BRB Stress with Live Load Scale Factor, Service II Load Pattern 3

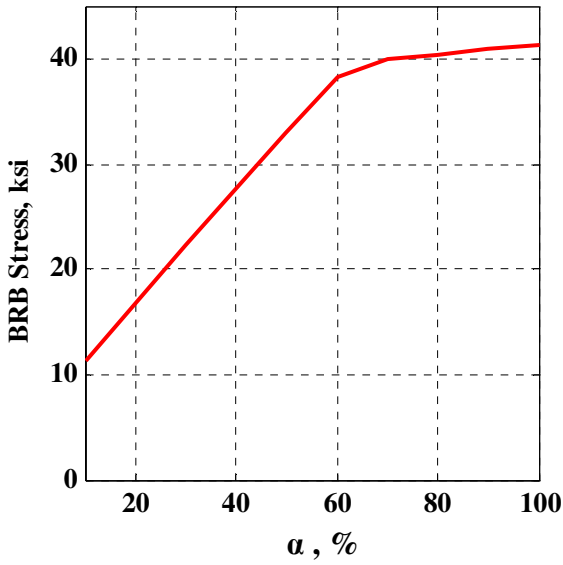


(a) Patterned Lane Loading
(see Figure C.4)

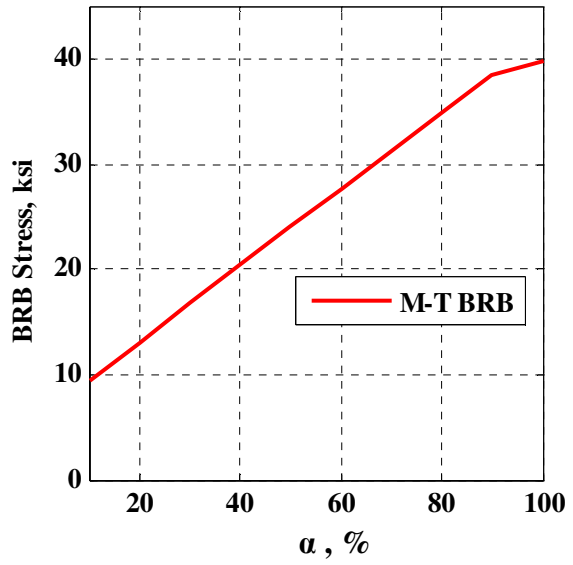


(b) Continuous Lane Loading
(see Figure C.5)

Figure C.8 BRB Stress with Live Load Scale Factor, Live Load Deflection Pattern 2



(a) Patterned Lane Loading
(see Figure C.4)



(b) Continuous Lane Loading
(see Figure C.5)

Figure C.9 BRB Stress with Live Load Scale Factor, Live Load Deflection Pattern 3



Figure C.10 Main and Side Span End Hinges

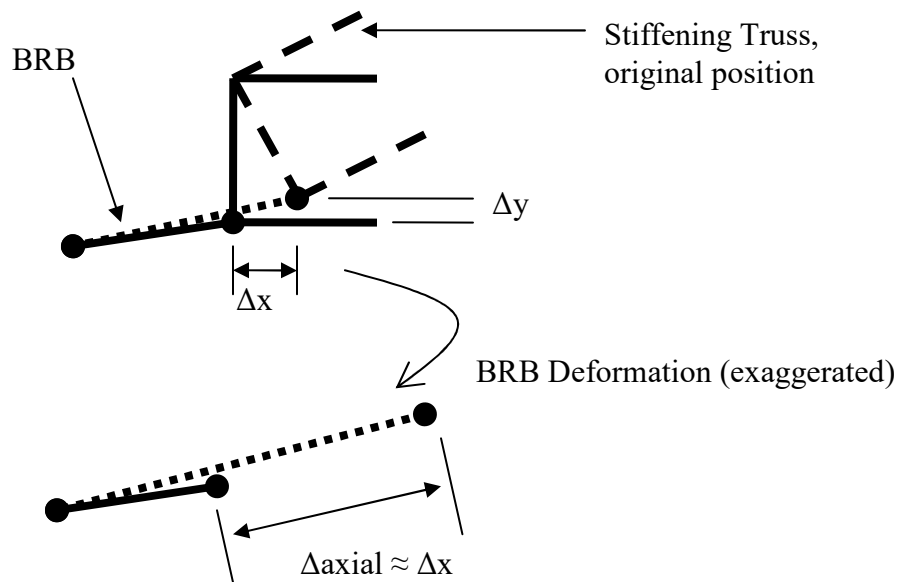


Figure C.11 Illustration of Truss Rotation to BRB Axial Deformation

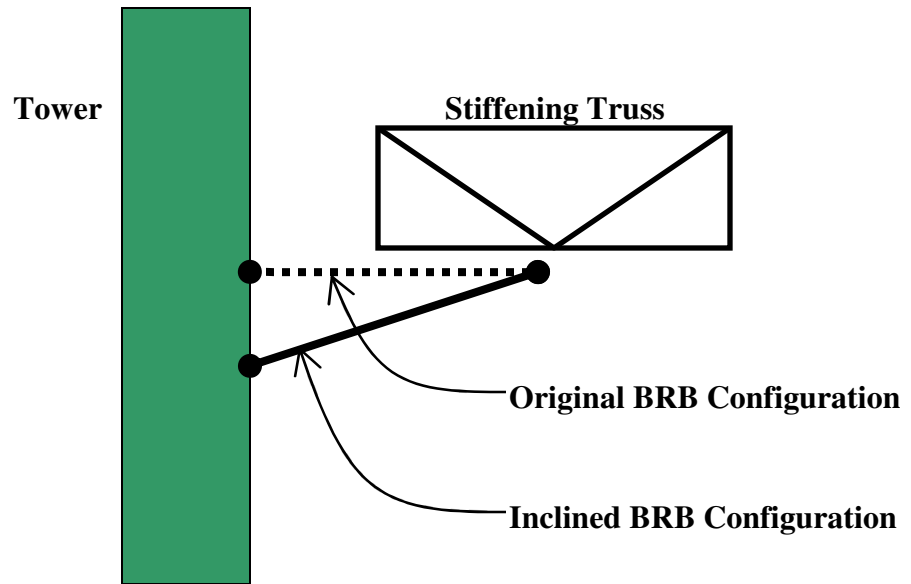


Figure C.12 Schematic Representation of Inclined BRB Orientation

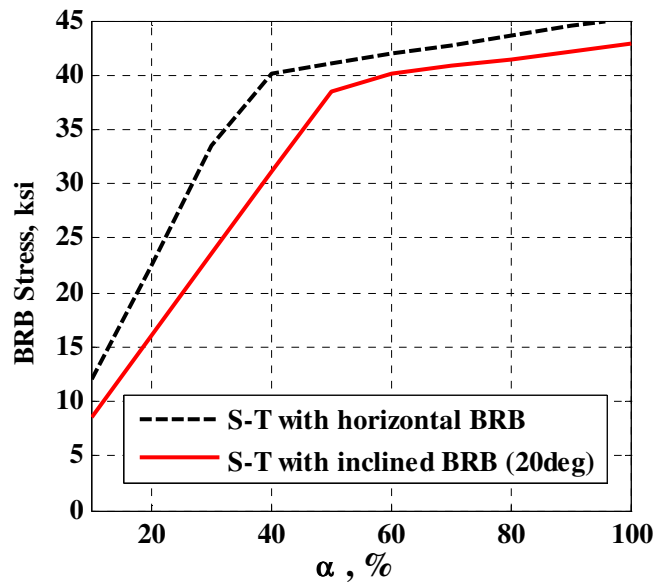


Figure C.13 Effect of BRB Inclination